

X-RAY IMAGING OF SUPERCONDUCTING RADIO FREQUENCY CAVITIES

By

Susan Elizabeth Musser

A DISSERTATION

Submitted to  
Michigan State University  
in partial fulfillment of the requirements  
for the degree of

DOCTOR OF PHILOSOPHY

Department of Physics and Astronomy

2006

# ABSTRACT

## X-RAY IMAGING OF SUPERCONDUCTING RADIO FREQUENCY CAVITIES

By

Susan Elizabeth Musser

The goal of this research was to develop an improved diagnostic technique to identify the location of defects that limit superconducting radio frequency (SRF) cavity performance during cavity testing or in existing accelerators.

SRF cavities are primarily constructed of niobium. Electrons within the metal of a cavity under high electric field gradient have a probability of tunneling through the potential barrier, *i.e.* leave the surface or are field emitted in regions where defects are encountered. Field emitted electrons are accelerated in the electric fields within the cavity. The electrons can have complicated trajectories and strike the cavity walls thus producing x-rays via Coulomb interactions and/or bremsstrahlung radiation. The endpoint energy of an x-ray spectrum predicts the electron maximum final kinetic energy within the cavity. Field emission simulations can then predict the source of the field-emitted electrons and the defect(s).

In a multicell cavity the cells are coupled together and act as a set of coupled oscillators. There are multiple passbands of excitation for a multicell structure operating in a particular mode. For different passbands of operation the direction and amplitude of the fields within a cavity change from that of the normal accelerating mode. Field emitted electrons have different trajectories depending on the mode and thus produce x-rays in different locations.

Using a collimated sodium iodide detector and subjecting a cavity to multiple passband modes at high electric field gradient the source of a cavity's x-rays can be determined. Knowing the location of the x-rays and the maximum electron kinetic energy, field emission simulations for different passband modes can be used to deter-

mine and verify the source of the field emitted electrons from mode to mode. Once identified, the defect(s) can be repaired or modifications made to the manufacturing process.

Copyright by  
SUSAN ELIZABETH MUSSER  
2006



To Alex, De Anna, and Dustin Clark for encouraging me to follow my dreams too.



I thank god every day that all of my prayers have not been answered.



## ACKNOWLEDGMENTS

First, I thank my advisor Terry Grimm for his perseverance as I navigated the Ph.D. program. I thank him for taking a chance in me, a non-traditional student. When I joined the accelerator group, my goal was to gain experience that I could apply to the field of medical physics. The inspiration for this study came from him, and the work in x-ray imaging perpetuated my interest in medical physics.

Secondly, I thank Walter Hartung for his inexhaustible patience and support. He generously gave his time to discuss topics with me, most often multiple times. With his unselfish guidance, particularly in computer program revisions, I am completing this degree. It has been an honor to work with him. He is a true gentleman and scholar.

Next, the members of my dissertation committee, S. D. Mahanti, Felix Marti, Stan Schriber, and Kirsten Tollefson, I thank for patiently awaiting my completion.

Only I have read this dissertation more times than Renate Snider. I thank her over and over for the numerous critiques of my writings. She not only made the writing group an exhaustive punctuation and grammar lesson, but fun. I also thank her for the incorporeal box of hyphens and commas for my birthday.

I thank John Bierwagen for his input in the design of the x-ray imaging device. His initiation in constructing the device gave me the boost of confidence I needed to complete it. I also thank James Colthorp and Ahmad Aizaz for their help with the data acquisition system.

I could not have made it through this program without the support of friends Elaine Kwan and Chandana Sumithrarachchi. I am thankful for our many insightful conversations in the use of ORIGIN and Latex, as well as their tolerance of my eccentricities. They are true friends. I also thank friends Mark Wallace, for guiding me to the accelerator group, and Carla Gates, for encouraging me to attend Michigan State University.

Debbie Simmons was the physics undergraduate secretary when I was an undergraduate student. Around the time that she became the physics graduate secretary, I became a graduate student. I hope she never has to tolerate another student as long she has tolerated me. I thank her for the semesterly enrollment reminders, the course overrides, the required signatures, the answers to numerous questions about ... everything.

I thank Doug Harris, Allyn McCartney, Kurt Niemeyer, Dan Scott, Mark Stoddard, Shelly Villarreal, and Jim Vincent for teaching me their interpretation of Hoyle's rules of euchre. These lessons and memories I will cherish forever.

A special thank you goes to the Michigan State University Intercollegiate Figure Skating Team for accepting me, the oldest figure skater in the country, as a teammate and friend. The comradery and joy of skating I experienced with this group was not only instrumental in retaining my sanity but made my collegiate experience complete. For those that were of legal drinking age, thanks for including me.

Finally, I thank Alex, De Anna, and Dustin Clark, my children. They cannot remember a time when I was not engaged in some type of coursework. They have witnessed the anxiety, apprehension, and frustration that I experienced. The greatest pleasure of my life is supporting and encouraging my children as they pursue their dreams. I have recently come to the realization, that at the same time, they have supported and encouraged me to pursue mine. For this I am forever grateful.

# Contents

<b>1</b>	<b>Introduction</b>	<b>1</b>
<b>2</b>	<b>Background</b>	<b>5</b>
2.1	SRF Cavity Operation . . . . .	7
2.1.1	Electric Fields . . . . .	7
2.1.2	Field Emission . . . . .	18
2.1.3	X-rays . . . . .	26
2.1.4	Photon Interactions with Matter . . . . .	33
2.2	X-ray Detection . . . . .	46
2.2.1	Detector . . . . .	46
2.3	SRF Cavity Testing . . . . .	53
2.3.1	Modulated Wave . . . . .	54
2.3.2	Continuous Wave . . . . .	56
<b>3</b>	<b>Design</b>	<b>58</b>
3.1	Experimental Setup . . . . .	58
3.1.1	Cavity and Cryostat . . . . .	58
3.1.2	Detector and Collimator . . . . .	62
<b>4</b>	<b>Experimental Results</b>	<b>68</b>
4.1	Detector Calibration . . . . .	68
4.1.1	Energy . . . . .	68
4.1.2	Spatial Resolution . . . . .	69
4.1.3	Spectrum . . . . .	71
4.1.4	Detector and Collimator Performance . . . . .	73
4.2	Cavity Testing . . . . .	77
4.2.1	Cavity #2 Performance . . . . .	77
4.2.2	Cavity #2 $\pi$ Mode . . . . .	79
4.2.3	Cavity #2 $\frac{5\pi}{6}$ Mode . . . . .	86
4.2.4	Cavity #2 $\frac{4\pi}{6}$ Mode . . . . .	90
4.2.5	Cavity #1 Performance . . . . .	93
4.2.6	Cavity #1 $\pi$ Mode . . . . .	95
4.2.7	Cavity #1 $\frac{5\pi}{6}$ Mode . . . . .	97

<b>5</b>	<b>Simulations</b>	<b>101</b>
5.1	SUPERLANS . . . . .	101
5.2	Multipacting/Field Emission Simulation . . . . .	104
5.2.1	Program Operation . . . . .	107
5.2.2	Input Parameters . . . . .	107
5.2.3	Code Output . . . . .	115
<b>6</b>	<b>Comparison Between Data and Simulations</b>	<b>128</b>
6.1	Cavity #2 . . . . .	128
6.1.1	$\frac{5\pi}{6}$ Mode . . . . .	128
6.1.2	$\pi$ Mode . . . . .	131
6.1.3	$\frac{4\pi}{6}$ Mode . . . . .	133
6.2	Additional Field Emitters Cavity #2 . . . . .	136
6.3	Cavity #1 . . . . .	140
6.3.1	$\pi$ Mode . . . . .	140
6.3.2	$\frac{5\pi}{6}$ Mode . . . . .	142
<b>7</b>	<b>Discussion and Conclusion</b>	<b>146</b>
7.1	Summary . . . . .	146
7.2	Previous Work . . . . .	148
7.3	Future Work . . . . .	149
<b>A</b>	<b>Electromagnetic Fields</b>	<b>150</b>
A.1	Fields Within a Rectangular Waveguide . . . . .	150
A.2	Fields Within a Circular Waveguide . . . . .	155
A.3	Fields Within a Cavity . . . . .	158
<b>B</b>	<b>Field Emission</b>	<b>161</b>
B.1	Transmission Coefficient $D(W)$ . . . . .	161
B.2	Number of Electrons $P(W)$ . . . . .	166
B.3	Current Density $j$ . . . . .	168
B.4	RF Current $\langle I \rangle$ . . . . .	170
<b>C</b>	<b>Photon Interactions</b>	<b>172</b>
C.1	Compton Effect . . . . .	172
<b>D</b>	<b>Definitions</b>	<b>174</b>
<b>E</b>	<b>Floquet Theorem</b>	<b>177</b>
E.1	Derivation . . . . .	177
<b>F</b>	<b>Data and Endpoint Energy</b>	<b>183</b>
F.1	Cavity #2 $\pi$ Mode . . . . .	183
F.2	Cavity #2 $\frac{5\pi}{6}$ Mode . . . . .	184
F.3	Cavity #2 $\frac{4\pi}{6}$ Mode . . . . .	186
F.4	Cavity #1 $\pi$ Mode . . . . .	188
F.5	Cavity #1 $\frac{5\pi}{6}$ Mode . . . . .	189



# List of Figures

2.1	Rectangular Waveguide . . . . .	10
2.2	Circular Waveguide . . . . .	11
2.3	Electric and Magnetic Fields in a Cylindrical Cavity. . . . .	15
2.4	Single-Cell Cavity . . . . .	16
2.5	Six-Cell Cavity . . . . .	17
2.6	Surface Electric and Magnetic Fields . . . . .	18
2.7	Q and X-rays . . . . .	19
2.8	Discharge Tube . . . . .	19
2.9	Potential Barrier . . . . .	21
2.10	Image Force . . . . .	22
2.11	Bertha Roentgen's Hand . . . . .	27
2.12	Bremsstrahlung Radiation . . . . .	30
2.13	Kramers Approximation . . . . .	31
2.14	X-ray Angular Distribution . . . . .	32
2.15	Compton Scattering . . . . .	34
2.16	Compton Cross Section . . . . .	39
2.17	Photoelectric Process . . . . .	40
2.18	Photoelectric Cross Section . . . . .	41
2.19	Pair Production . . . . .	42
2.20	Pair Production Cross Section . . . . .	43
2.21	Photon Interaction . . . . .	44

2.22	Mass Attenuation . . . . .	45
2.23	Energy Bands . . . . .	47
2.24	Scintillator Detector . . . . .	48
2.25	Collimator . . . . .	51
2.26	Slit Spatial Resolution . . . . .	52
2.27	Gamma Camera . . . . .	53
2.28	Quality Factor Calculation . . . . .	55
3.1	Cryostat End View . . . . .	60
3.2	Cryostat Side View . . . . .	61
3.3	Device Overhead View . . . . .	63
3.4	Device Front, Back Views . . . . .	64
3.5	Device Photograph . . . . .	65
3.6	Wiring Diagram . . . . .	66
3.7	Collimator . . . . .	67
4.1	Detector Calibration . . . . .	69
4.2	Spatial Resolution . . . . .	70
4.3	X-ray Energy Spectrum . . . . .	72
4.4	Test Set-up . . . . .	74
4.5	Diagram of a Cryostat Scan . . . . .	76
4.6	Cavity #2, $\pi$ Mode, Q and X-rays <i>versus</i> Electric Field . . . . .	78
4.7	Cavity #2, $\pi$ mode, Fowler-Nordheim Field Enhancement Factor . . . . .	78
4.8	Cavity #2, $\pi$ Mode, Data . . . . .	80
4.9	Cavity #2, $\pi$ Mode, Energy Binning . . . . .	81
4.10	High Energy Binning . . . . .	82
4.11	Cavity #2, $\pi$ Mode, Endpoint Energy Linear Projection During Scan . . . . .	84
4.12	Cavity #2, $\pi$ Mode, Endpoint Energy Linear Projection Stationary . . . . .	85
4.13	Cavity #2, $\frac{5\pi}{6}$ Mode, Data . . . . .	87

4.14	Cavity #2 $\frac{5\pi}{6}$ Mode Energy Binning . . . . .	89
4.15	Cavity #2 Spectra Comparison of $\pi$ and $\frac{5\pi}{6}$ Modes . . . . .	89
4.16	Cavity #2, $\frac{4\pi}{6}$ Mode, Data . . . . .	91
4.17	Cavity #2, $\frac{4\pi}{6}$ Mode, Energy Binning . . . . .	92
4.18	Cavity #2 Spectra Comparison of $\pi$ , $\frac{5\pi}{6}$ , and $\frac{4\pi}{6}$ Modes . . . . .	92
4.19	Cavity #1, $\pi$ Mode, Q and X-rays <i>versus</i> Electric Field . . . . .	94
4.20	Cavity #1, $\pi$ Mode, Fowler-Nordheim Field Enhancement Factor . . . . .	94
4.21	Cavity #1, $\pi$ Mode, Data . . . . .	96
4.22	Cavity #1, $\pi$ Mode, Energy Binning . . . . .	97
4.23	Cavity #1, $\frac{5\pi}{6}$ Mode, Data . . . . .	99
4.24	Cavity #1, $\frac{5\pi}{6}$ Mode, Energy Binning . . . . .	100
4.25	Cavity #1 Spectra Comparison of $\pi$ and $\frac{5\pi}{6}$ Modes . . . . .	100
5.1	Cavity Mesh . . . . .	102
5.2	SUPERLANS Output Symmetric and Antisymmetric Wave Functions . . . . .	102
5.3	Electric Fields On Axis Six-Cell Cavity . . . . .	104
5.4	Surface Electric Fields . . . . .	105
5.5	Different Emitter Locations . . . . .	109
5.6	Different Peak Surface Electric Fields . . . . .	111
5.7	$\pi$ Mode Different Cell Same S0, and $\pm S0$ . . . . .	112
5.8	$\frac{4\pi}{6}$ Mode, Different Cell Same S0, and $\pm S0$ . . . . .	113
5.9	Different Mode Same S0 . . . . .	114
5.10	Electron Trajectories and Power Spectrum . . . . .	116
5.11	Simulated Power Spectra, Different Number of Field Emitted Electrons . . . . .	117
5.12	Simulated Power Spectra for Different Emitter Locations . . . . .	118
5.13	Simulated Power Spectra for Doubling $E_p$ . . . . .	120
5.14	$\pi$ Mode Simulated Power Spectra for Different Cells and $\pm S0$ . . . . .	121
5.15	$\frac{4\pi}{6}$ Mode Simulated Power Spectra for Different Cells and $\pm S0$ . . . . .	122

5.16	$\pi$ , $\frac{5\pi}{6}$ , and $\frac{4\pi}{6}$ Modes Simulated Power Spectra Same $S_0$ . . . . .	123
5.17	Power Spectrum with Increased $\beta_{FN}$ . . . . .	124
5.18	Similar Simulated Power Spectra . . . . .	125
5.19	Binned Simulated Power Spectra . . . . .	126
5.20	X-ray to Power Spectrum . . . . .	127
6.1	Cavity #2, $\frac{5\pi}{6}$ Mode, Data and Simulated Power Spectrum . . . . .	130
6.2	Cavity #2, $\pi$ Mode, Data and Simulated Power Spectrum . . . . .	132
6.3	Cavity #2 $A_e$ . . . . .	133
6.4	Cavity #2, $\frac{4\pi}{6}$ Mode, Data and Simulated Power Spectrum . . . . .	135
6.5	Cavity #2, 3 Modes, $S_0 = 13.266$ cm . . . . .	137
6.6	Cavity #2, 3 Modes, $S_0 = 13.5$ cm . . . . .	138
6.7	Cavity #1, $\pi$ Mode, Data and Simulated Power Spectrum . . . . .	141
6.8	Cavity #1 $A_e$ . . . . .	142
6.9	Cavity #1, $\frac{5\pi}{6}$ Mode, Data and Simulated Power Spectrum . . . . .	144
A.1	Rectangular Waveguide . . . . .	154
A.2	Fields in a Cylindrical Cavity . . . . .	160
B.1	Potential Barrier . . . . .	164
E.1	Periodic Structure . . . . .	179
E.2	SUPERLANS Output . . . . .	181
E.3	Symmetric and Antisymmetric Wave Output . . . . .	182
F.1	Cavity #2 $\pi$ Mode Data . . . . .	184
F.2	Cavity #2 $\frac{5\pi}{6}$ Mode Data . . . . .	185
F.3	Cavity #2 $\frac{4\pi}{6}$ Mode Data . . . . .	187
F.4	Cavity #1 $\pi$ Mode Data . . . . .	189
F.5	Cavity #1 $\frac{5\pi}{6}$ Mode Data . . . . .	191

# List of Tables

3.1	Absorber Materials . . . . .	62
4.1	Detector Calibration . . . . .	69
4.2	Absorber Materials . . . . .	71
4.3	Characteristic X-rays . . . . .	73
6.1	Cavity #2, $\frac{5\pi}{6}$ Mode . . . . .	131
6.2	Cavity #2, $\pi$ Mode . . . . .	133
6.3	Cavity #2, $\frac{4\pi}{6}$ . . . . .	136
6.4	Cavity #2, $\frac{5\pi}{6}$ , $S_0 = 13.266$ cm . . . . .	139
6.5	Cavity #1, $\pi$ Mode . . . . .	142
6.6	Cavity #1, $\frac{5\pi}{6}$ Mode . . . . .	145
F.1	Cavity #2, $\pi$ Mode Endpoint Energy . . . . .	183
F.2	Cavity #2, $\frac{5\pi}{6}$ Mode Endpoint Energy . . . . .	186
F.3	Cavity #2, $\frac{4\pi}{6}$ Mode Endpoint Energy . . . . .	188
F.4	Cavity #1, $\pi$ Mode Endpoint Energy . . . . .	190
F.5	Cavity #1, $\frac{5\pi}{6}$ Mode Endpoint Energy . . . . .	190

# Chapter 1

## Introduction

The goal of this research was to develop an improved x-ray imaging technique for locating field emission sources in superconducting radio frequency (SRF) cavities. Unlike other techniques, the present technique is unique in that it can be used after the cavities are installed in an operating accelerator. Once defects are identified, cavities can be subjected to high power pulsed processing or helium processing to suppress field emission from an emitter source. For cavities being manufactured, x-ray imaging could be used to locate defects resulting from the manufacturing process such as improper clean room procedures or die defects. Appropriate steps could then be taken to remedy the cause of the defects [1].

Cavities are tested and operated at high electric field gradients. In the region of an inner surface defect the electric field is enhanced, causing electrons to leave the surface of the metal. These field-emitted electrons are accelerated in the cavity electric field, strike the cavity walls, dissipate power and create heat, and generate bremsstrahlung x-rays. The maximum energy of the x-rays is equal to the maximum energy of the impacting electrons (Duane and Hunt's Law) [2], which is needed for the particle tracking simulation to determine the location of defects.

The x-rays travel through the cryostat materials such as magnetic shielding, thermal shielding, 2 cm thick steel, and through detector shielding of 6-10 cm thick lead

and collimator, before entering the scintillator material of the detector. For these materials and observed x-ray energies, Compton scattering is the most probable interaction. During a Compton event, an x-ray interacts with an electron and both the electron and x-ray are scattered, the x-ray to a lower energy and the electron only traveling a short distance. The probability of a Compton event depends upon the x-ray energy and the  $Z$  of the material through which it is traveling. There is a small probability that an x-ray will have no interactions prior to entering the detector [2]. Sodium iodide was chosen for the detector scintillator since it provides adequate energy resolution and good efficiency [1].

A particle tracking code was used to infer the locations of the electron emitters and the emitter parameters. The code provides information about the electron impact site such as electron final kinetic energy, current, and power, which were fit to the data.

Quality factor ( $Q$ ) is a measure of cavity performance and is inversely proportional to dissipated power. As cavities are pushed to high electric field gradients they experience a decline in  $Q$ . High electric field power loss mechanisms include field emission, thermal breakdown, and exceeding the critical magnetic field. All radio frequency (rf) cavities exhibit a surface resistance due to the nature of superconductivity. This small resistance causes a cavity to heat at high electric field without the x-rays produced during field emission being observed. All can lead to a quench of the cavity. Low field power loss mechanisms include flux trapping, adsorbed gases, and resistive particles. Of these, field emission is the chief degrader of cavity performance [3].

If the decline of  $Q$  is due to field emission, the general area radiation monitoring equipment registers an x-ray exposure rate of the bremsstrahlung-generated x-rays. X-ray energies cannot be determined based on the exposure rate and since the x-rays enter the detector from all directions, the source location, and the possibility of multiple sources, cannot be determined. Although a good indicator of field emission, this equipment cannot be used in conjunction with a particle tracking code to determine

defect sites.

A second technique for locating x-ray sources uses resistors arranged on the outer cavity wall to locate an increase in temperature where electrons impact. With the impact locations known, electron energies are calculated based on temperature, and particle-tracking codes determine the source of the electrons, i.e., the locations of defects. Verification of the defect and impact sites requires a cavity to be disassembled and inspected under special conditions to prevent contamination [4]. This method has proven very successful for cavity testing but is capital and labor-intensive, and impractical for operating accelerators where cavities, housed in cryostats, are not accessible.

The technique developed here identifies x-ray sources using a slit collimated sodium iodide detector moving continuously along the cavity, outside the cryostat, while cavities are tested. The collimator and detector housing are made of lead to attenuate x-rays other than those entering the detector through the collimator. The sodium iodide detector measures the energy spectrum of x-rays. Slit collimation makes it possible to determine x-ray sources to within the slit resolution.

Particles are accelerated in cavities operated in the  $\pi$  mode, where successive cells are  $\pi$  radians out of phase with each other. Operating a multicell cavity in a different mode of excitation, such as the  $\frac{5\pi}{6}$  mode for a six cell cavity, changes the electric fields within the cavity. A particle emitted from a single defect has a different trajectory and impact site from that of the  $\pi$  mode [4]. Thus x-ray imaging and the resulting particle tracking of electrons from a cavity operated in another mode is used as a verification of a defect site without having to cannibalize the cavity.

Operating accelerator cavities can develop defects from contaminants entering the cavity through vacuum leaks or venting for maintenance. Once defects are identified, cavities can be subjected to high power pulsed processing or helium processing to suppress field emission from an emitter source. High power pulsed processing is accomplished by raising the electric field as high as possible for a very short duration.

The high current destroys the emitter in an explosive event. Helium processing introduces helium gas into the cavity, where the field-emitted electrons ionize the gas. Since they are of opposite charge, ions bombard the emitter at the same time electrons are being emitted. Pressure builds in the area of the defect until it explodes [4].

During cavity manufacturing, if a defect or dimple develops in the die used to form the cavities, x-ray imaging provides a simple technique for locating the defect so necessary repairs can be made. X-ray imaging can also be used to locate defects resulting from the manufacturing process such as improper clean room procedures that lead to cavity contamination. High power pulsed processing or helium processing can then be used to eliminate the defect. This method of x-ray imaging is the first diagnostic technique for locating cavity defects from outside of a cryostat.

This work can be expanded upon with the accumulation of data in two dimensions with a device similar to the one used in this study or with a gamma camera. Multiple images acquired from multiple angles by using a gamma camera could be reconstructed to yield a three dimensional image similar to PET or SPECT imaging.

Chapter 2 covers the mathematical background of cavity fields, field emission, x-rays, and briefly discusses detector operation and the function of a collimator. In Chapter 3 the experimental designs of the cavity, cryostat, detector, and collimator are presented. Chapter 4 offers the experimental results of the data accumulated during testing of two cavities in a cryostat. Chapter 5 covers the particle tracking code used for this study. Chapter 6 compares the data and the simulated results. Finally, Chapter 7 gives a summary of the study.

# Chapter 2

## Background

The attractiveness of superconducting over normal conducting cavities is that much less power is dissipated in the cavity walls. The surface resistance of a superconductor is on the order of  $10^5$  times lower than that of a normal conductor. This equates to a quality factor ( $Q$ ) on the order of  $10^5$ - $10^6$  times higher (Equation 2.1).

Current flows in the cavity walls at the surface thus supporting the electromagnetic fields in the cavity. As current flows through a defect, Joule heating heats the surrounding area. If the temperature rises above a critical temperature ( $T_c$ ) for the material, the area becomes normal conducting, followed by a quench. Quench is the sudden drop in a cavities  $Q$  due to the rapid increase in the power dissipation at the defect:

$$Q = \frac{\omega U}{P_d}, \quad (2.1)$$

where  $\omega$  is the angular frequency,  $U$  the stored energy, and  $P_d$  the dissipated power [4].

The DC resistance of a superconductor is zero below a critical temperature ( $T_c$ ) for the material. The rf resistance though, is on the scale of  $n\Omega$  for high purity superconductors. According to a theory developed by Bardeen, Cooper, and Schrieffer (BCS) in 1957, electrons in superconductors form Cooper pairs. Electrons in the pair are of opposite momentum and spin. At  $T = 0$  K all electrons are paired. At higher temperatures there exists a finite probability of pair splitting due to thermal excitation

(two fluid model). The Cooper pairs and free electrons can collide with lattice defects, impurities, or phonons [4].

In the DC case, collisions are of insufficient energy to scatter Cooper pairs out of the ground state, so the pairs flow frictionlessly, i.e. without resistance. The free electrons can be scattered and dissipate energy but the Cooper pairs shield the applied field from the free electrons. The result is that electrical resistance vanishes [4].

In the rf case, Cooper pairs are again not scattered but do possess inertia and do not shield the applied field completely. The free electrons of the fluid are continually accelerated and decelerated leading to power dissipation, i.e. surface resistance. The residual resistance of a superconductor depends in part upon impurities and microscopic particles that scatter the free electrons, trapped flux localized at impurities, called pinning centers, making the superconductor unable to expel the magnetic field, and adsorbed gases such as  $N_2$  and  $O_2$  that possess dielectric properties that increase the residual resistance. The rf surface resistance is:

$$R_s = A \left( \frac{f^2}{T} \right) \exp \left( \frac{-\Delta(T)}{kT} \right) + R_0, \quad (2.2)$$

where  $A$  is a material dependent constant,  $f$  is the frequency,  $k$  is the Boltzmann constant,  $T$  is the temperature,  $2\Delta$  is the energy needed to break the Cooper pairing, and  $R_0$  is the residual resistance [4]. Due to this surface resistance, all cavities exhibit power losses that limits cavity performance. The losses are present throughout the entire cavity. With this as the only power loss mechanism present, the Q drops at high electric fields (Equation 2.1) , but no x-rays associated with field emission are detected.

The reduced resistance of SRF cavities, and thus power consumption, translates to reduced operating costs even when the cost of refrigeration is considered. Higher electric field gradients are attained due to lower power consumption. Lower power consumption also means fewer klystrons are needed to power a bank of cavities.

Most importantly, higher currents can be accelerated due to the larger apertures that minimize intrusive interactions of the cavity with the beam [3].

## 2.1 SRF Cavity Operation

### 2.1.1 Electric Fields

For this study the electric fields within a cavity need to be known in order to track the trajectories of field emitted electrons from their impact sites back to their origin. To explain the fields within a cavity one first begins with the fields within a waveguide. A waveguide is a structure that guides a wave in a given direction in planes perpendicular to that direction. In accelerator applications, rectangular and circular waveguides are commonly used for high power transmissions between power sources and accelerating structures. A circular waveguide structure with conducting end surfaces is called a pill-box cavity [5]. Appropriate boundary conditions are then applied to the circular waveguide to obtain the fields within a cylindrical or pill box cavity [5]. To allow a beam through the cavity, beam pipes are added to both ends and cavity shapes are generally elliptical due to multipacting issues. The addition of beam pipes increases the peak surface electric field and peak surface magnetic field, thus increasing the probability of field emission. Multipacting occurs when electrons that leave the cavity wall impact and produce secondary electrons until an avalanche of electrons exist. Due to the absorption of rf power, cavity fields cannot be raised. This phenomenon can take place in regions along the cavity wall where the surface magnetic field is nearly constant. When cavity walls are rounded, the surface magnetic field varies along the entire wall, thus minimizing multipacting.

The addition of these features makes it very difficult to calculate the fields analytically. The computer code SUPERLANS was used for numerical analyses in this study [4].

## Waveguide

The following derivation for the fields within a cylindrical cavity begins with the fields within a rectangular waveguide, whose solutions are transformed to cylindrical coordinates for the fields within a circular waveguide.

The derivation of fields within a rectangular waveguide begins with Maxwell's equations:

$$\begin{aligned} \text{(i)} \quad \vec{\nabla} \cdot \vec{E} &= \frac{\rho}{\epsilon} & \text{(ii)} \quad \vec{\nabla} \times \vec{E} &= -\frac{\partial \vec{B}}{\partial t} \\ \text{(iii)} \quad \vec{\nabla} \cdot \vec{B} &= 0 & \text{(iv)} \quad \vec{\nabla} \times \vec{B} &= \mu \vec{J} + \frac{1}{c^2} \frac{\partial \vec{E}}{\partial t}, \end{aligned}$$

where  $\rho$  is electric charge density,  $\epsilon$  the permittivity, and  $\mu$  the permeability. In a region free of charge, or free of current, Maxwell's equations become:

$$\begin{aligned} \text{(i)} \quad \vec{\nabla} \cdot \vec{E} &= 0 & \text{(ii)} \quad \vec{\nabla} \times \vec{E} &= -\frac{\partial \vec{B}}{\partial t} \\ \text{(iii)} \quad \vec{\nabla} \cdot \vec{B} &= 0 & \text{(iv)} \quad \vec{\nabla} \times \vec{B} &= \frac{1}{c^2} \frac{\partial \vec{E}}{\partial t}. \end{aligned}$$

The fields within a rectangular waveguide are given dependent upon  $E_z$  and  $B_z$  (Appendix A.1):

$$E_y = \frac{i}{k_c^2} \left( \pm k_z \frac{\partial E_z}{\partial y} - \omega \frac{\partial B_z}{\partial x} \right), \quad (2.3)$$

$$B_x = \frac{i}{k_c^2} \left( \pm k_z \frac{\partial B_z}{\partial x} - \frac{\omega}{c^2} \frac{\partial E_z}{\partial y} \right), \quad (2.4)$$

$$E_x = \frac{i}{k_c^2} \left( \pm k_z \frac{\partial E_z}{\partial x} + \omega \frac{\partial B_z}{\partial y} \right), \quad (2.5)$$

$$B_y = \frac{i}{k_c^2} \left( \pm k_z \frac{\partial B_z}{\partial y} - \frac{\omega}{c^2} \frac{\partial E_z}{\partial x} \right), \quad (2.6)$$

$$\left( \frac{\partial^2}{\partial x^2} + \frac{\partial^2}{\partial y^2} + \frac{\omega^2}{c^2} - k_z^2 \right) E_z = 0, \quad (2.7)$$

$$\left( \frac{\partial^2}{\partial x^2} + \frac{\partial^2}{\partial y^2} \right) E_z = -k_c^2 E_z = \nabla_T^2 E_z, \quad (2.8)$$

$$\left( \frac{\partial^2}{\partial x^2} + \frac{\partial^2}{\partial y^2} + \frac{\omega^2}{c^2} - k_z^2 \right) B_z = 0, \quad (2.9)$$

$$\left( \frac{\partial^2}{\partial x^2} + \frac{\partial^2}{\partial y^2} \right) B_z = -k_c^2 B_z = \nabla_T^2 B_z, \quad (2.10)$$

where  $k_z$  is the wave number in the  $z$  direction ( $k_z = \frac{2\pi}{\lambda}$ ),  $\omega$  the angular frequency ( $\omega = kc$ ),  $k_c$  the cutoff wave number ( $k_c = \sqrt{k^2 - k_z^2}$ ), and  $\nabla_T = \frac{\partial^2}{\partial x^2} + \frac{\partial^2}{\partial y^2}$  where  $T$  implies the transverse plane. For  $k > k_z$  propagation occurs, but for  $k < k_z$  the modes are called cutoff, or evanescent and decay exponentially along the waveguide.

The wave solutions are classified into the following types:

- 1) Transverse electromagnetic waves (TEM) if both  $E_z$  and  $B_z$  are zero. That is to say the waves contain neither electric nor magnetic fields in the direction of propagation.
- 2) Transverse magnetic waves (TM) if  $B_z$  is zero. That is to say waves where the magnetic field lies entirely in transverse planes and the electric field is oriented in the direction of propagation.
- 3) Transverse electric waves (TE) if  $E_z$  is zero. That is to say waves where the electric field lies entirely in transverse planes and the magnetic field is in the direction of propagation.

Of interest here is the derivation of the TM mode since it is the accelerating mode, but a similar derivation could be carried out for the TE mode.

Boundary conditions dictate that  $E_z(x = 0, a) = 0$ ,  $E_z(y = 0, b) = 0$ , and  $E_z(x = \frac{a}{2}, y = \frac{b}{2}) = E_0$  (Figure 2.1):

$$E_z = E_0 \sin \frac{m\pi x}{a} \sin \frac{n\pi y}{b} e^{\pm ik_z z}. \quad (2.11)$$

For the TM mode, Equation 2.11 is substituted into Equations 2.3 through 2.6 to solve for:

$$E_x = \frac{i}{k_c^2} \left[ \pm k_z E_0 \frac{m\pi}{a} \cos \left( \frac{m\pi x}{a} \right) \sin \left( \frac{n\pi y}{b} \right) \right] e^{\pm ik_z z},$$

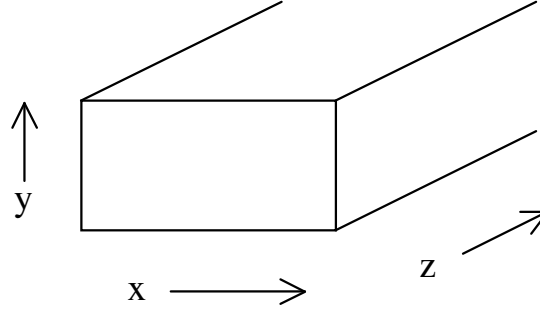


Figure 2.1: Rectangular Waveguide where lengths  $x = a$  and  $y = b$ .

$$E_y = \frac{i}{k_c^2} \left[ \pm k_z E_0 \frac{n\pi}{b} \sin\left(\frac{m\pi x}{a}\right) \cos\left(\frac{n\pi y}{b}\right) \right] e^{\pm i k_z z},$$

$$B_x = \frac{i}{k_c^2} \left[ -\frac{\omega}{c^2} E_0 \frac{n\pi}{b} \sin\left(\frac{m\pi x}{a}\right) \cos\left(\frac{n\pi y}{b}\right) \right] e^{\pm i k_z z},$$

$$B_y = \frac{i}{k_c^2} \left[ -\frac{\omega}{c^2} E_0 \frac{m\pi}{a} \cos\left(\frac{m\pi x}{a}\right) \sin\left(\frac{n\pi y}{b}\right) \right] e^{\pm i k_z z}.$$

A similar set of equations could be derived for the TE mode [6].

For waveguides of circular cross section, Equations 2.3 to 2.6 are transformed to cylindrical coordinates (Appendix A.2):

$$E_r = \frac{i}{k_c^2} \left( \pm k_z \frac{\partial E_z}{\partial r} + \frac{\omega}{r} \frac{\partial B_z}{\partial \phi} \right), \quad (2.12)$$

$$B_r = \frac{i}{k_c^2} \left( \pm k_z \frac{\partial B_z}{\partial r} - \frac{\omega}{c^2 r} \frac{\partial E_z}{\partial \phi} \right), \quad (2.13)$$

$$E_\phi = \frac{i}{k_c^2} \left( \pm \frac{k_z}{r} \frac{\partial E_z}{\partial \phi} - \omega \frac{\partial B_z}{\partial r} \right), \quad (2.14)$$

$$B_\phi = \frac{i}{k_c^2} \left( \pm \frac{k_z}{r} \frac{\partial B_z}{\partial \phi} + \frac{\omega}{c^2} \frac{\partial E_z}{\partial r} \right), \quad (2.15)$$

$$E_z = AJ_m(x) \cos(m\phi)e^{\pm ik_z z}, \quad (2.16)$$

where  $A$  is a constant and  $J_m$  is a Bessel function of the first kind [7]:

$$J_m(x) = \left(\frac{x}{2}\right)^m \sum_{j=0}^{\infty} \frac{(-1)^j}{j! \Gamma(j+m+1)} \left(\frac{x}{2}\right)^{2j}.$$

Bessel functions have an infinite number of roots with zeros occurring at integer values of  $n$ :  $x_{m1}, x_{m2}, x_{m3} \dots$  (See Appendix A.2 for more details). For integer values of  $m$ , the first few roots are

$$x_{01} = 2.405, x_{02} = 5.520, x_{03} = 8.654, \dots$$

$$x_{11} = 3.832, x_{12} = 7.016, x_{13} = 10.173, \dots$$

$$x_{21} = 5.136, x_{22} = 8.417, x_{23} = 11.620, \dots [8].$$

Since the electric field is perpendicular to a conducting surface and the magnetic field parallel, the boundary conditions for the circular waveguide are (Figure 2.2)  $E_z(r = R) = 0$ ,  $E_\phi(r = R) = 0$ , and  $B_r(r = R) = 0$ .

$$E_z = AJ_m(x) \cos(m\phi)e^{\pm ik_z z},$$

$$E_r = \frac{\pm ik_z}{k_c} AJ'_m(x) \cos(m\phi)e^{\pm ik_z z},$$

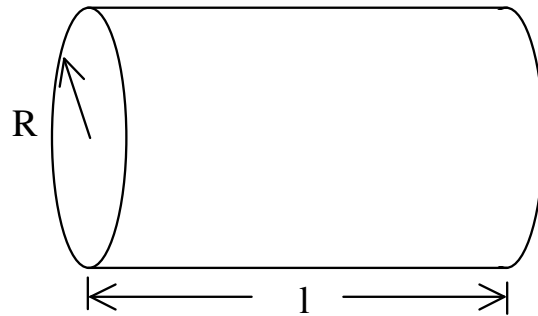


Figure 2.2: Circular Waveguide where lengths  $r=R$  and  $z=l$ .

$$E_\phi = \frac{\mp ik_z m}{k_c^2 r} A J_m(x) \sin(m\phi) e^{\pm ik_z z},$$

$$B_r = \frac{i\omega m}{k_c^2 c^2 r} A J_m(x) \sin(m\phi) e^{\pm ik_z z},$$

$$B_\phi = \frac{i\omega}{k_c c^2} A J'_m(x) \cos(m\phi) e^{\pm ik_z z},$$

$$B_z = 0.$$

Phase velocity is the velocity that any frequency component of a wave propagates. Phase velocity is determined by setting [9]:

$$\psi = \omega t - k_z z = \text{constant}$$

$$\dot{\psi} = \omega - k_z \dot{z} = 0$$

$$v_{ph} = \dot{z} = \frac{\omega}{k_z} \tag{2.17}$$

$$= \frac{\omega}{\sqrt{\frac{\omega^2}{c^2} - k_c^2}} \tag{2.18}$$

$$= \frac{c}{\sqrt{1 - \frac{k_c^2 c^2}{\omega^2}}} \tag{2.19}$$

$$> c. \tag{2.20}$$

A propagating wave has the form

$$\vec{E}(r, z, t) = \vec{E}_d(r, z) e^{i(\omega t - k_z z)}, \tag{2.21}$$

where  $E_d$  is some periodic function with period  $d$ , such as  $\sin(z + nd)$  for  $n = 1, 2, \dots$

The phase velocity exceeds the speed of light and the velocity that a particle can reach. This is not useful for particle acceleration because the phase will roll over

the particles making net acceleration zero. To obtain a  $v_{ph} < c$ , structures with recurring geometry or periodic geometries are used. Group velocity is the velocity of the electromagnetic energy along a waveguide [9]:

$$\begin{aligned}
v_g &= \frac{d\omega}{dk_z} \\
\omega^2 &= (k_c^2 + k_z^2) c^2 \\
\omega &= \sqrt{k_c^2 + k_z^2} c \\
\frac{d\omega}{dk_z} &= \frac{ck_z}{\sqrt{k_c^2 + k_z^2}} = \frac{c^2 k_z}{\omega} = \frac{c^2}{v_{ph}} < c.
\end{aligned} \tag{2.22}$$

A cutoff frequency is defined as  $\frac{\omega}{c} > k_c$ :

$$\omega_c = ck_c = c \frac{2.405}{R}, \tag{2.23}$$

where  $R$  is the diameter of the waveguide.

## Cavity

A cavity is formed when conductive ends are placed on the cylindrical waveguide at  $z = 0$  and at  $z = l$ . Now the cavity is filled with incident and reflected waves with additional boundary conditions  $E_r(z = 0, l) = 0$ ,  $E_\phi(z = 0, l) = 0$ , and  $B_z(z = 0, l) = 0$ .

The electric fields become (Appendix A.3):

$$E_z = E_0 J_m(x) \cos(m\phi) \cos\left(\frac{p\pi z}{l}\right),$$

$$E_r = \frac{\mp p\pi}{lk_c} E_0 J'_m(x) \cos(m\phi) \sin\left(\frac{p\pi z}{l}\right),$$

$$E_\phi = \frac{\pm mp\pi}{rlk_c^2} E_0 J_m(x) \sin(m\phi) \sin\left(\frac{p\pi z}{l}\right),$$

and magnetic fields:

$$B_z = 0,$$

$$B_r = \frac{i\omega m}{k_c^2 c^2 r} E_0 J_m(x) \sin(m\phi) \cos\left(\frac{p\pi z}{l}\right),$$

$$B_\phi = \frac{i\omega}{k_c c^2} E_0 J'_m(x) \cos(m\phi) \cos\left(\frac{p\pi z}{l}\right),$$

$$\text{where } k_c^2 = \frac{\omega^2}{c^2} - k_z^2 \Rightarrow \omega = c\sqrt{k_c^2 + k_z^2},$$

$$\text{and } f = \frac{\omega}{2\pi} = \frac{c}{2\pi} \sqrt{(k_c)^2 + \left(\frac{p\pi}{l}\right)^2}.$$

In the  $TM_{010}$  mode the zero order Bessel function provides an accelerating field in the longitudinal direction (direction of particle travel) and a magnetic field in the  $\phi$  direction.

Charged particles must enter the cavity at the right time in order to receive the maximum acceleration by the electric field in the direction of travel; they must also be traveling at a velocity such that they traverse the length of the cavity in roughly half an rf period. Electric and magnetic field lines are one direction (Figure 2.3) for half of the rf period and are opposite in direction in the second half of the rf period.

Changing the shape of a cavity, from cylindrical to elliptical (Figure 2.4), or adding cells to construct a multicell cavity (Figure 2.5), makes it very difficult to calculate the fields. Codes such as Superfish, SUPERLANS and MAFIA, to name a few, numerically solve the wave equation constructed from Maxwell's equations.

A multicell cavity provides an accelerating electric field in successive cells by

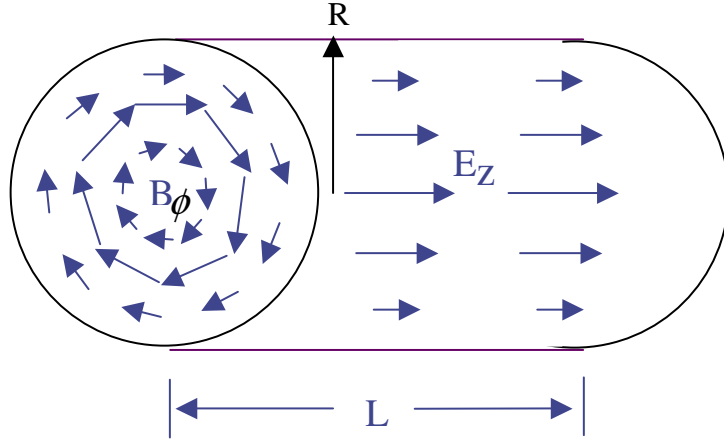


Figure 2.3: Electric and magnetic fields in a cylindrical cavity. The maximum electric field occurs on axis to accelerate the beam and falls to zero at the cavity wall (R). The magnetic field is zero on axis and has a maximum at  $0.77 R$ .

making the fields in neighboring cells  $\pi$  radians out of phase with each other (the  $\pi$  mode of operation) requiring the particle to cross a cell in half an rf period. As a charged particle travels through each cell, an accelerating electric field points in its direction of travel, providing continuous acceleration through the cavity.

The cells in a multicell cavity are coupled together and act as a set of coupled oscillators. There are six modes of excitation for the full six-cell structure operating in the  $TM_{010}$  mode of operation, the  $\pi$ ,  $\frac{5\pi}{6}$ ,  $\frac{4\pi}{6}$ ,  $\frac{3\pi}{6}$ ,  $\frac{2\pi}{6}$ , and  $\frac{\pi}{6}$  modes. Electric fields in each cell have different amplitude and direction compared to the accelerating or  $\pi$  mode. For different modes of excitation one expects different field emitted electron trajectories and impact locations for the same emitter.

### Cavity Geometry

A charged particle enters a cavity on axis at time  $t = 0$  and exits at time  $t = \frac{l}{v}$ , where  $l$  is the length of the cell and  $v$  the charged particle velocity. The length of the cell is determined by the charged particle velocity and the rf frequency:

$$l = \frac{v}{2f} = \frac{\beta_g c}{2f} = \frac{\beta_g \lambda}{2}, \quad (2.24)$$

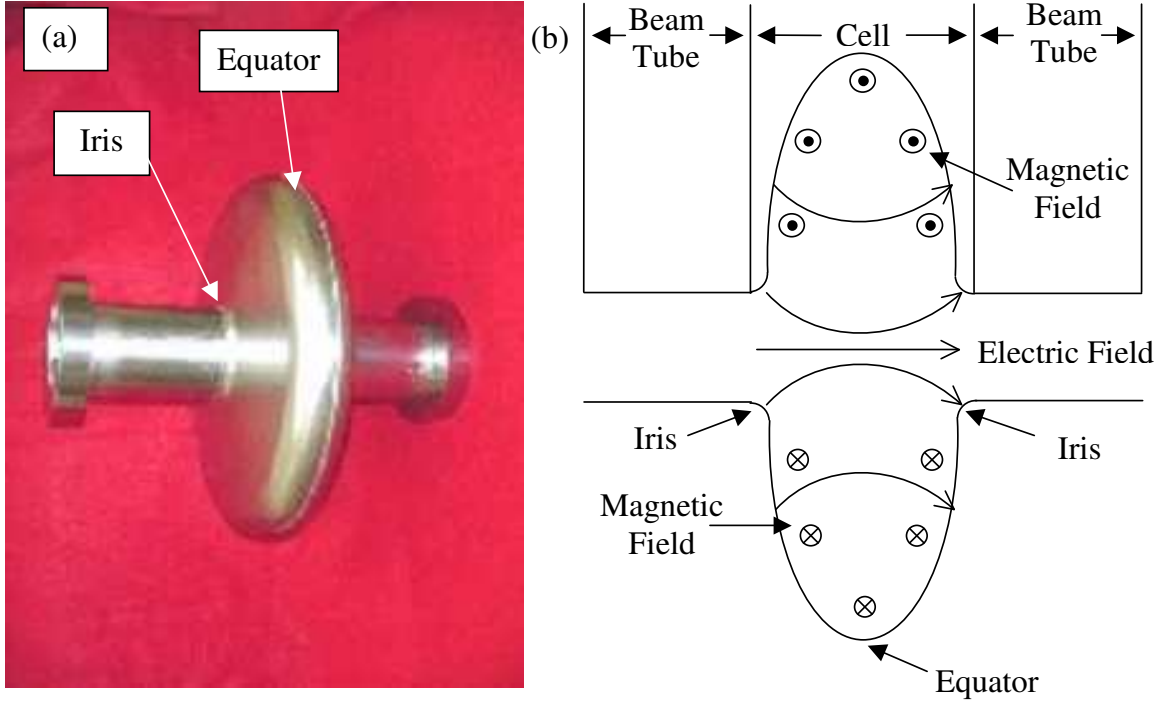


Figure 2.4: Panel (a): Photograph of a single-cell elliptical cavity. The cavity's inner diameter at the equator is 32.9 cm, the inner diameter at the iris is 7.72 cm, and the active length is 8.78 cm. Panel (b): Electric and magnetic fields are shown in the right panel.

where  $\beta_g$  is the cavity geometric  $\beta$  and  $\lambda$  the rf wavelength. Since it is desirable for the particle to traverse the cell in half an rf period:

$$t = \frac{l}{v} = \frac{1}{2f}, \quad (2.25)$$

where  $f$  is the rf frequency [4].

The accelerating voltage ( $V_{acc}$ ) of a cavity is given by integrating the electric field, in a particles direction of travel, over the length of the cell:

$$V_{acc} = \left| \int_0^l E_z(r=0, z) e^{ik_z z} dz \right|.$$

For a pillbox cavity operating in the  $TM_{010}$  mode:

$$V_{acc} = E_0 l \frac{\sin \frac{k_z l}{2}}{\frac{k_z l}{2}} = l E_0 T,$$

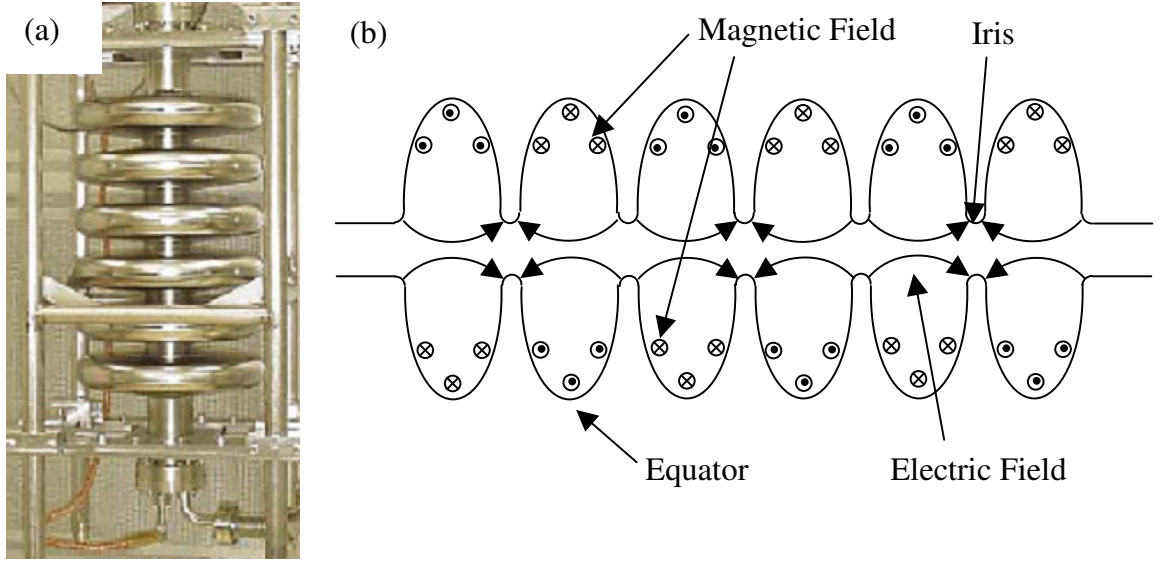


Figure 2.5: Panel (a): Photograph of a six-cell elliptical cavity in a vertical test stand. The cavity's inner diameter at the equator is 32.9 cm, the inner diameter at the iris is 7.72 cm, and active length is 52.7 cm. Panel (b): Electric and magnetic fields are shown in the right panel.

where  $T$  is referred to as the transit factor. For a pill-box cavity operating in the  $TM_{010}$  mode,  $T = \frac{2}{\pi}$  if Equation 2.25 is satisfied [4].

Most commonly referred to is the average accelerating electric field ( $E_a$ ) that a particle experiences as it transits a cell:

$$E_a = \frac{V_{acc}}{l}.$$

The accelerating fields in SRF cavities are limited by the peak surface electric field ( $E_p$ ) and the peak surface magnetic field ( $H_p$ ) (Figure 2.6) [4].

It is desirable to maximize the accelerating electric field so the ratios  $\frac{E_p}{E_a}$  and  $\frac{H_p}{E_a}$  are minimized. Adding beam tubes to a cavity cell increases these ratios. An SRF cavity will quench if  $H_p$  exceeds a critical magnetic field ( $H_c$ ) [4] and a cavity's performance will be degraded if electrons are field emitted in regions of high  $E_p$ .

During cavity testing, as  $E_a$ , and thus  $E_p$ , is increased, the cavity  $Q$  remains constant until an additional loss mechanism is triggered (Figure 2.7 (a)). If the loss is due to field emission, x-rays are detected on the area radiation monitoring equipment

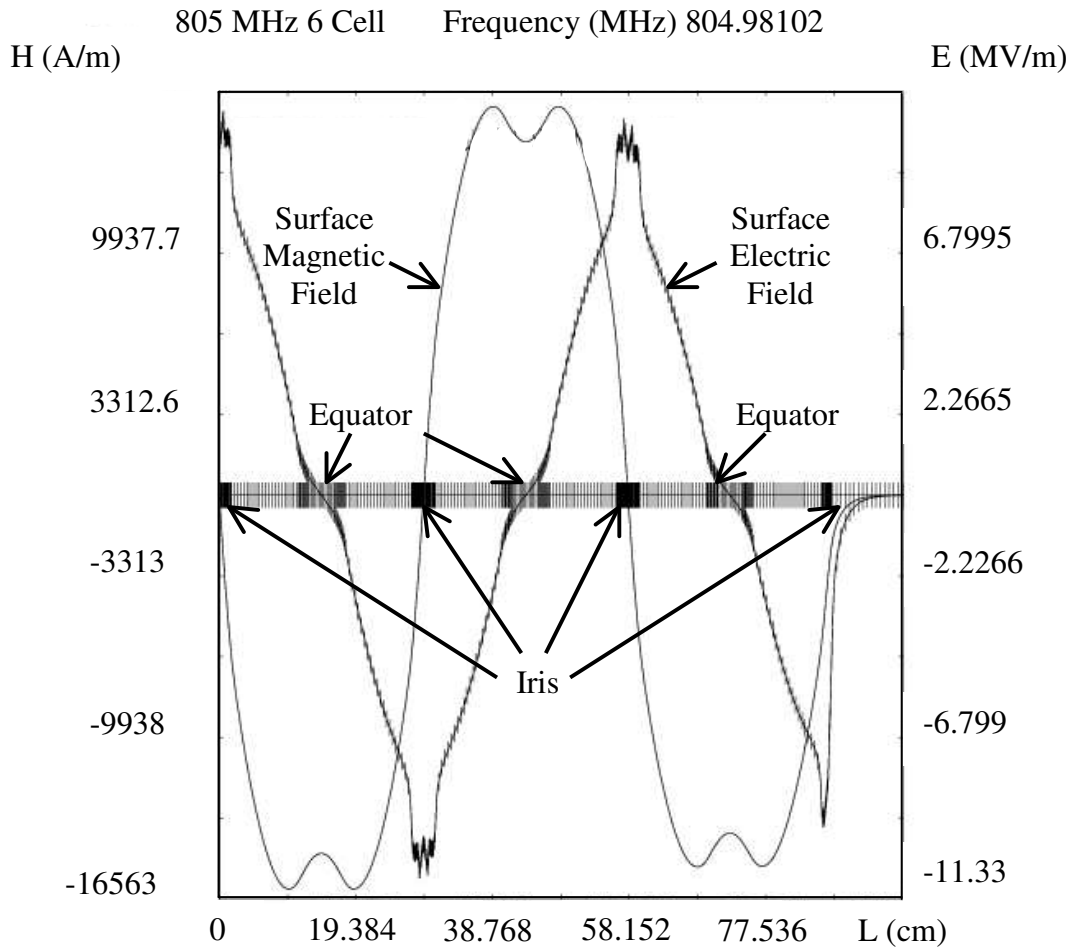


Figure 2.6: Surface electric and surface magnetic fields as a function distance along the axis of 3 cells of a 6 cell cavity with beam tube, in the  $\pi$  mode.

(Figure 2.7 (b)).

### 2.1.2 Field Emission

The advantage of superconducting over normal conducting cavities is the much lower power dissipation in the cavity walls. Cavities are designed to have as high an accelerating electric field as possible, although the surface electric field must be kept as low as possible to prevent field emission [4]. Field emission is the emission of an electron from the surface of a metal in the presence of a high electric field gradient. “The first one to describe this phenomenon in detail was R. W. Wood, in 1897, who reported enthusiastically what one would call today a kind of fire-works in his

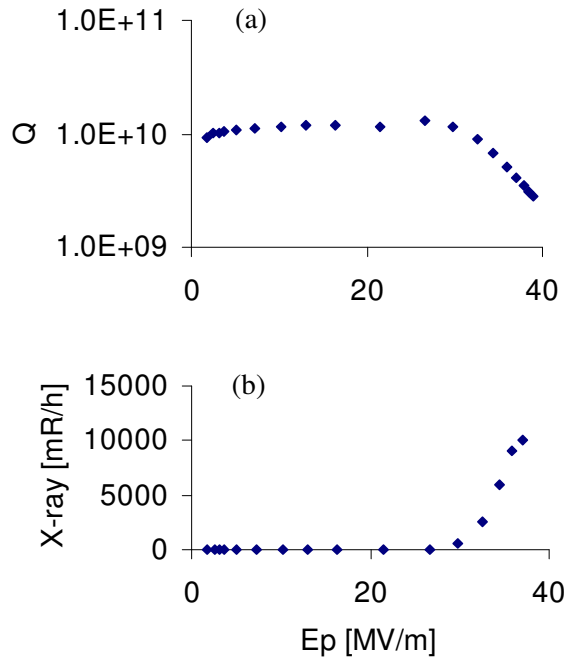


Figure 2.7: Panel (a): The cavity  $Q$  remains constant as  $E_p$  is increased until the triggering of field emitted electrons. Panel (b): X-rays are detected when the loss mechanism is due to field emission.

discharge tube” [10] (Figure 2.8).

Sources of field emission in cavities include surface roughness, metallic dust, micro-particles, grain boundaries, and impurities in the material. Field-emitted electrons are accelerated in the cavity electric field and have complex trajectories. When they impact the cavity walls they dissipate power, creating heat, and generate bremsstrahlung x-rays [4].

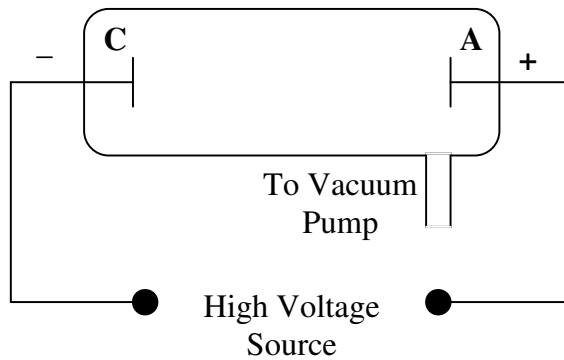


Figure 2.8: Discharge tube where electrons are field emitted from the cathode, travel to, and impact the anode.

For this study the average current, from which the average power is calculated, is needed to determine the degree of electric field enhancement, Fowler-Nordheim (FN) field enhancement factor (FEF), from the data. This FEF is used by the particle tracking simulation to determine the current and power of an impacting electron. The simulated power is fitted to the x-ray power data until a likely electron source is found.

### Calculation of Current

The abundance of electrons inside a metal is almost inexhaustible. Within a metal an electron has a potential energy of some constant value,  $W_a$ , relative to zero when the electron and metal are separated. The Fermi energy ( $\zeta$ ) is the highest energy level filled with electrons at 0 K. The energy required to take an electron from the Fermi level within a metal and remove it to infinity, assuming a particle at infinity has zero energy, is the work function  $\phi$  of the metal.

Under normal circumstances the energy of an electron, confined inside a metal by a potential well, has insufficient energy to escape from the metal (Figure 2.9 (a)) [4]. To escape from the surface an electron must receive extra energy. Applying an electric field to a metal,  $E$  in  $\frac{\text{Volts}}{\text{meter}}$ , an electron encounters a potential of  $V(x) = -eEx$ . Quantum mechanically, the electron wave function attenuates outside the surface potential barrier. If the potential barrier is lowered, the attenuation is not complete and there is a finite probability that some electrons will tunnel through the barrier, i.e. leave the surface (Figure 2.9 (b)) [4].

Once an electron has left the surface it also experiences an attractive force due to the presence of the conducting surface. This force is represented as an image force and lowers the height of the potential barrier by  $\frac{e^2}{4x}$  (Figure 2.9 (c)). The image force is shown in Figure 2.10 [10].

The two contributions affecting the potential [11]:

$$V(x) = -W_a \quad \text{for } x < 0 \quad (2.26)$$

$$= -\frac{e^2}{4x_0} - eEx_0 \quad \text{for } x > 0. \quad (2.27)$$

By maximizing  $V(x)$ ,  $x_0 = \left(\frac{e}{4E}\right)^{1/2}$ , the maximum decrease of the potential barrier is found to occur at  $\varphi = e^{3/2}E^{1/2}$ . The final potential barrier is in Figure 2.9 (d) [4].

Charge density, at the surface of a metal, is not identical to that within a metal. Work is required to move an electron through the surface layer,  $W_s$ . So the work

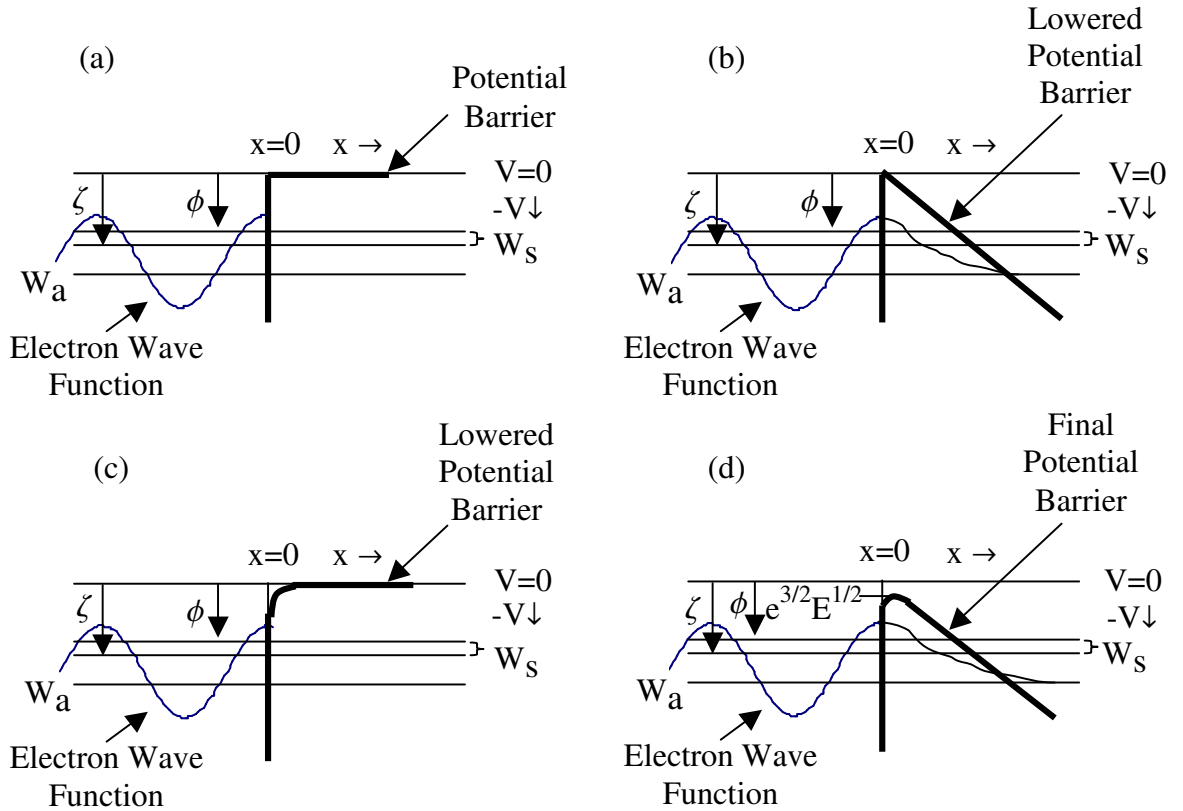


Figure 2.9: Panel (a): An electron wave function at a potential barrier where  $x$  is zero at the metal surface,  $V$  the potential height,  $\phi$  the work function,  $\zeta$  the Fermi Energy,  $W_a$  the electron potential energy, and  $W_s$  the surface potential energy. Panel (b): Effect of an electric field lowers the potential barrier to a triangular shape so electrons have a higher probability of tunneling from the metal into the vacuum. Panel (c): Effect of an image force in lowering the potential barrier. Panel (d): The potential barrier is lowered due to the applied electric field and the electron image force.

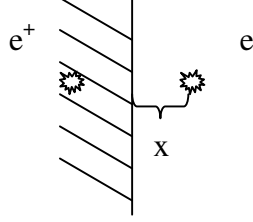


Figure 2.10: An electron that has left the metal surface also encounters an image force that lowers the height of the potential barrier by  $\frac{e^2}{4x}$ .

function is lower than the Fermi energy,  $\phi = -\zeta + W_s$ .

Fowler and Nordheim assumed that the conduction electrons in the metal form a gas of free particles, which obey Fermi-Dirac statistics. They then calculated the number,  $dn$ , of electrons within a volume,  $v$ , and with momenta within the range  $dp_x dp_y dp_z$  arriving at the surface of the metal [10]:

$$dn = \frac{2v dp_x dp_y dp_z}{h^3 \left[ \left( \frac{\exp(E-\zeta)}{kT} \right) + 1 \right]}, \quad (2.28)$$

where  $h$  is Plank's constant,  $k$  is Boltzmann's constant,  $\zeta$  the Fermi energy,  $E$  the total energy, i.e.  $W + \frac{p_y^2 + p_z^2}{2m}$ , and  $T$  the temperature. The supply of electrons, or supply function  $N(W)$ , is found by integrating Equation 2.28 over all  $p_y$  and  $p_z$  [10]:

$$\begin{aligned} N(W) &= \frac{2}{h^3} \int_{-\infty}^{+\infty} \int_{-\infty}^{+\infty} \frac{dp_y dp_z}{\exp\left(\frac{E-\zeta}{kT}\right) + 1} \\ &= \frac{4\pi m k T}{h^3} \ln \left( 1 + \exp \left[ \frac{-W + \zeta}{kT} \right] \right). \end{aligned} \quad (2.29)$$

Once at the potential barrier or surface, the probability of an electron tunneling through or leaving the surface, is given by the transmission coefficient  $D(W)$  [10] (Appendix B.1):

$$D(W) = \exp \left( -\frac{2\sqrt{2m|W|^3}}{3eE\hbar} v(y) \right), \quad (2.30)$$

where  $v = \frac{1}{\sqrt{2}}a\sqrt{[E(k) - b^2K(k)]}$ ,  $K(k)$  and  $E(k)$  are elliptical integrals of the first and second kind,  $a$ ,  $b$ , and  $k$  are defined in Appendix B.1.

The number of electrons within energy  $dW$  emerging from the surface per unit area [10] (Appendix B.2):

$$P(W)dW = N(W)D(W)dW. \quad (2.31)$$

$$P(W)dW = \frac{4\pi mkT}{h^3} \ln \left[ 1 + \exp \left( \frac{-W + \zeta}{kT} \right) \right] \exp \left( \frac{-4\sqrt{2m|W|^3}}{3eE\hbar} v(y) \right),$$

$$P(W) = \frac{4\pi mkT}{h^3} \ln \left[ 1 + \exp \left( \frac{-W + \zeta}{kT} \right) \right] \exp \left( -c + \frac{W - \zeta}{d} \right),$$

where

$$c = \frac{4\sqrt{2m\phi^3}}{3eE\hbar} v,$$

$$d = \frac{eE\hbar}{2\sqrt{2m\phi t}}.$$

In the low temperature limit [10]:

$$\begin{aligned} kT \ln \left( 1 + \exp \left( \frac{-W + \zeta}{kT} \right) \right) &= 0 && \text{when } W > \zeta \\ &= \zeta - W && \text{when } W < \zeta, \end{aligned}$$

$$\begin{aligned} \text{thus } P(W) &= 0 && \text{when } W > \zeta \\ &= \frac{4\pi m}{h^3} \exp \left( -c + \frac{W - \zeta}{d} \right) (\zeta - W) && \text{when } W < \zeta. \end{aligned}$$

The current density is found by integrating  $P(W)$  over all energies, i.e. from  $-W_a$  to  $\infty$ . Good and Müller [10] assumed  $-W_a$  is far below the Fermi energy  $\zeta$ , so the

lower limit is  $-\infty$  (Appendix B.3):

$$\begin{aligned} j &= e \int_{-\infty}^{\zeta} P(W) dW \\ &= \frac{1.54 \times 10^{-6} E^2}{\phi t^2} \exp \left( -6.83 \times 10^9 \frac{\phi^{\frac{3}{2}}}{E} v \right), \end{aligned} \quad (2.32)$$

where  $h =$  Planck's constant,  $e^2 = \frac{197 \text{ MeVfm}(4\pi\epsilon_0)}{137}$ , and  $m = 9.109 \times 10^{-13} \text{ Kg}$ .

The elliptic function is defined as [11]:

$$v(s) = 0.956 - 1.062s^2$$

$$s = 3.79 \times 10^{-5} \frac{E^{1/2}}{\phi}$$

Both Good and Müller [10] and Wang and Loew [11] set  $t = 1$  in Equation 2.32 since  $1 \leq t \leq 1.11$ :

$$\begin{aligned} j &= \frac{1.54 \times 10^{-6} E^2}{\phi} \exp \left[ \frac{\phi^{3/2}}{E} \left( -6.529 \times 10^9 + 10.42 \frac{E}{\phi^2} \right) \right] \\ &= \frac{1.54 \times 10^{-6} \times 10^{4.52} \times \phi^{-\frac{1}{2}} E^2}{\phi} \left[ \exp \left( -6.529 \times 10^9 \frac{\phi^{3/2}}{E} \right) \right]. \end{aligned} \quad (2.33)$$

No metal surface is perfectly flat and clean therefore large variations in the microscopic surface field lead to enhanced field emission. A few examples include roughness, scratches, dust or micro particles, grain boundaries, and absorbed gas [11].

In a superconducting cavity, the current collected by a pickup probe and the x-ray intensity outside the cavity follow the functional dependence of the Fowler-Nordheim law. But, just as Schottky observed in 1923, the function has to be modified by a factor,  $\beta_{FN}$ , referred to as the Fowler-Nordheim field enhancement factor [10]. Thus  $E$  is replaced with  $\beta_{FN}E$  in the equations for current density and current. The current

is  $I = jA_e$ , where  $A_e$  is the effective emitting area. Without the field enhancement factor, current and x-ray intensity are many orders of magnitude lower than observed. Therefore, current becomes [11]:

$$\frac{I}{E^2} = \frac{1.54 \times 10^{-6} \times 10^{4.52} A_e \beta_{FN}^2 \exp(\phi^{-1/2}) \exp \left[ -6.529 \times 10^9 \frac{\phi^{3/2}}{\beta_{FN} E} \right]}{\phi},$$

$$\ln \frac{I}{E^2} = \ln \left( 1.54 \times 10^{-6} \frac{A_e \beta_{FN}^2}{\phi} \right) + 10.42 \phi^{-1/2} - 6.529 \times 10^9 \frac{\phi^{3/2}}{\beta_{FN} E},$$

$$\frac{d \left( \ln \frac{I}{E^2} \right)}{d \left( \frac{1}{E} \right)} = \frac{-6.529 \times 10^9 \phi^{3/2}}{\beta_{FN} E},$$

$$\begin{aligned} \frac{d \left( \log_{10} \frac{I}{E^2} \right)}{d \left( \frac{1}{E} \right)} &= (\log_{10} e) \left( -6.529 \times 10^9 \frac{\phi^{3/2}}{\beta_{FN} E} \right) \\ &= \frac{-2.84 \times 10^9 \phi^{3/2}}{\beta_{FN} E}. \end{aligned} \quad (2.34)$$

For DC electric fields the numerical value of  $\beta_{FN}$  for a particular surface can be obtained from I, E, and  $\phi$  and by plotting  $\log_{10} \left( \frac{I}{E^2} \right)$  versus  $\frac{1}{E}$ . The  $\beta_{FN}$  value is the slope of the line.

Electron emission for RF fields is modified from the DC version by assuming that the microscopic electric field on a metal surface is of the form  $E = E_0 \sin \omega t$ . The average field emission current is calculated by a time averaging substitution into Equation 2.33 (Appendix B.4):

$$\begin{aligned} \langle I \rangle &= \frac{1}{T} \int_0^T I(t) dt \\ &= \frac{5.7 \times 10^{-12} \times 10^{4.52} A_e \beta_{FN}^{2.5} E_0^{2.5} \exp(\phi^{1.5})}{\phi^{1.75}} \exp \left( \frac{-6.529 \times 10^9 \phi^{1.5}}{\beta_{FN} E_0} \right), \end{aligned}$$

$$\ln \left( \frac{\langle I \rangle}{E^{2.5}} \right) = \ln \left( \frac{5.7 \times 10^{-12} A_e \beta_{FN}^{2.5}}{\phi^{1.75}} \right) + (10.41 \phi^{-0.5}) - \left( \frac{6.529 \times 10^9 \phi^{1.5}}{\beta_{FN} E_0} \right),$$

$$\begin{aligned} \frac{d \left( \log_{10} \frac{\langle I \rangle}{E^{2.5}} \right)}{d \left( \frac{1}{E} \right)} &= \frac{-(\log_{10} e) 6.529 \times 10^9 \phi^{1.5}}{\beta_{FN}} \\ &= \frac{-2.84 \times 10^9 \phi^{1.5}}{\beta_{FN}}. \end{aligned} \quad (2.35)$$

Similar to the DC case, but with a plot of  $\log_{10} \left( \frac{\langle I \rangle}{E^{2.5}} \right)$  versus  $\frac{1}{E}$ , one can obtain  $\beta_{FN}$  from the slope of the line and  $A_e$  from the intercept [11]. For this study, a plot of  $\log_{10} \left( \frac{\langle I \rangle E}{E^{3.5}} \right) = \log_{10} \left( \frac{P}{E^{3.5}} \right)$  versus  $\frac{1}{E}$ , where  $P$  is power, was used to determine  $\beta_{FN}$  since power was measured. The physical significance of  $\beta_{FN}$  and  $A_e$  is still a matter of debate [4].

### 2.1.3 X-rays

In 1895, the German physicist Wilhelm Conrad Roentgen was attempting to produce radiation which would traverse matter opaque to ordinary light. He covered a discharge tube (Figure 2.8) with ordinary paper and found that a screen covered with crystals of platinum barium cyanide fluoresced. He found that the unknown radiation could penetrate a 100 page book, but heavier objects stopped the fluorescence. He also found that the radiation could expose a photographic plate. One of his earliest photographic plates shows an image of his wife's hand with a ring (Figure 2.11). He named this radiation "x-rays", indicating their mysterious nature [12]. Roentgen was awarded the first Nobel Prize in 1901 for his achievements in x-ray studies [12].

As charged particles travel through matter they lose energy in Coulomb interactions with electrons and nuclei, by emission of electromagnetic radiation (bremsstrahlung or braking radiation), in nuclear interactions, and by emission of Cerenkov radiation. The charged particle of interest in this study is the field emitted electron with



Figure 2.11: One of earliest photographic plates showing an x-ray image of Bertha Roentgen's hand with a ring produced on December 22, 1895 [13].

a maximum energy around 1 MeV, therefore, discussions of Coulomb interactions and bremsstrahlung radiation follow. Cavities developed for the International Linear Collider (ILC) could produce field emitted electrons with energies over 10 MeV.

### Coulomb Interactions

As an electron (or any charged particle) travels through a material it may interact with atomic electrons or the nucleus of the atom. The radius of the nucleus is approximately  $10^{-14}$  m and the radius of the atom approximately  $10^{-10}$  m. It is expected that:

$$\frac{\text{Number of interactions with electrons}}{\text{Number of interactions with nuclei}} = \frac{(R^2)_{\text{atom}}}{(R^2)_{\text{nucleus}}} = \frac{(10^{-10})^2}{(10^{-14})^2} = 10^8$$

collisions are with atomic electrons and are more important than collisions with nuclei [14].

Inelastic collisions with bound atomic electrons result in either one or more atomic electrons transitioning to an excited state (excitation) or to an unbound state (ionization). Elastic collisions are significant in cases of very-low-energy ( $< 100$  eV) electrons and therefore are omitted from this discussion [2].

Excitation occurs when a bound electron of the material acquires enough energy,

from electrons traversing the material, to transition to an empty state in another orbit of higher energy. Transitions are typically between the  $K$ ,  $L$ ,  $M$ , ... shells in atoms. In a time of  $10^{-10}$  to  $10^{-8}$  seconds the electron will transition to a lower energy state, provided one is empty. The excess energy is emitted in the form of x-rays characteristic of the material [14].

Ionization occurs when an electron in the material acquires enough energy, from electrons traversing the material, to leave the atom and become a free particle. The kinetic energy of the freed electron is:

$$(KE)_e = (\text{energy given by electron}) - (\text{ionization potential}).$$

The freed electron may cause ionization of another atom if its kinetic energy is high enough. Fast freed electrons produced in ionizing collisions are called  $\delta$  (delta) rays which produce secondary interactions while being brought to rest [14] [2].

An electron traveling through a material exerts Coulomb forces on many atoms simultaneously. Since every atom has many electrons, the incident electron interacts with millions of atomic electrons, each occurrence producing an energy loss. It is impossible to calculate the energy loss from individual collisions; therefore, an average energy loss is calculated per unit distance traveled. The energy loss or stopping power per unit path length due to ionization-excitation for electrons is given by [14]:

$$\begin{aligned} \left(\frac{dT}{ds}\right)_{ion} &= 4\pi r_0^2 \frac{m_0 c^2}{\beta^2} N Z \left[ \ln \left( \frac{\beta \gamma \sqrt{\gamma - 1}}{I} m_0 c^2 \right) \right] \\ &+ 4\pi r_0^2 \frac{m_0 c^2}{\beta^2} N Z \frac{1}{2\gamma^2} \left[ \frac{(\gamma - 1)^2}{8} + 1 - (\gamma^2 + 2\gamma - 1) \ln 2 \right] \end{aligned} \quad (2.36)$$

in ( $\frac{\text{MeV}}{\text{m}}$ ), where

$$\begin{aligned}
 r_0 &= \frac{e^2}{m_0 c^2} = 2.818 \times 10^{-15} \text{ m} = \text{classical electron radius} \\
 \gamma &= \frac{1}{\sqrt{1 - \beta^2}} \\
 \beta &= \frac{v}{c} \\
 N &= \rho \left( \frac{N_A}{A} \right) = \text{density} \frac{\text{Avogadro's Number}}{\text{Atomic Weight}} \\
 Z &= \text{atomic number of material} \\
 I &= \text{mean excitation potential of material} \\
 &\sim (9.76 + 58.8Z^{-1.19})Z \text{ in eV.}
 \end{aligned}$$

A complete derivation can be found in [2].

In this study, the maximum electron kinetic energy was measured to be around 1 MeV, implying an electron velocity of 0.941  $c$ . The energy loss per unit path length in niobium was calculated to be approximately  $7.64 \frac{\text{MeV}}{\text{cm}}$ .

### Bremsstrahlung Radiation

Whenever a charged particle accelerates, part of its energy is converted to electromagnetic radiation in the form of bremsstrahlung x-rays (Figure 2.12). In this study, the charged particles of interest are the field emitted electrons impacting the walls within a niobium cavity. For electrons with kinetic energy  $T$  (MeV) traversing a material with atomic number  $Z$ , the energy loss or stopping power per unit path length due to bremsstrahlung x-rays, is given in terms of the ionization and excitation energy loss (Equation 2.36) [14]:

$$\left( \frac{dT}{ds} \right)_{brem} = \frac{ZT}{750} \left( \frac{dT}{ds} \right)_{ion} . \quad (2.37)$$

Bremsstrahlung emission increases with electron energy and atomic number of the material. A full derivation is given in [2].

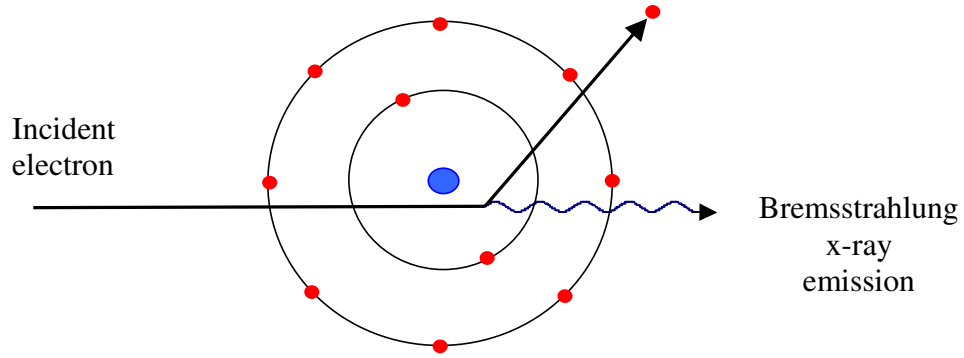


Figure 2.12: An electron accelerating near a nucleus and emitting bremsstrahlung radiation.

In this study  $\left(\frac{dT}{ds}\right)_{ion}$  (Equation 2.36) was calculated to be  $7.64 \frac{\text{MeV}}{\text{cm}}$ ,  $Z$  for niobium is 41, and the maximum electron kinetic energy,  $T$  in MeV, 1 MeV.

$$\left(\frac{dT}{ds}\right)_{brem} = 0.055 \left(\frac{dT}{ds}\right)_{ion},$$

which means 5.5% of the 1 MeV x-rays are due to bremsstrahlung radiation.

The energy of x-ray photons can range from very small values up to the energy of the incident electron, which is known as Duane and Hunt's Law [2]. In 1922, Kühlenkampff [15] reported that the intensity of the continuous x-ray spectrum could be represented experimentally by:

$$I_{\lambda} = CZ \frac{1}{\lambda^2} \left( \frac{1}{\lambda_0} - \frac{1}{\lambda} \right) + BZ^2 \frac{1}{\lambda^2}, \quad (2.38)$$

where  $I_{\lambda}$  is the x-ray intensity in units of  $\frac{\text{ergs}}{\text{cm}^2 \text{sec}}$ ,  $B$  and  $C$  are constants,  $Z$  the atomic number of the material,  $\lambda_0$  the wavelength of the incident electron, and  $\lambda$  the wavelength of the x-ray photons.

H. A. Kramers furthered Kühlenkampff's work by theoretically deriving (to first

order) the constant C [16]:

$$\begin{aligned}
 I_\lambda &= s \frac{8\pi}{3l\sqrt{3}} \frac{e^2 h}{mc} Z \frac{1}{\lambda^2} \left( \frac{1}{\lambda_0} - \frac{1}{\lambda} \right) \\
 &= 45 \times 10^{-30} s Z \frac{1}{\lambda^2} \left( \frac{1}{\lambda_0} - \frac{1}{\lambda} \right) \\
 &= 2.35 \times 10^{-2} s Z E^2 (E_0 - E),
 \end{aligned} \tag{2.39}$$

where  $s$  is the number of electrons entering the material, and  $E$  and  $E_0$  are in keV. Equation 2.39 is known as Kramers approximation. Figure 2.13 shows a plot of the continuous bremsstrahlung x-ray spectrum for 1 MeV and 0.5 MeV electrons in niobium. In this study electrons of varying energies impact the cavity walls, thus the x-ray spectrum is a sum of all the individual electron spectra.

Koch and Motz [17] describe the angular distribution of bremsstrahlung x-rays by the fraction of the total incident electron kinetic energy that is radiated per steradian

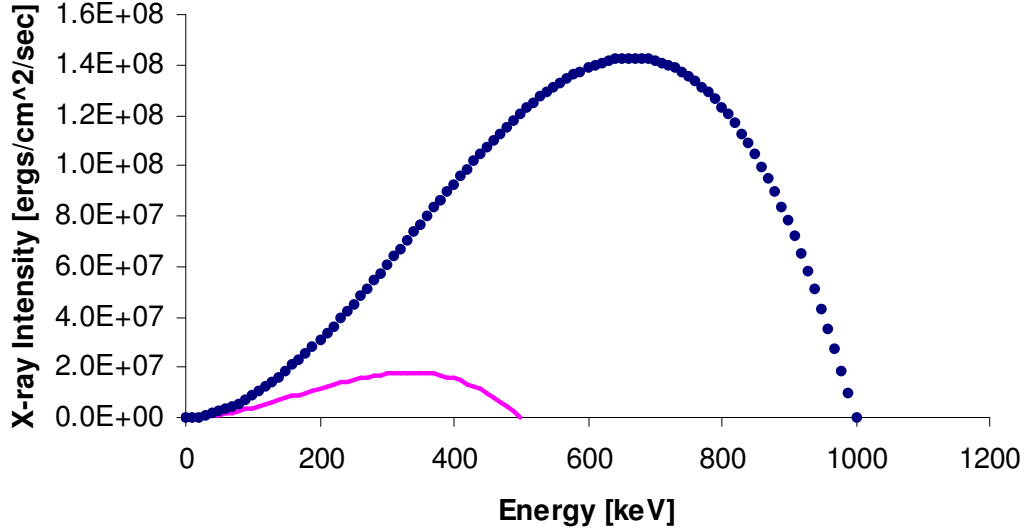


Figure 2.13: X-ray spectrum for a 1 MeV (dotted line) and a 0.5 MeV (solid line) electron traveling through niobium as predicted by Kramers approximation (Equation 2.39). The maximum x-ray energy ranges from very small values up to the energy of the incident electron according to Duane and Hunt's Law.

at the angle  $a$  as:

$$R_a = \frac{K\xi_0^2}{1760\pi} \left[ -E_i \left( \frac{-\xi_0^2 a^2}{1760t} \right) + E_i \left( \frac{-\xi_0^2 a^2}{7.15} \right) \right], \quad (2.40)$$

where  $K$  depends on the initial electron kinetic energy and atomic number of the material,  $\xi_0$  is the incident electron energy in units of  $m_0c^2$ ,  $a$  is the angle of the bremsstrahlung x-rays in radians,  $t$  is the length given in units of radiation length,  $E_i$  is the exponential integral:

$$-E_i(-y) = \int_y^\infty \frac{e^{-z}}{z} dz, \quad (2.41)$$

and

$$R_{a=0} = \frac{K\xi_0^2}{1760} \ln 246t. \quad (2.42)$$

Figure 2.14 is a plot of the bremsstrahlung angular distribution of x-rays for an electron with energy 1 MeV and 300 keV incident on niobium. Incident electrons with an energy of 1 MeV, typical of this study, show an anisotropic tendency. The number of x-rays entering the detector through a collimator will be lower at angles

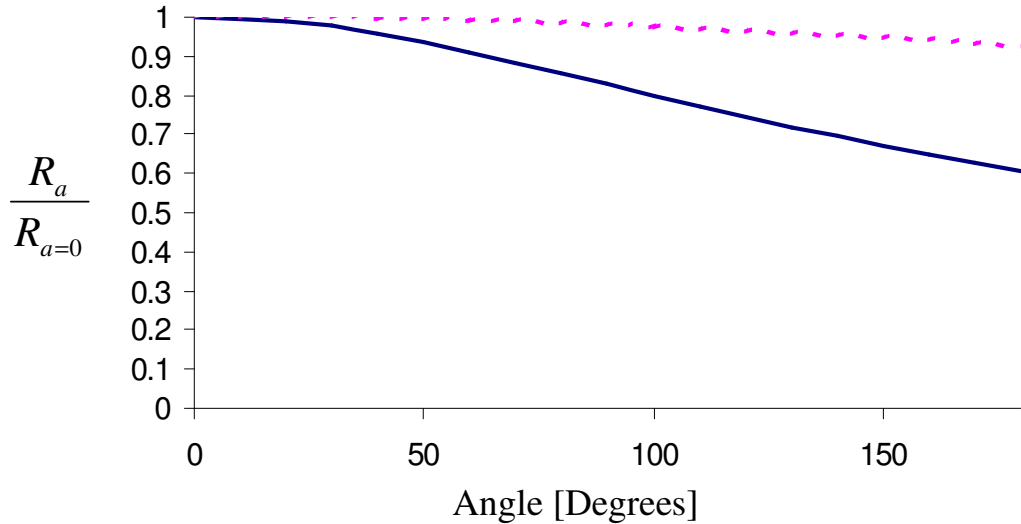


Figure 2.14: Angular distribution of bremsstrahlung x-rays. Electrons with incident energy of 1 MeV are shown as a solid line and 300 keV as a dotted line.

not parallel with the electron forward motion.

### 2.1.4 Photon Interactions with Matter

Photons are classified according to their mode of origin, not their energy. Thus,  $\gamma$  rays are the electromagnetic radiations accompanying nuclear transitions. Bremsstrahlung or continuous x-rays are the result of the acceleration/deceleration of charged particles. Characteristic x-rays are emitted in atomic transitions of bound electrons between the  $K$ ,  $L$ ,  $M$ , ... shells in atoms. Annihilation radiation is emitted when a positron and electron combine. Interactions of photons with matter are independent of the mode of origin of the photon and dependent only upon the photon quantum energy [2].

Photons may be treated as electromagnetic waves or as particles. An electromagnetic wave is characterized by its wavelength ( $\lambda$ ) or frequency ( $\nu$ ),  $\nu = \frac{c}{\lambda}$ . As a particle, a photon has zero charge and zero rest mass and travels at the speed of light. The quantum energy of photons is expressed as:

$$E = h\nu = \frac{hc}{\lambda},$$

where  $h$  is Planck's constant =  $4.136 \times 10^{-15}$  eVs [2] [14],  $\nu$  the photon frequency, and  $\lambda$  the photon wavelength.

A number of processes can cause photons to be scattered or absorbed. The energy domains met in this study, 0.01 to 2 MeV, are explained in terms of photoelectric effect, Compton effect and pair production. Other processes such as Rayleigh scattering, Thomson scattering by the nucleus, and Delbruck scattering are explained in Appendix 1.

## Compton Effect

The Compton effect or Compton scattering is a collision between a photon and an unbound or free electron (rest mass =  $m_0c^2 = 0.511$  MeV) considered at rest. An electron is considered unbound when the electron binding energy is much less than the energy of the incident photon. The collision results in a scattered photon and a scattered electron (Figure 2.15) [2]. The scattered electron loses energy by ionization and excitation (Coulomb interactions) or by emission of bremsstrahlung radiation. The scattered photon loses energy by Compton scattering, the photoelectric effect, or at very high energies, pair production.

The incident photon momentum ( $\frac{h\nu_0}{c}$ ) must be conserved between the scattered photon and the struck electron. The relations for the conservation of momentum in the direction of the incident photon for the collision of Figure 2.15 is expressed as:

$$\frac{h\nu_0}{c} = \frac{h\nu'}{c} \cos \theta + p \cos \varphi, \quad (2.43)$$

where  $h\nu_0$  is the incident photon energy,  $h\nu'$  the scattered photon energy,  $\theta$  the scattered photon angle,  $p$  the scattered electron momentum, and  $\varphi$  the scattered

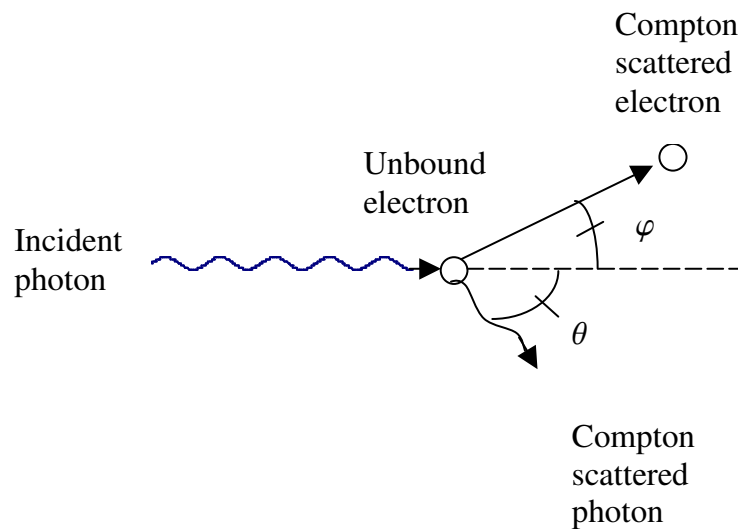


Figure 2.15: Compton scattering, a collision between a photon and an unbound electron. The photon is scattered at an angle  $\theta$  and the electron at an angle  $\varphi$  [13].

electron angle [2].

Conservation of momentum normal to the direction of the incident photon is expressed as:

$$0 = -\frac{h\nu'}{c} \sin \theta + p \sin \varphi. \quad (2.44)$$

By the conservation of energy

$$h\nu_0 = h\nu' + T, \quad (2.45)$$

where T is the scattered electron kinetic energy, and by using the relativistic relationship

$$pc = \sqrt{T(T + 2m_0c^2)} \quad (2.46)$$

any two parameters can be eliminated from the conservation equations 2.43, 2.44, 2.45 and relativistic relationship 2.46 [2].

Energy of the scattered photon (Appendix C.1):

$$h\nu' = \frac{m_0c^2}{1 - \cos \theta + \frac{1}{\alpha}}, \quad (2.47)$$

$$\frac{\nu'}{\nu_0} = \frac{1}{1 + \alpha(1 - \cos \theta)}, \quad (2.48)$$

where  $\alpha = \frac{h\nu_0}{m_0c^2}$ . For very large incident photon energy  $\frac{h\nu_0}{m_0c^2} = \alpha \gg 1$ , the energy of the backscattered photon,  $\theta = 180^\circ$  approaches  $h\nu' \sim m_0c^2 = 0.511$  MeV. Energy of the struck electron, or shift in the photon energy, is found from Equation 2.45, and substituting Equation 2.47 for  $h\nu'$ :

$$\begin{aligned} T &= h\nu_0 - \frac{m_0c^2}{1 - \cos \theta + \frac{1}{\alpha}} \\ &= \frac{h\nu_0\alpha(1 - \cos \theta)}{1 + \alpha(1 - \cos \theta)}. \end{aligned} \quad (2.49)$$

Maximum energy transfer to the electron,  $T_{max}$ , occurs at  $\theta = 180^\circ$ :

$$T_{max} = \frac{h\nu_0}{1 + \frac{1}{2\alpha}}, \quad (2.50)$$

and minimum at  $\theta = 0^\circ$  in which case  $T_{min} = 0$  [2].

During Compton scattering, it is impossible for all the energy of the incident photon to be given to the electron. The energy given to the electron will be dissipated in the material within a distance equal to the range of the electron [14]. The kinetic energy of the Compton scattered electron can be found dependent upon the electrons scattering angle ( $\varphi$ ) [2]:

$$T = \frac{2h\nu_0\alpha \cos^2 \varphi}{(1 + \alpha)^2 - \alpha^2 \cos^2 \varphi}.$$

The maximum electron kinetic energy occurs at  $\varphi = 0^\circ$  and the minimum at  $\varphi = 90^\circ$  [2].

Another interesting effect is the Compton shift in wavelength of the incident photon to the scattered photon [2]:

$$\begin{aligned} \lambda' - \lambda_0 &= \frac{c}{\nu'} - \frac{c}{\nu_0} \\ &= \frac{hc}{h\nu'} - \frac{hc}{h\nu_0}, \text{ substituting } h\nu' \text{ from Equation 2.47,} \\ &= \frac{hc - hc \cos \theta + \frac{hc m_0 c^2}{h\nu_0}}{m_0 c^2} - \frac{hc}{h\nu_0} \\ &= \frac{hc(1 - \cos \theta)}{m_0 c^2}. \end{aligned} \quad (2.51)$$

The Compton shift in wavelength is independent of the energy of the incident photon ( $h\nu_0$ ) where as the Compton shift in energy,  $h\nu_0 - h\nu'$ , is strongly dependent upon  $h\nu_0$ . Thus low energy photons are scattered with moderate energy change but high-energy photons experience a very large change in energy. For example, at  $\theta = 90^\circ$  if  $h\nu_0 = 10$  keV then  $h\nu' = 9.8$  keV, a 2% change; but if  $h\nu_0 = 10$  MeV then

$h\nu' = 0.49$  MeV, a 95% change [2].

The Compton wavelength is defined as the wavelength of a photon whose energy is equal to the rest mass of the electron [2]:

$$\begin{aligned}\lambda_c &= \frac{c}{\nu_c} = \frac{hc}{h\nu_c} = \frac{hc}{m_0c^2} = \frac{h}{m_0c} \\ &= \frac{4.136 \times 10^{-21} \text{MeVs}}{\frac{0.511 \text{MeV}c}{c^2}} \\ &= 2.424 \times 10^{-12} \text{ m.}\end{aligned}\tag{2.52}$$

The probability that Compton scattering will occur is called the Compton cross section [14]. To derive the Compton cross section from the initial state  $O(\frac{h\nu_0}{c}, p = 0)$  to the final state  $F(\frac{h\nu}{c}, p)$ , consideration must be given to the intermediate states. The following two intermediate states are possible [18] [2]:

I) The incident photon is absorbed by the electron, which then has momentum  $\frac{h\nu_0}{c}$ , and no photon is present. As the electron transitions to the final state of momentum  $p$ , a photon of energy  $h\nu'$  is emitted by the electron.

II) The electron first emits a photon of energy  $h\nu'$ , leaving the electron with momentum  $-\frac{h\nu'}{c}$ . Two photons are present until the electron transitions to the final state when the incident photon is absorbed.

This representation of the scattering mechanism leads to the Klein-Nishina formula of differential collision cross section:

$$d\sigma = \frac{r_0^2}{4} d\Omega \left(\frac{\nu'}{\nu_0}\right)^2 \left(\frac{\nu_0}{\nu'} + \frac{\nu'}{\nu_0} - 2 + 4 \cos^2 \Theta\right),$$

where  $r_0 = \frac{e^2}{m_0c^2} = 2.818 \times 10^{-15}$  m is the classical electron radius,  $d\Omega = \sin \theta d\theta d\phi$  is the element of solid angle through which the scattered photon emerges after the collision, and  $\Theta$  is the angle between the electric vectors of the incident and scattered radiation.

The total collision cross section,  $\sigma$ , is the probability of photon removal from a beam while passing through an absorber containing one electron per  $\text{cm}^2$ . To obtain the expression for  $\sigma$ , substitutions for  $d\Omega = 2\pi \sin\theta d\theta$  and  $\frac{\nu'}{\nu_0}$  from Equation 2.48 are made and integration taken for all values of  $\theta$ :

$$\sigma = \int_0^\pi d\sigma = 2\pi r_0^2 \left[ \frac{1+\alpha}{\alpha^2} \left[ \frac{2(1+\alpha)}{1+2\alpha} - \frac{1}{\alpha} \ln(1+2\alpha) \right] + \frac{1}{2\alpha} \ln(1+2\alpha) - \frac{1+3\alpha}{(1+2\alpha)^2} \right],$$

in units of  $\frac{\text{cm}^2}{\text{electron}}$  [2].

As photons travel through a material they encounter  $NZ$  electrons per  $\text{cm}^3$ , where  $N = \rho \frac{N_A}{A}$ ,  $\rho$  the density,  $N_A = \text{Avagadro's Number} = 6.022 \times 10^{23} \frac{\text{atoms}}{\text{mol}}$  and  $A$  the atomic weight, and  $Z$  the atomic number of the material. Let  $n$  be the number of incident photons and  $dn$  the number of photons removed from the number incident per second:

$$-\frac{dn}{n} = (NZ dx)\sigma = \sigma_{lin} dx.$$

$\sigma_{lin}$  is defined as the Compton total linear attenuation coefficient [2]:

$$\sigma_{lin} = NZ\sigma \left[ \text{cm}^{-1} \right]. \quad (2.53)$$

Linear coefficients for various incident photon energies and materials can be found in numerous reference books and on the web. Figure 2.16 shows how  $\sigma_{lin}$  changes as a function of incident photon energy  $h\nu_0$  and  $\frac{Z}{A}$  [14]. When a significant number of photon interactions are due to Compton scattering, the fractional transmission,  $\frac{n}{n_0}$ , of unmodified photons through a material of thickness  $x$  is:

$$\frac{n}{n_0} = e^{-\sigma_{lin}x}. \quad (2.54)$$

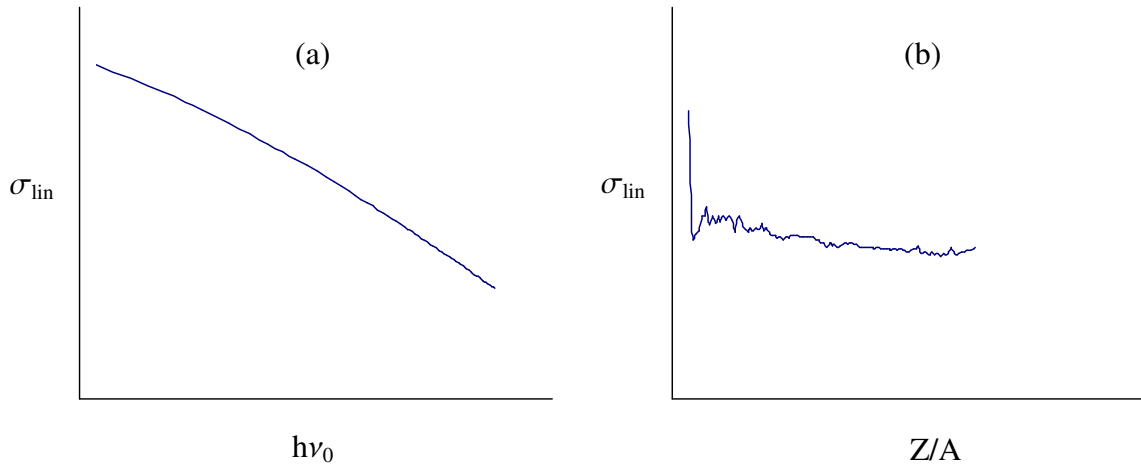


Figure 2.16: Dependence of the Compton cross section  $\sigma_{lin}$  on (a) the incident photon energy  $h\nu_0$  (ln vs ln scale) and (b) the atomic number of the material (linear vs linear scale).

### Photoelectric Effect

An incident photon cannot be totally absorbed by a free electron as evidenced from the momentum relationships in Compton collisions. The photoelectric effect takes place when an incident photon is totally absorbed by an electron initially bound in an atom. The photon disappears and one of the atomic electrons is ejected as a free electron, creating an ion. The photoelectron loses energy by ionization and excitation (Coulomb interactions) or by emission of bremsstrahlung radiation. The electron vacancy can be filled through the capture of a free electron and/or by the rearrangement of electrons from other shells of the atom, thus generating one or more characteristic x-ray photons [19] (Figure 2.17). If the emitted x-ray photon has sufficient energy and is absorbed by a second electron within the atom, it is emitted as an Auger electron. The atom becomes doubly ionized [2] [19].

In a photoelectric interaction momentum is conserved by the recoil of the atom. The most tightly bound electrons, K shell, have the highest probability, 80%, of absorption when the incident photon energy exceeds the K-shell binding energy. The

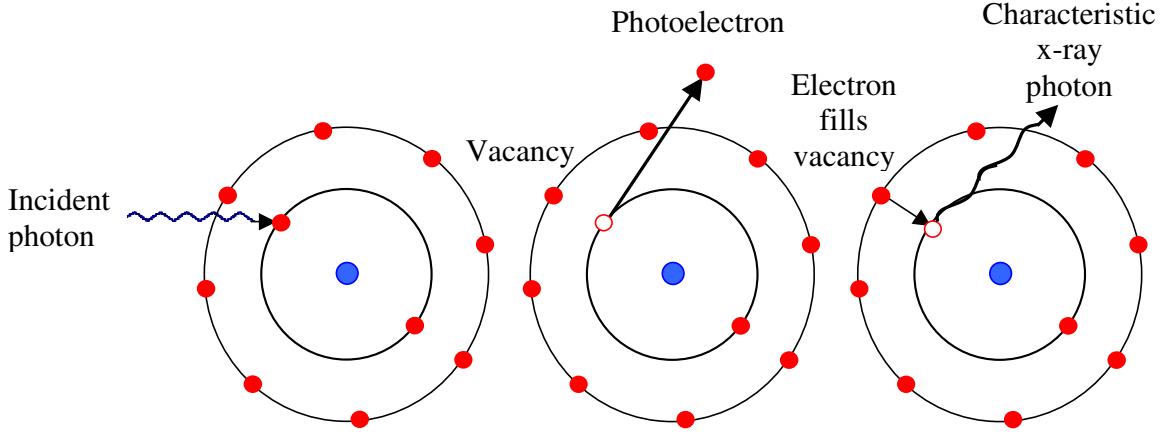


Figure 2.17: Diagram of the photoelectric process. The incident photon is absorbed and a photoelectron is ejected with energy  $T = h\nu_0 - B_e$ . When the vacancy is filled the excess energy is carried off by a characteristic x-ray photon. Momentum is conserved by the recoil of the atom.

kinetic energy of the free electron is:

$$T = h\nu_0 - B_e, \quad (2.55)$$

where  $B_e$  is the binding energy of the electron [2] [14].

The probability of the photoelectric effect occurring is called the photoelectric cross section. Unlike the Compton effect, exact solutions are difficult and tedious. In the energy region of interest in this study (0.35 to 2 MeV), reference [20] provides complete solutions. For a crude approximation of the total photoelectric cross section:

$$\tau \simeq a \frac{Z^n}{h\nu_0^3}, \quad (2.56)$$

where  $a$  is a constant and  $n$  increases from 4-4.6 for  $h\nu_0$  increasing from 0.1 to 3.0 MeV [2].

Similar to the Compton cross section, the linear photoelectric cross section is defined as [2]:

$$\tau_{lin} = \tau N. \quad (2.57)$$

Figure 2.18 shows how  $\tau_{lin}$  changes as a function of incident photon energy and  $Z$  [14].

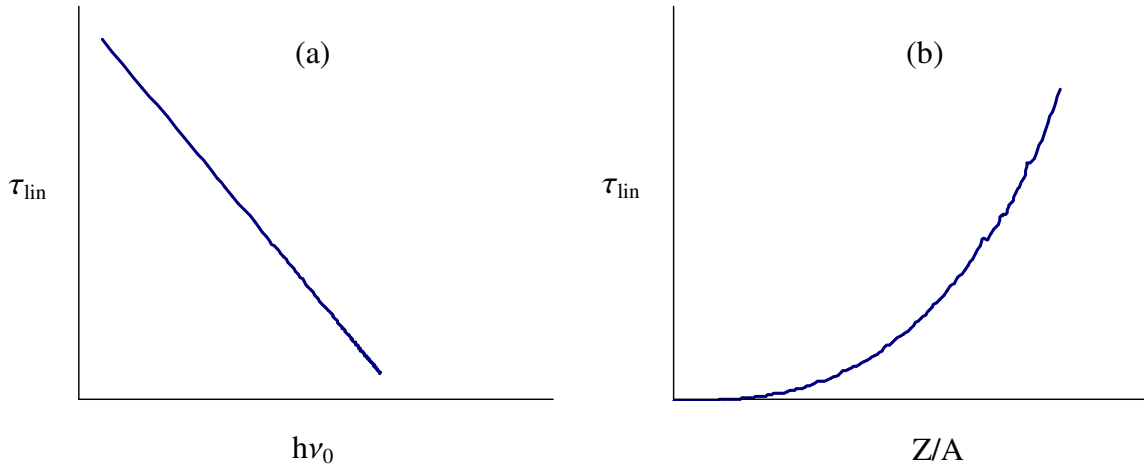


Figure 2.18: Dependence of the photoelectric cross section  $\sigma_{lin}$  on (a) the incident photon energy  $h\nu_0$  (ln vs ln scale) and (b) the atomic number of the material (linear vs linear scale).

### Pair Production

Pair production is an interaction between an incident photon with an energy above 1.022 MeV and a nucleus within a material. The photon is completely absorbed and in its place a positron-electron pair appears. The nucleus does not undergo any change. By conservation of energy:

$$h\nu_0 = (T_- + m_0c^2) + (T_+ + m_0c^2),$$

where  $T_-$  and  $T_+$  are the kinetic energy of the electron and positron respectively [2] [14].

The positron is not a stable particle and travels only a short distance before combining with an electron or annihilating, creating two photons separated by  $180^\circ$  and each with energy of  $m_0c^2$  (0.511 MeV). The electron travels a few millimeters at most before losing energy by ionization and excitation (Coulomb interactions) or by emission of bremsstrahlung radiation (Figure 2.19) [2] [19].

The probability of the pair production occurring is called the pair production cross section. Pair production was not a concern for the photon energies encountered in

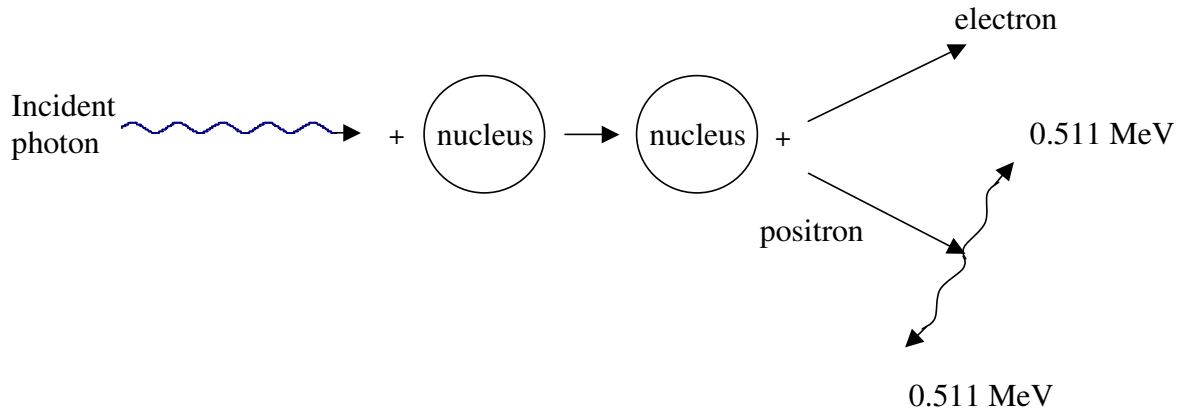


Figure 2.19: Pair production. The incident photon disappears and a positron-electron pair is created, followed by two 0.511 MeV photons produced when the positron annihilates.

this study. Unlike the Compton effect, the total pair production cross section is a complicated function of  $h\nu_0$  and a complete derivation can be found in [2]. It may be written in the form [2]:

$$\kappa = \sigma Z^2 \left( \frac{28}{9} \ln \frac{2h\nu_0}{m_0c^2} - \frac{218}{27} \right).$$

Similar to the Compton cross section, the linear pair production cross section is defined as [2]:

$$\kappa_{lin} = \kappa N. \tag{2.58}$$

Figure 2.20 shows how  $\kappa_{lin}$  changes as a function of incident photon energy and  $Z$  [14].

### Attenuation of Electromagnetic Radiation

In the previous three subsections, photon interactions with matter were discussed. The following is a discussion of the over-all effects of these processes on photons as they pass through a material.

The probability of a photon traversing a thickness  $t$  of absorbing material without a Compton collision is  $e^{-\sigma_{lin}t}$ , photoelectric interaction is  $e^{-\tau_{lin}t}$ , and a pair

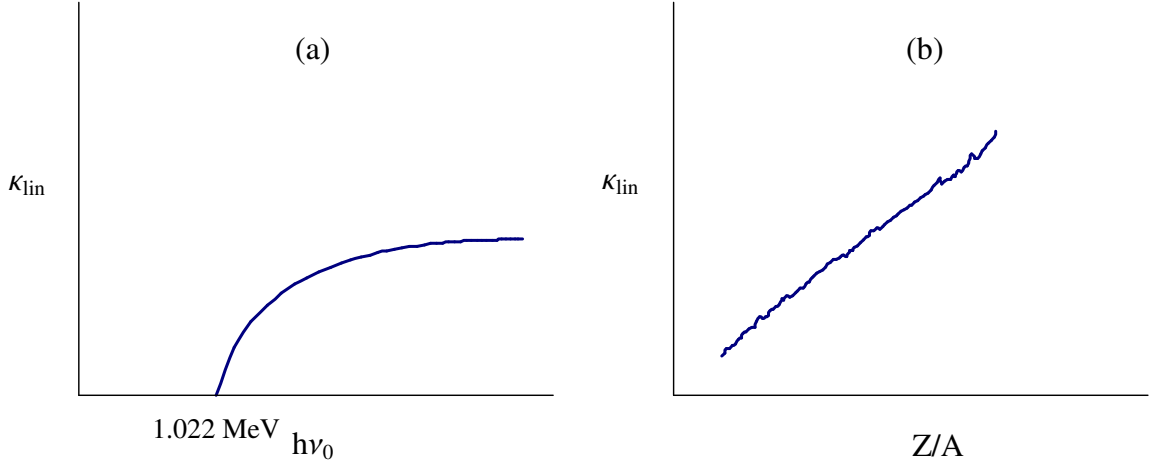


Figure 2.20: Dependence of the pair production cross section  $\kappa_{lin}$  on (a) the incident photon energy  $h\nu_0$  (ln vs ln scale) and (b) the atomic number of the material (linear vs linear scale).

production collision is  $e^{-\kappa_{lin}t}$ . Let  $I_0$  be the initial intensity of photons traversing a material of thickness  $t$ . From Equation 2.54 the number of unaffected photons,  $I_f$ , is:

$$\begin{aligned}
 I_f &= I_0 e^{-\sigma_{lin}t - \tau_{lin}t - \kappa_{lin}t} \\
 &= I_0 e^{-(\sigma_{lin} + \tau_{lin} + \kappa_{lin})t} \\
 &= I_0 e^{\mu_{lin}t},
 \end{aligned} \tag{2.59}$$

where  $\mu_{lin}$  is the total linear attenuation coefficient. A graphical relationship between the three types of interactions is shown in Figure 2.21. The photoelectric interaction is important at low photon energies and high  $Z$  materials, pair production at high photon energies and high  $Z$  materials, and Compton effect at intermediate energies and intermediate  $Z$  materials.

The total linear attenuation coefficient is distinguished from the total mass absorption coefficient, which is a smaller quantity and measures the energy absorbed by

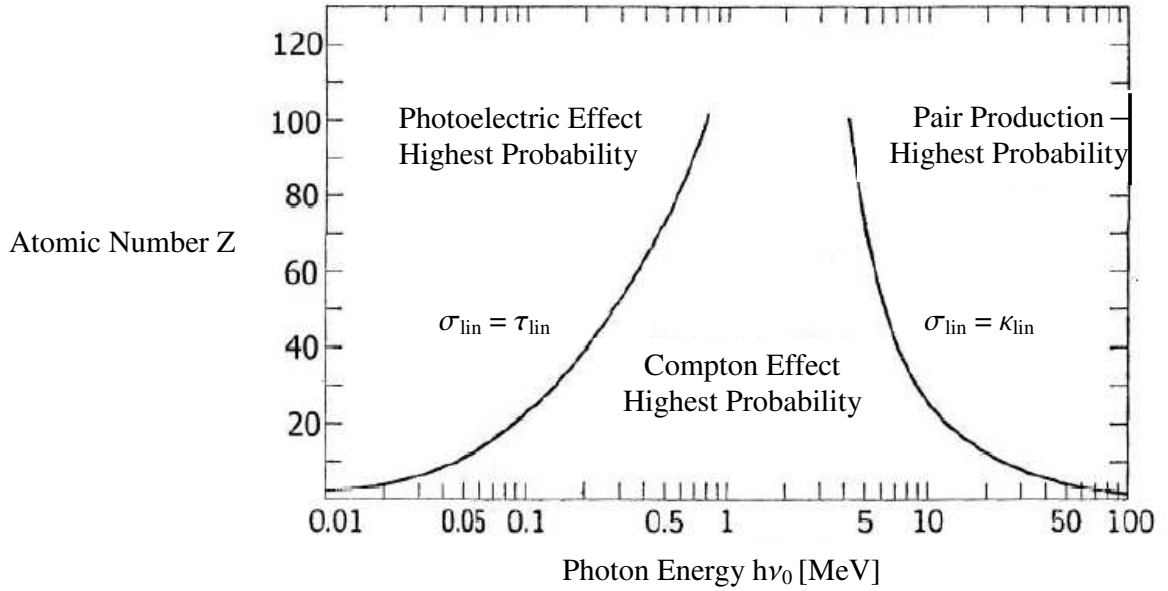


Figure 2.21: Relative importance of the three main types of photon interaction as they traverse a material. The lines show the values of  $h\nu$  and  $Z$  for which the probability of the effects are equal.

the material. Often it is useful to know the mass attenuation coefficient:

$$\begin{aligned}
 \mu_{ma} \left[ \frac{\text{cm}^2}{\text{g}} \right] &= \frac{\mu_{lin} [\text{cm}^{-1}]}{\rho \left[ \frac{\text{g}}{\text{cm}^3} \right]} \\
 &= \sigma_{ma} + \tau_{ma} + \kappa_{ma} \\
 &= \frac{\sigma_{lin} + \tau_{lin} + \kappa_{lin}}{\rho}.
 \end{aligned}$$

The thickness of the material is now measured in units of  $\rho x \left[ \frac{\text{g}}{\text{cm}^2} \right]$ :

$$\frac{I_f}{I_0} = e^{-\frac{\sigma_{lin}}{\rho}(\rho x)} = e^{-\sigma_{ma}\rho x}.$$

The advantage of measuring material thickness in units of  $\frac{\text{g}}{\text{cm}^2}$  is that the mass attenuation coefficient is nearly independent of the nature of the material since  $\frac{Z}{A}$  is approximately constant for all elements.

There are many reference books and websites with figures and tables [21] that give  $\mu_{lin}$  and  $\mu_{ma}$  for nearly all the elements and energies. Figure 2.22 shows the mass

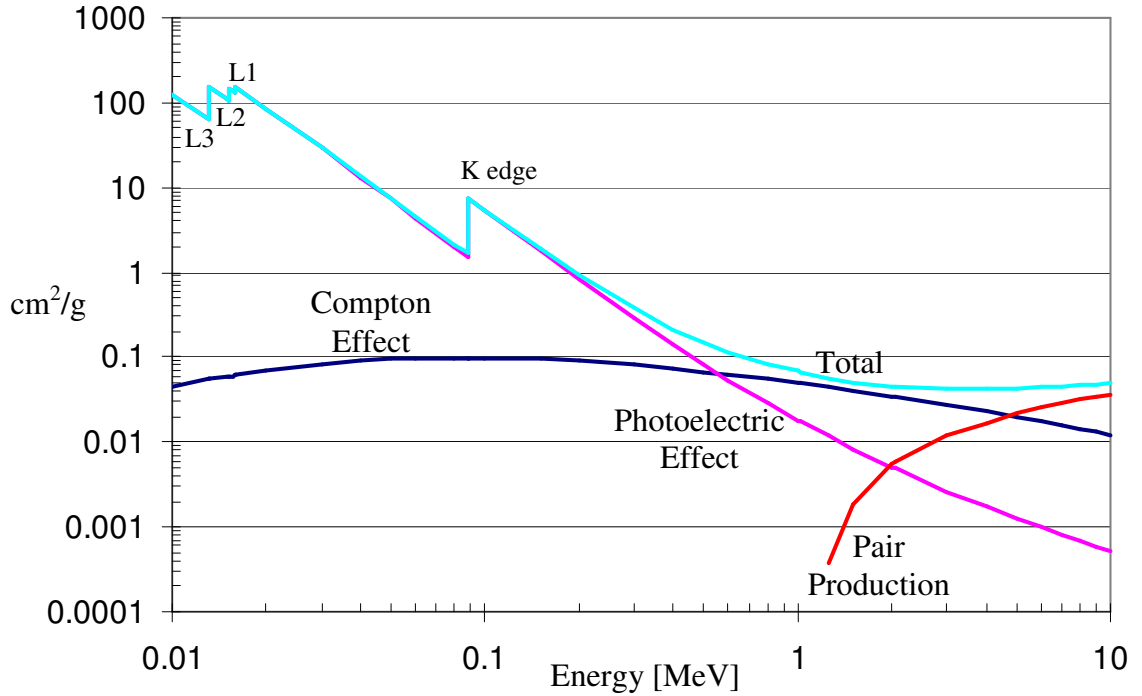


Figure 2.22: Mass attenuation coefficient versus energy for photons in lead. This plot was constructed from data retrieved from the NIST program XCOM [21].

attenuation coefficients for photons of different energies in lead. The plot shows the photoelectric effect as the primary interaction at low energies. The discontinuities are due to electrons being ejected from their shells and the vacancies filled. At intermediate energies the Compton effect is the primary interaction. Pair production comes into play at 1.022 MeV, which is the minimum energy needed to produce an electron and a positron.

For mixtures of elements, an over-all mass attenuation coefficient is given by:

$$\frac{\mu_{lin}}{\rho} = \frac{\mu_{lin1}}{\rho_1}w_1 + \frac{\mu_{lin2}}{\rho_2}w_2 + \dots, \quad (2.60)$$

where  $w_1, w_2, \dots$  are the fractions by weight of the elements that make up the absorber.

As a photon traverses a material with a total linear attenuation coefficient of  $\mu_{lin}$ , the probability that it can travel a distance  $x$  without experiencing an interaction is  $e^{-\mu_{lin}x}$ . The mean free path length is the mean distance a photon will travel before

its first interaction:

$$l_{mfp} = \frac{1}{\mu_{lin}}. \quad (2.61)$$

Photons with an energy of 1 MeV traversing lead have a mean free path of 1.25 cm.

## 2.2 X-ray Detection

When photons enter the scintillator material of a detector, sparks or scintillations of light are produced. The amount of light produced is very small; to be detectable it must be amplified with a device known as the photomultiplier tube (PMT). The resulting voltage is proportional to the energy of the incident x-ray photon and is displayed on a multichannel analyzer (MCA) [14].

### 2.2.1 Detector

Unlike the discrete electronic energy states of an atom (Subsection 2.1.4), the allowed energy states in a crystal widen into bands. The luminescence of inorganic scintillators, such as the one used in this study, is explained in terms of the valence, conductance, and forbidden bands of a crystal. The valence band is completely filled with electrons bound at lattice sites. The conduction band is void of electrons while in the ground state. At energies between the valence and conduction bands lies the forbidden band, in which electrons are never found in a pure crystal. Electrons that have obtained sufficient energy from incident photons move from the valence band to the conduction band and are free to migrate throughout the crystal. The displaced electron leaves a hole in the valence band, which also moves freely. At energies insufficient to produce complete ionization the electron stays bound to the hole and is called an exciton (Figure 2.23) [14] [19].

In a pure crystal, when the electron de-excites and returns to the valence band, a photon is emitted in the ultraviolet range. To enhance the probability of visible

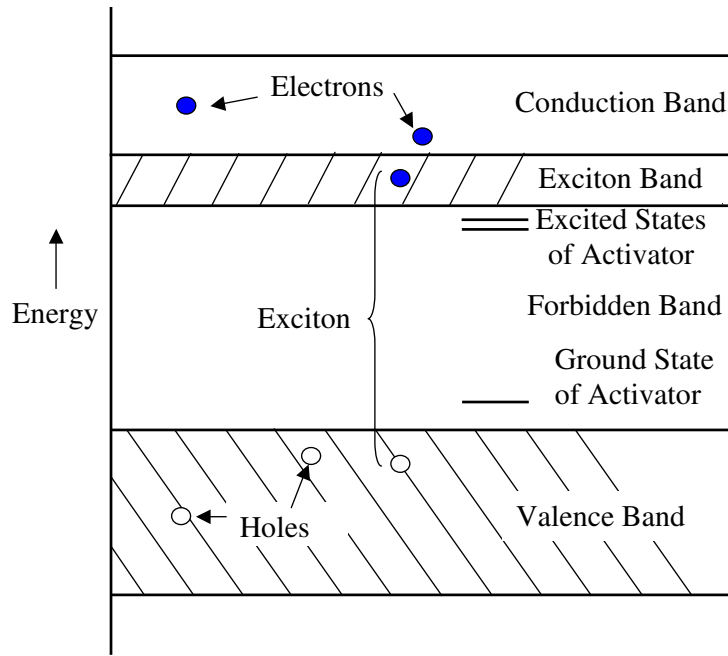


Figure 2.23: Valence, conductance, forbidden, and excited states of activator for a typical scintillator material. The energy between the valence and conductance bands is around 8 eV.

photon emission, impurities, called activators, are added to the scintillator, creating energy states within the forbidden band through which the electron can de-excite back to the valence band. Electron transitions produce visible photons because the energy is less than the full forbidden band. The light yield is proportional to the deposited radiation energy. To prevent the entry of stray light and the escape of light from the surface, both of which can influence the results, the scintillator is surrounded by a reflector on all surfaces except where the PMT is mounted [19].

Photons emitted from the scintillator strike the photo cathode of a PMT and transfer energy to electrons in the photo cathode. The electrons migrate to the surface and escape (photoemission) [19].

Once free, an electron gains energy as it travels, guided by an electric field, to the first dynode. The creation of an excited electron in the dynode requires energy on the order of 2 to 3 eV. An electron traversing a 100 V gap may create 30 excited electrons. Many of these electrons will not reach the surface due to energy loss and their random

motion. Others may have insufficient energy to overcome the work function once they reach the surface. The secondary emission ratio is around 10% for 1 keV electrons entering cesiated antimony, such as the dynodes in the PMT used in this study [19].

Secondary electrons, from the dynode surface, travel to the second dynode where they multiply again. Voltage between successive dynodes (up to 15) range from 80 to 150 V, thus amplifying the photon energy received from the scintillator material (Figure 2.24) [19] [14]. Magnetic fields can misdirect some electrons away from the next dynode, so that the photomultiplier must be covered with a thin sheet of mu metal (magnetic shield comprised of nickel and iron) [14].

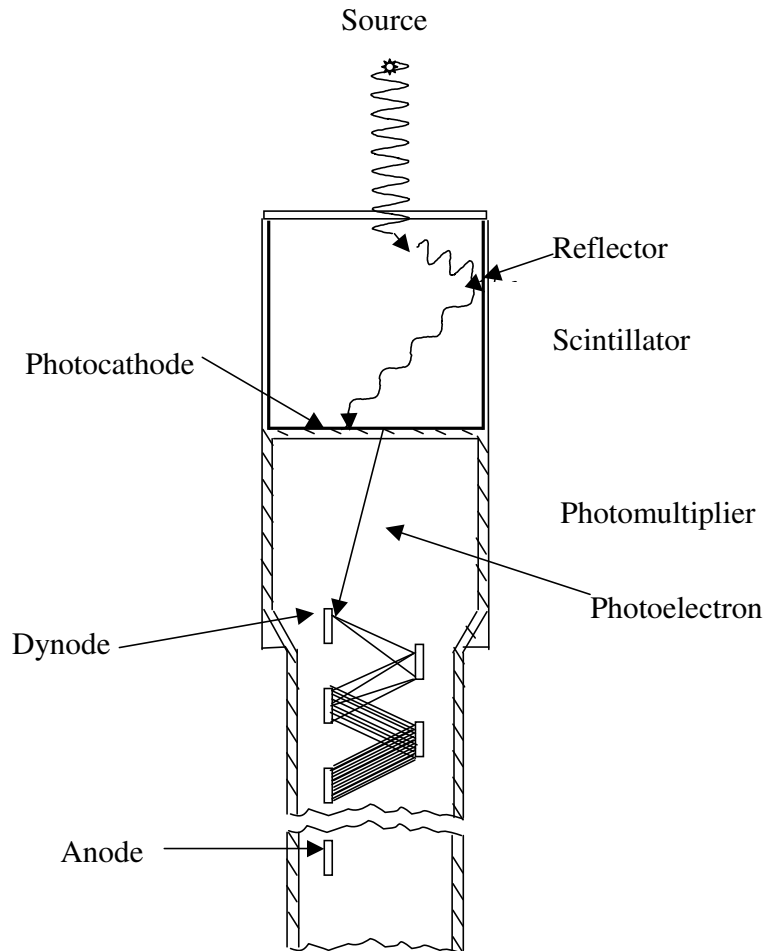


Figure 2.24: Scintillator detector. A photon travels through the scintillator producing visible photons that strike the photo cathode producing free electrons. The free electrons are multiplied by the dynode system ending at the anode where an MCA displays a pulse proportional to the original incident photo energy.

An anode is located at the end of the series of dynodes and collects electrons. A corresponding voltage pulse develops across a load resistor. An MCA, operated in the pulse height analysis (PHA) mode, sorts out the incoming pulses according to their height and stores the number of pulses of a particular height in a corresponding channel. The MCA channels are calibrated by recording radioactive spectra of sources with known discrete energies [19] [14].

The energy resolution of a detector is a measure of its ability to distinguish photon peaks that are close in energy:

$$R = \frac{C_R - C_L}{C_{peak}} = \frac{FWHM}{C_{peak}}, \quad (2.62)$$

where  $C_R$  and  $C_L$  are the channel numbers on either side of the peak at half of its maximum,  $C_{peak}$  the channel number of the peak, and FWHM the full width of the peak at half the maximum value [19] [14].

When a photon enters the scintillator material of a detector it may not be counted. The photon may travel through the detector without having an interaction, the intensity of visible light produced may be too low to be recorded, or it may be scattered out of the detector by the detector shielding. The absolute detector counting efficiency is defined as [14]:

$$\epsilon_{abs} = \frac{\text{number of pulses recorded}}{\text{number of radiation quanta emitted by source}}.$$

In practice, the detector counting efficiency depends on:

1. the fraction of space that a detector subtends:

$$G = \frac{\text{area of detector face}}{4\pi R^2},$$

where R is the source detector distance;

2. the fraction of photons absorbed by the intervening material:

$$I = e^{-\mu_{lin1}d_1} \times e^{-\mu_{lin2}d_2} \times \dots,$$

where  $\mu$  is the linear attenuation coefficient of the intervening material and  $d$  its thickness;

3. the fraction of photons absorbed by the detector scintillator material (M):

$$M = 1 - e^{-\mu d},$$

where  $\mu$  is the linear attenuation coefficient of the scintillator and  $d$  the scintillator height.

The calculated detector efficiency becomes [22]:

$$D = GIM. \tag{2.63}$$

The measured detector counting efficiency is determined by:

$$DE = \frac{P}{RN}, \tag{2.64}$$

where P is a ratio of the number of photons in the energy peaks to the total photon count, R the number of counts in the photopeak, and N the number of photons emitted by the source. N is calculated as:

$$N = TB \times T \times A,$$

where TB is the total branching ratio, T the total counting time interval in seconds, and A the activity of the source in disintegrations per second. The activity of the

source is calculated as:

$$A = A_0 e^{-\frac{t}{\tau}},$$

where  $A_0$  is the activity of the source when it was calibrated,  $t$  the time interval since the source was calibrated, and  $\tau$  the half-life of the source in the same units as the time interval.

### Collimator

X-ray and gamma ray imaging utilize collimators since such short wavelengths cannot be focused with lenses as are optical or near optical wavelengths. A collimator is a narrow tube, or slit in this case, through a strong radiation absorbing material. X-rays traveling nearly parallel to the collimator axis traverse the entire length to the detector. Other rays are absorbed by striking the front surface or side of the aperture (Figure 2.25). Collimators are used to improve image resolution, but they also reduce the intensity of the signal.

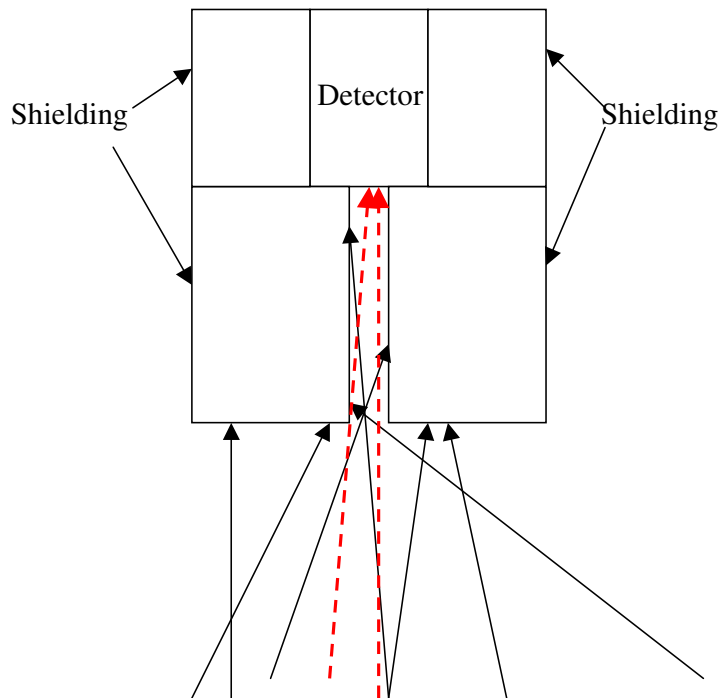


Figure 2.25: A collimator showing only x-rays traveling nearly parallel to the collimator axis reach the detector.

The slit spatial resolution is determined using the geometry configuration of Figure 2.26 and the following calculation:

$$y = \frac{2dx - tx}{t}.$$

The slit was traveling horizontally at an average velocity ( $\langle v \rangle$ ) and data accumulated in time intervals, so the total spatial resolution becomes:

$$y = \frac{2dx - tx}{t} + \langle v \rangle (\text{time}). \quad (2.65)$$

Since their discovery, x-rays have been the most important medical imaging diagnostic tool. A gamma camera consists of one or more PMT's mounted to a scintillator to map radiation entering through a, usually lead, collimator speckled with thousands of holes (Figure 2.27). No material totally attenuates photons so the crosstalk between holes produces a blurred image. Gamma cameras are used to image patient organs, track blood flow, scan shipping containers for radiation, and scan nuclear warheads for fissile materials.

Nuclear medical imaging utilizes gamma cameras in the Single Photon Emission

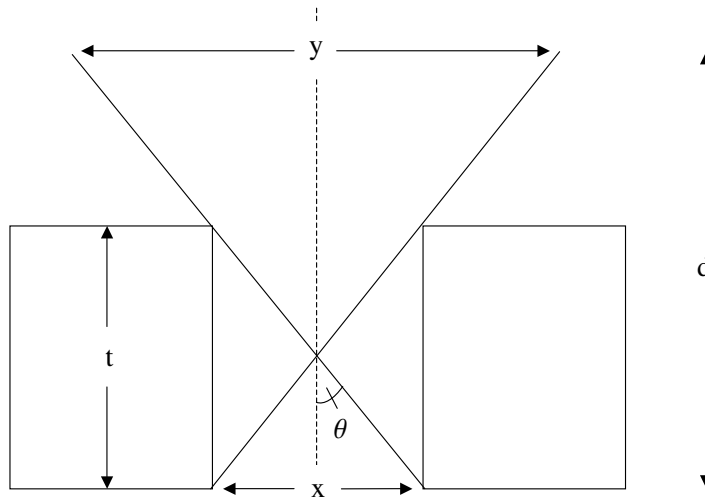


Figure 2.26: Geometric configuration of slit spatial resolution. The slit spatial resolution is  $y$ , the lead brick shielding thickness is  $t$ , and the detector to source distance is  $d$ .

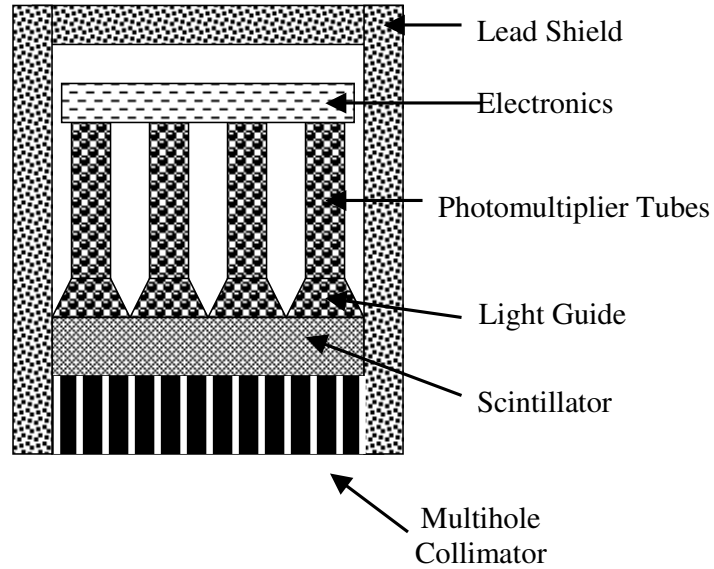


Figure 2.27: Basic diagram of a gamma camera.

Computed Tomography (SPECT) scanning device. Patients are injected with a short-lived radioactive tracer isotope mixed with a molecular probe. The isotope emits gamma rays as it decays. The gamma camera is rotated around a patient. Multiple images at multiple angles are obtained. A tomographic reconstruction algorithm yields a 3 dimensional image.

In optics, a collimating lens focuses light to form a parallel beam. Medical collimators are not only used for detection of radiation but for beam delivery as in proton radiotherapy.

## 2.3 SRF Cavity Testing

The purpose of testing a cavity is to determine its response to rf fields. The unloaded quality factor or quality factor of the cavity itself ( $Q_0$ ) as a function of the peak electric field ( $E_p$ ) is considered the most important cavity evaluation.

$Q_0$  of a cavity can be determined either in a modulated, or pulsed, wave mode or a continuous wave mode. Constants, determined by the modulated wave mode, are needed for the calculation of  $Q_0$  in the continuous wave mode. Thus, the calculation

of  $Q_0$  for the modulated wave mode is presented first.

### 2.3.1 Modulated Wave

During cavity testing the frequency, forward power ( $P_f$ ), reflected power ( $P_r$ ), transmitted power ( $P_t$ ), standing wave transmitted power ( $P_t(SW)$ ) are recorded. Power measurements are made in dBm and converted to Watts:

$$P(W) = \frac{10^{\frac{P(\text{dBm})+A(\text{dBm})}{10}}}{1000}, \quad (2.66)$$

where  $A_f$ ,  $A_r$ ,  $A_t$ , and  $A_t(SW)$  are the coupling factors for each of the measured quantities.

The calculation of the electric field on axis ( $E_a$ ) of the cavity, operated in the modulated wave mode, begins with the calculation of the loaded  $Q$  ( $Q_L$ ) or the quality factor of the total system, circuitry plus cavity. When power is removed from the cavity, the time taken for the cavity's stored energy to dissipate ( $\tau_L$ ), or "ring-down", is measured and  $Q_L$  is calculated:

$$Q_L = \omega\tau_L, \quad (2.67)$$

where  $\omega$  is the angular frequency.

Next, the coupling strength ( $\beta$ ) of the cavity is calculated from the measurements of  $P_f$  and  $P_r$  (Figure 2.28):

$$\begin{aligned} \beta &= \frac{\sqrt{P_f} \pm \sqrt{P_r}}{\sqrt{P_f} \mp \sqrt{P_r}} \\ &= \frac{Q_0}{Q_{ext,1}}, \end{aligned} \quad (2.68)$$

where the upper sign is for an overcoupled cavity ( $\beta > 1$ ) and the lower sign is for an

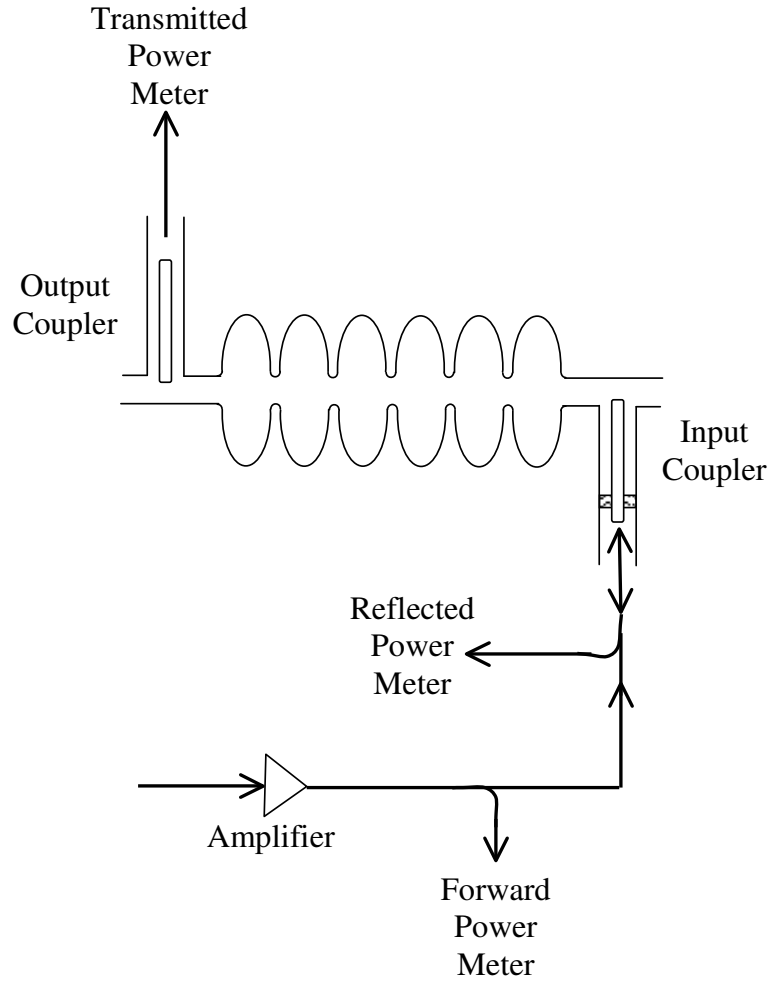


Figure 2.28: Diagram of measured quantities used to calculate  $Q_0$ .

undercoupled cavity ( $\beta < 1$ ),  $Q_0$  the quality factor of the cavity itself, and  $Q_{ext,1}$  a quality factor of the input coupler.

The quality factor due to each loss mechanism:

$$\frac{P_{tot}}{\omega U} = \frac{P_d + P_e + P_t}{\omega U}, \quad (2.69)$$

where  $P_e$  is power emitted back out the input coupler when  $P_f = 0$  (switched off), and  $U$  is the stored energy of the cavity.  $P_d$  is the power dissipated in just the cavity  $P_d = P_f - P_r - P_t - P_d(SW)$ , where  $P_d(SW)$  is calculated from  $P_t(SW)$ . The ratio

of  $P_d(SW)$  to  $P_t(SW)$  was found to be 19.98. Equation 2.69 becomes:

$$\begin{aligned}\frac{1}{Q_L} &= \frac{1}{Q_0} + \frac{1}{Q_{ext,1}} + \frac{1}{Q_t} \\ &\approx \frac{1}{Q_0} + \frac{1}{Q_{ext,1}} \\ &= \frac{1}{Q_0} + \frac{\beta}{Q_0},\end{aligned}\tag{2.70}$$

where  $\frac{1}{Q_t}$  is negligible.  $Q_0$  is calculated:

$$Q_0 = Q_L(1 + \beta)\tag{2.71}$$

The stored energy of the cavity is calculated:

$$U = \frac{Q_0 P_d}{\omega}.\tag{2.72}$$

### 2.3.2 Continuous Wave

Knowing  $U$ ,  $E_a$  and  $Q_0$  can be calculated for the continuous wave mode. First a quality factor for the transmitted power is assumed:

$$Q_t = \frac{\omega U}{P_t},\tag{2.73}$$

where  $U$  was calculated from data acquired in the modulated wave mode and  $P_t$  measured. A constant,  $k_1$ , is defined as:

$$k_1 = \sqrt{\frac{Q_t}{\omega}} = \sqrt{\frac{U}{P_t}}.\tag{2.74}$$

So,  $\sqrt{U} = k_1 \sqrt{P_t}$ .

Since  $U \propto E_a^2$ , another constant,  $k_2$ , is defined by the output from SUPERLANS:

$$k_2 = \frac{U}{E_a^2}. \quad (2.75)$$

The calculation of  $E_a$  is now possible:

$$E_a = \sqrt{\frac{U}{k_2}} = \frac{k_1 \sqrt{P_t}}{\sqrt{k_2}}, \quad (2.76)$$

$$E_p = 3.34E_a. \quad (2.77)$$

$Q_0$  is calculated:

$$Q_0 = \frac{\omega U}{P_d} = \frac{\omega k_1 \sqrt{P_t}}{P_d}. \quad (2.78)$$

# Chapter 3

## Design

Field emission (FE) in superconducting radio frequency (SRF) cavities is a primary factor limiting the surface electric field. The field-emitted electrons are accelerated by the rf field and strike the cavity wall, generating bremsstrahlung x-rays of a continuous spectrum (Section 2.1.3). The purpose of this study was to locate the source, intensity, and energy of the x-rays then, with a particle tracking code, show that the origin of the field-emitted electrons could be found.

### 3.1 Experimental Setup

#### 3.1.1 Cavity and Cryostat

A geometric beta  $\beta_g=0.47$  805 MHz six-cell cavity was designed and fabricated by a collaboration between Thomas Jefferson National Accelerator Facility, Istituto Nazionale di Fisica Nucleare Milano, and the NSCL for the Rare Isotope Accelerator (RIA) (Figure 2.5).

The cavities in this study were constructed of 4 mm thick sheet niobium with a nominal residual resistivity ratio (RRR) of 250. RRR is the ratio between the electrical resistivity at 273 K and the resistance in the normal conducting state extrapolated to 4.2 K and zero magnetic field [23]. The Holder Corporation of Lansing, Michigan

water-jet cut disks from sheet Nb. The dies used to form the cavity half cells were machined at the NSCL. The following procedures were performed at JLAB by NSCL faculty and staff. The disks were standard deep drawn into half cells and the equator and iris edges machined prior to electron beam welding.

After electron beam welding, the cavities were etched with a 1:1:1 buffered chemical polishing solution of phosphoric acid, hydrofluoric acid, and nitric acid [24]. Etching removes a potentially damaged layer as well as any evaporated niobium that may be deposited on the surface during welding; both are potential sources of field emission [4].

The concentration of H within a niobium cavity can increase during etching. Q disease, or residual losses from hydrides, is the accumulation of hydrides at the rf surface as a cavity is cooled for testing. This increases the surface resistance and, in some cases severely, lowers the cavity Q. Between 150 and 60 K the rate of accumulation is greatest. Therefore, a cavity is cooled as quickly as possible between this temperature range. The purpose of heat treatment of the cavity is to degas the H [4]. After heat treatment the cavities were etched once more then rinsed with ultra-pure water [24].

The cavities were then tuned for field flatness in a jig, designed and custom-built for the  $\beta_g=0.47$  cavity by NSCL staff. It is desirable to have equal accelerating fields in all cells of a cavity. This is accomplished by securing one end iris (Figure 2.5) and squeezing or stretching the cavity. The field flatness,  $\frac{\Delta E}{E}$ , was brought to near 5% for each cavity [24].

The cavities were tested in a vertical cryostat to verify their rf performance. The accelerating electric field ( $E_a$ ) was limited by the rf power available from the equipment. One cavity only reached a  $Q$  of  $8 \times 10^9$  so it was reetched and retested. During the second test an  $E_a = 8 \frac{\text{MV}}{\text{m}}$  and a  $Q = 10^{10}$  were achieved. The other cavity had similar results [24]. Each cavity was housed in a titanium helium vessel with a wall thickness of 0.48 cm and shipped to the NSCL, under partial vacuum, by truck [25].

At the NSCL, the helium vessels were surrounded by two  $\mu$ -metal shields that

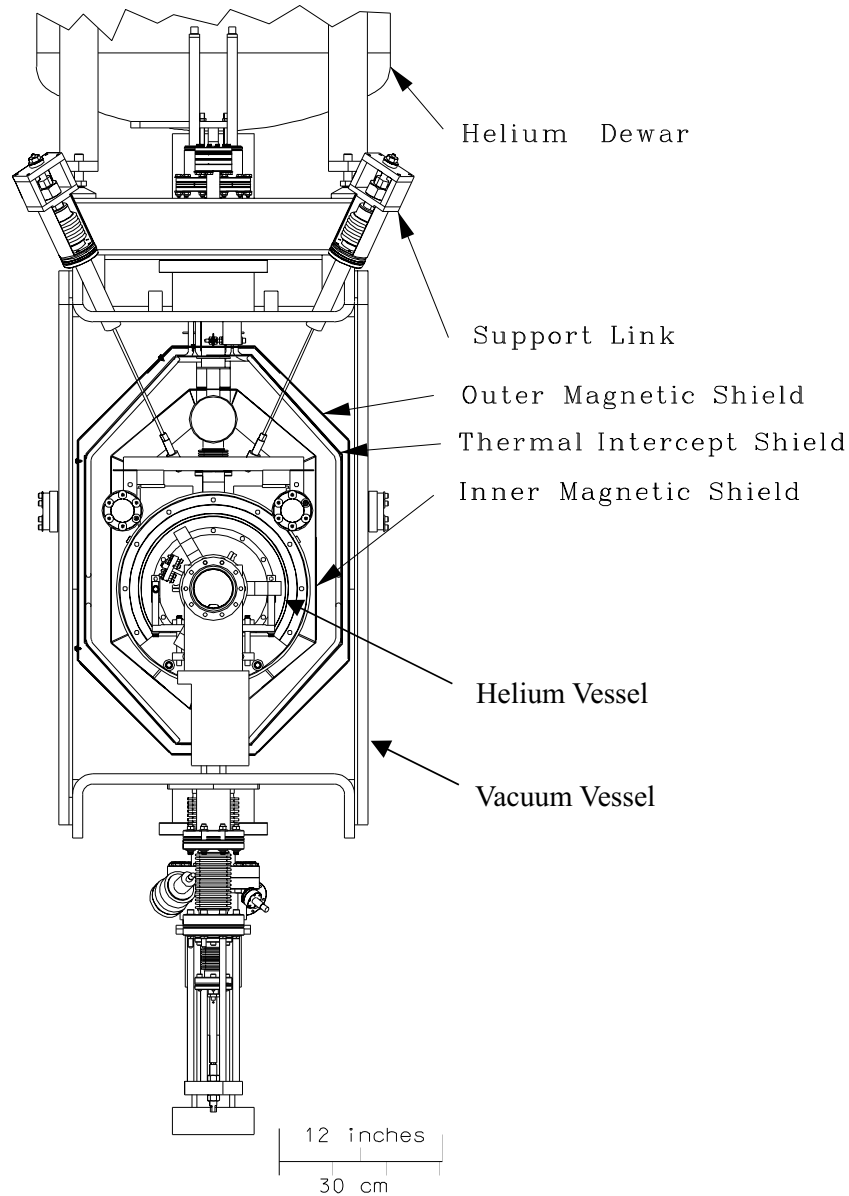


Figure 3.1: Each cavity is housed in a titanium helium vessel, surrounded by two  $\mu$ -metal shields and a copper thermal shield, inside a rectangular vacuum vessel.

reduce stray magnetic fields to  $0.5\text{-}1\ \mu\text{T}$ . The  $\mu$ -metal shields also serve as passive thermal shields. A  $0.16\ \text{cm}$  thick copper sheet between the  $\mu$ -metal shields, served as the thermal shield. Liquid nitrogen was used in the thermal shield. The outer rectangular vacuum vessel was made of  $1.91\ \text{cm}$  thick low-carbon steel plates (Figure 3.1, 3.2). The cryostst absorber materials encountered by photons in this study are given in Table 3.1 [21].

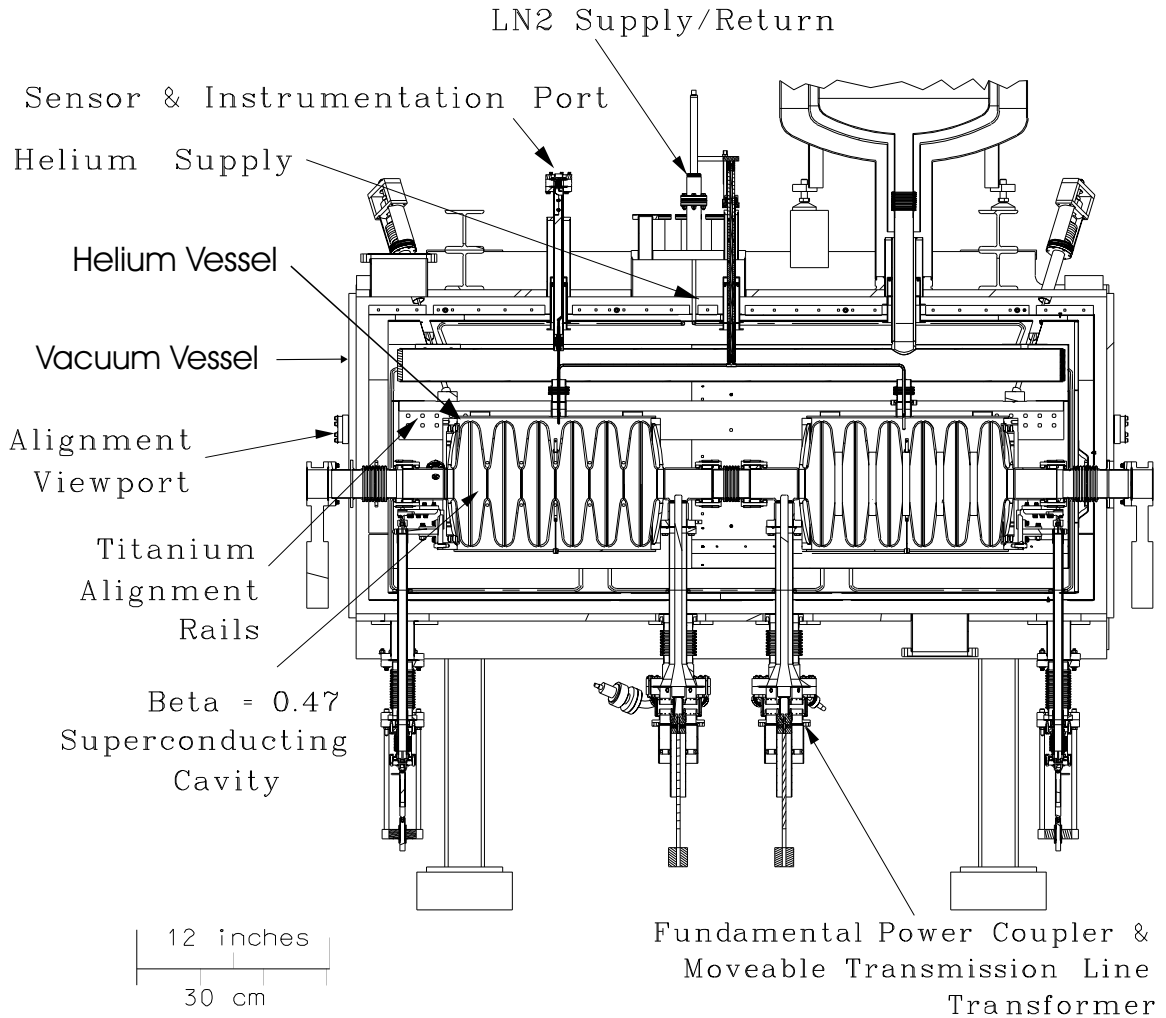


Figure 3.2: Each cavity is housed in a titanium helium vessel, surrounded by two  $\mu$ -metal shields and a copper thermal shield, inside a rectangular vacuum vessel.

Prior to testing, the cavities were rapidly cooled to 20 K to avoid  $Q$  disease. The cavities became superconducting ( $9.25 \pm 0.02$  K) after approximately 5 hours. Cooling proceeded to 4.3 K then to 2 K by vacuum pumping on the helium reservoir. Vacuum pumping lowers the pressure on the liquid helium, causing it to boil at a lower temperature. Heat is removed as the liquid reverts to a gaseous state.

Radio frequency power was supplied to each cavity via a coaxial cable in a transverse electromagnetic (TEM) mode (Section 2.1.1). The center conductor couples power to the input coupler, which protrudes into the beam tube, and excites a standing wave in the coupler (Figure 3.2). The outer conductor is connected through the

Table 3.1: Absorber materials.

Material	t [cm]	$\rho$ [ $\frac{\text{g}}{\text{cm}^3}$ ]	$\mu_{ma}$ [ $\frac{\text{cm}^2}{\text{g}}$ ]	$\mu_{lin}$ [ $\frac{1}{\text{cm}}$ ]
Nb	0.4	8.57	0.0587	0.503
He(liquid 2.2 K)	2.54	0.147	0.0636(gas)	0.009
Ti	0.48	4.54	0.0589	0.267
mu(80% Ni, 20% Fe)	0.10	8.70	0.0613	0.533
Ni	-	8.90	0.0616	0.548
Fe	-	7.87	0.0600	0.472
Cu	0.16	8.96	0.0590	0.529
Steel(75% Fe, 17% Cr, 8% Ni)	1.91	7.84	0.0600	0.470
Cr	-	7.18	0.0593	0.426

power coupler to the cavity. A fixed output coupler, or transmitted power probe, picks up power transmitted through the cavity. A sliding short provided input coupling adjustment. Forward power ( $P_f$ ), reflected power ( $P_r$ ), transmitted power ( $P_t$ ), and the standing wave transmitted power ( $P_t(SW)$ ) were recorded during testing.

### 3.1.2 Detector and Collimator

The continuous spectrum of x-ray photons of interest in this study were produced at field-emitted electron impact sites. The field emitted electrons were emitted while the cavities were rf tested. The cryostat materials and lead shielding surrounding the detector imply a significant probability of an x-ray interacting before reaching the detector (Subsection 2.1.4).

In this study the regions of x-ray emission were located by using a shielded, slit collimated NaI detector placed outside the cryostat. The front of the detector assembly was positioned 4 cm from the outer cryostat wall and moved perpendicular to the slit orientation along the entire cavity length (Figure 3.3).

The single rail system was mounted on a 22.9 cm  $\times$  128.3 cm  $\times$  1.9 cm aluminum platform. The 1.9 cm diameter shaft, Metric Shaft Support Blocks, and Super Ball Bushing Bearing Pillow Blocks were purchased from Thomson Industries, Inc. (Port Washington, NY). A 0.6 cm thick aluminum plate served as the detector-assembly

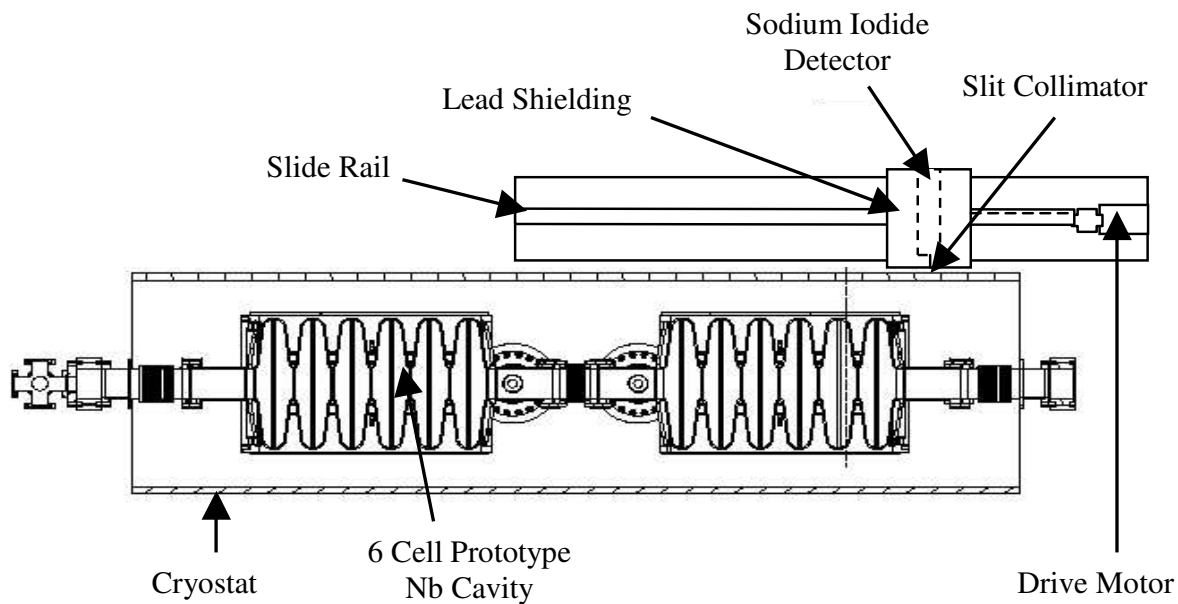


Figure 3.3: Schematic drawing showing an overhead view of the vertically oriented slit collimator moving parallel to the cryostat wall.

table. The plate was mounted to the shaft by four bushing pillow blocks and supported on the platform by three, 2.5 cm diameter roller bearings. The rail allowed 90.2 cm travel of the table (Figure 3.4).

Table motion was accomplished by a 0.6 cm Berg drive chain (W. M. Berg, Inc., East Rockaway, NY) attached to the table and a  $\frac{1}{16}$  HP Dayton gear motor (Dayton Electric Mfg. Co., Chicago, IL). The platform sat atop a Unistrut support system assembled so the collimator slit was aligned with the cavity axis. Figure 3.5 shows a photograph of the entire x-ray scanning device.

Motion control was achieved by a manual start and stop station attached to the gear motor by 8 m of liquidtight flexible metallic conduit. Limit switches were mounted near the rail supports to prevent table overtravel. The wiring diagram is shown in Figure 3.6.

This study required the knowledge of x-ray photon energies and their number. This eliminated the possibility of utilizing a Geiger-Müller counter since their signal

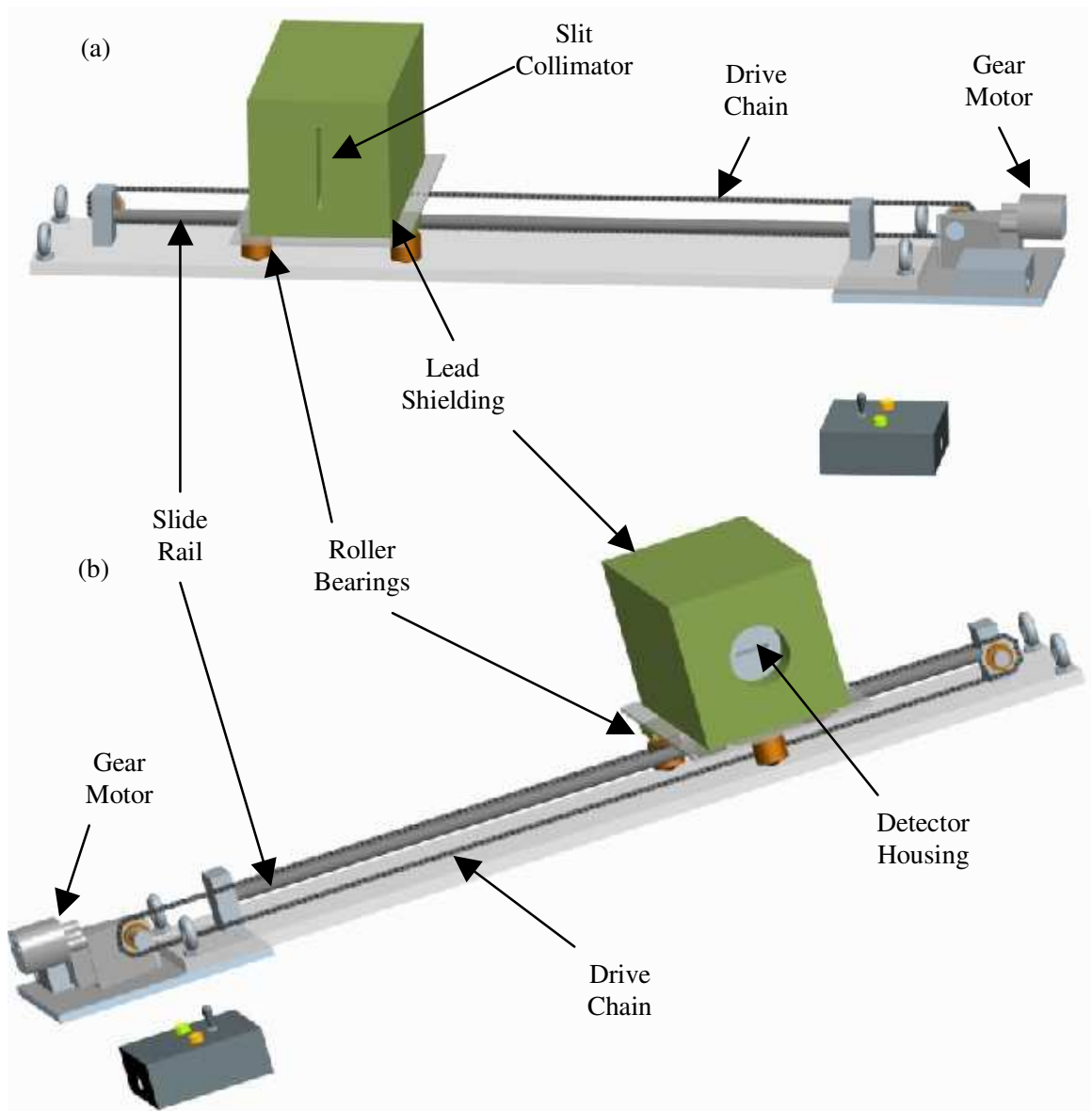


Figure 3.4: a) Front view of the slit collimator slide table. b) Back view of the slit collimator table.

is independent of particle energy. Proportional counters were not a possibility since they detect charged particles. Ionization chambers are used mainly for detection of alphas, protons, fission fragments, and other heavy ions. A scintillation detector, with required hardware, was deemed most appropriate since both x-ray photon energies and their number could be measured [14].

The choice of scintillator was restricted by the goals of the study, specifically scintillator linearity over a wide range of x-ray energy, scintillator efficiency, x-ray count,

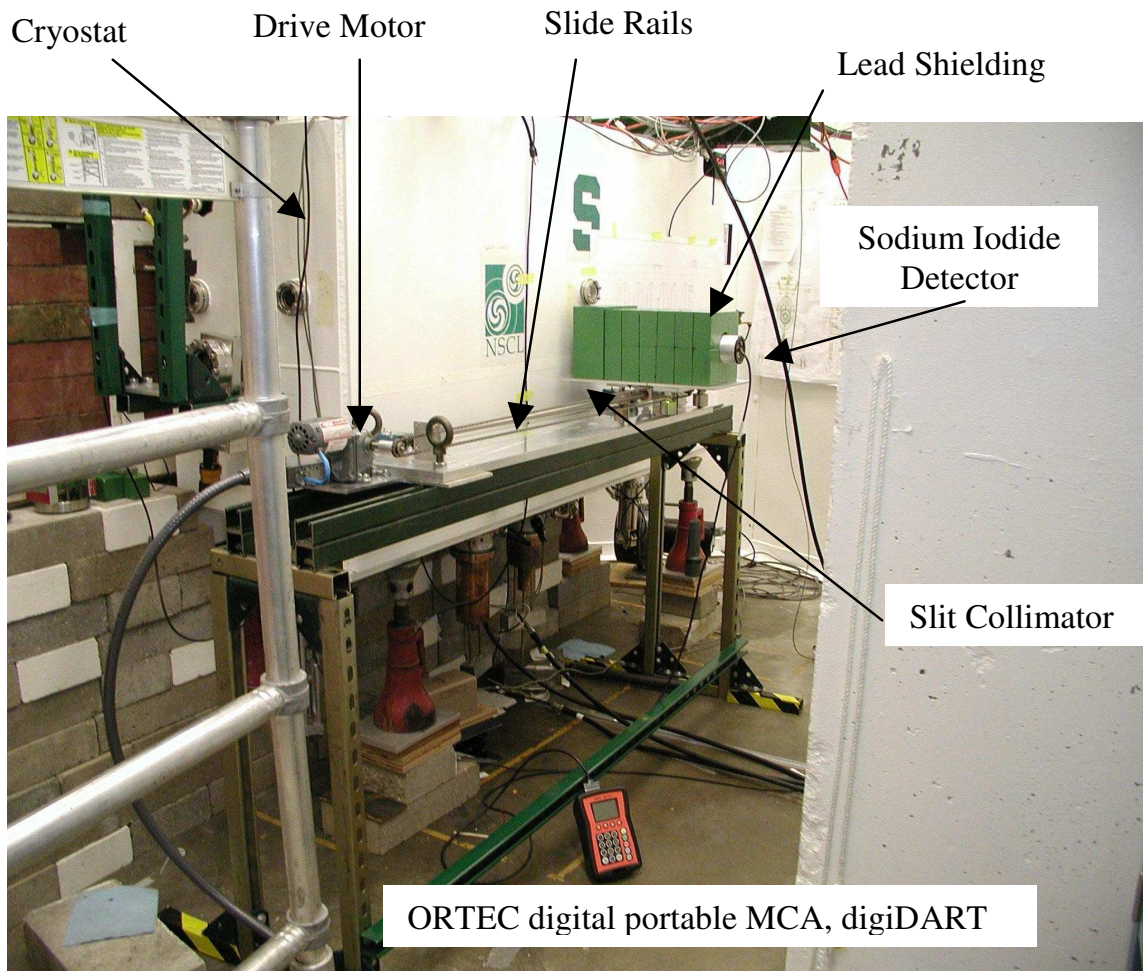


Figure 3.5: Photograph of the x-ray scanning device situated for a cavity scan.

and cost. Scintillator efficiency is the fraction of incident radiation that is converted into visible light [19]. The inorganic scintillator, sodium iodide (NaI), was chosen over plastic organic scintillators since it has better light output and linearity. High energy resolution was not necessary for measurement of a continuous spectrum so Germanium (Ge) was not chosen as the scintillator. Also, NaI does not require the constant cooling by liquid nitrogen that is required of Ge [19]. A complete arrangement consisting of an ORTEC 50 mm  $\times$  50 mm integral NaI crystal, PMT, and digital portable MCA (digiDART) was selected. The detector and portable MCA are indicated in Figure 3.5.

For this study the NaI(Tl) detector was surrounded by lead shielding with an isosceles trapezoid shaped slit open to the detector face (Figure 3.7). The lead shield-

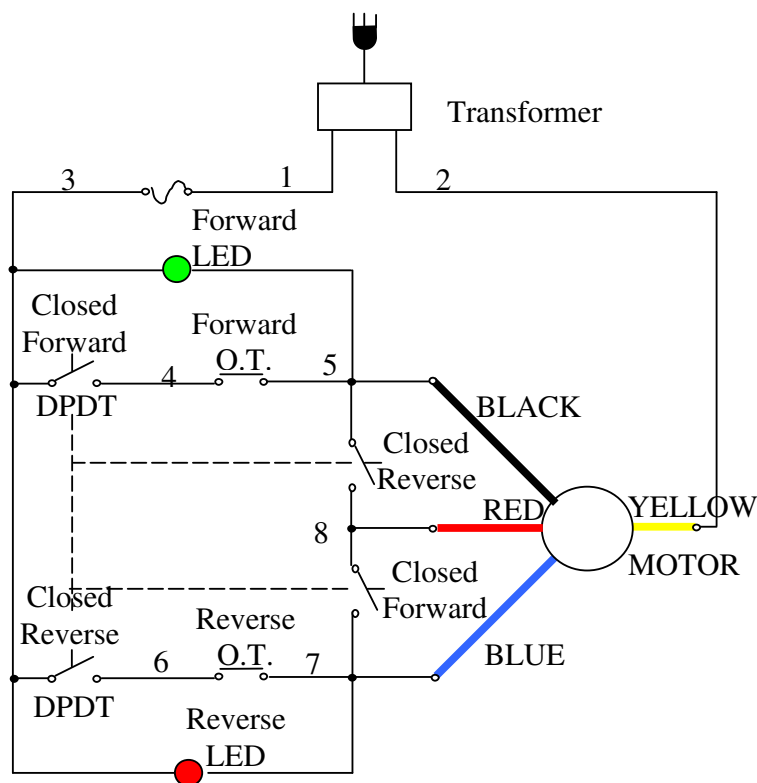


Figure 3.6: Wiring diagram of the manually operated gear motor driving the slide table.

ing was thick enough that photons from a  $20 \mu\text{Cu } ^{60}\text{Co}$  radioactive source had a very low probability of penetration.

Slit collimation of the x-rays was achieved by placing sheet lead pieces, shaped to detect x-rays from full cavity diameter, between two lead blocks. The lead blocks were water-jet cut at Holder Corporation of Lansing, Michigan. The smooth surfaces provided a tight fit, and minimized x-ray entry. Blocks were also cut to house the detector. A schematic diagram of the slit collimator and shielding is shown in Figure 3.7. The slit was oriented vertically and moved on slide rails parallel to the cryostat wall as shown schematically in Figures 3.3 and 3.4. A photograph of the detector assembly is indicated in Figure 3.5.

The portable MCA was interfaced to a local computer with a USB cable. Continuous accumulation of x-rays in two-second time intervals was achieved through a LABVIEW 7.0 program. LABVIEW labeled each two-second time interval file with

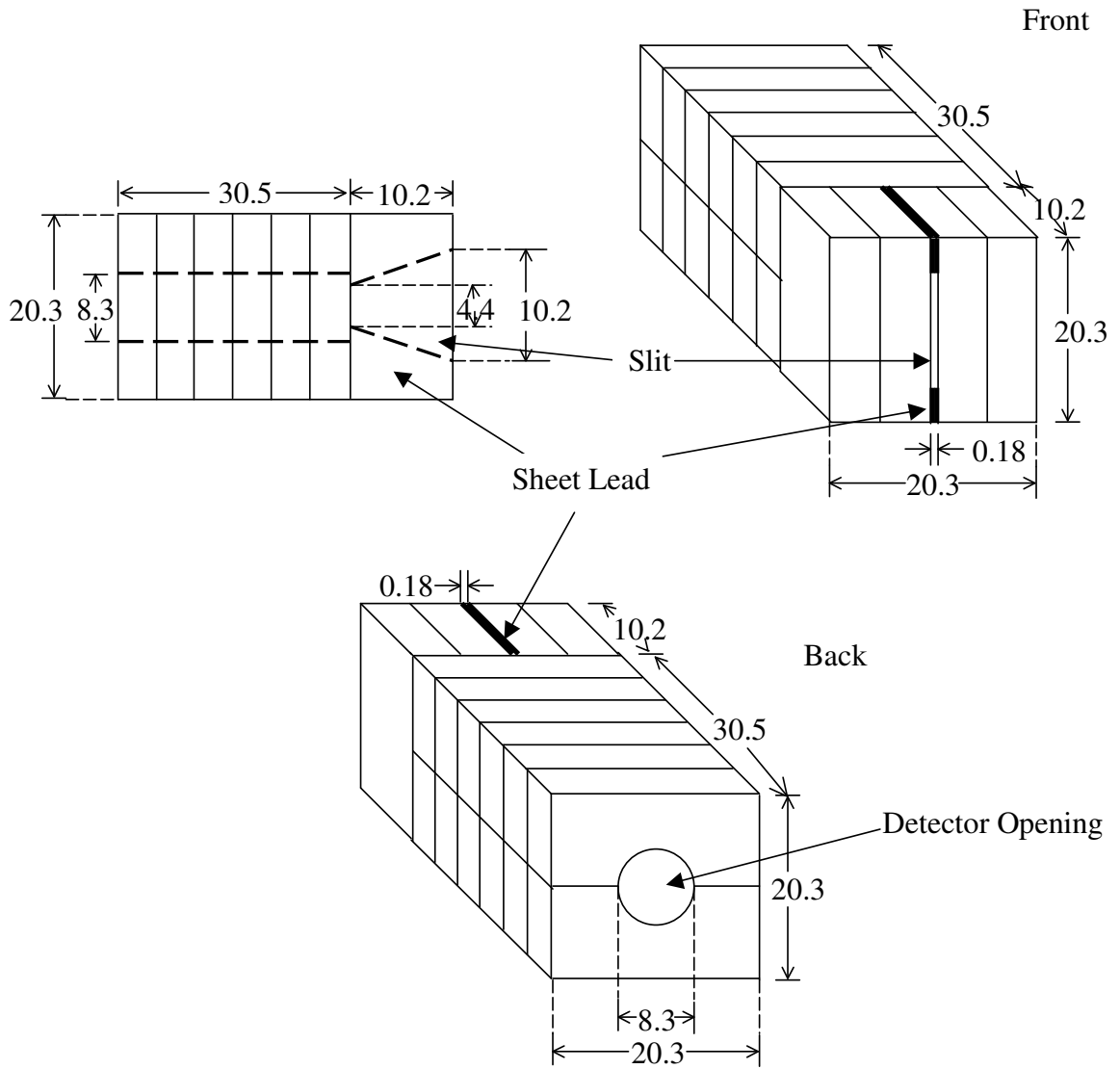


Figure 3.7: Schematic diagram of slit collimation and lead shielding, dimensions in cm.

the date and time and stored the files on the NSCL network.

# Chapter 4

## Experimental Results

The data for this study were collected at the National Superconducting Cyclotron Laboratory (NSCL) situated on the campus of Michigan State University. At the time of this study, the NSCL pursued a full range of Rare Isotope Accelerator (RIA) related research, including the development of superconducting radio frequency (SRF) accelerating structures. Superconducting (niobium) cavities were tested under continuous wave (CW) conditions. To test a cavity, radio frequency (rf) power was supplied to the structure while in vacuum and at superconducting temperature. When the quality factor ( $Q$ ) began to drop and x-rays were measured on the general radiation monitoring equipment, field emission was present. The field emitted electrons, accelerated in the cavity electric field, struck the cavity walls and generated bremsstrahlung x-rays. These were the x-rays of interest in this study.

### 4.1 Detector Calibration

#### 4.1.1 Energy

The energy per channel relationship of the NaI(Tl) detector was calibrated using  $^{137}\text{Cs}$  (662 keV),  $^{60}\text{Co}$  (1173 and 1332 keV), and  $^{22}\text{Na}$  (511 and 1280 keV) radioisotope sources (Figure 4.1 (a)). The peak channel number of the radioisotope was found

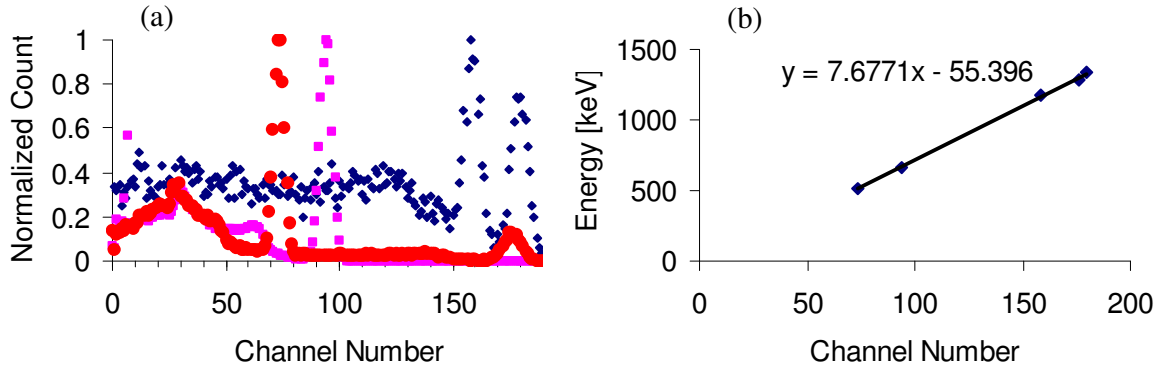


Figure 4.1: Panel (a): Calibration sources: circles are  $^{22}\text{Na}$ , squares are  $^{137}\text{Cs}$ , and diamonds are  $^{60}\text{Co}$ . Panel (b): Plot of channel number *versus* energy of the peaks in panel (a).

by applying a Gaussian fit to the peak with the scientific graphing and analysis software, ORIGIN. Table 4.1 shows the channel number and the associated energy. A linear trendline applied to the data produced the equation  $y = 7.6771x - 55.396$ , which was used to calculate the energy per channel of the detector. Zero energy was found at channel 7.22 (Figure 4.1 (b)).

Table 4.1: Detector Calibration

Channel Number	Energy [keV]
73.4	511
94.2	662
158.5	1173
176.3	1280
179.5	1332

The energy resolution was calculated using Equation 2.62 and determined to be 7.3% for the  $^{137}\text{Cs}$  at channel 94.2 (662 keV), with a *FWHM* of 6.9 channels. Both the peak channel number and the *FWHM* were determined using ORIGIN.

#### 4.1.2 Spatial Resolution

The thickness of the lead shielding ( $t$ ) around the slit measured  $10.2 \pm 0.2$  cm and the slit width ( $x$ )  $0.16 \pm 0.02$  cm (Figure 3.7). The most intense source of x-rays was presumed near an iris, therefore the source-detector distance ( $d$ ) varied from

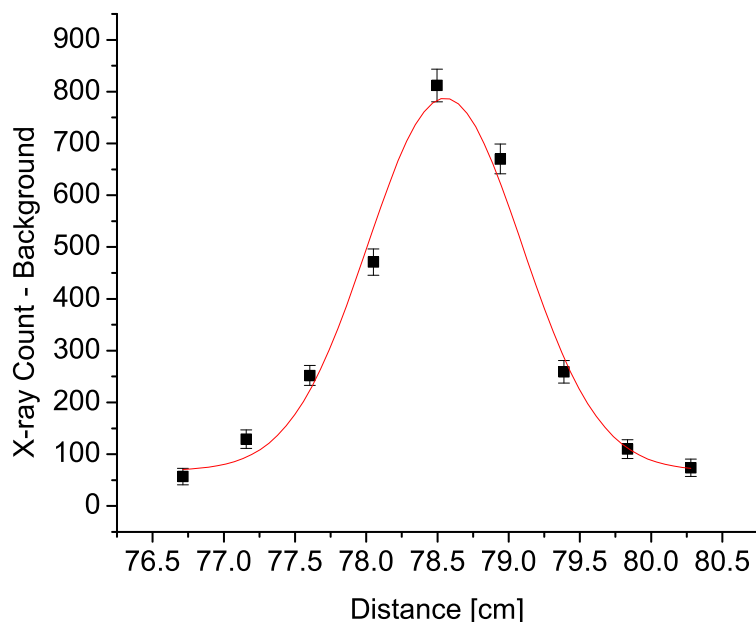


Figure 4.2: High x-ray flux peak centered at 78.6 cm for the scan of cavity #2,  $\pi$  mode.  $FWHM = 1.3 \pm 0.1$  cm. Error bars are included in the figure (Equation 4.2).

$39 \pm 0.5$  cm to  $47 \pm 0.5$  cm. The collimator was also traveling at an average velocity of  $0.22 \pm 0.02 \frac{\text{cm}}{\text{s}}$ . Data were acquired in two-second intervals, making the total calculated spatial resolution (Equation 2.65)  $1.5 \pm 0.2$  cm to  $1.8 \pm 0.2$  cm.

Spatial resolution was measured using the x-ray peak centered around 79 cm of one of the test cavities operated in the  $\pi$  mode (Figure 4.8 (c)). The data were plotted in ORIGIN and, using a Gaussian fit, the centroid was found to be at 78.6 cm and the  $FWHM$  was found to be  $1.3 \pm 0.1$  cm (Figure 4.2). The calculated and measured  $FWHM$  values fell within the estimated error. The difference between the calculated and measured  $FWHM$  is due to the uncertainty in the distance between the x-ray source (electron impact site) and the detector. It has been assumed that electrons impact at the iris. Electrons impacting off iris in the cell, and closer to the detector, would yield a smaller calculated spatial resolution.

### 4.1.3 Spectrum

The cryostat absorber materials encountered by photons as they traveled to the detector are given in Table 4.2. For an initial number of photons,  $I_0$ , with energy 1 MeV:

$$\begin{aligned} I_{Final} &= I_0 e^{-\mu_{Nb}t} e^{-\mu_{He}t} e^{-\mu_{Ti}t} e^{-\mu_{mu}t} e^{-\mu_{Cu}t} e^{-\mu_{steel}t} \\ &= I_0(0.27). \end{aligned}$$

Around one fourth of the 1 MeV photons traverse the cryostat materials without an interaction. The number of interactions increases for lower energy photons and  $I_{Final}$  decreases.

A continuous x-ray energy spectrum of the high x-ray flux peak centered at 78.6 cm (cavity #2,  $\pi$  mode, Figure 4.8 (c)) and scattered through the materials listed in Table 4.2, is shown in Figure 4.3. X-ray energies are plotted along the abscissa and x-ray count with background subtracted along the ordinate. The background count of x-rays ( $y$ ) was subtracted from the data ( $x$ ):

$$u = x - y. \tag{4.1}$$

Table 4.2: Absorber materials.

Material	t [cm]	$\rho \left[ \frac{\text{g}}{\text{cm}^3} \right]$	$\mu_{ma} \left[ \frac{\text{cm}^2}{\text{g}} \right]$	$\mu_{lin} \left[ \frac{1}{\text{cm}} \right]$
Nb	0.4	8.57	0.0587	0.503
He(liquid 2.2 K)	2.54	0.147	0.0636(gas)	0.009
Ti	0.48	4.54	0.0589	0.267
mu(80% Ni, 20% Fe)	0.10	8.70	0.0613	0.533
Ni	-	8.90	0.0616	0.548
Fe	-	7.87	0.0600	0.472
Cu	0.16	8.96	0.0590	0.529
Steel (75% Fe, 17% Cr, 8% Ni)	1.91	7.84	0.0600	0.470
Cr	-	7.18	0.0593	0.426

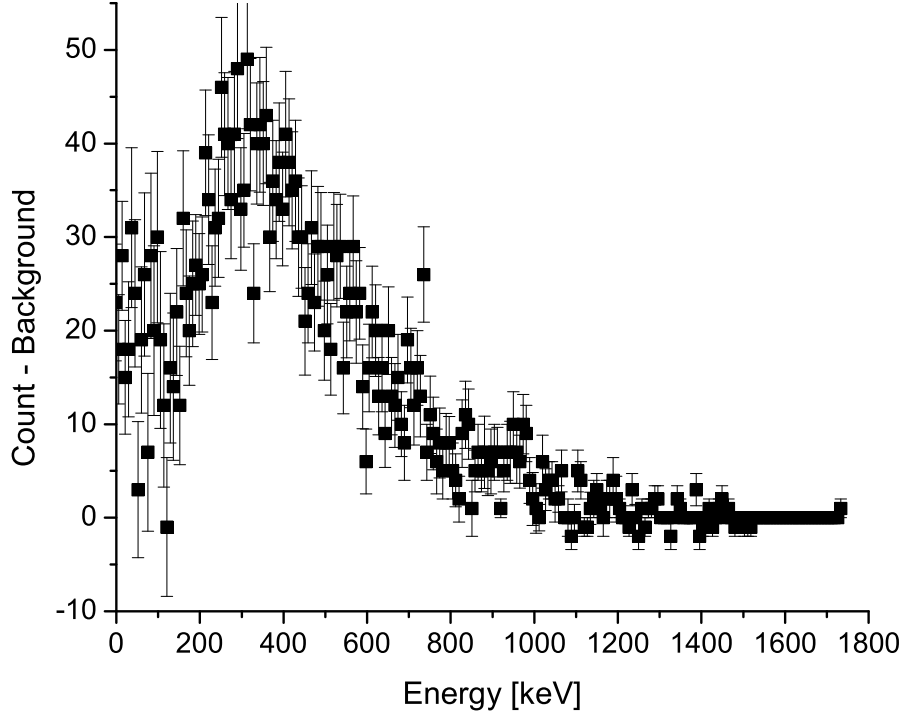


Figure 4.3: Continuous x-ray energy spectrum of the high x-ray flux peak centered at 78.6 cm in cavity #2,  $\pi$  mode. Lead shielding in front of the slit collimator attenuates 40% of the 400 keV x-rays. Error bars are included in the figure (Equation 4.2).

Uncertainty was calculated from the error propagation formula [19]:

$$\sigma_u^2 = \left(\frac{\partial u}{\partial x}\right)^2 \sigma_x^2 + \left(\frac{\partial u}{\partial y}\right)^2 \sigma_y^2 + \left(\frac{\partial u}{\partial z}\right)^2 \sigma_z^2 + \dots, \quad (4.2)$$

where  $u = u(x, y, z, \dots)$ , and  $\sigma_x, \sigma_y, \sigma_z, \dots$  are the errors of the variables  $x, y, z, \dots$ . A lead shield 0.34 cm thick placed in front of the collimator attenuates 40% of the 400 keV x-rays. Figure 4.3 shows a continuous x-ray spectrum for one high x-ray flux peak.

The low energy of the characteristic x-rays (Sections 2.1.3 and 2.1.4) of Nb could not be distinguished from the continuous x-ray spectrum. There is also a high probability of them having an interaction in the cryostat materials. The energy of characteristic x-rays of Nb are shown in Table 4.3.

Table 4.3: Characteristic x-ray energies of Nb. \* denotes a level which is unresolved from the level above it [26].

Level	Energy (eV)
<i>K</i>	18985.6
<i>L<sub>I</sub></i>	2697.7
<i>L<sub>II</sub></i>	2464.7
<i>L<sub>III</sub></i>	2370.5
<i>M<sub>I</sub></i>	468.4
<i>M<sub>II</sub></i>	378.4
<i>M<sub>III</sub></i>	363.0
<i>M<sub>IV</sub></i>	207.4
<i>M<sub>V</sub></i>	204.3
<i>N<sub>I</sub></i>	58.1
<i>N<sub>II</sub></i>	33.9
<i>N<sub>III</sub></i>	33.9*
<i>N<sub>IV,V</sub></i>	3.2

#### 4.1.4 Detector and Collimator Performance

The performance of the detector and collimator was initially tested by scanning a  $^{60}\text{Co}$  radioisotope source mounted on a 2.54 cm diameter disk. A diagram of the arrangement, not to scale, is shown in Figure 4.4 (a). As the slit collimated NaI detector moved past the radioisotope source, x-ray spectra (energy *versus* number of x-rays at that energy) were collected in two-second intervals. Figure 4.4 (b) shows the total number of x-rays entering the detector in each two-second interval. The detector-collimator assembly moved 0.32 cm per two-second interval ( $0.16 \frac{\text{cm}}{\text{s}}$ ). Error bars are included in the figure (Equation 4.2). ORIGIN was used to measure the *FWHM* weighted by the error. The *FWHM* was measured as 2.75 cm, a difference of 8% from the calculated value.

A diagram of the slit collimated detector scanning the cryostat, not to scale, is shown in Figure 4.5 (a) and (b). This simplified diagram shows two electrons leaving one defect and impacting at two different sites. In reality, large numbers of electrons are field emitted from defects, have complicated trajectories, and may impact anywhere within the cavity or connecting structure.

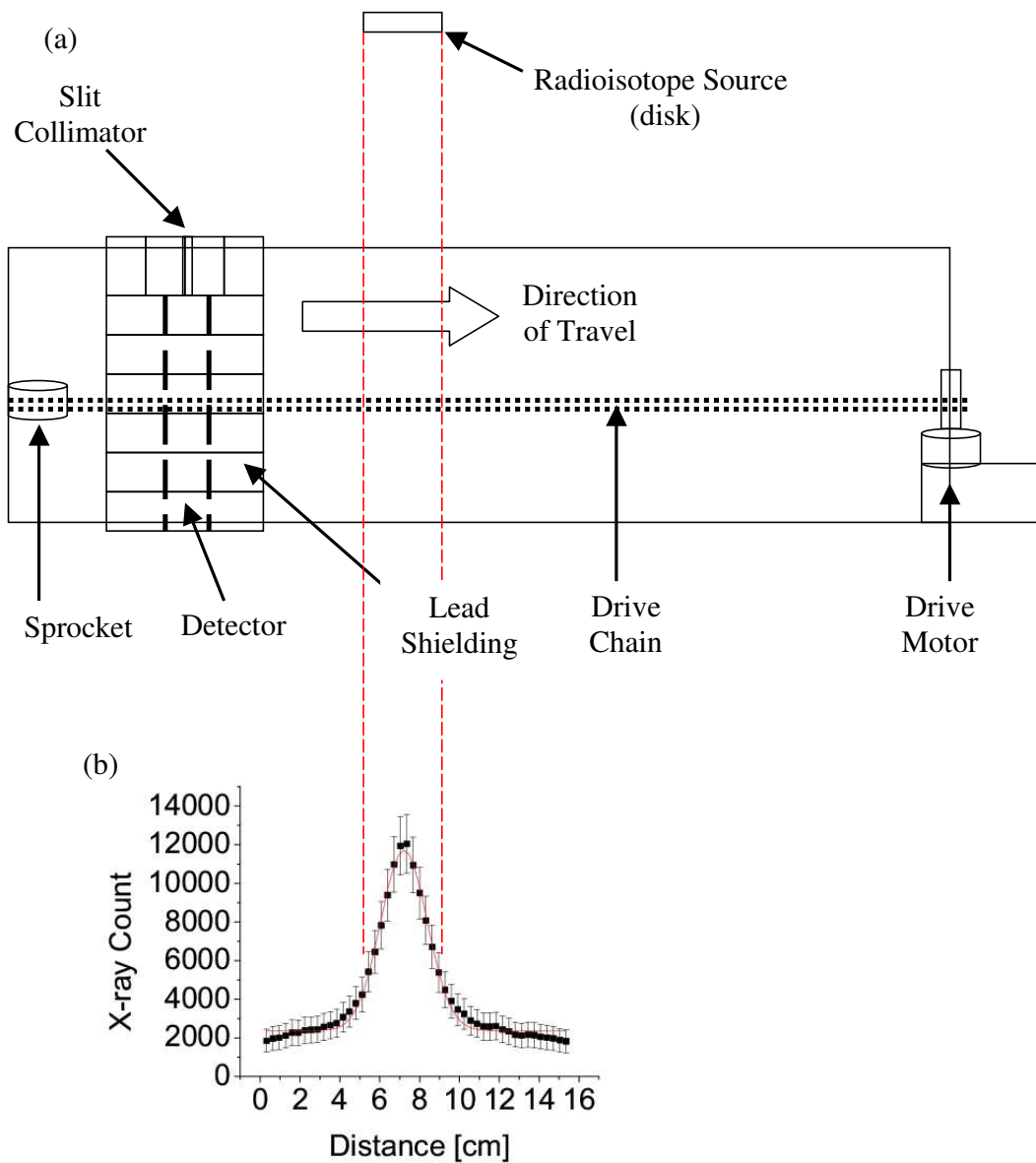


Figure 4.4: Panel (a): Diagram (not to scale) of a slit collimated detector scanning a radioisotope source. The disk is 2.54 cm in diameter. Panel (b): Total number of x-rays entering the detector per two-second interval. The detector-collimator assembly moved 0.32 cm per two-second interval. The  $FWHM$  was measured as 2.75 cm. Error bars are included in panel (b) (Equation 4.2).

The predicted performance of the slit collimated detector scanning the cryostat is shown in Figure 4.5 (c). A silhouette of the cavity has been superimposed on the mock data. When the slit is not opposite an x-ray source, x-rays that are primarily Compton scattered in the cryostat materials can travel through the slit and enter the detector. X-rays can also travel through the lead shielding and be Compton scattered or experience no interaction. To compensate for the x-rays entering the detector from the lead shielding, data acquired during a scan of the cryostat with the slit closed (hereafter referred to as background) is subtracted from the scan with the slit open.

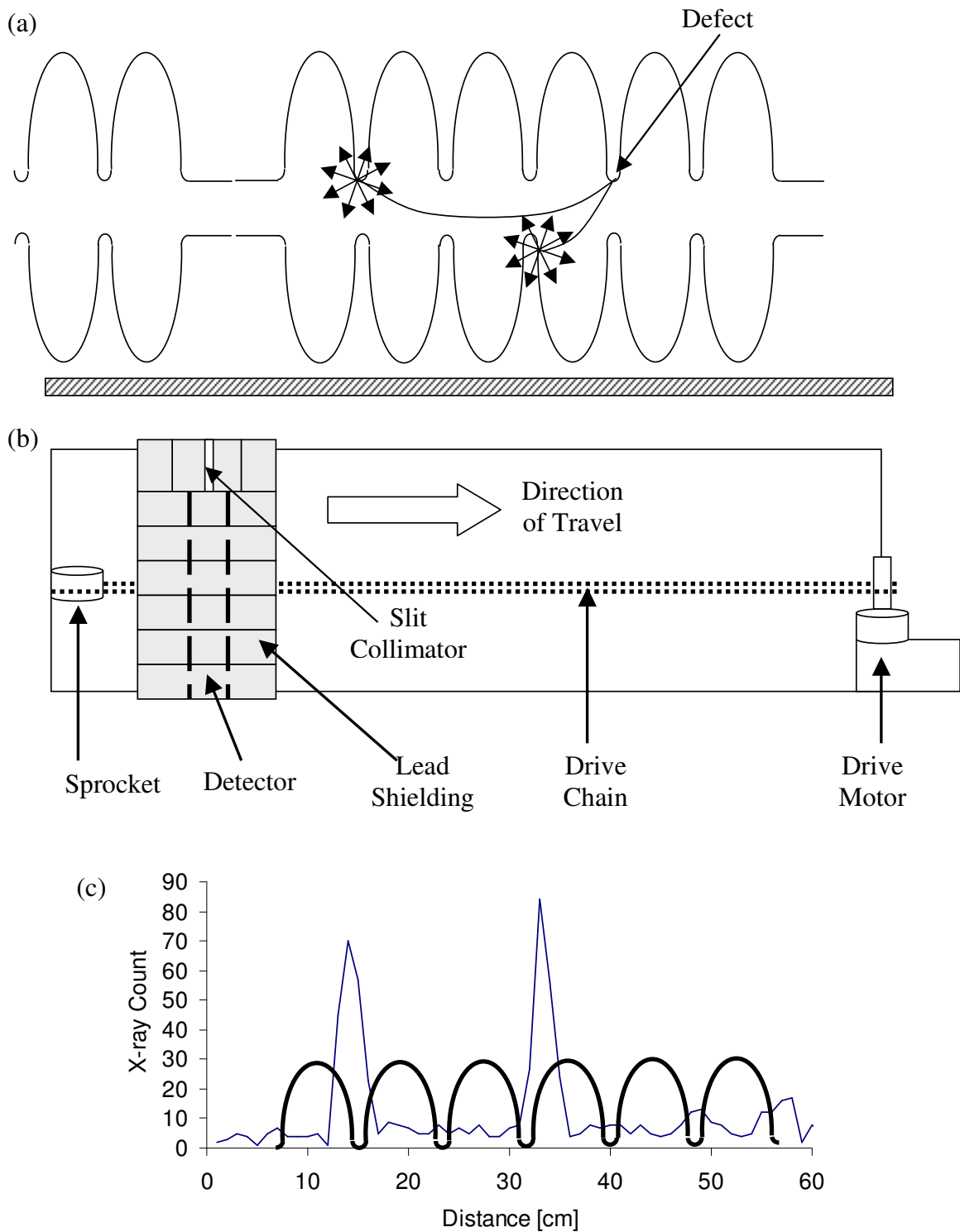


Figure 4.5: Panels (a) and (b): Diagram (not to scale) of a slit collimated detector scanning half of a cryostat containing two six-cell cavities. Panel (c): Predicted spectrum of the total number of x-rays entering the detector per two second interval. A silhouette of the cavity has been superimposed on the mock data.

## 4.2 Cavity Testing

### 4.2.1 Cavity #2 Performance

The detector assembly and unistrut stand were positioned so that the front of the collimator was 4 cm from the cryostat wall opposite cavity #2. Both cavities were cooled to 1.99 K. Forward power to cavity #2 ( $\pi$  mode) was raised until x-ray detection on the area radiation monitoring equipment measured an x-ray exposure rate of  $25 \frac{\text{mR}}{\text{hr}}$ , signifying the drop in  $Q$  to be due to field emission. Forward power was held nearly constant to maintain that level of x-ray exposure rate.

During the test, the forward, reflected, transmitted, and standing wave transmitted power, bath pressure, frequency, liquid helium level, and cavity temperature were recorded. From this data ( $\pi$  mode), the cavity  $Q$  was measured (Equation 2.78)) as  $1.25 \times 10^{10}$  while  $E_a$  was held nearly constant at  $7.6 \frac{\text{MV}}{\text{m}}$  (Equation 2.76), or  $E_p = 25.5 \frac{\text{MV}}{\text{m}}$  (Equation 2.77). The  $Q$  for cavity #2, for this study ( $\pi$  mode), was similar to the  $Q$  obtained from the previous cavity test ( $\pi$  mode) (Figure 4.6 (a)). The x-ray exposure rate for this study ( $\pi$  mode) and the previous cavity test ( $\pi$  mode) are also shown to be similar (Figure 4.6 (b)). The x-ray exposure rate was difficult to measure since the needle on the meter was in constant motion. (The x-ray exposure rate appears to level off at 10,000  $\frac{\text{mR}}{\text{h}}$ , which is the scale maximum of the meter.) The two plots demonstrate that no major changes in cavity performance occurred between tests.

For this study the electric field was held nearly constant, thus a direct calculation of the Fowler-Nordheim field enhancement factor ( $\beta_{FN}$ ), needed for the particle tracking code, could not be made.  $\beta_{FN}$  was inferred from  $\pi$  mode data acquired during two previous tests and compared with data ( $\pi$  mode) for this study (Figure 4.7)(Equation 2.35).  $\beta_{FN}$  for cavity #2 operated in the  $\pi$  mode was in the range  $120 \leq \beta_{FN} \leq 220$ . This range was also used for the  $\frac{5\pi}{6}$  and  $\frac{4\pi}{6}$  modes.

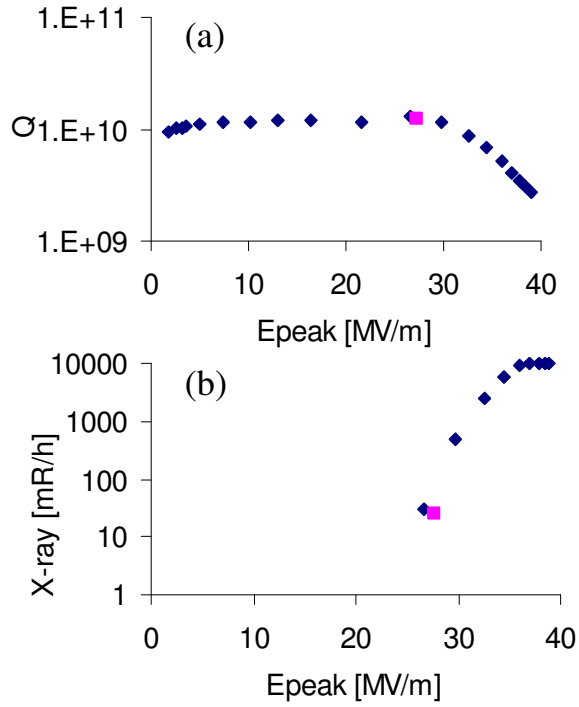


Figure 4.6: Cavity #2 performance,  $\pi$  mode. In both panels, diamonds indicate the previous cavity test. The square indicates the measured quantity for this study. Panel (a): Peak electric field *versus*  $Q$ . Panel (b): X-ray exposure rate detected on the area radiation monitoring equipment when the observed drop in  $Q$  was due to field emission. The area radiation monitoring equipment has a maximum scale of 10,000  $\frac{\text{mR}}{\text{h}}$ . The two plots demonstrate that no major changes in cavity performance occurred between tests.

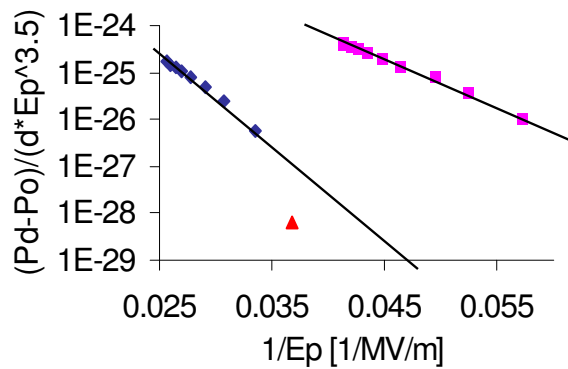


Figure 4.7: Cavity #2,  $\pi$  mode, Fowler-Nordheim Field Enhancement Factor. Diamonds and squares represent data from two previous cavity tests; the triangle represents data from this study ( $\pi$  mode).  $120 \leq \beta_{FN} \leq 220$ .

### 4.2.2 Cavity #2 $\pi$ Mode

Two scans of the cryostat were made with the collimator open to show that the data were reproducible (Figure 4.8 (a)). One scan was made with the collimator closed (background) (Figure 4.8 (b)). The background was subtracted from the data acquired with the collimator open (Figure 4.8 (c)). High x-ray flux peaks appear at three irises (28, 37, and 46 cm). Peaks also appear in each beam tube, indicating electrons traveled out of the cavity and impacted in the beam tube.

The highest probability for x-rays to enter the detector without having had an interaction, is when the open slit is opposite the x-ray source (electron impact site). To determine if the highest flux peaks in the data are real x-ray sources, and not just x-rays scattered into the detector, energy binning was employed. Energy binning is the method of examining the number of x-rays in a particular energy range. Real x-ray sources contain the highest number of high energy x-rays.

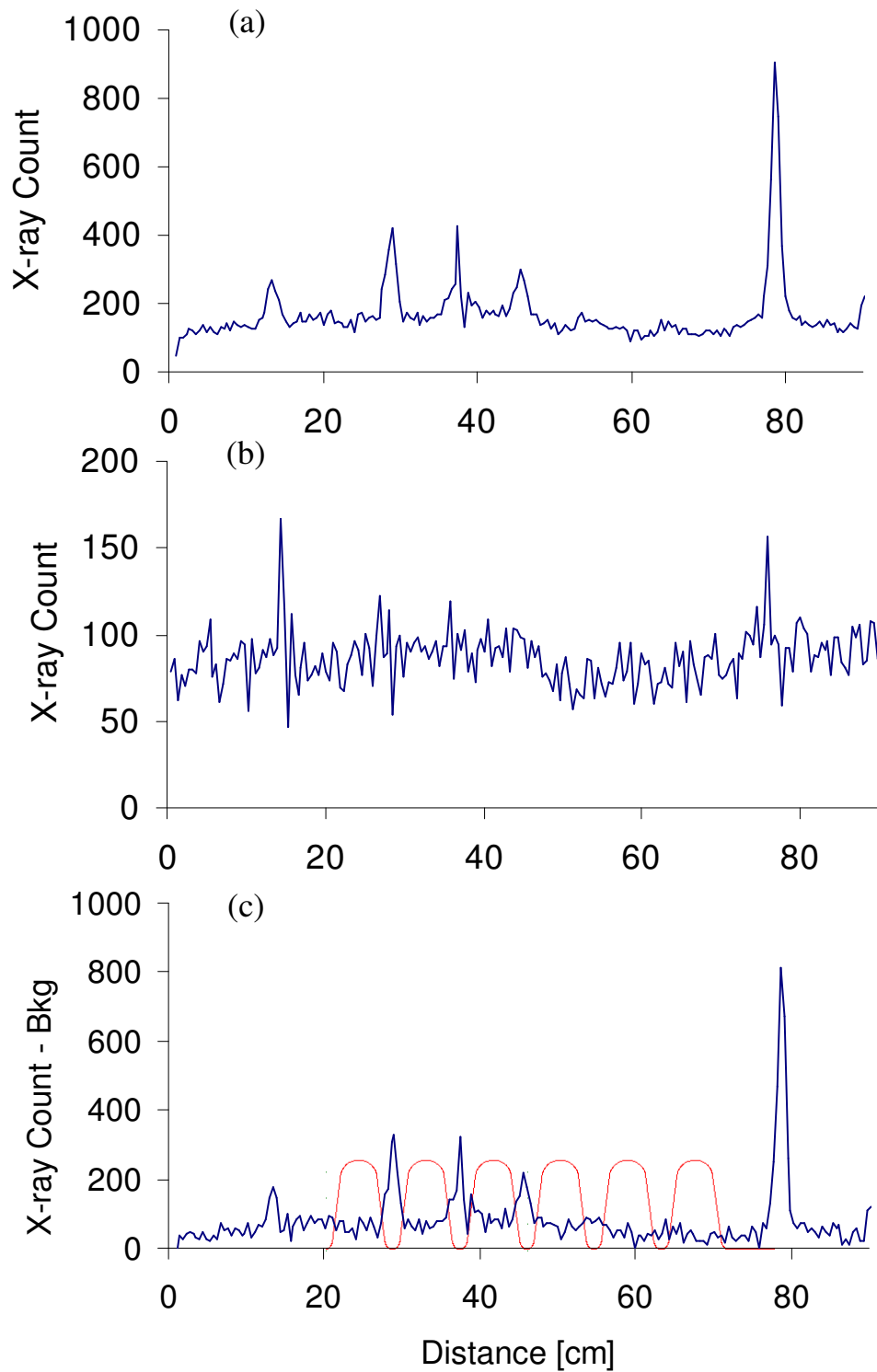


Figure 4.8: Cavity #2 operated in the  $\pi$  mode. X-ray count acquired in two-second intervals. Panel (a): Slit of the collimator open. Panel (b): Slit of the collimator closed (background). Panel (c): X-ray count with the background subtracted. A silhouette of the cavity has been superimposed on the data.

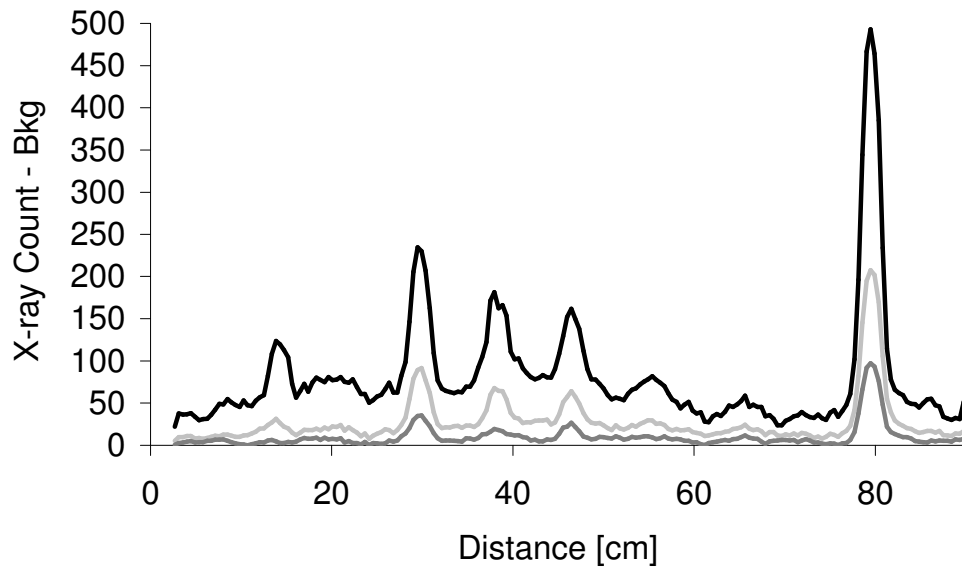


Figure 4.9: Cavity #2,  $\pi$  mode, energy binning of data presented in Figure 4.8 (c). The black line represents the number of x-rays at all energies, the light-gray line represents the number of x-rays with a minimum energy of 400 keV, and the medium-gray line represents the number of x-rays with a minimum energy of 600 keV. A moving average was applied to the data to smooth inconsistencies between adjacent two-second intervals.

Figure 4.9 shows the energy binning for the data presented in Figure 4.8 (c). As higher energies are binned, the x-ray flux decreases. The x-ray flux peak around 18 cm has disappeared at 600 keV, indicating an endpoint energy between 400 and 600 keV. X-ray flux peaks at 28, 37, 46, and 79 cm all have endpoint energies over 600 keV. Endpoint energy will be considered when compared with the results of the particle tracking code (Chapter 6). To better pinpoint endpoint energy, minimum energies of 1000 keV, 1100 keV, and 1200 keV are plotted in Figure 4.10. It appears that the endpoint energy for this peak is around 1100 keV since the peak is indistinguishable at 1200 keV.

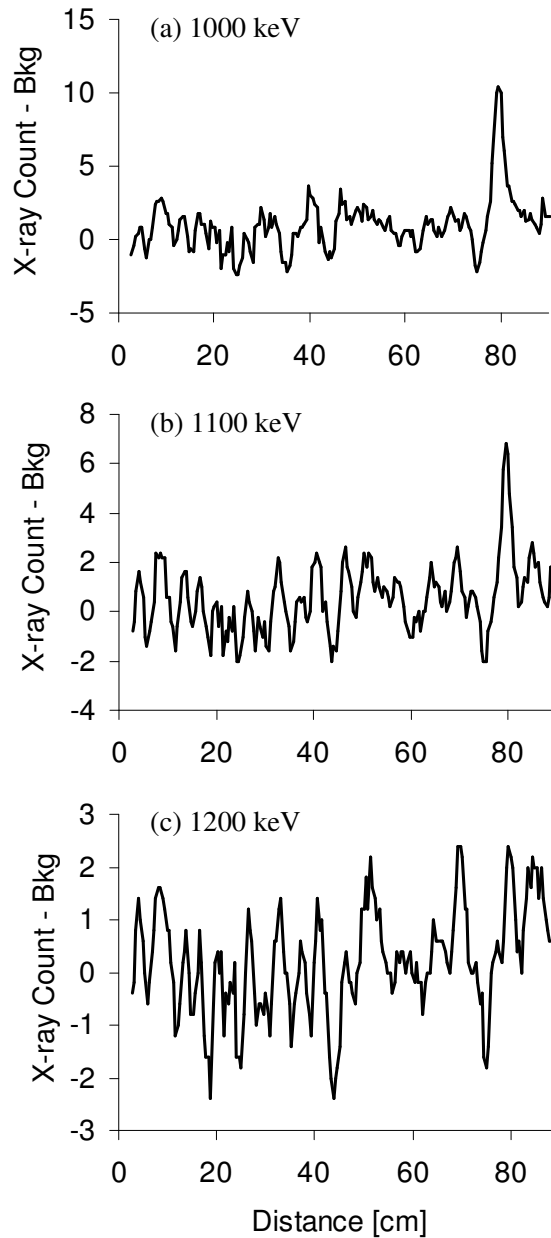


Figure 4.10: Energy binning. Panel (a): 1000 keV minimum x-ray energy. Panel (b): 1100 keV minimum x-ray energy. Panel (c): 1200 keV minimum x-ray energy. The moving average of the data is shown. The endpoint energy for the peak at 78 cm is around 1100 keV since the peak is indistinguishable at 1200 keV.

An alternative evaluation of endpoint energy was achieved by a linear projection of the high energy range of the x-ray spectrum. Each high x-ray flux peak in Figure 4.8 (c) is a collection of two-second energy spectra. The sum of individual energy spectra was taken for each high x-ray flux peak. The energy spectrum for the high flux peak at 78.6 cm is shown in Figure 4.11 (a). The endpoint energy projection, for the same peak, is shown in Figure 4.11 (b). The endpoint energy obtained using this method is 1062 keV. For consistency, the energy range considered for the linear fit was chosen at an energy greater than the peak of the spectrum to a value where the “X-ray Count - Background” becomes negative (Figure 4.11 (a)). This method is in good agreement with the energy binning method where the endpoint energy was found to be near 1100 keV. The endpoint energy of each peak and peak location (centroid) in cavity #2,  $\pi$  mode, can be found in Appendix F.1.

To check the linear projection method, the detector was positioned at the location of the highest x-ray flux peak in the  $\pi$  mode (79 cm). Data were acquired for 30 second intervals with the detector assembly stationary. The energy spectrum and endpoint energy projection are shown in Figure 4.12 (a) and (b). The endpoint energy for the 30 second time interval was found to be 1084 keV. The good agreement between the three methods demonstrates that linear projection is an acceptable method in determining x-ray endpoint energy.

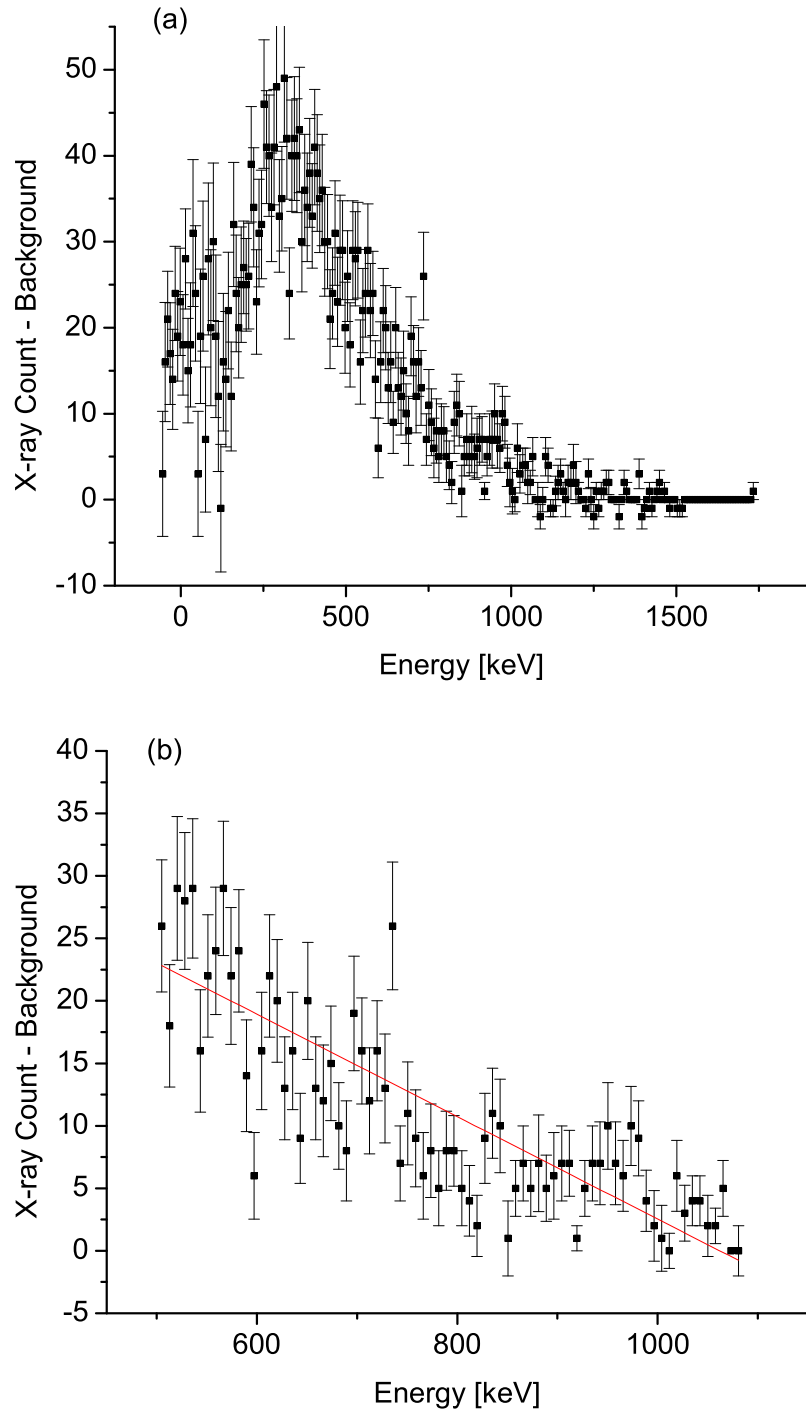


Figure 4.11: Cavity #2,  $\pi$  mode. Panel (a): X-ray energy spectrum for high x-ray flux peak at 78.6 cm. Data were acquired during a scan of the cavity. Individual two-second spectra within the peak were summed. Panel (b): Endpoint energy determined by the linear projection method was found to be 1062 keV. Error bars are included in the figures (Equation 4.2).

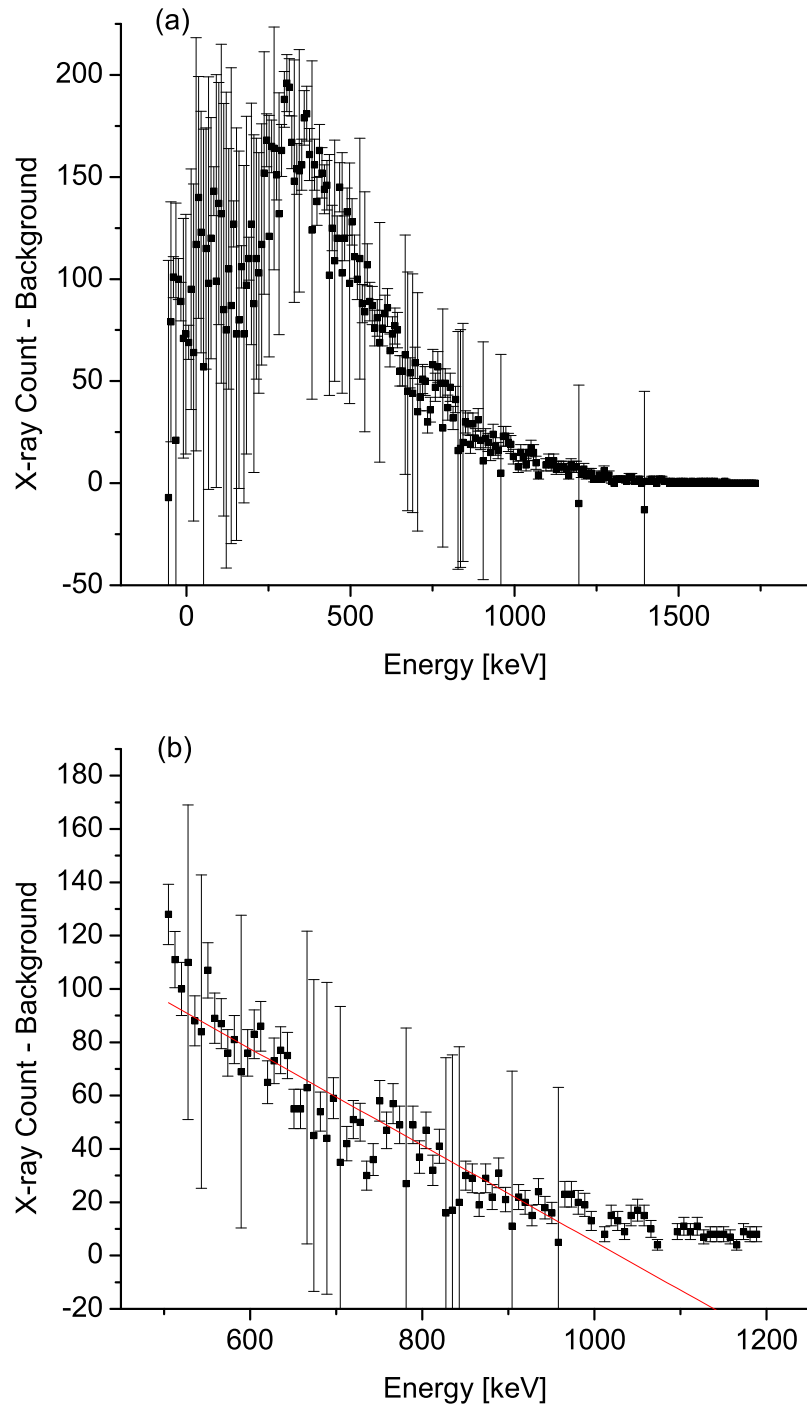


Figure 4.12: Cavity #2,  $\pi$  mode. Panel (a): X-ray energy spectrum for high x-ray flux peak at 78.6 cm. Data were acquired with the detector stationary at 78.6 cm. Panel (b): Endpoint energy determined by the linear projection method was found to be 1084 keV. Error bars are included in the figures (Equation 4.2). Some error bars are larger due to the increased background count.

The linear projection method accounts for pile-up or summation effects in the detector. Electrons, from a single emitter, are field emitted at differing times during half of an rf period. The electrons are accelerated by the electric fields and guided by the magnetic fields within the cavity. Electron trajectories are complex and, as a result, impact at different sites at different times and with different final kinetic energies. The electrons travel through the material they impact and generate x-rays. The x-rays travel through the cryostat materials having interactions described in Subsection 2.1.4. This leads to the arrival of x-rays at the detector that are randomly spaced in time. X-rays arriving at the detector sufficiently close together in time are treated as a single event by the analysis system, called peak pile-up or summation effects. Not only are counts recorded at higher energies, but removed from lower energies. The method of linear projection to estimate the x-ray endpoint energy ignores the highest energy events due to pile-up. The endpoint energy and location for each high flux peak for both scans of cavity #2 operated in the  $\pi$  mode can be found in Appendix F.1.

### 4.2.3 Cavity #2 $\frac{5\pi}{6}$ Mode

After data collection for the  $\pi$  mode was completed, the frequency was adjusted for the  $\frac{5\pi}{6}$  mode. Again, forward power was raised until an x-ray exposure rate of  $25 \frac{\text{mR}}{\text{hr}}$  was measured.  $E_p$  was held nearly constant at  $32.0 \frac{\text{MV}}{\text{m}}$ . Two scans of the cryostat were made with the collimator open to show that the data were reproducible. One scan was made with the collimator closed (background).

Figure 4.13 shows the x-ray count acquired in two-second intervals with the slit of the collimator, panel (a) open, panel (b) closed (background), and panel (c) x-ray count with the background subtracted. Similar to the  $\pi$  mode spectrum, the highest x-ray flux regions appear in the beam tube, at four irises, and possibly at 46 and 54 cm. The x-ray flux between peaks at 12 and 23 cm, 23 and 29 cm, and 29 and 37 cm may be regions of high Compton scattered x-rays entering the detector.

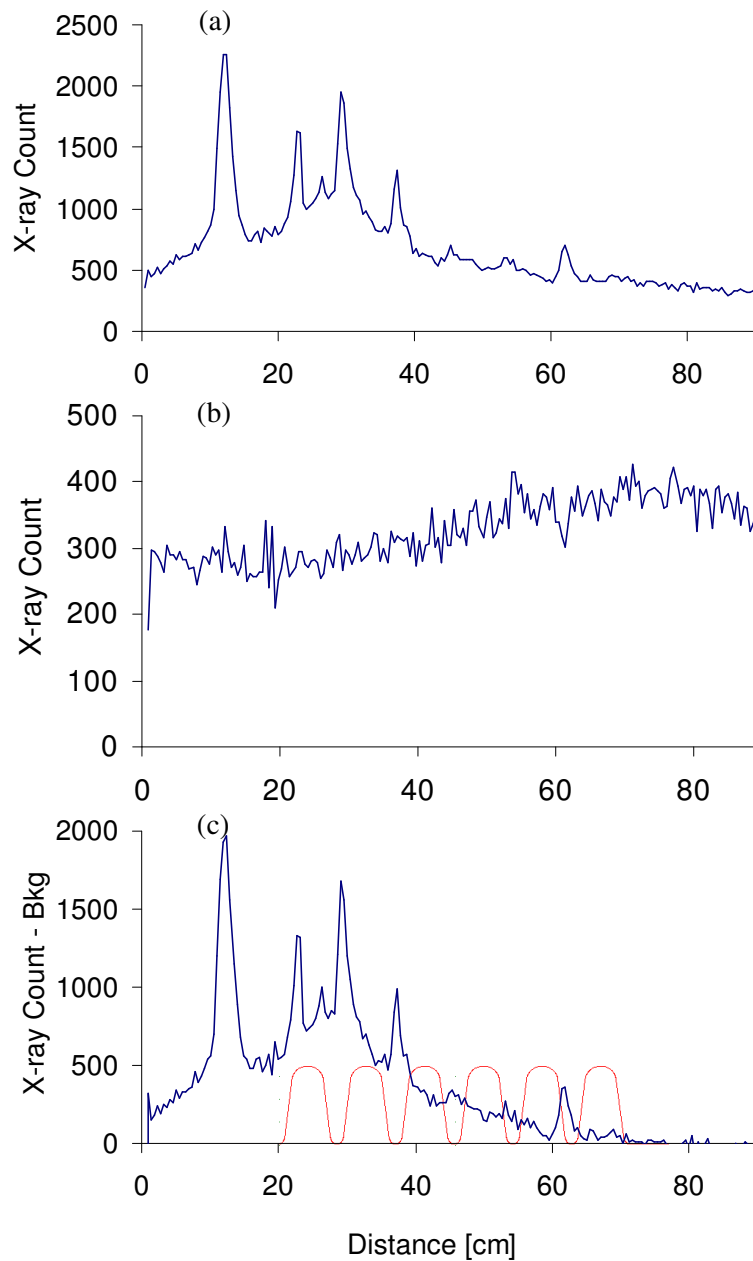


Figure 4.13: Cavity #2 operated in the  $\frac{5\pi}{6}$  mode. X-ray count acquired in two-second intervals. Panel (a): Slit of the collimator open. Panel (b): Slit of the collimator closed (background). Panel (c): X-ray count with the background subtracted. A silhouette of the cavity has been superimposed on the data.

Energy binning was performed for the  $\frac{5\pi}{6}$  mode (Figure 4.14). The highest x-ray flux peak at 12 cm becomes the lowest when x-rays are observed at a minimum energy of 600 keV. This could be due to the low final kinetic energy of the electrons, or a region of many x-rays being Compton scattered into the detector, or both. The highest energy peak is around 30 cm. The possible peaks at 46 and 54 cm appear to have x-ray endpoint energies between 400 and 600 keV. The endpoint energy and location for each high flux peak, both scans of cavity #2 operated in the  $\frac{5\pi}{6}$  mode, can be found in Appendix F.2.

A comparison of the x-ray spectra obtained for both the  $\pi$  and  $\frac{5\pi}{6}$  modes clearly identifies differing electron impact sites and thus differing electron trajectories (Figure 4.15). The higher x-ray flux of the  $\frac{5\pi}{6}$  mode spectrum is addressed in Chapter 5. Both modes indicate electrons leaving the cavity and impacting in a beam tube. Both modes also indicate electron impacts near irises.

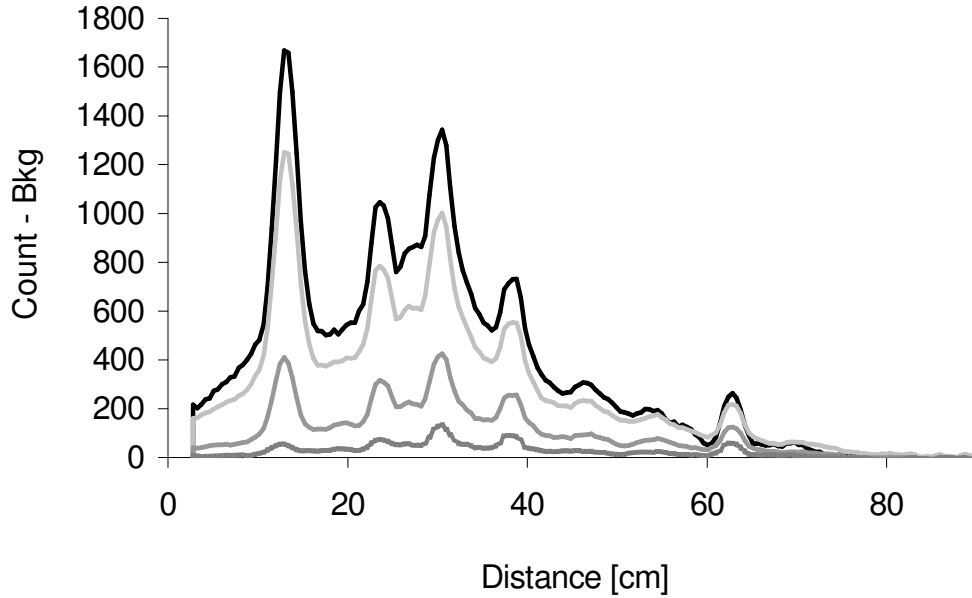


Figure 4.14: Cavity #2,  $\frac{5\pi}{6}$  mode, energy binning of data presented in Figure 4.13 (c). The black line represents the number of x-rays at all energies, the light-gray line represents the number of x-rays with a minimum energy of 200 keV, the medium-gray line represents the number of x-rays with a minimum energy of 400 keV, and the darkest gray plot represents x-rays with a minimum energy of 600 keV. A moving average was applied to the data to smooth inconsistencies in adjacent two-second intervals.

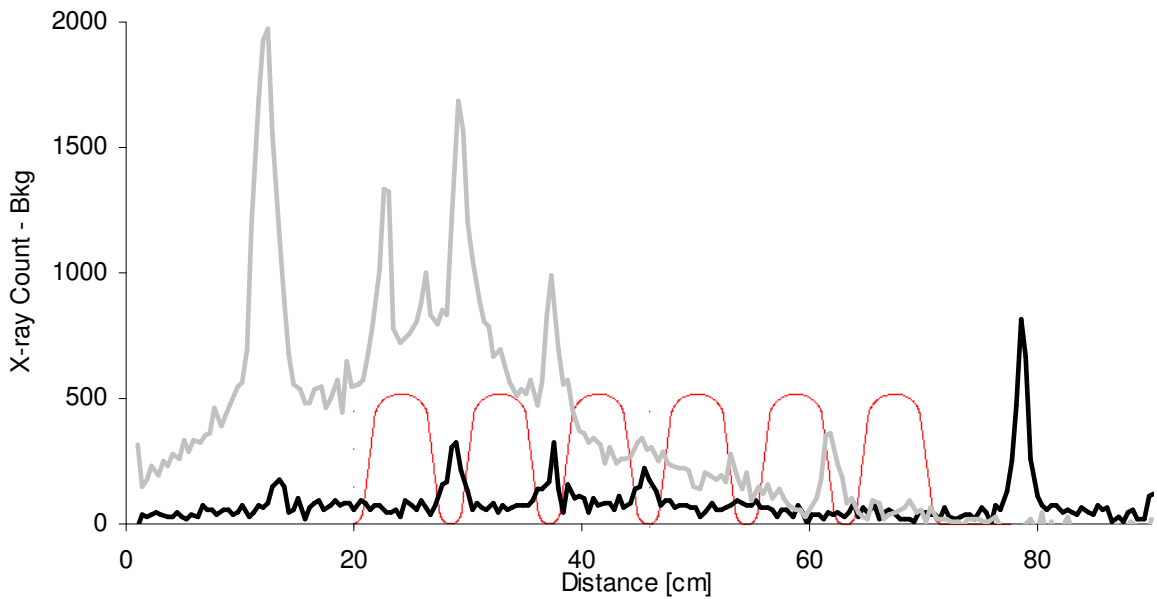


Figure 4.15: Cavity #2 spectra comparison of  $\pi$  (black line) and  $\frac{5\pi}{6}$  (gray line) modes. A silhouette of the cavity has been superimposed on the data.

#### 4.2.4 Cavity #2 $\frac{4\pi}{6}$ Mode

Data were also collected for the  $\frac{4\pi}{6}$  mode. Again, forward power was raised until an x-ray exposure rate of  $25 \frac{\text{mR}}{\text{hr}}$  was measured.  $E_p$  was held nearly constant at  $31.6 \frac{\text{MV}}{\text{m}}$ . Two scans of the cryostat were made with the collimator open to show that the data were reproducible. One scan was made with the collimator closed (background) (Figure 4.16). Both scans, collimator open and closed, show an increase in x-ray flux from the beginning to the end of the scan. Once the background is subtracted, high x-ray flux regions appear at 21, 28, 37, 45, and 66 to 76 cm.

High x-ray flux regions were difficult to identify so energy binning was also performed (Figure 4.17). Energy binning shows the same peaks identified at 21, 28, 37, 45, and 66 to 76 cm. The x-ray count with background subtracted (Figure 4.17 (c)) is negative around the 50-65 cm range. High x-ray flux peaks cannot be determined in this range. The endpoint energy and location for each high flux peak, both scans of cavity #2 operated in the  $\frac{4\pi}{6}$  mode, can be found in Appendix F.3.

A comparison of the x-ray spectra obtained for all three modes is shown in Figure 4.18. All three modes appear to have electrons impacting primarily on irises. The x-ray flux varies greatly between modes and is addressed in Chapter 5.

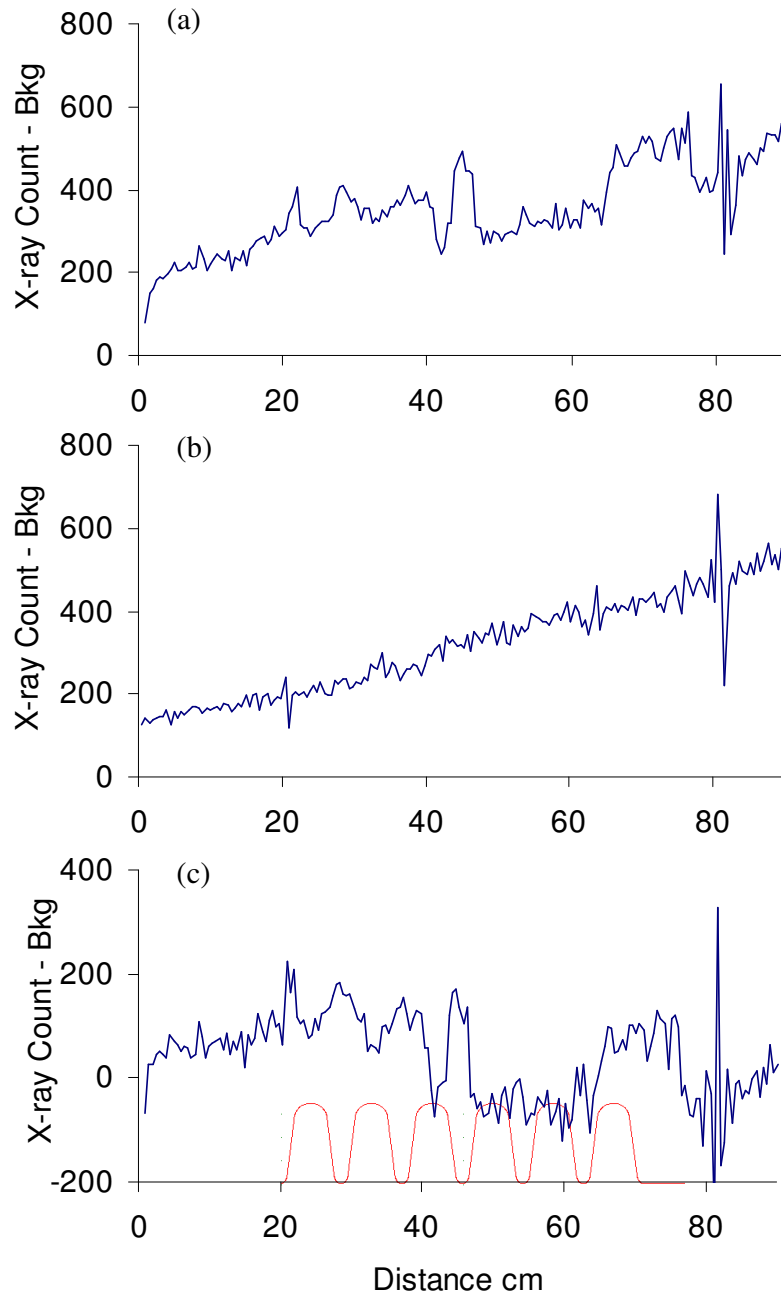


Figure 4.16: Cavity #2 operated in the  $\frac{4\pi}{6}$  mode. X-ray count acquired in two-second intervals. Panel (a): Slit of the collimator open. Panel (b): Slit of the collimator closed (background). Panel (c): X-ray count with the background subtracted. A silhouette of the cavity has been superimposed on the data.

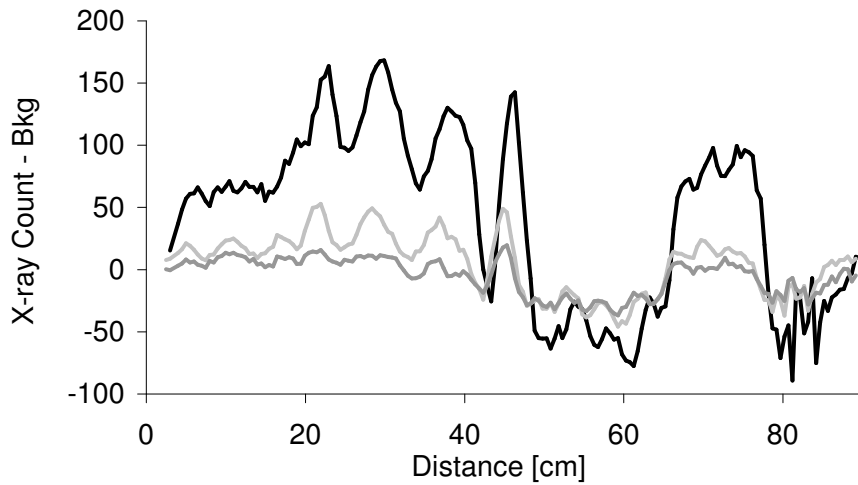


Figure 4.17: Cavity #2,  $\frac{4\pi}{6}$  mode, energy binning of data presented in Figure 4.16 (c). The black line represents the number of x-rays at all energies, the light-gray line represents the number of x-rays with a minimum energy of 400 keV, and the medium-gray line represents x-rays with a minimum energy of 600 keV. A moving average was applied to the data to smooth inconsistencies in adjacent two-second intervals.

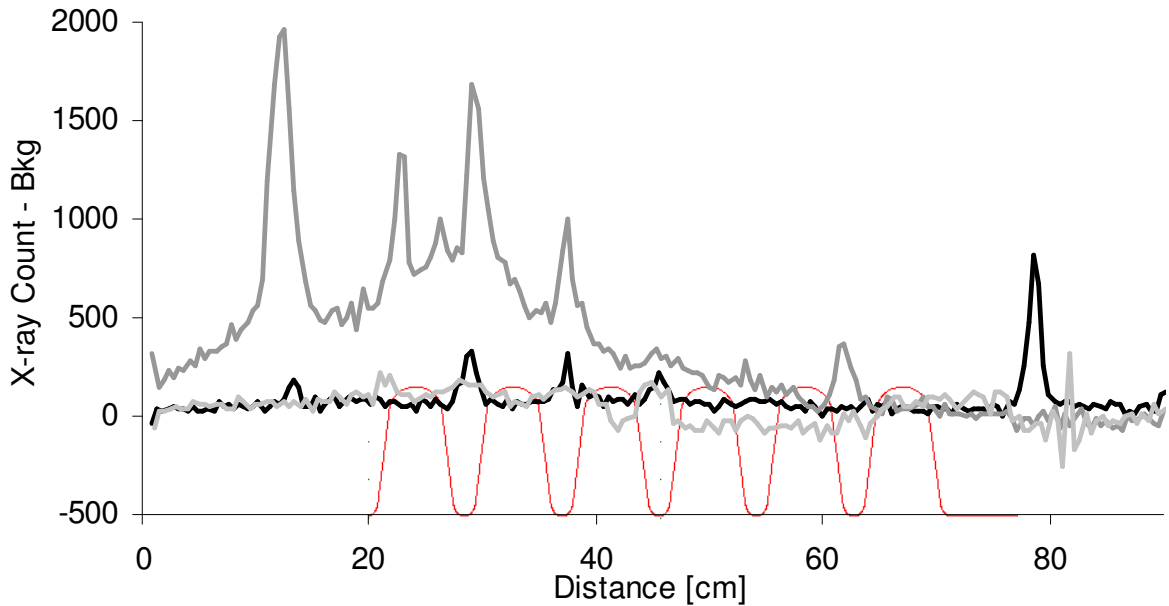


Figure 4.18: Cavity #2 spectra comparison of  $\pi$  (black line),  $\frac{5\pi}{6}$  (medium-gray line), and  $\frac{4\pi}{6}$  (light-gray line) modes. A silhouette of the cavity has been superimposed on the data. Each mode appears to have electrons impacting primarily on iris. The x-ray flux varies greatly between modes.

### 4.2.5 Cavity #1 Performance

Once the cryostat scans were completed on cavity #2 the entire detector assembly and unistrut stand were positioned to collect data for cavity #1. The front of the collimator was positioned 4.5 cm from the cryostat wall. Forward power to cavity #1 ( $\pi$  mode) was raised until x-ray detection on the area radiation monitoring equipment measured an x-ray exposure rate of  $25 \frac{\text{mR}}{\text{hr}}$ , signifying the drop in  $Q$  to be due to field emission. As with cavity #2, forward power was held nearly constant to maintain that level of x-ray exposure rate.

The cavity  $Q$  was measured (Equation 2.78) as  $8.97 \times 10^9$  while  $E_a$  was held nearly constant at  $7.5 \frac{\text{MV}}{\text{m}}$  (Equation 2.76), or  $E_p = 25.1 \frac{\text{MV}}{\text{m}}$  (Equation 2.77). The  $Q$  for cavity #1, for this study ( $\pi$  mode), was similar to the  $Q$  obtained from the previous cavity test ( $\pi$  mode) (Figure 4.19 (a)). The x-ray exposure rate for this study ( $\pi$  mode) and the previous cavity test ( $\pi$  mode) are also shown to be similar (Figure 4.19 (b)). The two plots demonstrate that no major changes in cavity performance occurred between tests.

As with cavity #2, the electric field was held nearly constant, thus a direct calculation of the Fowler-Nordheim field enhancement factor ( $\beta_{FN}$ ), needed for the particle tracking code, could not be made.  $\beta_{FN}$  was inferred from  $\pi$  mode data acquired during two previous tests and compared with data ( $\pi$  mode) for this study (Figure 4.20) (Equation 2.35).  $\beta_{FN}$  for cavity #1 was found to be in the range  $120 \leq \beta_{FN} \leq 300$ .

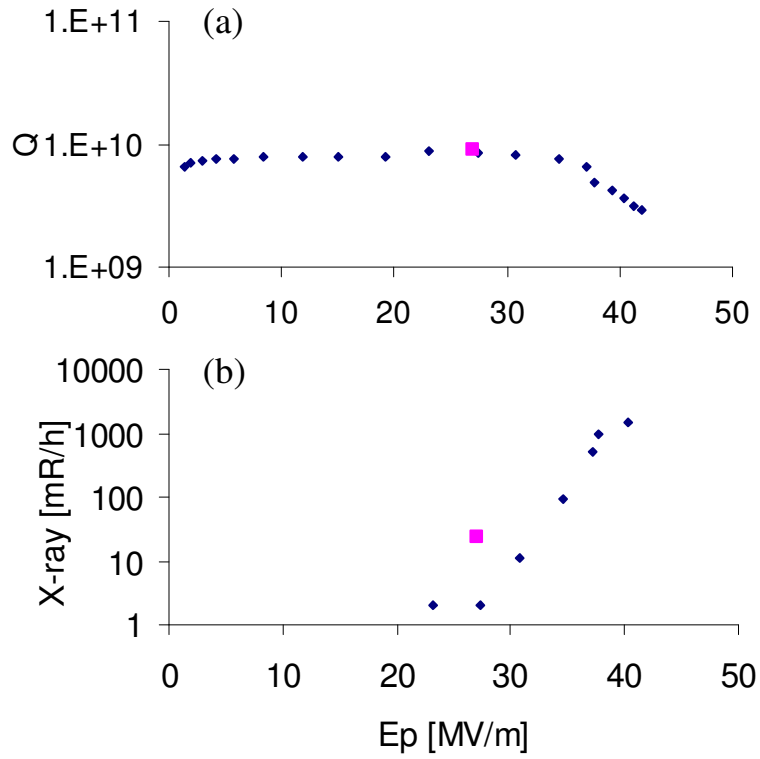


Figure 4.19: Cavity #1 performance,  $\pi$  mode. Panel (a): shows peak electric field *versus*  $Q$ . Diamonds indicate values of  $Q$  for a previous cavity test and the square, the value of  $Q$  during this study. Panel (b): shows the increase in x-ray exposure rate detected on the area radiation monitoring equipment when the observed drop in  $Q$  was due to field emission. The two plots demonstrate that no major changes in cavity performance occurred between tests.

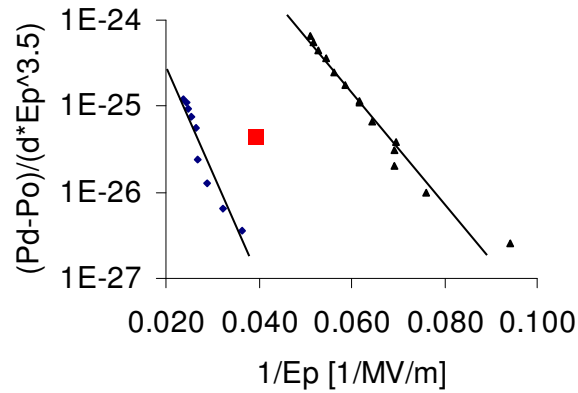


Figure 4.20: Diamonds and triangles represent data from two previous cavity tests and the square, data from this study.  $120 \leq \beta_{FN} \leq 300$ .

### 4.2.6 Cavity #1 $\pi$ Mode

Two scans of the cryostat were made with the collimator open to show that the data were reproducible as  $E_p$  was held nearly constant at  $25.1 \frac{\text{MV}}{\text{m}}$ . One scan was made with the collimator closed (background). Figure 4.21 shows the x-ray count acquired in two second intervals. The regions of high x-ray flux appear to be located on irises and possibly in the beam tubes. To aid in the determination of “real” x-ray flux peaks, energy binning was employed (Figure 4.22). The endpoint energy and location for each high flux peak, both scans of cavity #1 operated in the  $\pi$  mode, can be found in Appendix F.4.

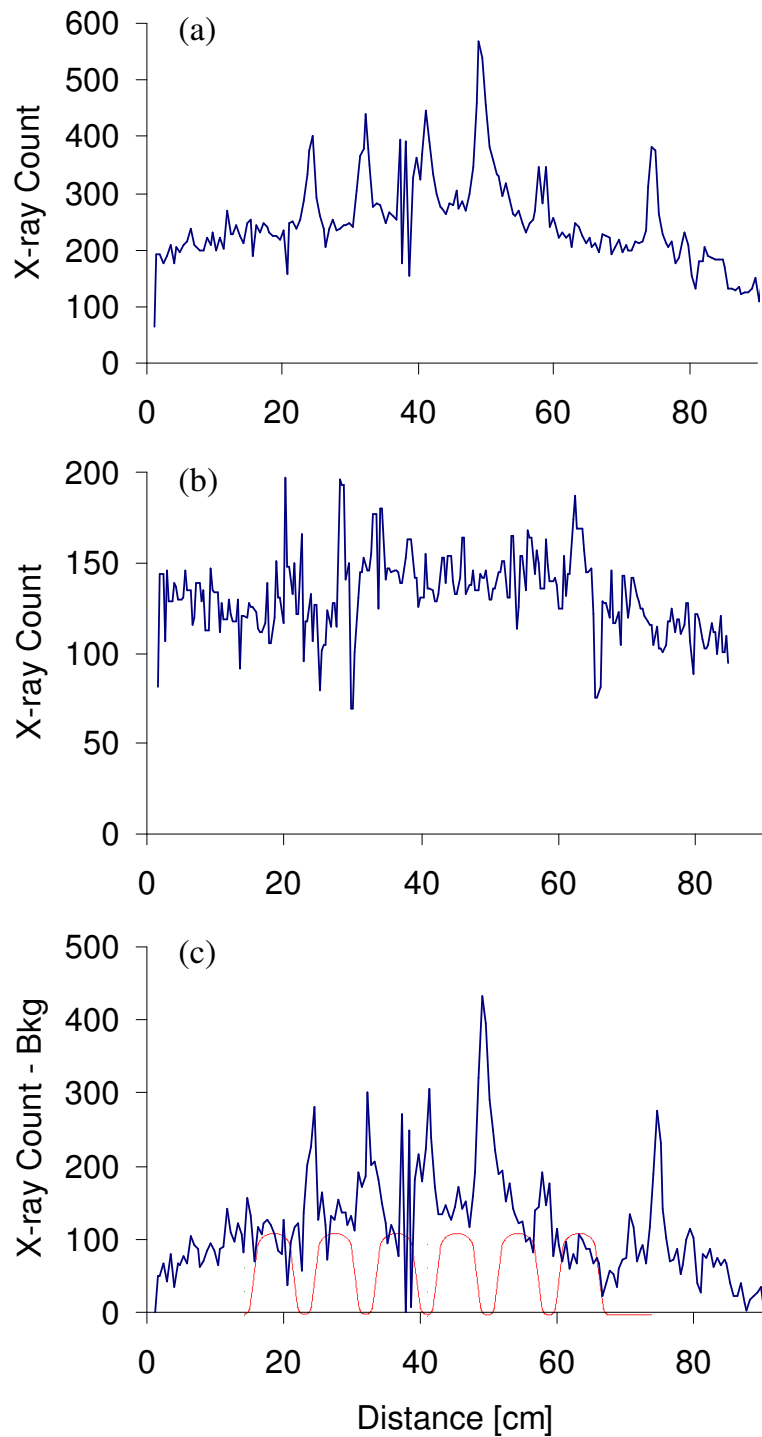


Figure 4.21: Cavity #1 operated in the  $\pi$  mode. X-ray count acquired in two-second intervals. Panel (a): Slit of the collimator open. Panel (b): Slit of the collimator closed. Panel (c): X-ray count with the background subtracted. A silhouette of the cavity has been superimposed on the data.

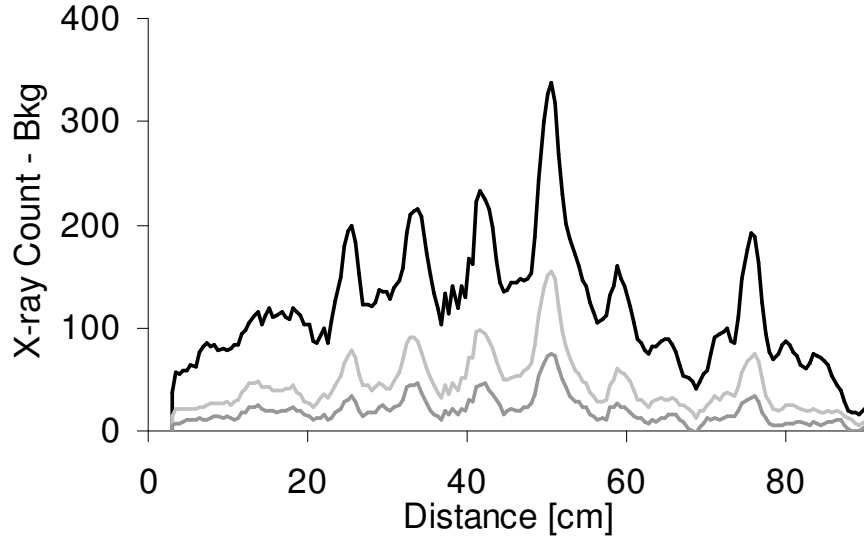


Figure 4.22: Cavity #1,  $\pi$  mode, energy binning of data presented in Figure 4.21 (c). The black line represents the number of x-rays at all energies, the light-gray line represents the number of x-rays with a minimum energy of 400 keV, and the medium-gray line represents the number of x-rays with a minimum of 600 keV. A moving average was applied to the data to smooth inconsistencies in adjacent two-second intervals.

#### 4.2.7 Cavity #1 $\frac{5\pi}{6}$ Mode

After data collection for the  $\pi$  mode was completed, the frequency was adjusted for the  $\frac{5\pi}{6}$  mode. Again, forward power was raised until an x-ray exposure rate of  $25 \frac{\text{mR}}{\text{hr}}$  was measured.  $E_p$  was held nearly constant at  $31.2 \frac{\text{MV}}{\text{m}}$ . Two scans of the cryostat were made with the collimator open to show that the data were reproducible. One scan was made with the collimator closed (background).

During the scans of cavity #1,  $\pi$  mode, the temperature rose to 2.08 K. The temperature continued to rise slightly during the  $\frac{5\pi}{6}$  mode scans. After these scans, liquid He was not available, so a scan of cavity #1 operated in the  $\frac{4\pi}{6}$  was not performed.

Figure 4.23 shows the x-ray count acquired in two-second intervals. The high x-ray flux peak at 60 cm is evident in the figure. In order to locate additional “real” peaks, energy binning and data smoothing were employed (Figure 4.24). High x-ray flux peaks now become apparent around 22, 30, 44, 52, 61, and 68 cm. The endpoint

energy and location for each high flux peak, both scans of cavity #1 operated in the  $\frac{5\pi}{6}$  mode, can be found in Appendix F.5.

A comparison of the x-ray spectra of cavity #1 operated in both the  $\pi$  and  $\frac{5\pi}{6}$  modes is shown in Figure 4.25. The  $\pi$  mode spectrum has a higher flux, an explanation follows in Chapter 5.

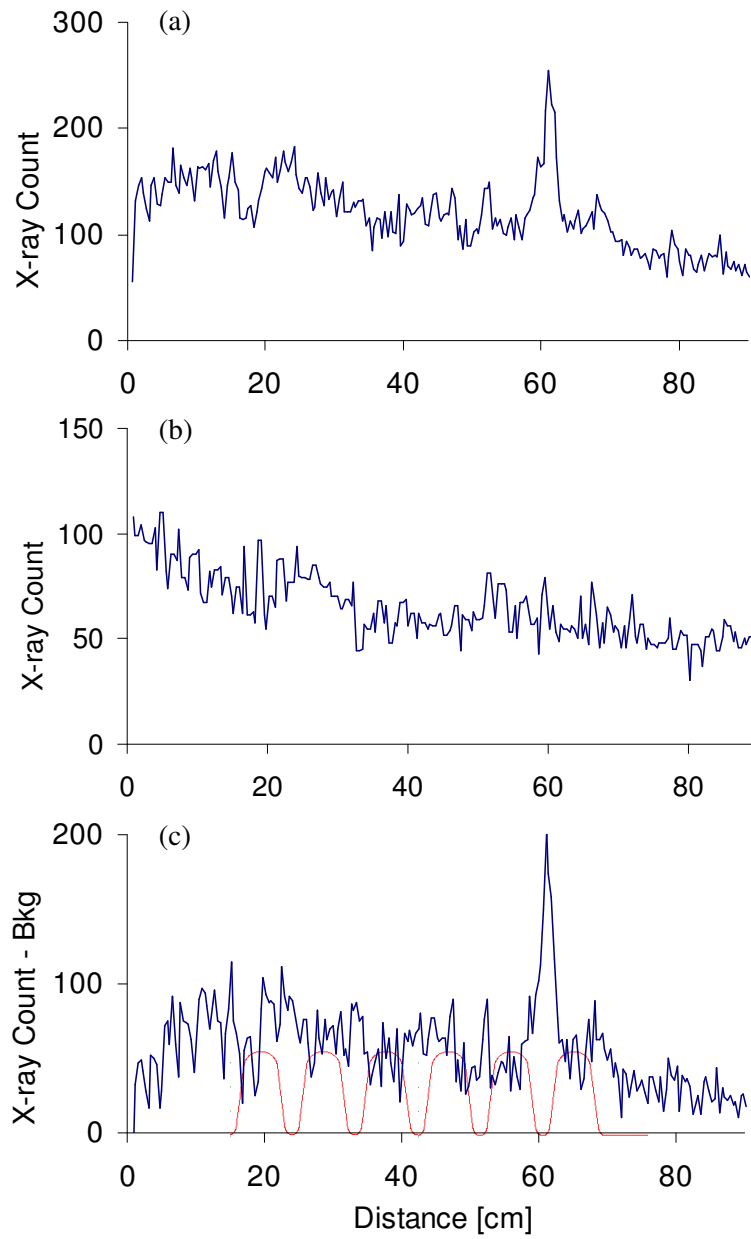


Figure 4.23: Cavity #1 operated in the  $\frac{5\pi}{6}$  mode. X-ray count acquired in two-second intervals. Panel (a): Slit of the collimator open. Panel (b): Slit of the collimator closed (background). Panel (c): X-ray count with the background subtracted. A silhouette of the cavity has been superimposed on the data.

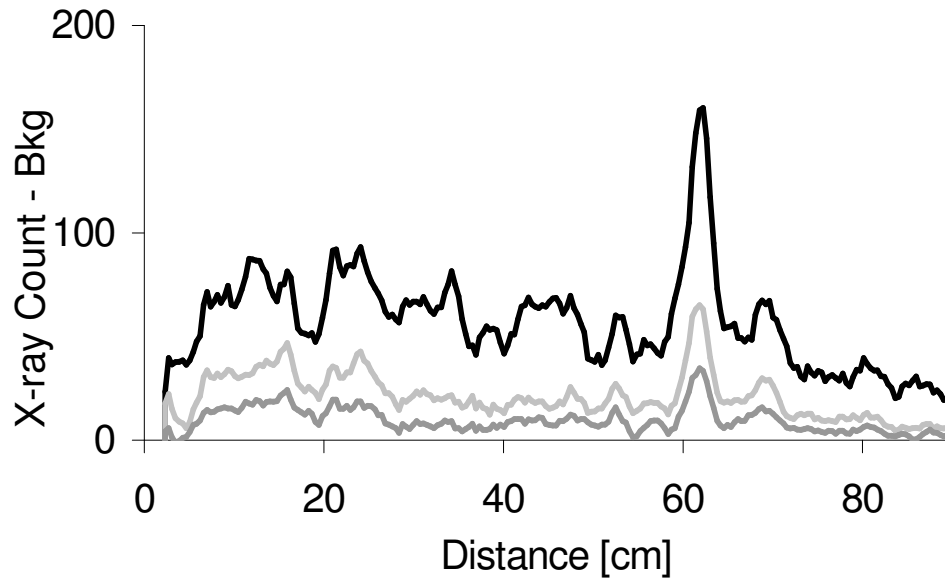


Figure 4.24: Cavity #1,  $\frac{5\pi}{6}$  mode, energy binning of data presented in Figure 4.23 (c). The black line represents the number of x-rays at all energies, the light-gray line represents the number of x-rays with a minimum energy of 400 keV, and the medium-gray line represents the number of x-rays with a minimum energy of 600 keV. A moving average was applied to the data to smooth inconsistencies in adjacent two-second intervals.

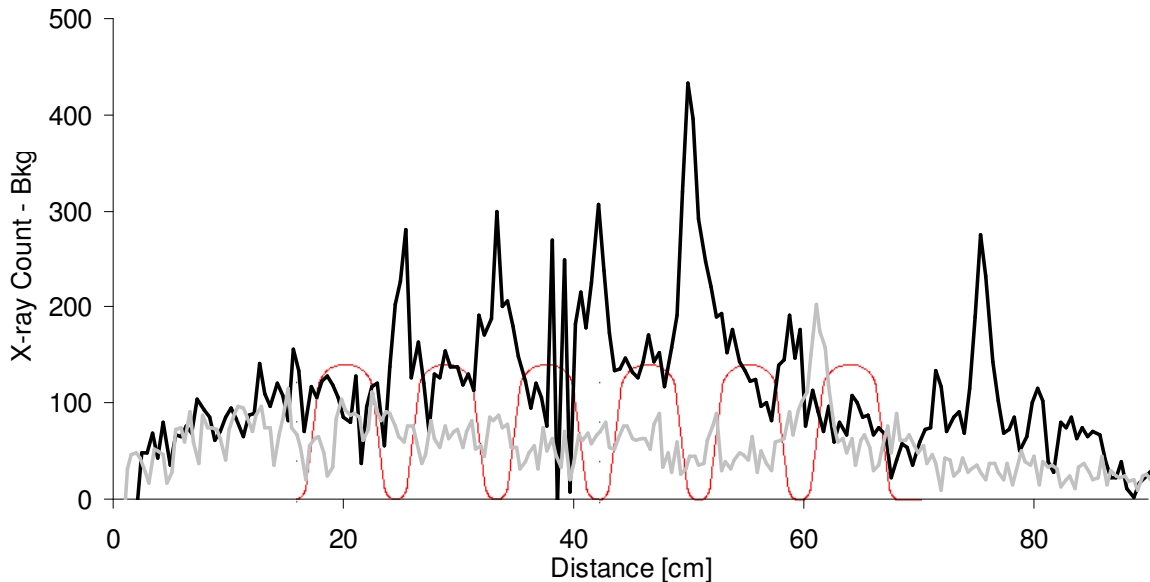


Figure 4.25: Cavity #1 spectra comparison of  $\pi$  (black line) and  $\frac{5\pi}{6}$  (gray line) modes. Both modes indicate electron impacts near iris. A silhouette of the cavity has been superimposed on the data.

# Chapter 5

## Simulations

### 5.1 SUPERLANS

SUPERLANS is a computer code that calculates electromagnetic fields within a cavity [27]. The code uses the finite element method with a quadrilateral mesh to calculate the modes in axisymmetrical cavities and periodic structures, and calculates the cut-off frequency in longitudinally-homogeneous waveguides [28]. The finite element method is a numerical technique for solving problems that are represented by partial differential equations. The range of interest is represented by a number of finite elements, or the quadrilateral mesh [28]. A plot of the quadrilateral mesh for half of a cell, required as input for a periodic structure, is shown in Figure 5.1. A fine heterogeneous mesh with increased mesh density at the iris was chosen since the fewest discontinuities were found in the surface electric field. The cavity has azimuthal symmetry about the  $z$  axis.

Output from SUPERLANS include symmetric and antisymmetric wave functions (Figure 5.2 (a)). The wave functions are reflected about zero as either symmetric or antisymmetric waves. The two wave functions for an entire six-cell cavity are shown in Figure 5.2 panel (b).

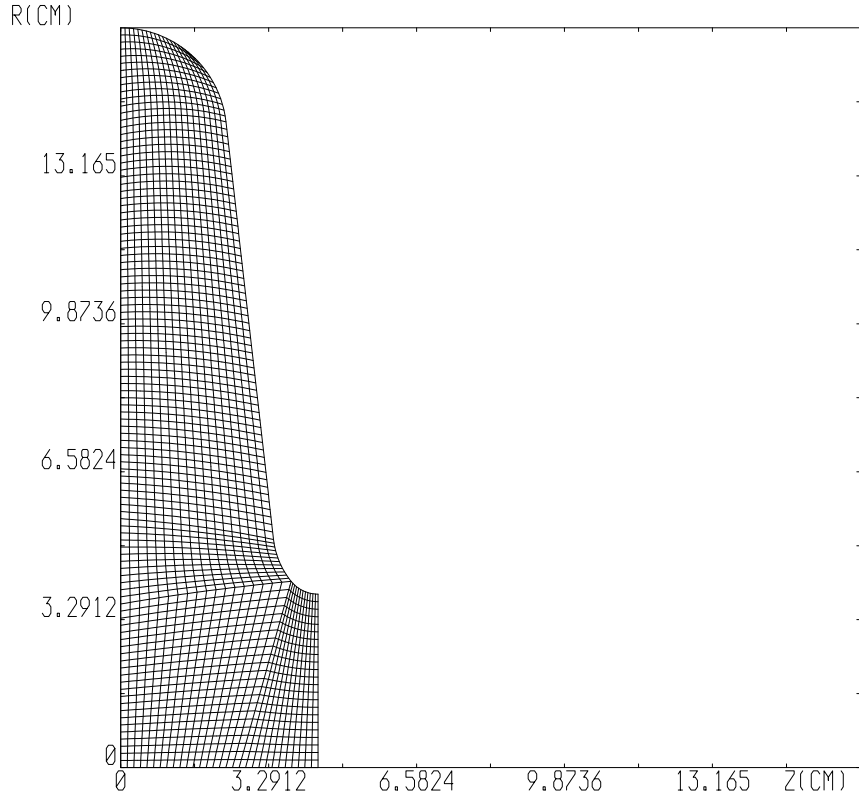


Figure 5.1: Quadrilateral mesh for a  $\beta=0.47$  805 MHz six-cell cavity. Half of a cell is required as input for a periodic structure. The cavity has azimuthal symmetry and the  $z$  axis is the contour in the axisymmetric problem.

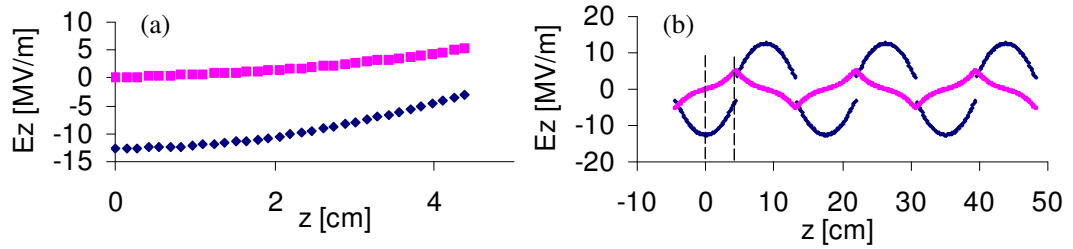


Figure 5.2: Panel (a): Symmetric (black diamonds) and antisymmetric (gray squares) wave function output from SUPERLANS for the  $\frac{4\pi}{6}$  mode. Panel (b): Symmetric (black line) and antisymmetric (gray line) wave functions for an entire six-cell cavity. The dashed lines in panel (b) identify the portion of the wave function shown in panel (a).

The two wave functions are combined in the particle tracking code, using the Floquet theorem (Appendix E), to construct a standing wave with the desired phase shift over a structure period. The electric field on axis of a six-cell cavity, constructed using the Floquet theorem, for the  $\pi$  ( $180^\circ$  phase shift),  $\frac{5\pi}{6}$  ( $150^\circ$  phase shift),  $\frac{4\pi}{6}$  ( $120^\circ$  phase shift),  $\frac{3\pi}{6}$  ( $90^\circ$  phase shift),  $\frac{2\pi}{6}$  ( $60^\circ$  phase shift), and  $\frac{\pi}{6}$  ( $30^\circ$  phase shift) modes is shown in Figure 5.3. The  $\pi$  mode is used for particle acceleration since each cell is  $\pi$  radians out of phase with the neighboring cell. The cavity magnetic fields are generated in the same manner.

Electrons, field emitted from the same defect are accelerated by mode dependent electric fields. The electron trajectories depend on which passband mode is excited, thus their impact sites result in different x-ray spectra.

Output, also from SUPERLANS, includes electromagnetic fields along the cavity surface. The absolute value of the surface electric fields, calculated for one Joule of stored energy, for a six-cell  $\beta = 0.47805$  MHz cavity,  $\pi$ ,  $\frac{5\pi}{6}$ , and  $\frac{4\pi}{6}$  modes, are shown in Figure 5.4. The field for the  $\frac{5\pi}{6}$  was normalized and the other two modes scaled accordingly. The surface electric field reverses direction at the equator. Field emission current is dependent upon the surface electric field at the emitter (Equation 2.35). The peak electric field on axis for the  $\pi$  mode is calculated using Equation 2.76. Data were acquired for these three modes so only these three are shown.

The surface electric field is identical from cell to cell for the  $\pi$  mode and is maximum at each iris and zero at each equator. The surface electric field for the  $\frac{5\pi}{6}$  mode is greater than the other two modes at the first and last irises (adjacent to the beam tube) and between the first and second and fifth and sixth cells. Data acquired with the highest x-ray flux for the  $\frac{5\pi}{6}$  mode, has the highest probability of a field emitter located along one of the irises where the surface electric field is greatest for the  $\frac{5\pi}{6}$  mode. The same is true for any mode with the highest x-ray flux.

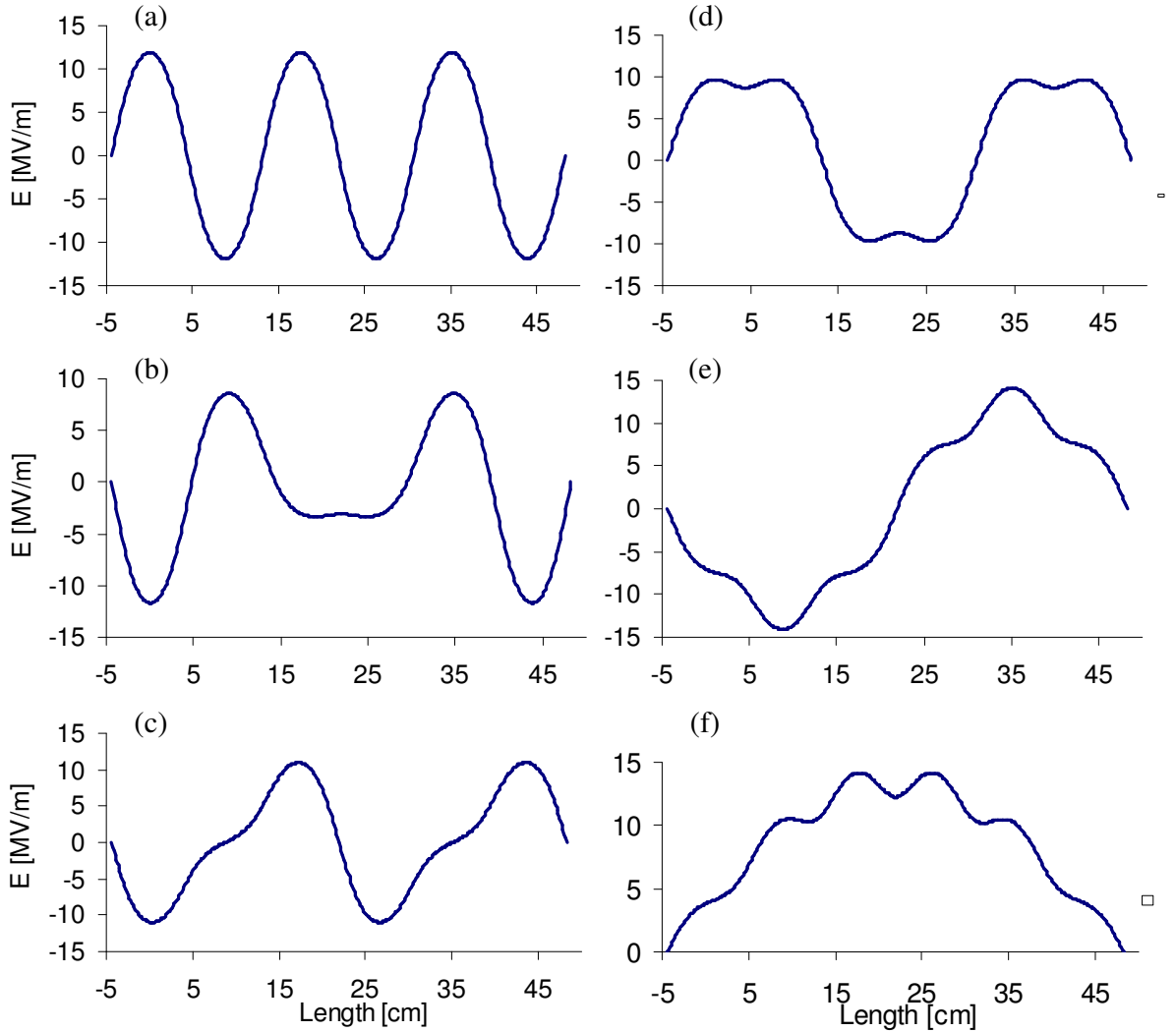


Figure 5.3: Electric fields on axis for a six-cell cavity. Panel (a):  $\pi$  mode ( $180^\circ$  phase shift). Panel (b):  $\frac{5\pi}{6}$  mode ( $150^\circ$  phase shift). Panel (c):  $\frac{4\pi}{6}$  mode ( $120^\circ$  phase shift). Panel (d):  $\frac{3\pi}{6}$  mode ( $90^\circ$  phase shift). Panel (e):  $\frac{2\pi}{6}$  mode ( $60^\circ$  phase shift). Panel (f):  $\frac{\pi}{6}$  mode ( $30^\circ$  phase shift). The electric fields were constructed from the symmetric and antisymmetric wave functions using the Floquet theorem.

## 5.2 Multipacting/Field Emission Simulation

The code used for predicting the trajectories of field-emitted electrons was “Multi-*tip*”, originally developed at Cornell University. The code predicts electron impact locations, impact energies, and the power deposition along the inner surface of the cavity [29]. The original code was modified to allow different passband modes with the electromagnetic field distribution numerically calculated using the Floquet theorem.

## Code Modifications

A significant part of this research, nearly one year, was devoted to code modifications and verifications. The modifications and verifications are outline in this subsection.

The first step to running the Multipacting/Field Emission Simulation is to produce a field table using SUPERLANS. For periodic boundary conditions, which the original code would not allow, SUPERLANS produces two field tables: one for the symmetric and one for the antisymmetric wave functions.

The symmetric and antisymmetric wave functions were first combined in EXCEL using equations derived from the Floquet theorem (Appendix E). The construction of the fields was verified with the electromagnetic field output from MAFIA [30].

Two sub-programs, one that reads the field tables, and another that calculates

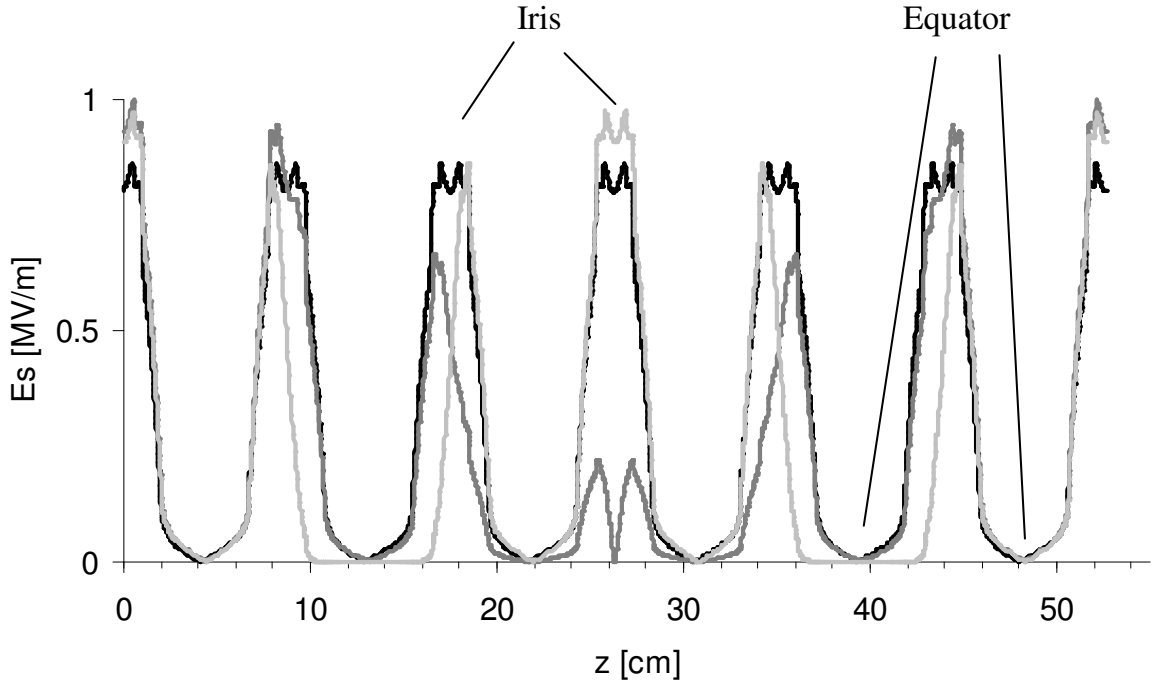


Figure 5.4: Normalized absolute value of the surface electric fields for a six-cell  $\beta = 0.47$  805 MHz cavity for the  $\pi$  (black line),  $\frac{5\pi}{6}$  (dark-gray line), and  $\frac{4\pi}{6}$  (light-gray line) modes. First and second irises, surface electric field greatest for the  $\frac{5\pi}{6}$  mode. Third iris, surface electric field greatest for the  $\pi$  mode. Fourth iris, surface electric field greatest for the  $\frac{4\pi}{6}$  mode. Fifth iris, surface electric field greatest for the  $\pi$  mode. Sixth and seventh irises, surface electric field greatest for the  $\frac{5\pi}{6}$  mode.

the electromagnetic field components were initially modified. The initialization code reads information from three text files and translates the information into a format compatible with the remaining programs. This program was modified to read two tables, symmetric and antisymmetric, and store the field tables as sets of ordered pairs. The other program was modified to calculate the electromagnetic field components using the Floquet theorem.

The initialization program also identifies the maximum surface electric field. The program originally examined only one cell since the fields do not vary from cell to cell for the  $\pi$  mode. The program was modified to examine an appropriate number of cells since the fields vary from cell to cell for modes other than the  $\pi$  mode. The appropriate number of cells depends on the phase advance per cell and number of cells. Another text file identifies the cell number and the field emitter location and stores that information.

Two programs are used to examine the tables graphically. One program draws the cavity boundary. The same program can also plot contour maps of  $|E|$ ,  $H_\phi$ , or  $rH_\phi$ . This code called the revised program to read the fields that were calculated using the Floquet theorem. Output for the  $\pi$  mode were compared to the unmodified output. It was assumed the other modes were functioning properly.

Another program has the capability of plotting the electric field magnitude, magnetic field magnitude, radial component of the electric field ( $E_r$ ), or axial component of the electric field ( $E_z$ ) as a function of R (radially), Z (horizontally), or S (along the cavity surface). This code was modified to call the revised programs to read the fields and calculate the field components. The fields for the  $\pi$  mode, periodic boundary conditions, were compared to the fields output for the unmodified program. The fields for the other modes were compared with the EXCEL output.

The next program for comparison calculates the energy stored in the magnetic and electric fields. This program also called the revised programs to calculate the fields. The correct output for all three programs verified that the Multipacting/Field

Emission Simulation was calculating the fields correctly.

### 5.2.1 Program Operation

The rf period is divided into a number of equal time intervals (number chosen by the user). At the beginning of each time interval an electron is emitted with a given velocity from a point on the cavity surface for a given amplitude of the surface electromagnetic field. Electron trajectories are calculated by integrating the following vector equations:

$$\frac{d\vec{r}(t)}{dt} = \frac{1}{\gamma}\vec{u}(t), \quad (5.1)$$

$$\frac{d\vec{u}(t)}{dt} = \frac{q}{m} \left[ \vec{E}(\vec{r}, t) + \frac{1}{\gamma}\vec{u}(t) \times \vec{B}(\vec{r}, t) \right], \quad (5.2)$$

where  $\vec{r}(t)$  is the position vector of the electron at time  $t$ ,  $\vec{E}(\vec{r}, t)$  and  $\vec{B}(\vec{r}, t)$  are the electric and magnetic field at position  $\vec{r}$  and time  $t$ ,  $q$  is the electron charge,  $m$  is the electron mass,  $\gamma = \frac{1}{\sqrt{1 - \left(\frac{|\vec{v}|}{c}\right)^2}}$ ,  $\vec{v}$  is the electron velocity, and  $\vec{u}$  is the proper velocity with  $\vec{u} \equiv \gamma\vec{v}$  [29].

The instantaneous field-emitted current is calculated from Equation 2.32, where the electric field at the time of emission  $\vec{E}(t)$  is replaced with the enhanced electric field  $\beta\vec{E}(t)$  and  $v(s)$  and  $t(s)$  (Appendix B.1) are evaluated in terms of complete elliptic integrals.

### 5.2.2 Input Parameters

Input parameters to the code include the cell number of the emitter, the location of the emitter along the cell wall (S0), the peak surface electric field ( $E_p$ ), the maximum number of rf periods that an electron trajectory is tracked, and the number of electrons tracked in an rf period. The average cavity current due to field emission depends on the Fowler-Nordheim field enhancement factor ( $\beta_{FN}$ ), the emitter area

( $A_e(\text{cm}^2)$ ), the work function ( $\varphi(\text{eV})$ ) of the metal, and the electric field at the emitter ( $E_{em}$ ) (Equation 2.35). A range of  $\beta_{FN}$  was determined from data for each cavity. Initially the default value of  $9 \times 10^{-11} \text{ cm}^2$  was used for  $A_e$ . Since the average cavity current is directly proportional to  $A_e$ , the shape of the simulated power spectrum (Subsection 5.2.3) is unchanged with changes in  $A_e$ . An estimate of  $A_e$  can be found in Chapter 6. The assumed value for  $\varphi$  was 4.3 eV; published values for Nb range from 4.0 to 4.9 eV, depending on the crystal orientation [26].  $E_{em}$  is calculated by the code for the input value of  $E_p$ .

Output from the code includes the time of electron emission during the rf period, the peak electric field at the emitter ( $E_{em}$ ), the electric field at the emitter at the time of emission  $\vec{E}(t)$ , the electron impact location along the cavity wall and with respect to the  $z$  axis, the electron impact kinetic energy ( $K_f$ ), and the angle at which the electron impacts with respect to the  $z$  axis. The number of electrons tracked during  $2\pi$  radians is chosen by the user ( $\frac{\Delta\phi}{2\pi}$ ). Electrons are only field emitted during half the RF period.

Changing S0 changes the field emitted electron trajectories. S0 is measured in cm from the cavity equator; negative S0 is to the left and positive S0 is to the right. An example of field emitted electron trajectories for two different emitters in cell #2 of a six-cell cavity is shown in Figure 5.5.  $E_{em}$  varies with field emitter location and the maximum  $K_f$  also varies. The change in the electron trajectories, and thus their impact sites, will produce different x-ray spectra. Electrons that appear to strike an end plate of the cavity, would exit the cavity and travel down the beam tube. Only 50 trajectories are shown. Increasing the number of trajectories to 10,000 increases the difficulty to visually trace individual electron trajectories, in most cases.

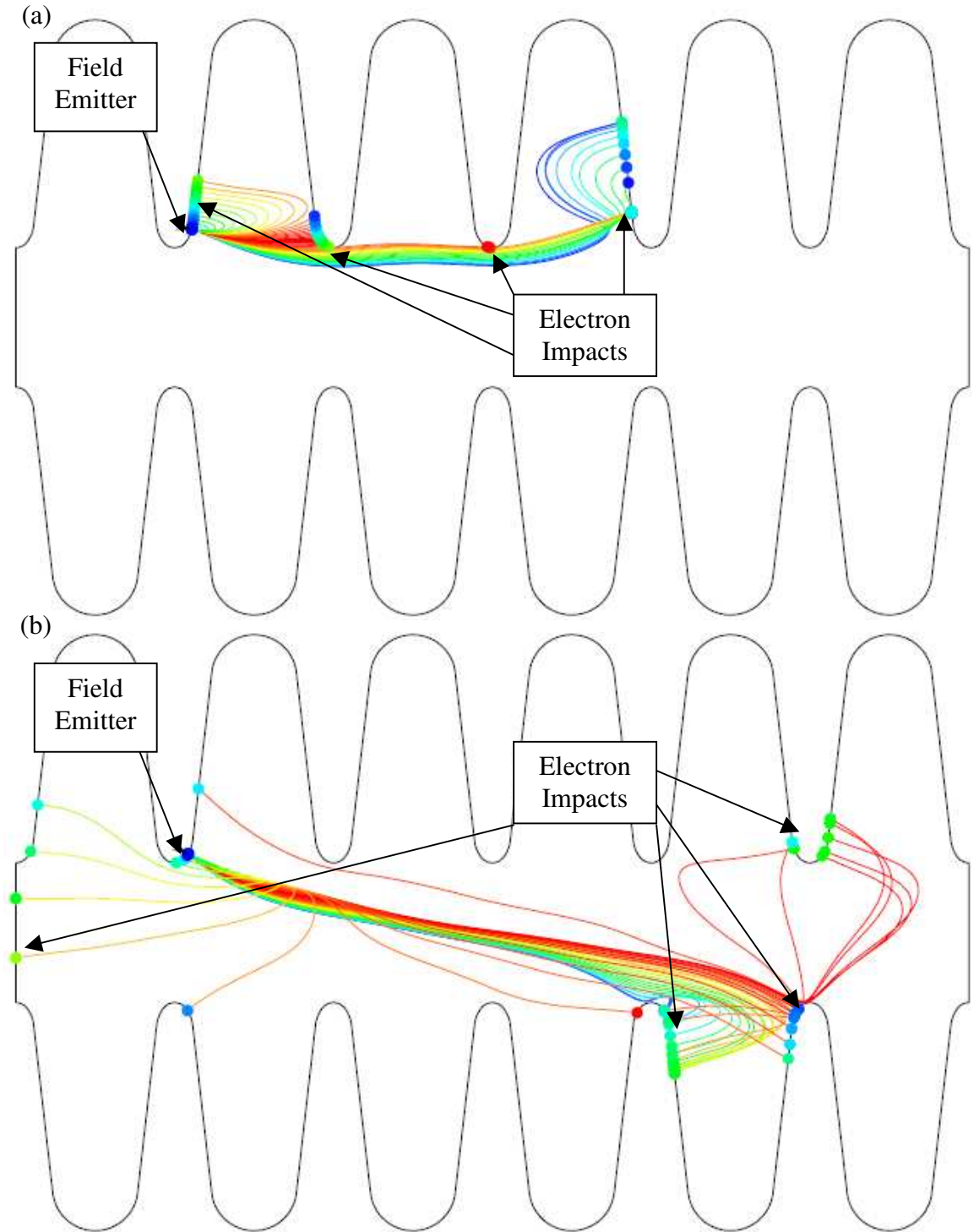


Figure 5.5:  $\pi$  mode field emitted electron trajectories differ for different emitter sites with all other input parameters equal. Field emitter in cell #2,  $E_p = 26.0 \frac{\text{MV}}{\text{m}}$ . Panel (a):  $S_0 = -13.0 \text{ cm}$ ,  $E_{em} = 24.26 \frac{\text{MV}}{\text{m}}$ , and  $K_f = 1.673 \text{ MeV}$ . Panel (b):  $S_0 = -13.6 \text{ cm}$ ,  $E_{em} = 24.41 \frac{\text{MV}}{\text{m}}$ , and  $K_f = 1.684 \text{ MeV}$ .

Changing  $E_p$ , the peak surface electric field, also changes the field emitted electron trajectories. An example of field emitted electron trajectories for two different  $E_p$  values are shown in Figure 5.6. All other input parameters are identical. Again, not only the electron trajectories but the x-ray spectra would change.

For the  $\pi$  mode, simulating a field emitter in another cell with the same  $S_0$ , shifts the electron trajectories since the electric fields are symmetric from cell to cell (Figure 5.7 (a) and (b)). Simulating a field emitter on the opposite side of a cell, the same distance from the equator ( $\pm S_0$ ), reverses the electron trajectories since the electric field is symmetric within the cell (Figure 5.7 (b) and (c)). This is an essential aid in locating field emitters for the  $\pi$  mode.

The electric field for the other cavity modes,  $\frac{5\pi}{6}$ ,  $\frac{4\pi}{6}$ ,  $\frac{3\pi}{6}$ ,  $\frac{2\pi}{6}$ , and  $\frac{\pi}{6}$ , are not symmetric from cell to cell, nor symmetric within a cell (Figure 5.3). Figure 5.8 (a) and (b) shows the electron trajectories of a field emitter in a neighboring cell but with the same  $S_0$  for the  $\frac{4\pi}{6}$  mode. The pattern of the electron trajectories does not shift by a cell as in the  $\pi$  mode. Figure 5.8 (c) shows the electron trajectories of a field emitter on the opposite side of a cell for the  $\frac{4\pi}{6}$  mode. Electron trajectories do not simply reverse direction as they do in the  $\pi$  mode.

Figure 5.9 shows electron trajectories from a field emitter in  $\pi$ ,  $\frac{5\pi}{6}$ , and  $\frac{4\pi}{6}$  modes with all input parameters, cell #,  $S_0$ , and  $E_p$ , identical. Changing modes changes the surface electric field distribution, which in turn changes  $E_{em}$ . The electrons are accelerated by the electric field within the cavity and the trajectories directed by the magnetic field. Changing modes changes these fields. Electrons impact with differing  $K_f$  from mode to mode. The number and energy of the x-rays produced from impacting electrons depends on  $K_f$ .

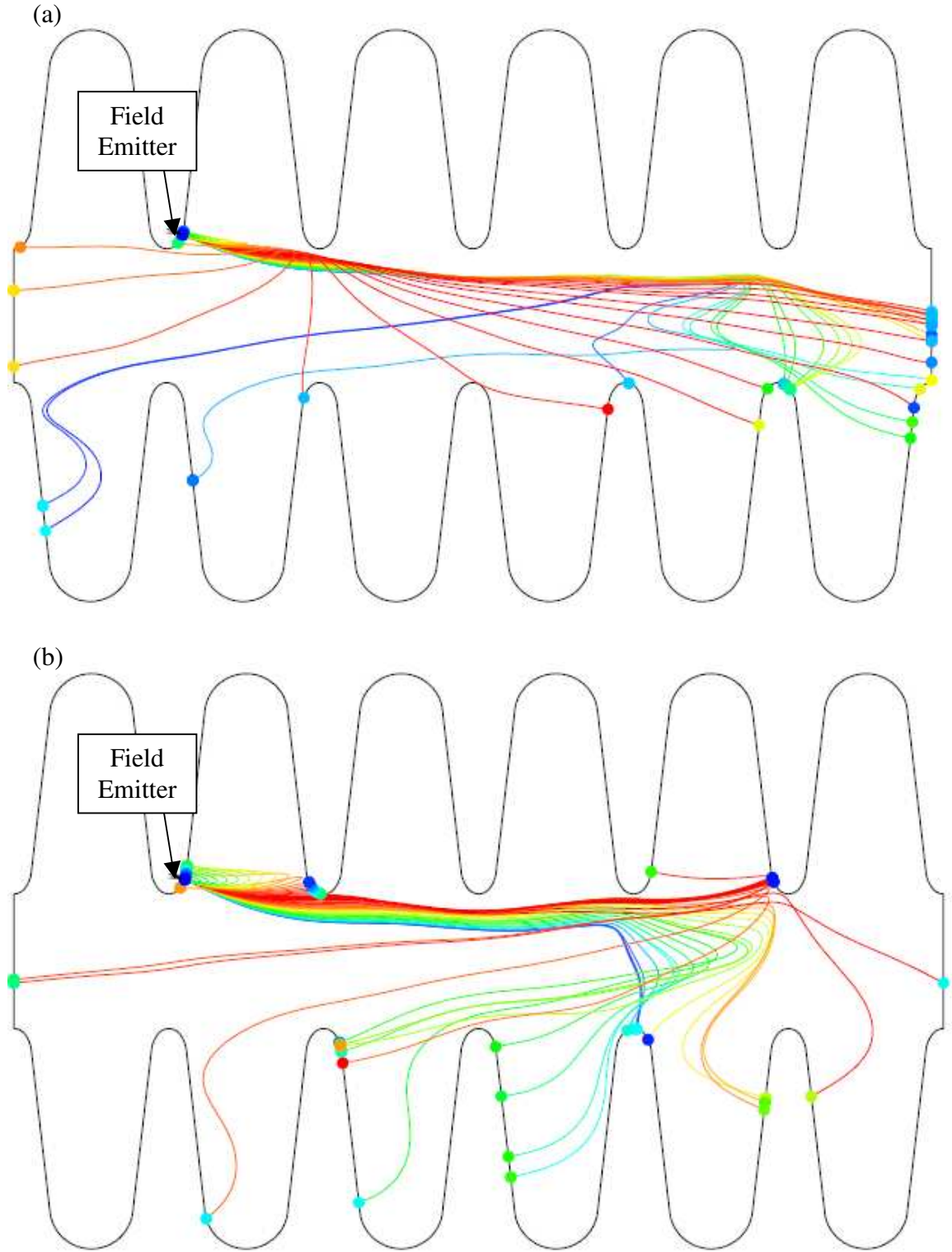


Figure 5.6: Field emitted electron trajectories differ for different peak surface electric fields with all other input parameters equal. Field emitter in cell #2,  $S_0 = -13.2$  cm. Panel (a):  $E_p = 13.0 \frac{\text{MV}}{\text{m}}$ ,  $E_{em} = 12.33 \frac{\text{MV}}{\text{m}}$ , and  $K_f = 861.8$  keV. Panel (b):  $E_p = 26.0 \frac{\text{MV}}{\text{m}}$ ,  $E_p = 24.67 \frac{\text{MV}}{\text{m}}$ , and  $K_f = 1.292$  MeV.

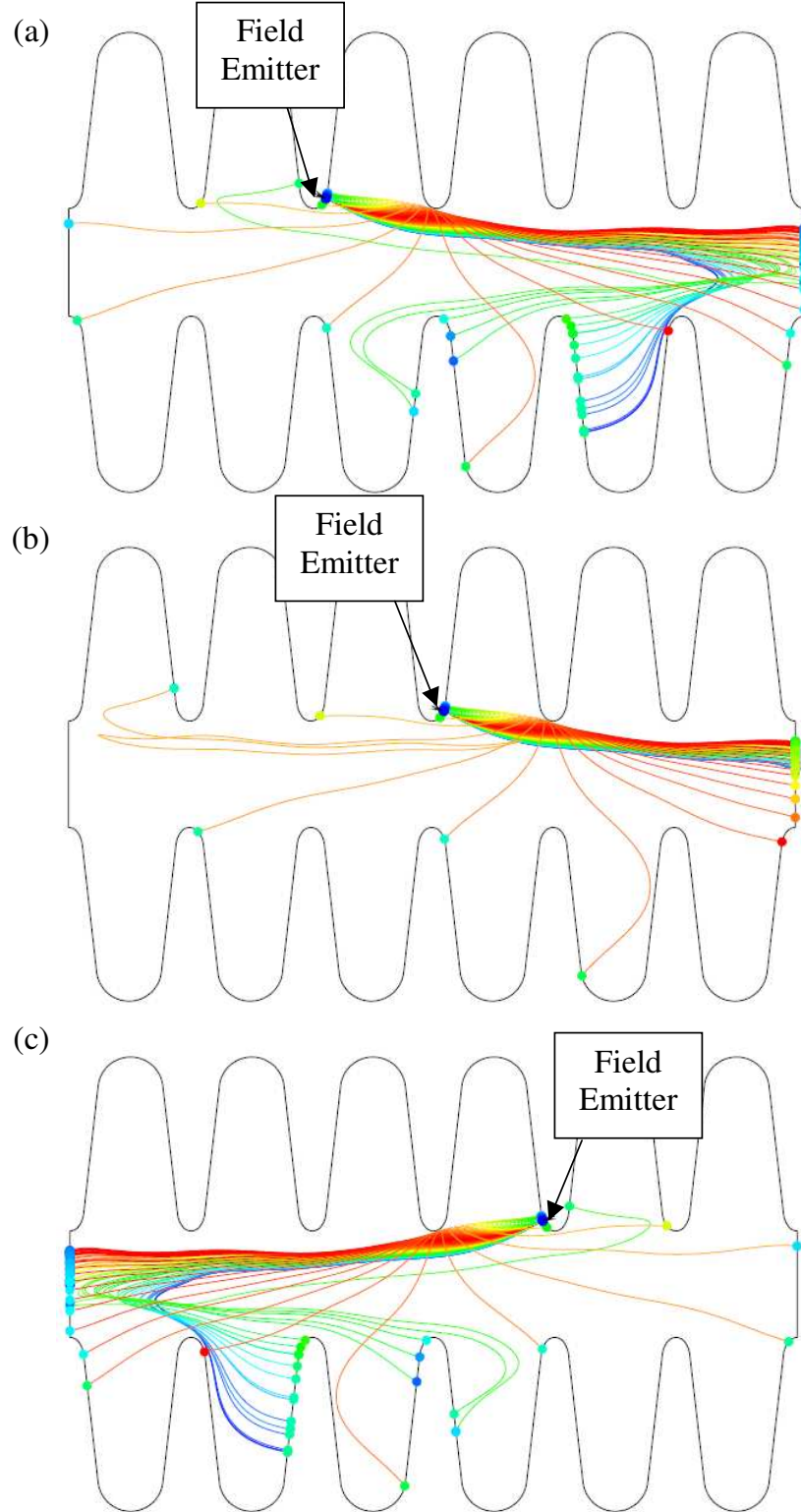


Figure 5.7:  $\pi$  mode,  $E_p = 26.0 \frac{\text{MV}}{\text{m}}$ ,  $E_{em} = 24.41 \frac{\text{MV}}{\text{m}}$ , and  $K_f = 1.684 \text{ MeV}$ . Panel (a): Field emitter in cell #3,  $S_0 = -13.3 \text{ cm}$ . Panel (b): Field emitter in cell #4,  $S_0 = -13.3 \text{ cm}$ . Panel (c): Field emitter in cell #4,  $S_0 = +13.3 \text{ cm}$ . In the  $\pi$  mode, the electric fields are symmetric from cell to cell and within the cell.

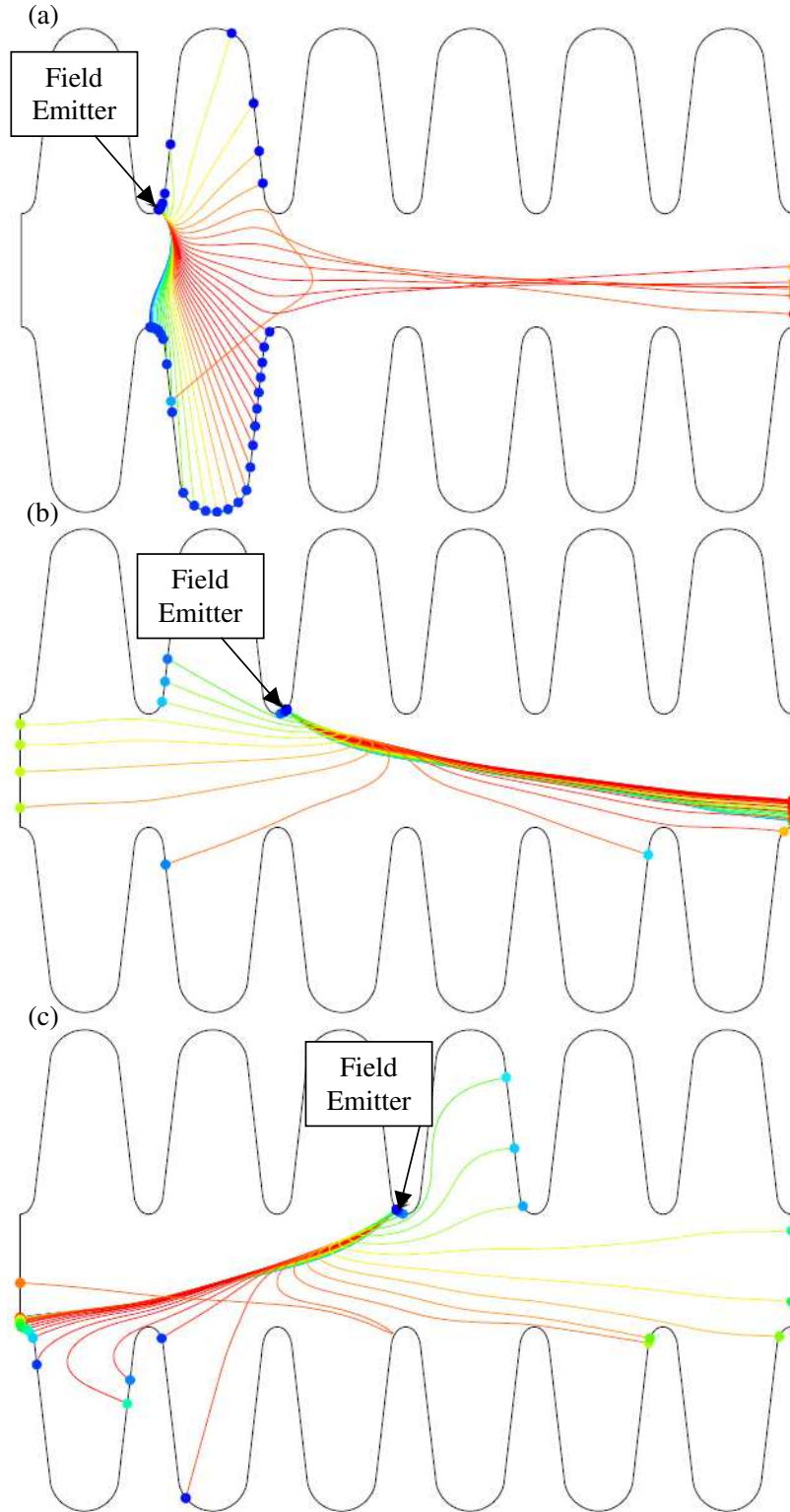


Figure 5.8:  $\frac{4\pi}{6}$  mode,  $E_p = 26.0 \frac{\text{MV}}{\text{m}}$ . Panel (a): Emitter in cell #2,  $S_0 = -13.8$  cm,  $E_{em} = 4.014 \frac{\text{MV}}{\text{m}}$ , and  $K_f = 2.607$  MeV. Panel (b): Emitter in cell #3,  $S_0 = -13.8$  cm,  $E_{em} = 21.11 \frac{\text{MV}}{\text{m}}$ , and  $K_f = 2.555$  MeV. Panel (c): Emitter in cell #3,  $S_0 = +13.8$  cm,  $E_{em} = 25.12 \frac{\text{MV}}{\text{m}}$ , and  $K_f = 2.304$  MeV. In all but the  $\pi$  mode, the electric fields are not symmetric from cell to cell and not symmetric within the cell.

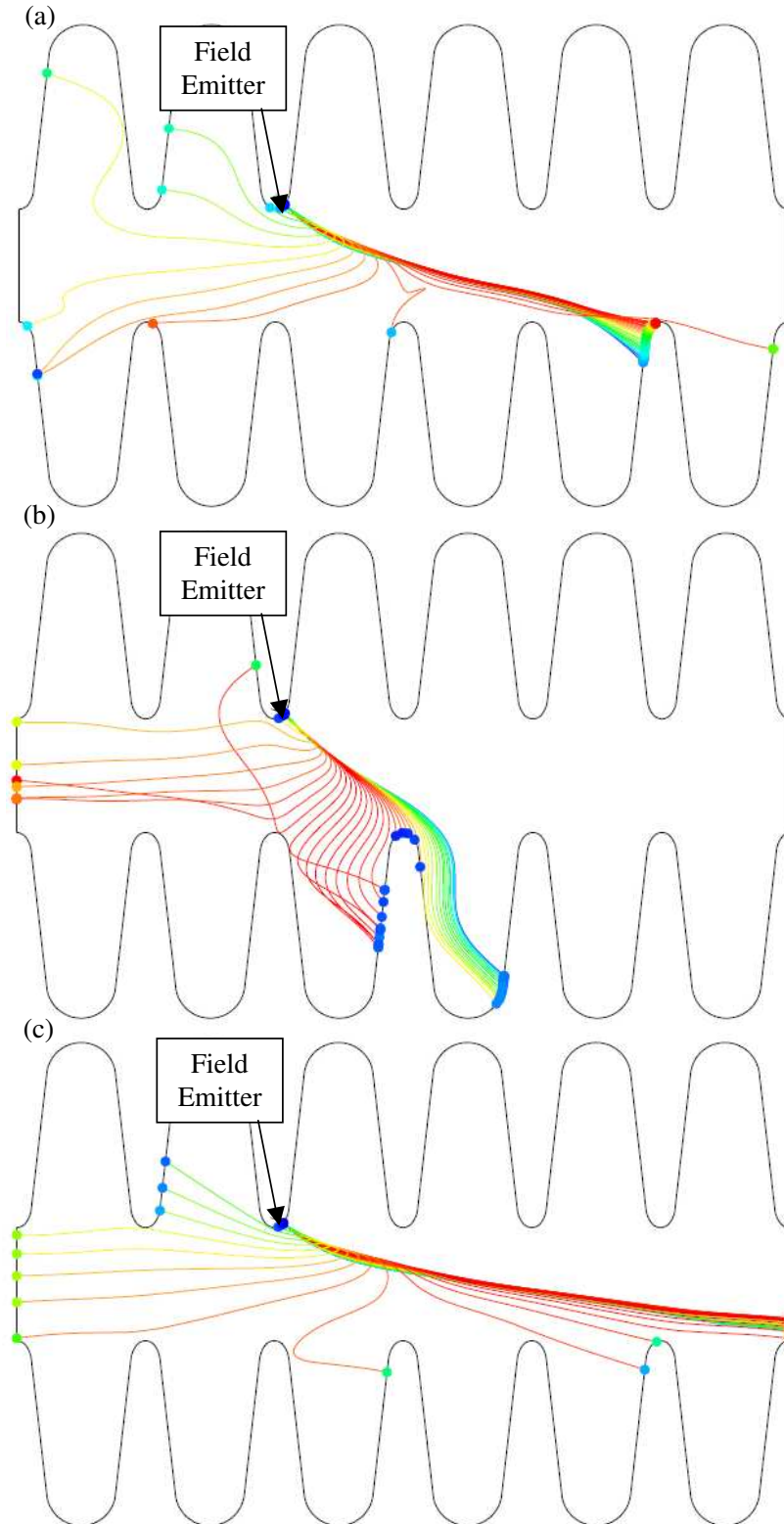


Figure 5.9: Field emitter in cell #3,  $S_0 = -13.8$  cm,  $E_p = 22 \frac{\text{MV}}{\text{m}}$ . Panel (a):  $\pi$  mode,  $E_{em} = 21.25 \frac{\text{MV}}{\text{m}}$ , and  $K_f = 1.422$  MeV. Panel (b):  $\frac{5\pi}{6}$  mode,  $E_{em} = 7.272 \frac{\text{MV}}{\text{m}}$ , and  $K_f = 1.039$  MeV. Panel (c):  $\frac{4\pi}{6}$  mode,  $E_{em} = 17.86 \frac{\text{MV}}{\text{m}}$ , and  $K_f = 2.221$  MeV.

Some symmetry of the field emitted electron trajectories does exist for modes other than the  $\pi$  mode. For example, referring to Figure 5.3, electrons emitted in cell #1 of the  $\frac{4\pi}{6}$  mode would have the same trajectories if field emitted at the same S0 but in cell #4, shifted by three cells. Also, electrons field emitted in cell #1 of the  $\frac{5\pi}{6}$  mode would have their trajectories reversed relative to those of electrons field emitted from -S0 in cell #6.

In the preceding examples of electron trajectories, the electrons travel in a plane through the cavity. According to the Lorentz Force Law, there are no forces acting on an electron in the  $\phi$  direction:

$$\vec{F} = q \left[ \vec{E} + (\vec{v} \times \vec{B}) \right], \quad (5.3)$$

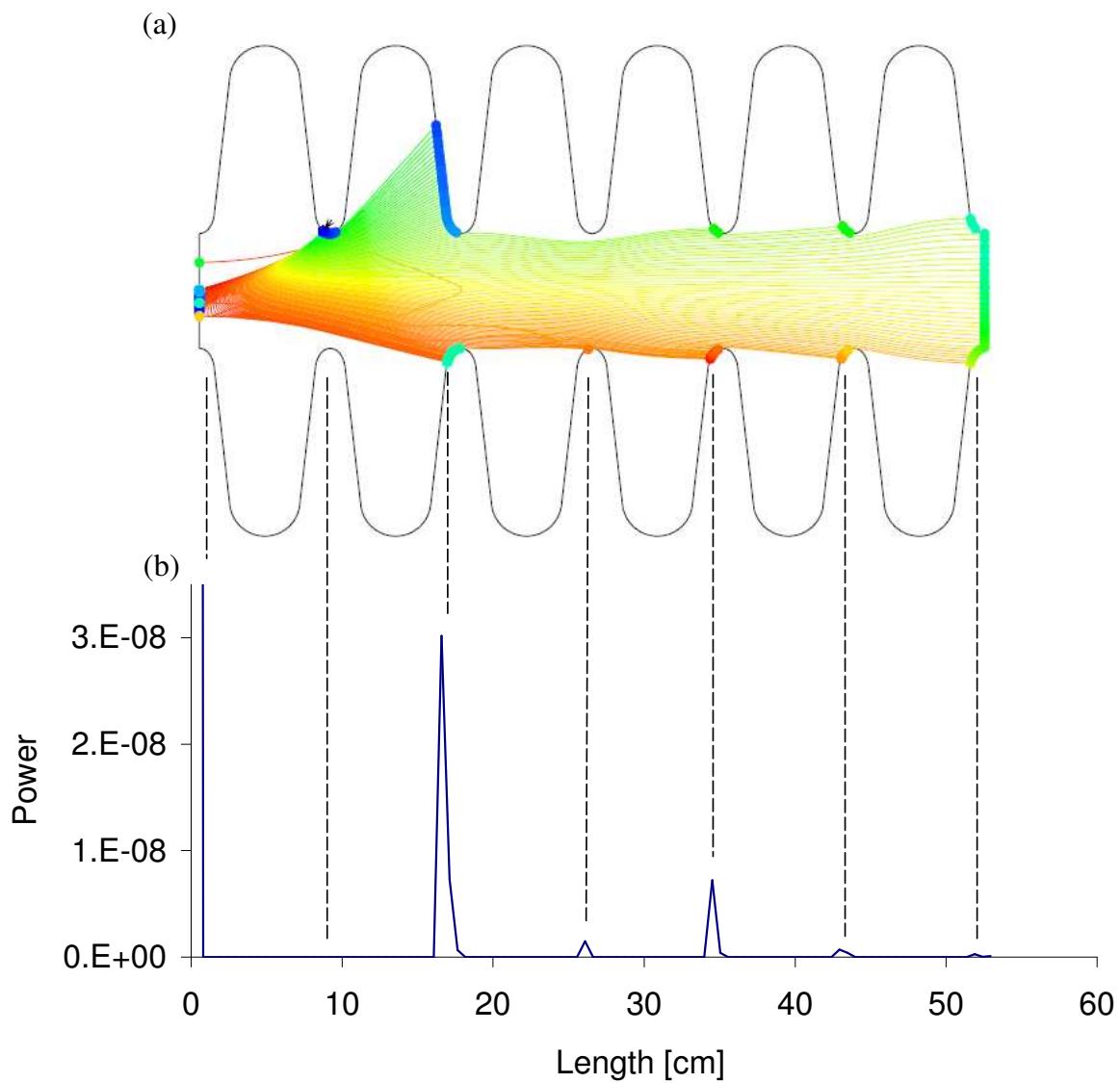
where  $q$  is the charge of an electron,  $\vec{E} = E_r \hat{r} + E_z \hat{z}$ ,  $\vec{v} = v_r \hat{r} + v_z \hat{z}$ , and  $\vec{B}_\phi = B_\phi \hat{\phi}$ .

### 5.2.3 Code Output

To compare the simulation output with the data, power was calculated for both. For each field emitted electron, the field emission simulation provides the electric field at the emitter  $E_{em}(t)$  ( $\frac{MV}{m}$ ),  $K_f$ (eV), and impact site both along the cavity wall and with respect to the  $z$  axis. Since power is the product of current and voltage, the power dissipated by each electron is calculated:

$$P_i = \frac{I_i K_{fi}}{e}, \quad (5.4)$$

where  $I_i$  is the instantaneous current (Equation 2.35) of the  $i$ th electron for a given  $\beta_{FN}$  and  $\varphi$ , and  $K_{fi}$  is the final kinetic energy of the  $i$ th electron. The power can now be summed for a given distance along the cavity  $z$  axis. Figure 5.10 (a) shows trajectories of electrons field emitted in the  $\frac{4\pi}{6}$  mode from cell #1, and (b) shows



Z [cm]	KE [keV]
1	1674
17	708
26	1852
35	2092
43	1821
52	1447
53	1219

Figure 5.10: Electrons field emitted in the  $\frac{4\pi}{6}$  mode from cell #1,  $S_0 = 13.99$  cm,  $E_p = 25.0 \frac{\text{MV}}{\text{m}}$ , and  $E_{em} = 19.28 \frac{\text{MV}}{\text{m}}$ . Panel (a): 500 electron trajectories. Panel (b): Corresponding power spectrum with  $\beta_{FN} = 100$  for the current calculation. The table lists the electron maximum final kinetic energy for each peak.

the corresponding simulated power spectrum with  $\beta_{FN} = 100$ . At 0 cm, electron  $K_f$ 's are found as if they strike an end plate on the cavity. In reality, those electrons travel out of the cavity and can account for x-rays detected in the beam tube. Around 9 cm, electrons impact an iris but their total power is very low ( $10^{-11}$ ). The highest  $K_f$  electrons impact around 35 cm. Power is left unitless since the shape of the spectrum will be compared with the data. A table with electron maximum final kinetic energy is included in Figure 5.10.

As the number of field emitted electrons increases, the number of impact sites increases, thus changing the simulated power spectrum. The power also increases due to the increasing number of electrons. Figure 5.11 shows the simulated power spectra

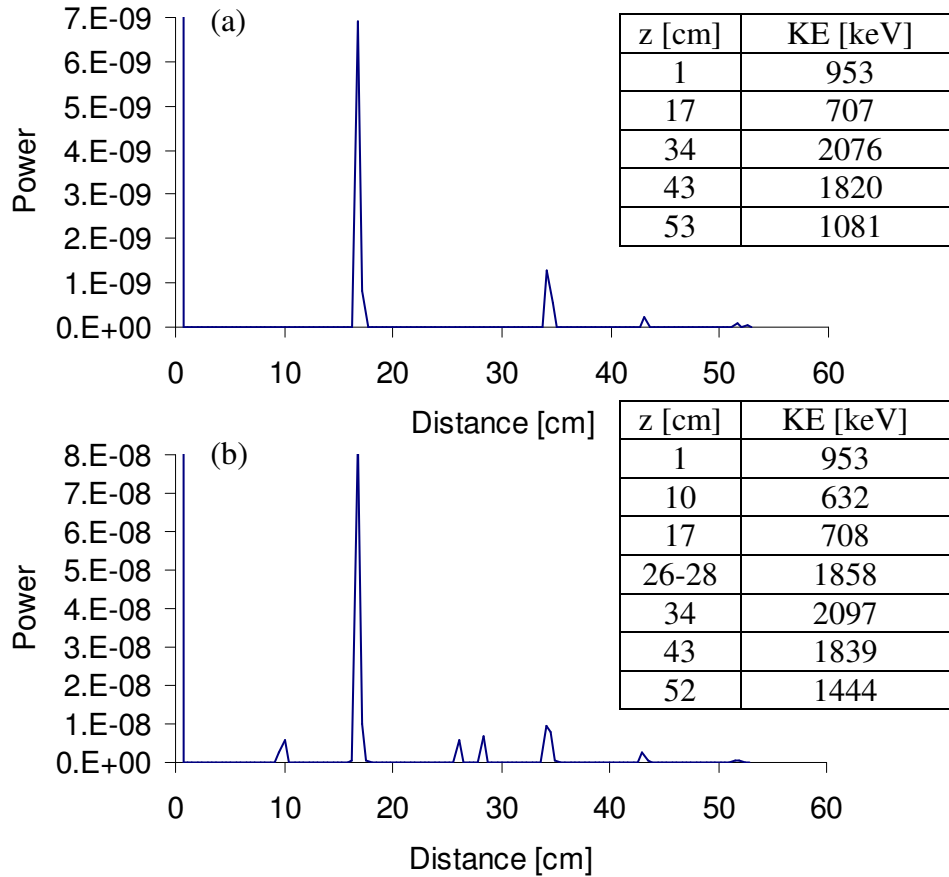


Figure 5.11: Simulated power spectra of electrons field emitted in the  $\frac{4\pi}{6}$  mode from cell #1,  $S_0 = 13.99$  cm,  $E_p = 25.0 \frac{\text{MV}}{\text{m}}$ , and  $E_{em} = 19.28 \frac{\text{MV}}{\text{m}}$ . Panel (a): 100 electron trajectories ( $\frac{\Delta\phi}{2\pi} = 0.005$ ). Panel (b): 1250 electron trajectories ( $\frac{\Delta\phi}{2\pi} = 0.0004$ ). The tables list the electron maximum final kinetic energy for each peak.

for the electron trajectories in Figure 5.10 but with the number of field emitted electrons increased from 100 to 1250 trajectories ( $\frac{\Delta\phi}{2\pi} = 0.005$  to 0.0004). Peaks in the simulated power spectrum emerge at 9, 26, and 28 cm. It was found that the shape of the simulated power spectrum for 1000 impacting electrons did not differ significantly from the power spectrum of 10,000 impacting electrons. Therefore, the simulated power spectra for 1000 field emitted electrons were used for comparison with the data power spectra.

Moving the field emitter location ( $S_0$ ) changed the electron trajectories (Figure 5.5), likewise, the simulated power spectrum changed. Figure 5.12 shows the

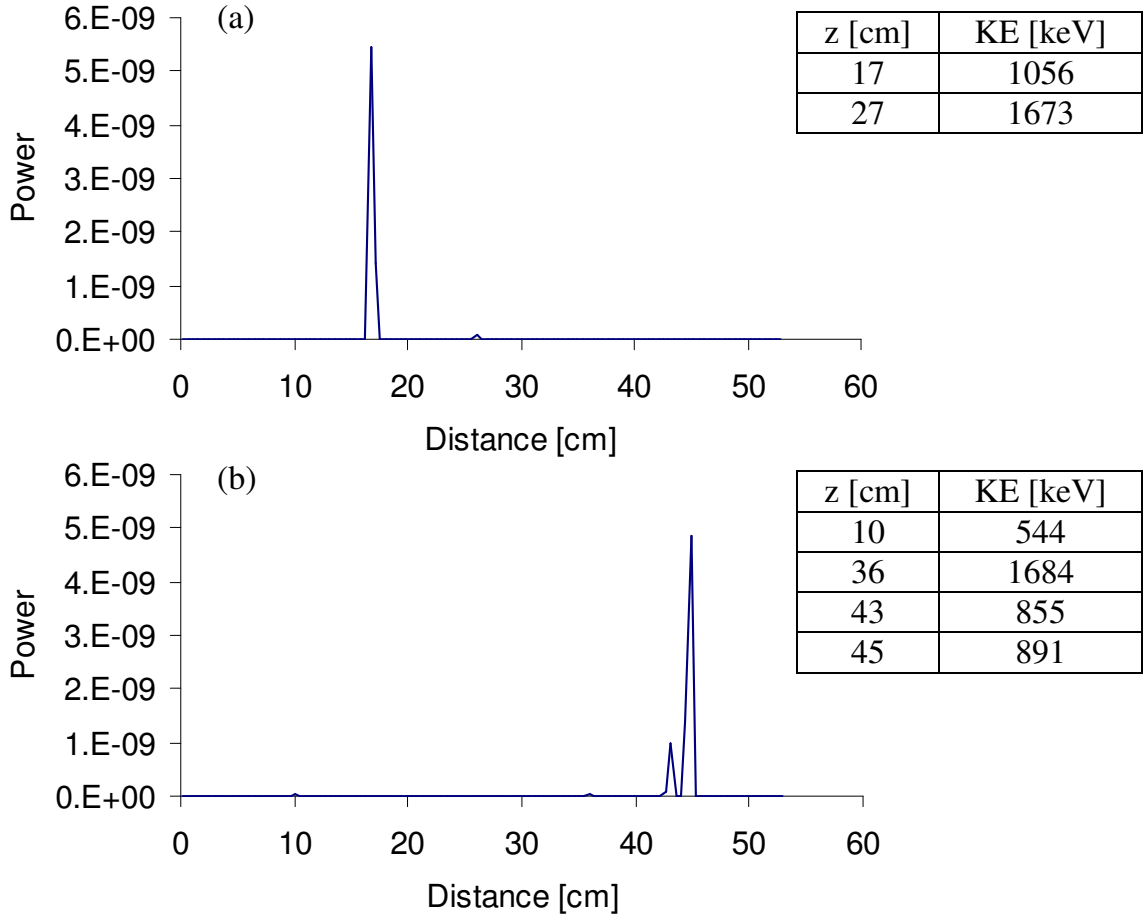


Figure 5.12:  $\pi$  mode simulated power spectra for different emitter sites  $E_p = 26.0 \frac{\text{MV}}{\text{m}}$ , and  $\frac{\Delta\phi}{2\pi} = 0.01$ . Panel (a): Field emitter in cell #2  $S_0 = -13.0$  cm, and  $E_{em} = 24.26 \frac{\text{MV}}{\text{m}}$ . Panel (b): Field emitter in cell #2  $S_0 = -13.6$  cm, and  $E_{em} = 24.41 \frac{\text{MV}}{\text{m}}$ . The tables list the electron maximum final kinetic energy for each peak.

simulated power spectra generated when S0 was moved by 0.6 cm within the same cell and with all other input parameters remaining the same. In some cases moving S0 by 0.001 cm significantly altered the simulated power spectrum.

Simulated power calculations depend upon current (Equation 5.4), current calculations depend upon  $E_{em}(t)$ , and  $E_{em}(t)$  calculations depend upon  $E_p$  (Equation 2.35). Figure 5.13 shows the change in a power spectrum when  $E_p$  is doubled (Figure 5.6). Doubling  $E_p$  increases the power by 10 orders of magnitude and greatly changes the shape of the spectrum, in most cases.

Identical to the electron trajectory example mapped in Figure 5.7, moving the field emitter to another cell in the  $\pi$  mode shifts the simulated power spectrum. Moving a field emitter to the opposite side of the cell reverses the spectrum (Figure 5.14).

It was also shown that moving a field emitter to a neighboring cell, in a mode other than the  $\pi$  mode (Figure 5.8), completely changes the electron trajectories and thus the simulated power spectrum. Figure 5.15 shows the simulated power spectrum for the  $\frac{4\pi}{6}$  mode when the field emitter site is moved to a neighboring cell. The low  $E_{em}$  in cell #2 (Figure 5.4) accounts for the simulated power spectrum of zero.

Changing modes, but keeping all input parameters identical, changed the electron trajectories (Figure 5.9) and the simulated power spectrum. Figure 5.16 shows the simulated power spectra for a field emitter in the same location for the  $\pi$ ,  $\frac{5\pi}{6}$ , and  $\frac{4\pi}{6}$  modes. When the emitter is near the tip of the iris ( $S0 = -14.49364$  cm) in cell #3,  $E_{em}$  is the greatest for the  $\pi$  mode, lower for the  $\frac{4\pi}{6}$  mode, and lowest for the  $\frac{5\pi}{6}$  mode. This is evidenced in the magnitude of the simulated power spectra for the three modes. Of course this would not be true for the simulated power spectra if the field emitter were on the opposite side of the cell (Figure 5.4).

Changing  $\beta_{FN}$  changes the instantaneous current and thus the power spectrum. Figure 5.17 shows the power spectrum when  $\beta_{FN}$  was increased from 100 to 300. Aside from the difference of 29 orders of magnitude between the two spectra, the overall shape of the spectrum changed. The peak at 28 cm went from equaling the

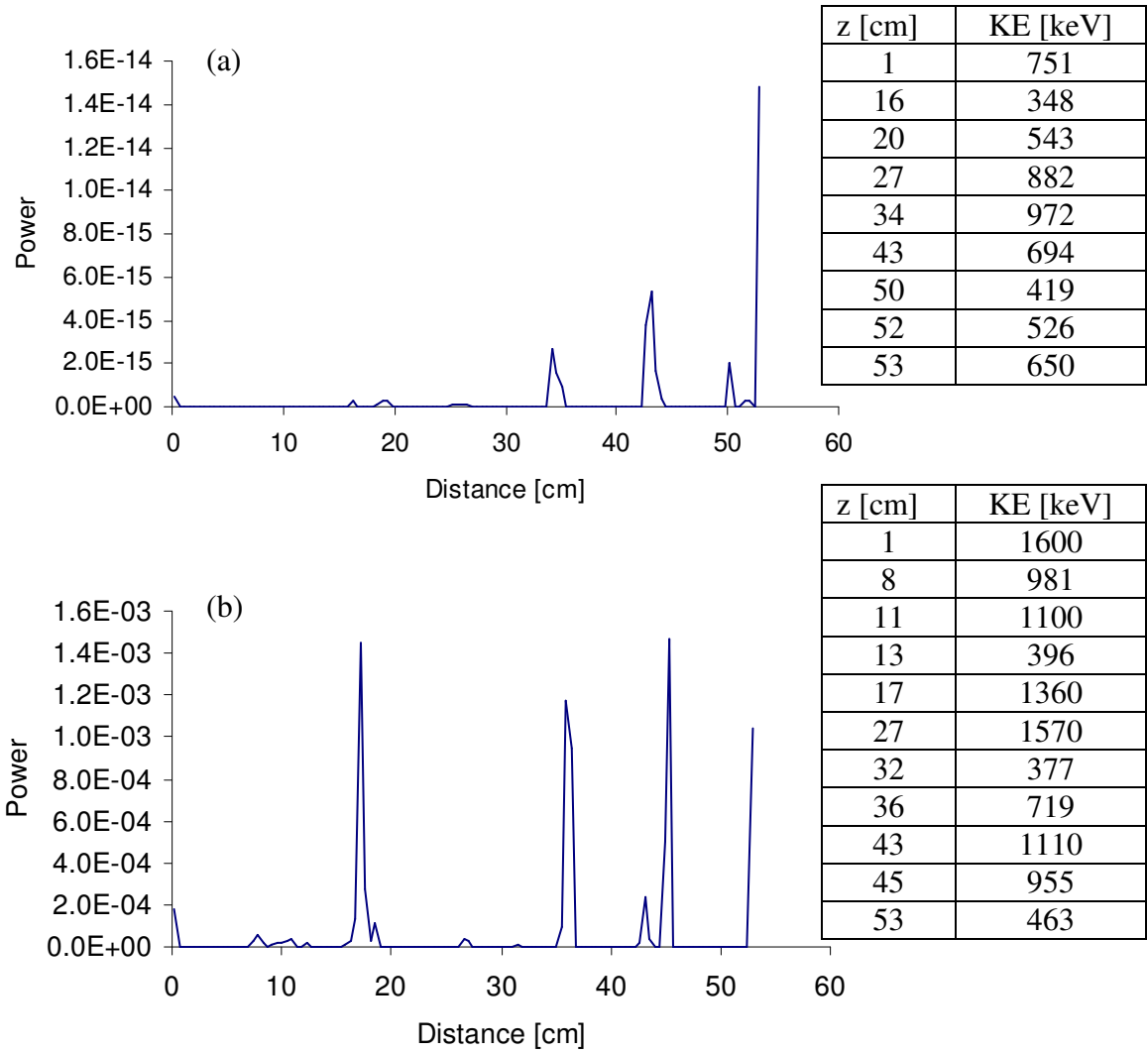


Figure 5.13:  $\pi$  mode simulated power spectra for doubling  $E_p$ . The emitter is in cell #2,  $S_0 = -13.2$  cm, and  $\frac{\Delta\phi}{2\pi} = 0.0005$ . Panel (a):  $E_p = 13.0 \frac{\text{MV}}{\text{m}}$ , and  $E_{em} = 12.33 \frac{\text{MV}}{\text{m}}$ . Panel (b):  $E_p = 26.0 \frac{\text{MV}}{\text{m}}$ , and  $E_{em} = 24.67 \frac{\text{MV}}{\text{m}}$ . The tables list the electron maximum final kinetic energy for each peak.

peak at 18 cm to half its value. A peak emerged at 44 cm that was absent from simulated power spectrum with  $\beta_{FN} = 100$ . The peak on the iris at 53 cm increased in relative height by a factor of 10. In many instances, changing  $\beta_{FN}$  by 1 allowed a better or worse fit of the simulated power spectrum to that of the data power spectrum.

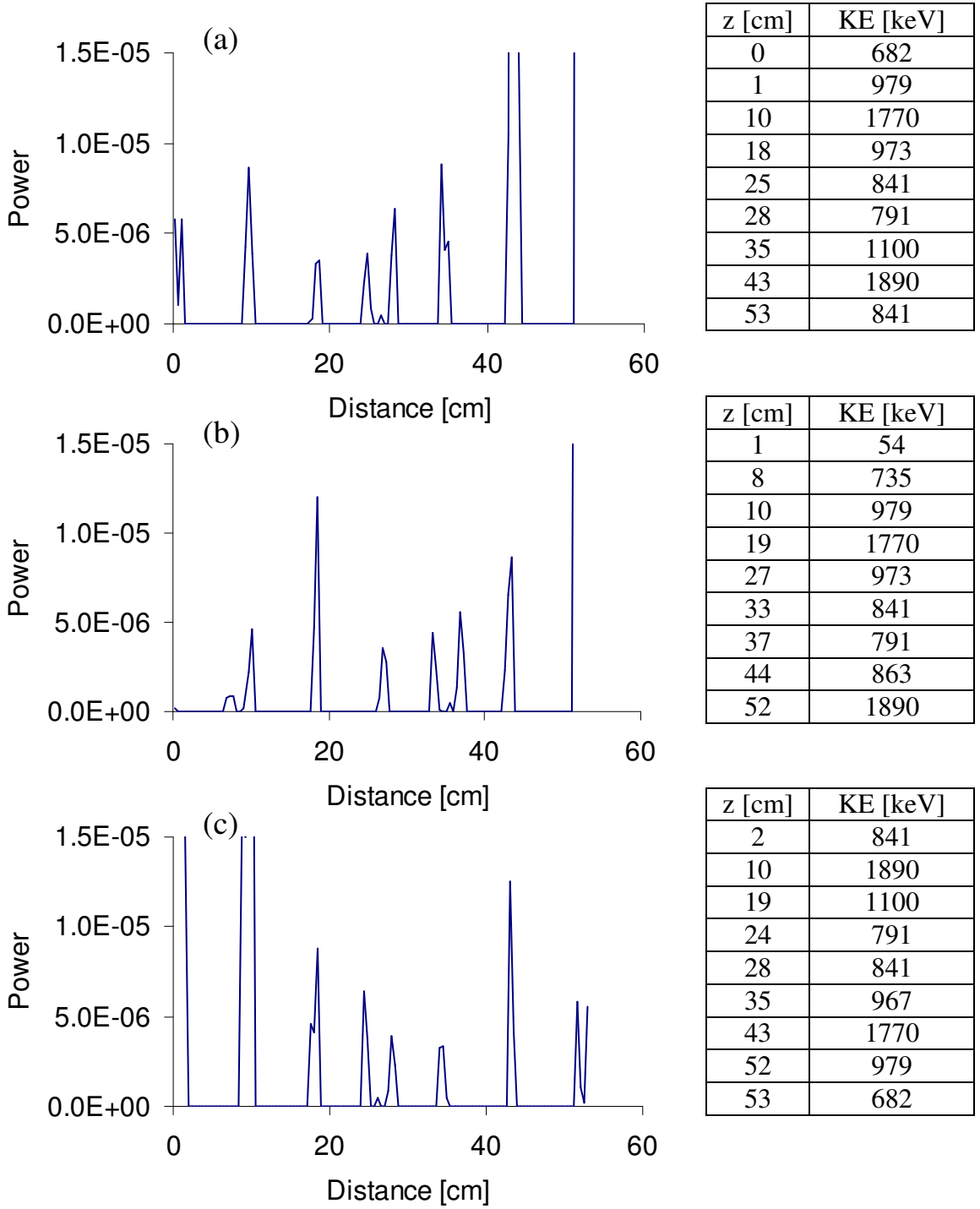


Figure 5.14:  $\pi$  mode simulated power spectra for  $S_0$  in a neighboring cell and on the opposite cell wall,  $E_p = 26.0 \frac{\text{MV}}{\text{m}}$ ,  $E_{em} = 24.67 \frac{\text{MV}}{\text{m}}$ ,  $K_f = 1.841 \text{ MeV}$ , and  $\frac{\Delta\phi}{2\pi} = 0.0005$ . Panel (a): Field emitter in cell #3,  $S_0 = -13.3 \text{ cm}$ . Panel (b): Field emitter in cell #4,  $S_0 = -13.3 \text{ cm}$ . Panel (c): Field emitter in cell #4,  $S_0 = +13.3 \text{ cm}$ . The tables list the electron maximum final kinetic energy for each peak.

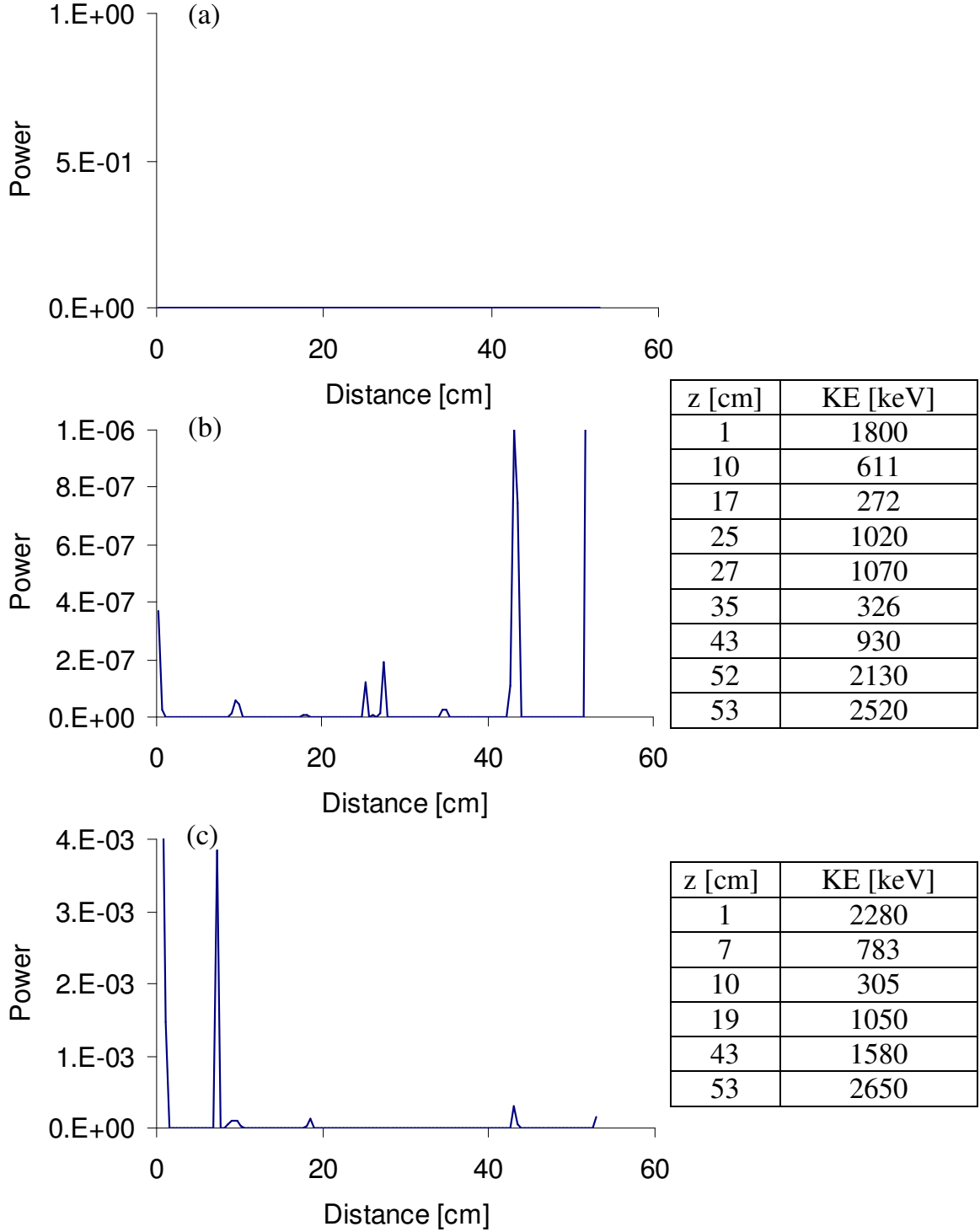


Figure 5.15:  $\pi$  mode simulated power spectra for S0 in different cells,  $E_p = 26.0 \frac{\text{MV}}{\text{m}}$  and  $\frac{\Delta\phi}{2\pi} = 0.0005$ . Panel (a): Field emitter in cell #2,  $S_0 = -13.8$  cm, and  $E_{em} = 4.014 \frac{\text{MV}}{\text{m}}$ . Panel (b): Field emitter in cell #3,  $S_0 = -13.8$  cm, and  $E_{em} = 21.11 \frac{\text{MV}}{\text{m}}$ . Panel (c): Field emitter in cell #3,  $S_0 = +13.8$  cm, and  $E_{em} = 25.15 \frac{\text{MV}}{\text{m}}$ . The tables list the electron maximum final kinetic energy for each peak.

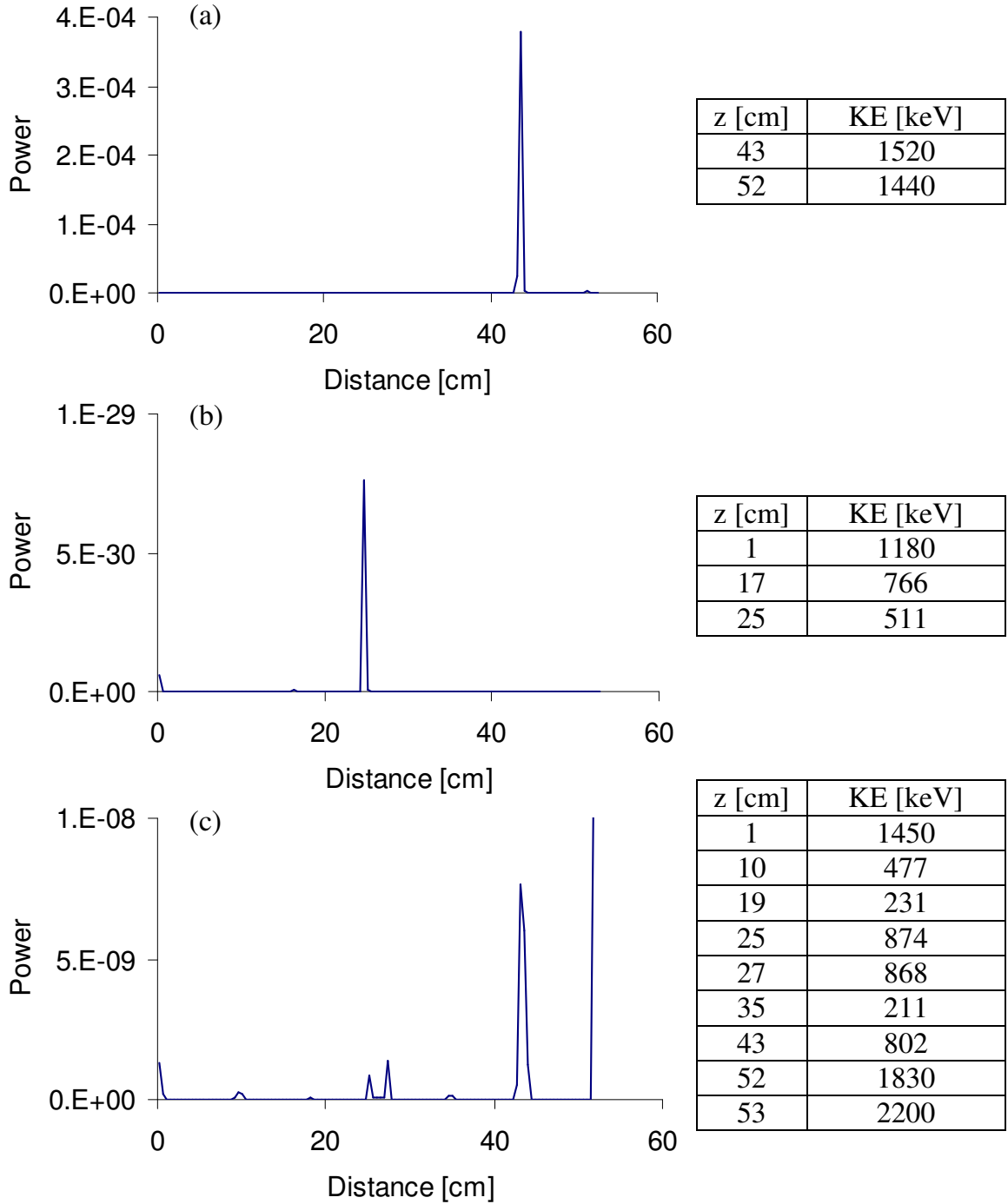


Figure 5.16: Simulated power spectra for a field emitter in cell #3,  $S_0 = -13.8$  cm,  $E_p = 26.0 \frac{\text{MV}}{\text{m}}$ , and  $\frac{\Delta\phi}{2\pi} = 0.0005$ . Panel (a):  $\pi$  mode, and  $E_{em} = 21.25 \frac{\text{MV}}{\text{m}}$ . Panel (b):  $\frac{5\pi}{6}$  mode, and  $E_{em} = 7.272 \frac{\text{MV}}{\text{m}}$ . Panel (c):  $\frac{4\pi}{6}$  mode, and  $E_{em} = 17.86 \frac{\text{MV}}{\text{m}}$ . The tables list the electron maximum final kinetic energy for each peak.

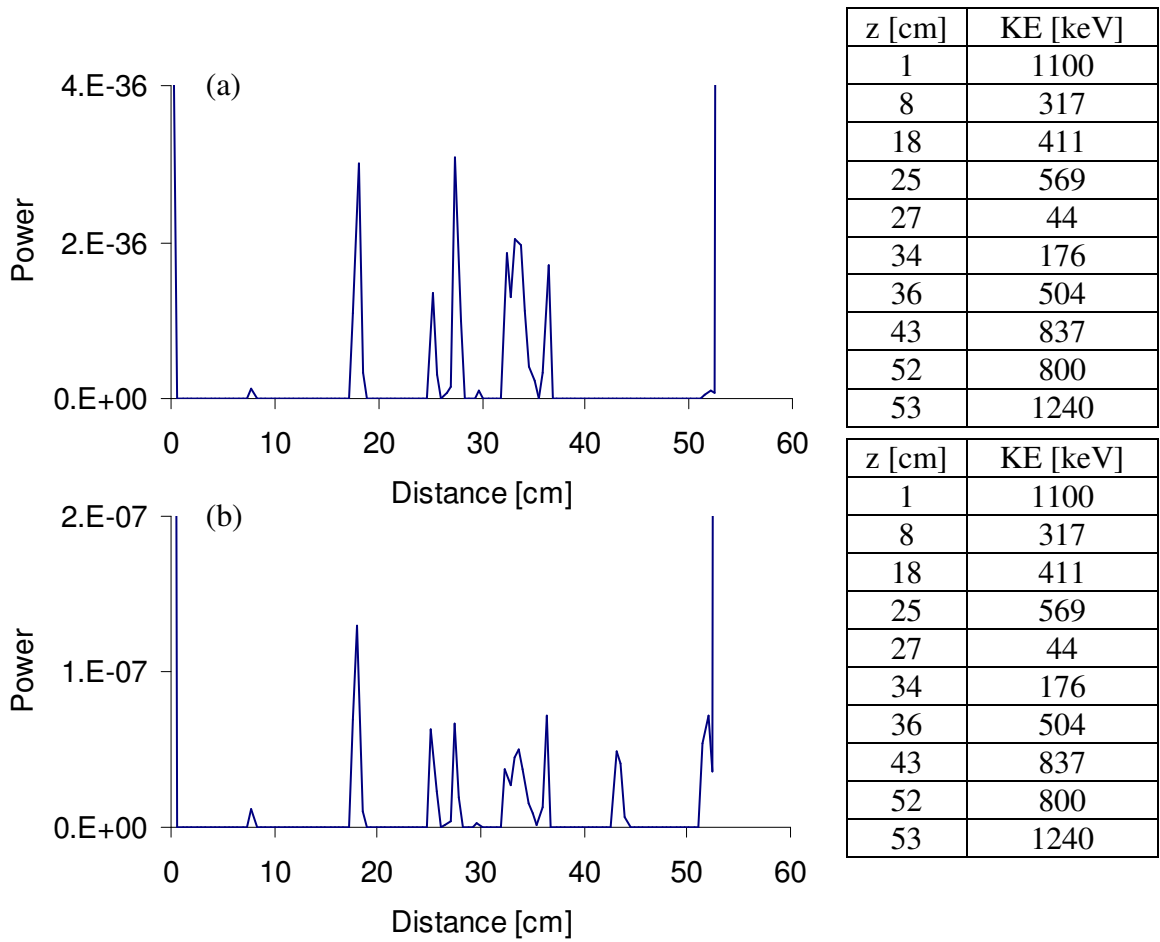


Figure 5.17: Field emitter in  $\frac{5\pi}{6}$  mode in cell #3,  $E_p = 26.0 \frac{\text{MV}}{\text{m}}$ , and  $E_{em} = 7.272 \frac{\text{MV}}{\text{m}}$ . Panel (a):  $\beta_{FN} = 100$ . Panel (b):  $\beta_{FN} = 300$ . The tables list the electron maximum final kinetic energy for each peak.

It was also possible to generate similar shaped simulated power spectra for different emitters. Figure 5.18 shows the simulated power spectra for the  $\pi$  mode with field emitters in different cells, located at a different S0, and with a different  $\beta_{FN}$ . Certainly the spectra are not identical, but the shape of either simulated power spectra would be a reasonable match to a data power spectrum. Thus when making a comparison with the data, the electron  $K_f$  for each peak should also be compared with the x-ray endpoint energy.

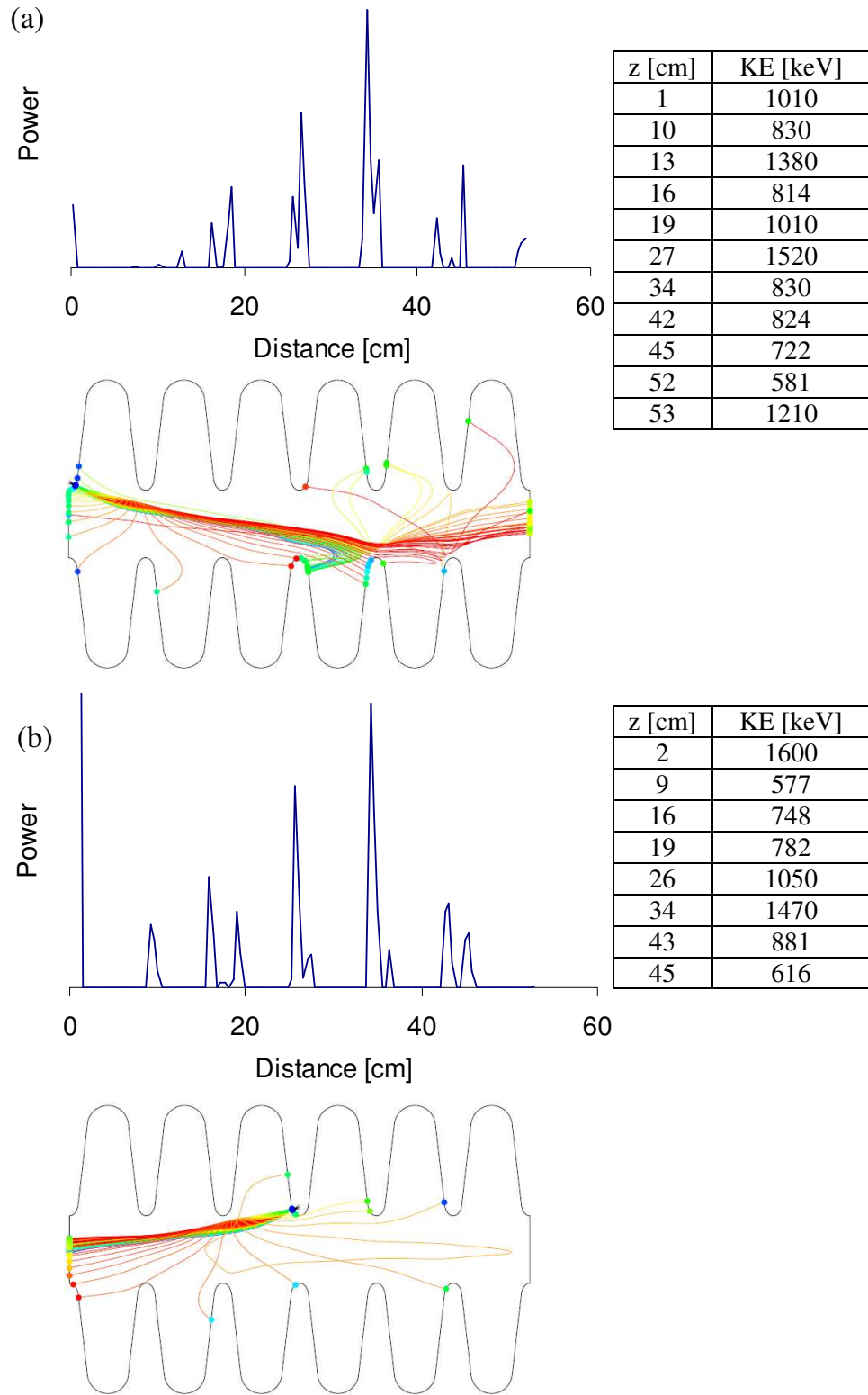


Figure 5.18: Two simulated power spectra for different emitters in the  $\pi$  mode. The spectra have the same general shape. Panel a): Field emitter located in cell #1,  $S_0 = -13.52$  cm,  $\beta_{FN} = 100$ , and  $E_p = 22.9 \frac{\text{MV}}{\text{m}}$ . Panel b): Field emitter located in cell #3,  $S_0 = 13.38$  cm,  $\beta_{FN} = 400$ , and  $E_p = 23.1 \frac{\text{MV}}{\text{m}}$ . The tables list the electron maximum final kinetic energy for each peak.

Finally, the simulated power spectrum can also be binned by  $K_f$ , similar to energy binning described in Subsection 4.2.2. Since power is proportional to  $K_f$ , the sum of the power bin is limited by choosing an electron final kinetic energy range. Figure 5.19 (a) shows the simulated power spectrum of Figure 5.18 (a) binned to an energy range of 500 keV to 2 MeV. The highest peak moved from 34 cm to 27 cm. Many of the electrons impacting around 34 cm have final kinetic energies below 500 keV and those impacting around 27 cm above 500 keV. Figure 5.19 (b) shows the impacting electron final kinetic energy as a function of distance along the cavity z axis.

The acquired data x-ray spectra includes information about the energy and number of x-rays entering the detector in two second intervals. Since power is defined as

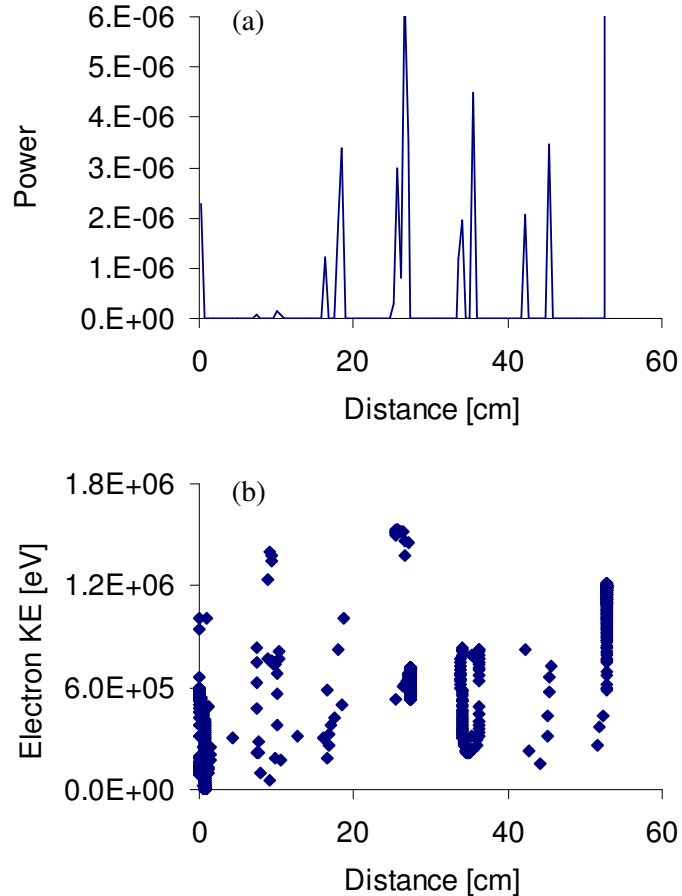


Figure 5.19: Panel (a): Binned simulated power spectrum of Figure 5.18 (a). Panel b): Impacting electron final kinetic energy.

energy per unit time, the x-ray spectra were converted to power spectra:

$$P_j = \sum_{i=1}^{233} \frac{E_i n_i}{2\text{sec}}, \quad (5.5)$$

where  $P_j$  is the power at distance interval  $j$ ,  $E_i$  is the energy of the acquired x-rays (233 energy intervals (subsection 4.1.1)), and  $n_i$  is the number of x-rays with energy  $E_i$ . The data x-ray spectrum becomes a data power spectrum for direct comparison with the simulated power spectrum. Figure 5.20 shows an x-ray spectrum acquired from cavity #2 operated in the  $\frac{5\pi}{6}$  mode (Figure 4.13 (c)) and the data power spectrum of the same scan. This method can be used for comparison of the data power spectra with the simulated power spectra.

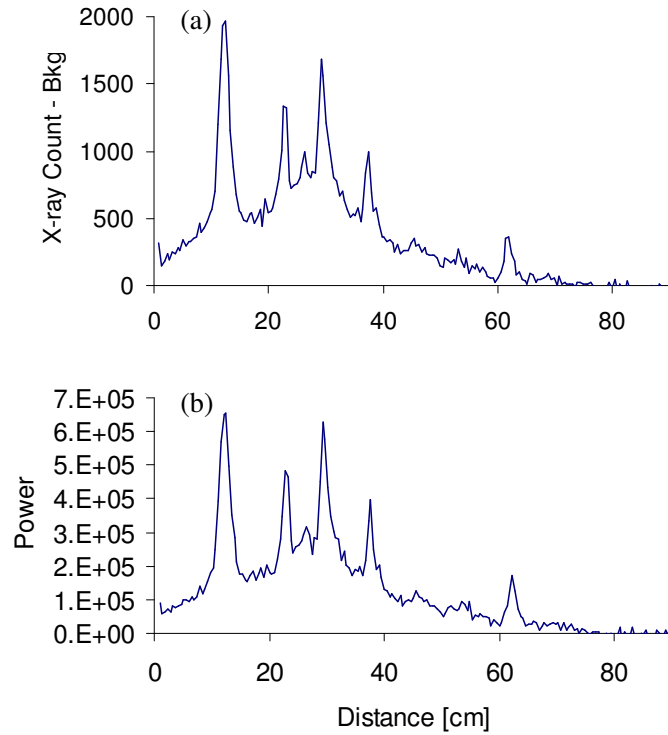


Figure 5.20: Cavity #2,  $\frac{5\pi}{6}$ , acquired data. Panel (a): X-ray flux spectrum. Panel (b): Power spectrum.

# Chapter 6

## Comparison Between Data and Simulations

Using the Multipacting/Field Emission Simulation, the simulated power spectra for field emitted electrons were examined until a reasonable match to the power spectra for the data was found. The task of finding a match of the simulation to the data meant defining field emitters along the cavity surface in 0.001 cm increments while varying  $\beta_{FN}$  and  $E_p$ . The number of power bins along the z axis was chosen to reflect the number of two-second time intervals (118) that the slit collimator was opposite the cavity as data were acquired. Once a reasonable match was found, the same field emitter parameters were applied as input to another mode to compare that simulated power spectrum with the data power spectrum.

### 6.1 Cavity #2

#### 6.1.1 $\frac{5\pi}{6}$ Mode

The  $\frac{5\pi}{6}$  mode had the highest x-ray flux (Figure 4.18) of the three modes of which data were acquired. Since a field emitter has the same  $S_0$ ,  $A_e$ , and  $\varphi$  for various modes, a field emitter in the  $\frac{5\pi}{6}$  mode is limited to regions where  $E_p \frac{5\pi}{6}$  was greatest, that is

along the irises of cells #1 and #6. Initially, current, and subsequently power, were calculated with nominal values of  $E_{p\frac{5\pi}{6}}$  ( $32 \frac{\text{MV}}{\text{m}}$ ) and  $\beta_{FN}$  (150) (Section 4.2). When a power spectrum resembling the data was found, closer evaluation of  $E_{p\frac{5\pi}{6}} \pm 5\%$  ( $30.4 \frac{\text{MV}}{\text{m}} \leq E_{p\frac{5\pi}{6}} \leq 33.6 \frac{\text{MV}}{\text{m}}$ ) and  $\beta_{FN}$  ( $120 \leq \beta_{FN} \leq 220$ ) (Section 4.2) were pursued until the best fit to the power spectrum was achieved.  $\beta_{FN}$  was measured for the  $\pi$  mode only, so a range was chosen between two previous cavity tests for use with the  $\frac{5\pi}{6}$  and  $\frac{4\pi}{6}$  modes.

Three power spectra resembling the data power spectrum were identified. The results of one emitter is presented in detail here, and the remaining two emitters are presented in Section 6.2.

The data power spectrum, generated from the x-ray flux spectrum presented in Figure 4.13 (c), is compared with the simulated power spectrum in Figure 6.1 (a). The field emitter is located in cell #1,  $S_0 = 14.025$  cm,  $E_{p\frac{5\pi}{6}} = 32.5 \frac{\text{MV}}{\text{m}}$ ,  $\beta_{FN} = 120$ , and  $A_e = 2.4 \times 10^{-9}$  cm<sup>2</sup>. Other than the peak at 22 cm, the simulated power spectrum is a reasonable match with the data. The high power, in the simulated power spectrum, at 21 and 74 cm are those electrons impacting the cell end caps of the simulated cavity. Figure 6.1 (b) shows 500 simulated electron trajectories and (c) shows the kinetic energy of 1000 impacting electrons. The x-ray endpoint energy of the acquired data and the kinetic energy of the impacting electrons are compared in Table 6.1

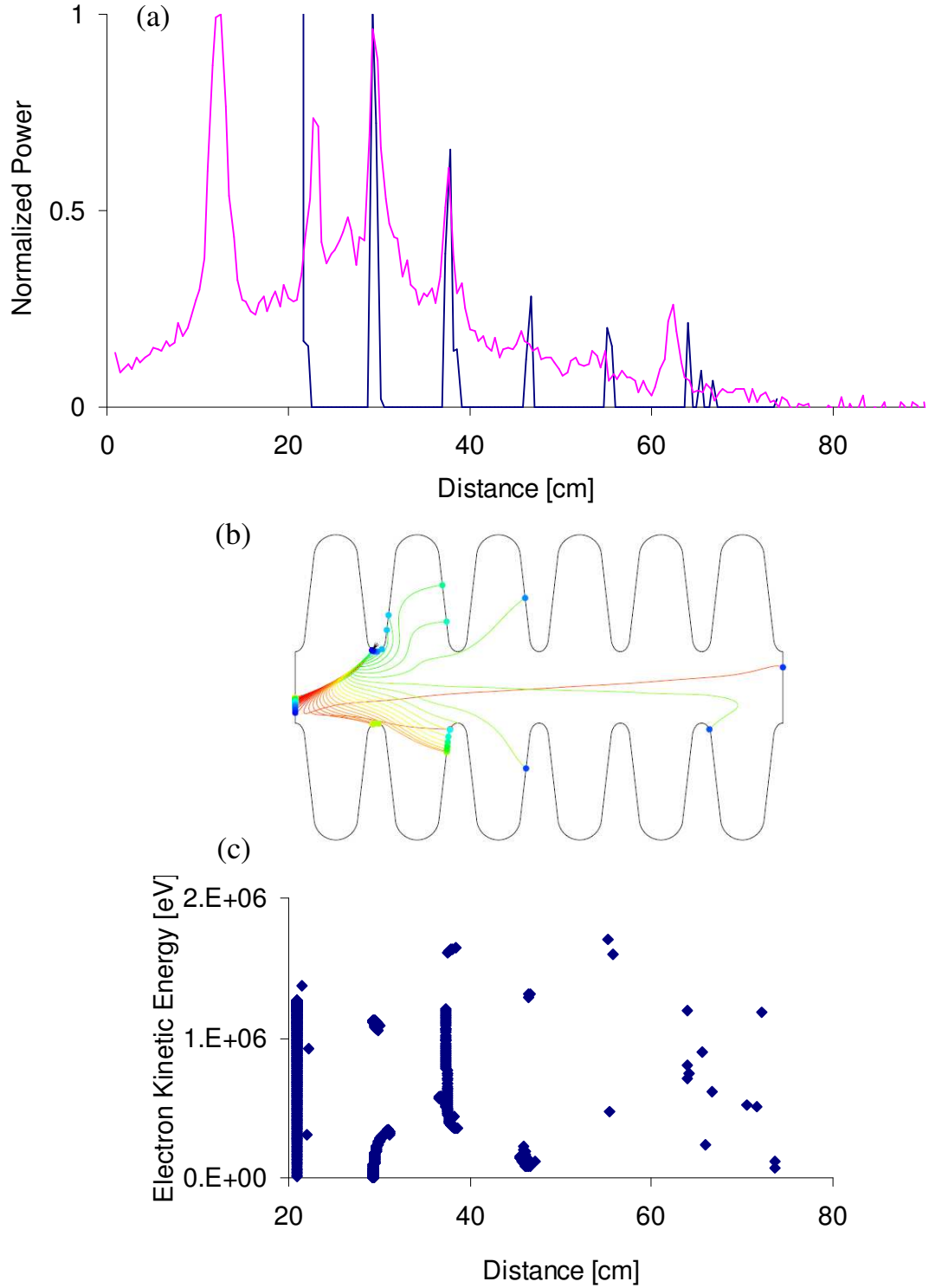


Figure 6.1: Cavity #2,  $\frac{5\pi}{6}$  mode, power spectrum. Panel (a): The black line represents the simulated power spectrum for a field emitter located in cell #1,  $S_0 = 14.025$  cm,  $E_{p\frac{5\pi}{6}} = 32.5 \frac{\text{MV}}{\text{m}}$ ,  $\beta_{FN} = 120$ , and  $A_e = 2.4 \times 10^{-9} \text{ cm}^2$ . The gray line represents the data power spectrum. Panel (b): 500 field emitted electron trajectories. Panel (c): Final kinetic energy of 1000 electrons.

Table 6.1: Cavity #2,  $\frac{5\pi}{6}$  mode, emitter in cell #1,  $S_0 = 14.025$  cm,  $E_{p\frac{5\pi}{6}} = 32.5 \frac{\text{MV}}{\text{m}}$ ,  $\beta_{FN} = 120$ , and  $A_e = 2.4 \times 10^{-9}$  cm<sup>2</sup>.

z [cm]	X-ray Endpoint Energy [keV]	Electron KE [keV]
12.3	755	1210
22.8	800	922
29.4	923	1110
37.4	874	1630
45.7	790	1310
53.9	752	1710
61.9	940	1200
73	—	1180

### 6.1.2 $\pi$ Mode

Using the same field emitter site and emitter parameters, the power spectrum and electron trajectories were generated for the  $\pi$  mode. The data power spectrum, from the x-ray flux spectrum presented in Figure 4.8 (c), is compared with the simulated power spectrum in Figure 6.2 (a). The  $\pi$  mode data power spectrum was normalized to the same scale as the  $\frac{5\pi}{6}$  mode data power spectrum. The  $\pi$  mode simulated power spectrum was normalized to the  $\frac{5\pi}{6}$  mode simulated power spectrum.  $E_{p\pi}$  was varied until the simulated power spectrum peak at 28 cm was just greater than the data. An  $E_{p\pi} = 22.5 \frac{\text{MV}}{\text{m}}$  was low compared to the measure range of  $24.1 \frac{\text{MV}}{\text{m}} \leq E_{p\pi} \leq 26.7 \frac{\text{MV}}{\text{m}}$ . The peaks at 37, 45, and 78 cm are absent from the simulated power spectrum. Figure 6.2 (b) shows 500 simulated electron trajectories and (c) shows the kinetic energy of 1000 impacting electrons. The x-ray endpoint energy of the acquired data and the kinetic energy of the impacting electrons are compared in Table 6.2.

The  $\pi$  mode power spectrum could be reproduced for this field emitter but with  $\beta_{FN} = 30$ . Not only was this an unreasonable value for  $\beta_{FN}$ , since it was determined that  $120 \leq \beta_{FN} \leq 220$ , but the  $\frac{5\pi}{6}$  mode power spectrum was no longer a match to the data power spectrum.

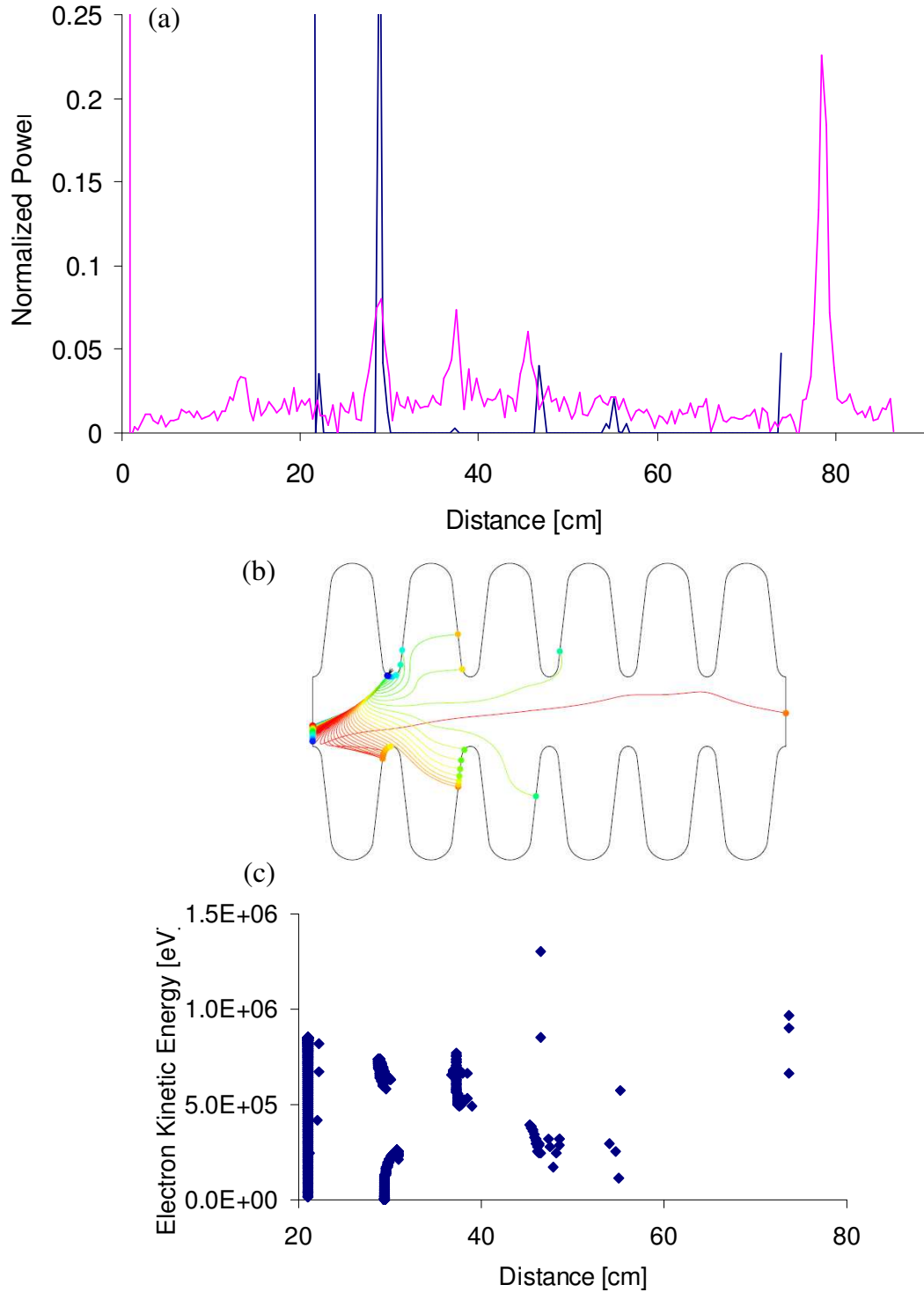


Figure 6.2: Cavity #2,  $\pi$  mode, power spectrum. Panel (a): The black line represents the simulated power spectrum for field a emitter located in cell #1,  $S_0 = 14.025$  cm,  $E_{p\pi} = 22.5 \frac{\text{MV}}{\text{m}}$ ,  $\beta_{FN} = 120$ , and  $A_e = 2.4 \times 10^{-9}$  cm<sup>2</sup>. The gray line represents the data power spectrum. Panel (b): 500 field emitted electron trajectories. Panel (c): Final kinetic energy of 1000 electrons.

Table 6.2: Cavity #2,  $\pi$  mode, emitter in cell #1,  $S0 = 14.025$  cm,  $E_{p\pi} = 22.5 \frac{\text{MV}}{\text{m}}$ ,  $\beta_{FN} = 120$ , and  $A_e = 2.4 \times 10^{-9}$  cm<sup>2</sup>.

z [cm]	X-ray Endpoint Energy [keV]	Electron KE [keV]
13.4	577	840
22	—	819
28.8	900	726
37.5	733	770
45.6	878	1310
55.3	—	576
78.6	1073	970

The emitter area,  $A_e$ , was determined by matching simulated values of the cavity dissipated power as a function of  $E_{p\pi}^2$  with the data (Figure 6.3). An emitter area of  $A_e = 2.4 \times 10^{-9}$  cm was used for the simulations.

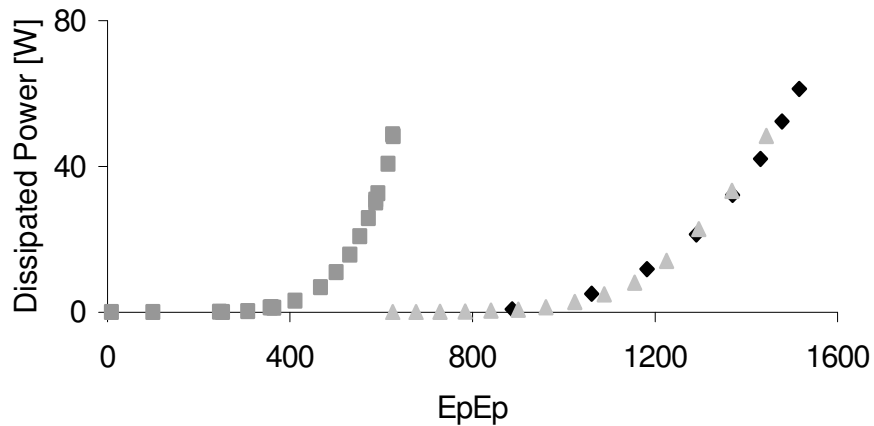


Figure 6.3: Cavity #2 Black diamonds - data acquired for the test just prior to this study. Medium-gray squares - data acquired for another cavity test. Light-gray triangles - simulated results for an emitter in cell #1,  $S0 = 14.025$  cm,  $\beta_{FN} = 120$ ,  $E_{p\pi} = 22.5 \frac{\text{MV}}{\text{m}}$ , and  $A_e = 2.4 \times 10^{-9}$  cm.

### 6.1.3 $\frac{4\pi}{6}$ Mode

Again, using the same field emitter site and emitter parameters, the power spectrum and electron trajectories were generated for the  $\frac{4\pi}{6}$  mode. The power spectrum, from the x-ray flux spectrum presented in Figure 4.16 (c), is compared with the simulated power spectrum in Figure 6.4 (a). The data and simulated power spectra were nor-

malized by the same method used for the  $\frac{5\pi}{6}$  and  $\pi$  modes. Figure 6.4 (b) shows the simulated electron trajectories. Figure 6.4 (c) shows the kinetic energy of the impacting electrons (1000). 1000 field emitted electrons were used to generate the simulated power spectrum.

For this field emitter site an  $E_{p\frac{4\pi}{6}} = 31.6 \frac{\text{MV}}{\text{m}}$  was needed to generate a power spectrum of a magnitude to match the data power spectrum ( $30.0 \frac{\text{MV}}{\text{m}} \leq E_{p\frac{4\pi}{6}} \leq 33.2 \frac{\text{MV}}{\text{m}}$ ). The x-ray endpoint energy of the acquired data and the kinetic energy of the impacting electrons are compared in Table 6.3

Binning of the data and simulated power spectra for the same emitter found in the  $\frac{5\pi}{6}$  mode was also tried, but the  $\pi$  and  $\frac{4\pi}{6}$  mode simulated power spectra still did not match the data power spectra. Another approach would be to locate a field emitter for the binned data power spectrum of the  $\frac{5\pi}{6}$  mode and then make comparisons with the other modes.

It is possible that multiple field emitters reside within the cavity. The other  $\frac{5\pi}{6}$  simulated power spectra, eliminated by comparison with the endpoint energy, would require multiple emitters as well in order to reproduce the data power spectra.

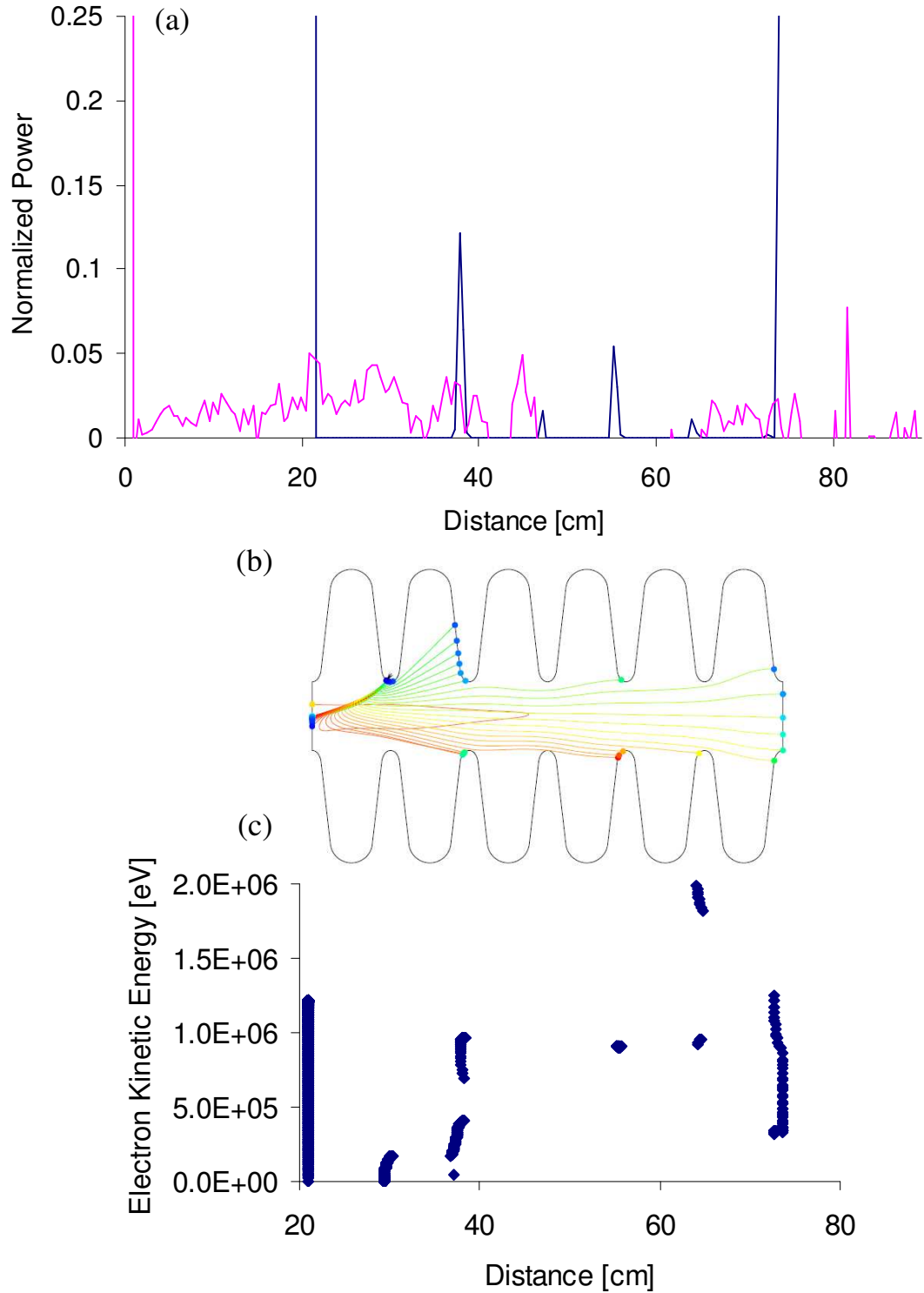


Figure 6.4: Cavity #2,  $\frac{4\pi}{6}$  mode, power spectrum. Panel (a): The black line represents the simulated power spectrum for field a emitter located in cell #1,  $S_0 = 14.025$  cm,  $E_p \frac{4\pi}{6} = 31.6 \frac{\text{MV}}{\text{m}}$ ,  $\beta_{FN} = 120$ , and  $A_e = 2.4 \times 10^{-9} \text{ cm}^2$ . The gray line represents the power spectrum for acquired data. Panel (b): 500 Field emitted electron trajectories. Panel (c): Final kinetic energy of 1000 electrons.

Table 6.3: Cavity #2,  $\frac{4\pi}{6}$  mode, emitter in cell #1,  $S_0 = 14.025$  cm,  $E_{p\frac{4\pi}{6}} = 31.6 \frac{\text{MV}}{\text{m}}$ ,  $\beta_{FN} = 120$ , and  $A_e = 2.4 \times 10^{-9}$  cm<sup>2</sup>.

z [cm]	X-ray Endpoint Energy [keV]	Electron KE [keV]
21.5	745	1220
28.5	670	1610
37.1	750	962
45.0	771	—
55	—	910
64	—	1990
70.1	669	1250

## 6.2 Additional Field Emitters Cavity #2

Two additional field emitters were likely candidates to match the data power spectrum of the  $\frac{5\pi}{6}$  mode. Both were located near an iris in cell #6. A plot comparing the data power spectrum with the simulated power spectrum for first field emitter,  $S_0 = 13.266$  cm, for all three modes is shown in Figure 6.5 . The x-ray endpoint energies and the electron kinetic energies are shown in Table 6.4. The emitter area was found using the method described in Section 6.1.2. The results of the second field emitter are shown in Figure 6.6 and Table 6.4. A decision as to which field emitter most closely matches the data cannot be made since  $\beta_{FN}$  is not known for each mode.

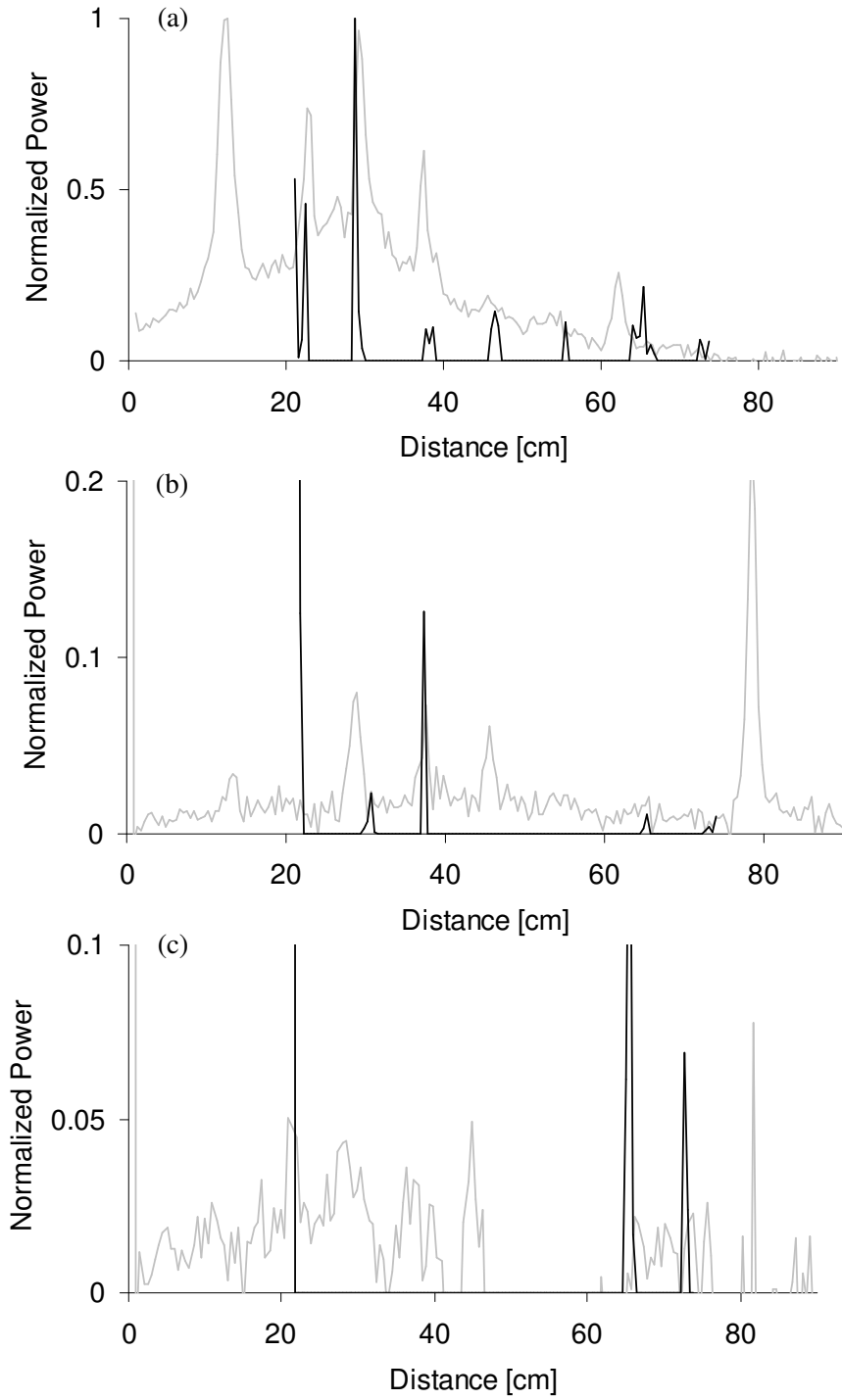


Figure 6.5: Cavity #2, cell #6,  $S_0 = 13.266$  cm,  $\beta_{FN} = 200$ , and  $A_e = 4 \times 10^{-12}$  cm<sup>2</sup>. Black line is the normalized simulated power spectrum and the gray line the normalized data power spectrum. Panel (a):  $\frac{5\pi}{6}$  mode,  $E_{p\frac{5\pi}{6}} = 32.0 \frac{\text{MV}}{\text{m}}$ . Panel (b):  $\pi$  mode,  $E_{p\pi} = 27.4 \frac{\text{MV}}{\text{m}}$ . Panel (c):  $\frac{4\pi}{6}$  mode,  $E_{p\frac{4\pi}{6}} = 31.6 \frac{\text{MV}}{\text{m}}$ .

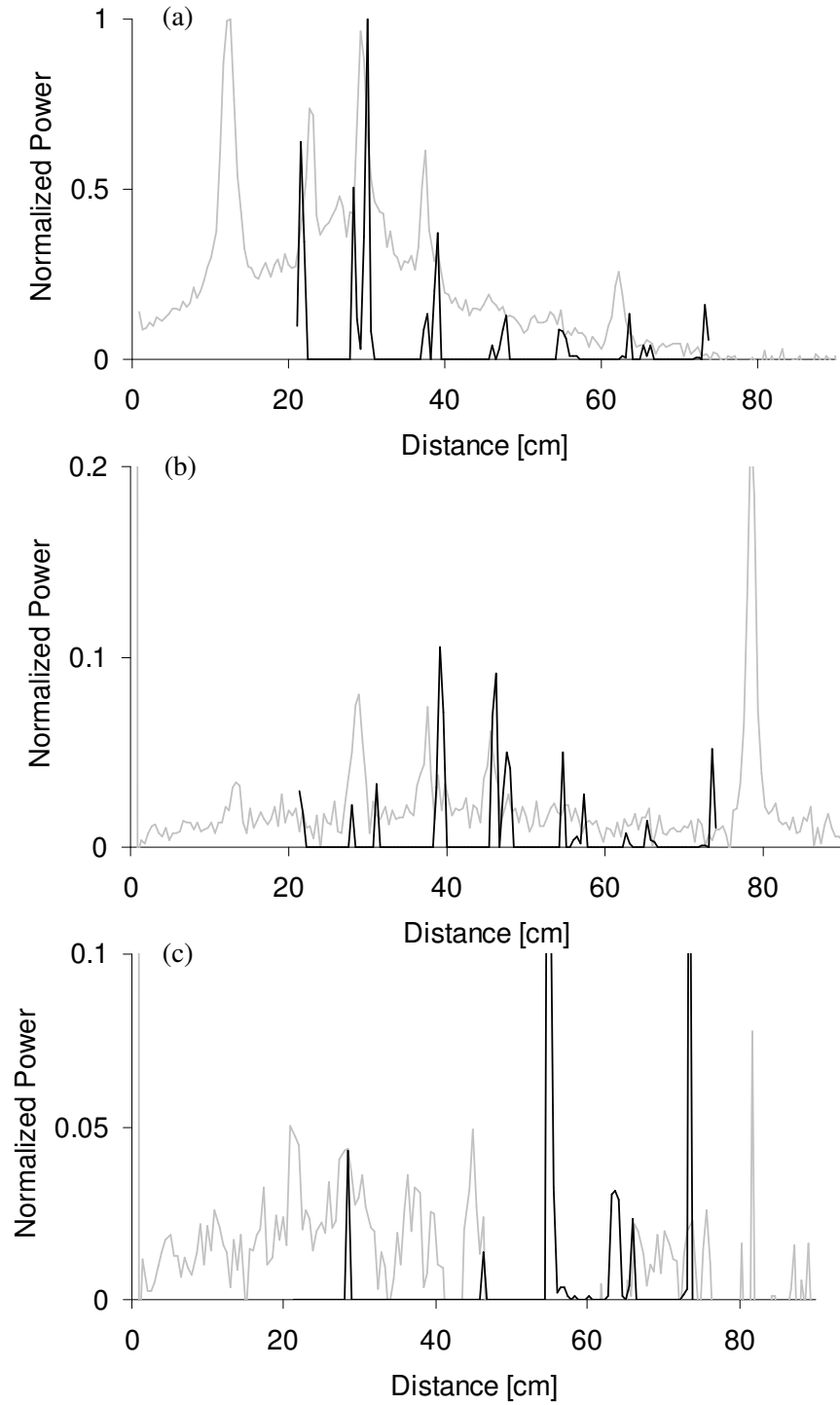


Figure 6.6: Cavity #2, cell #6,  $S_0 = 13.5$  cm,  $\beta_{FN} = 120$ , and  $A_e = 2.4 \times 10^{-9}$  cm<sup>2</sup>. Black line is the normalized simulated power spectrum and the gray line the normalized data power spectrum. Panel (a):  $\frac{5\pi}{6}$  mode,  $E_{p\frac{5\pi}{6}} = 33.0 \frac{\text{MV}}{\text{m}}$ . Panel (b):  $\pi$  mode,  $E_{p\pi} = 31.0 \frac{\text{MV}}{\text{m}}$ . Panel (c):  $\frac{4\pi}{6}$  mode,  $E_{p\frac{4\pi}{6}} = 31.5 \frac{\text{MV}}{\text{m}}$ .

Table 6.4: Cavity #2,  $\frac{5\pi}{6}$  mode, emitters in cell #6.

$\frac{5\pi}{6}$ Mode z [cm]	X-ray Endpoint Energy [keV]	Electron KE [keV] $S0 = 13.266$ cm	Electron KE [keV] $S0 = 13.5$ cm
12.3	755	855	354
22.8	800	1300	1240
29.4	923	1030	1980
37.4	874	1710	1890
45.7	790	1550	1530
53.9	752	1860	1890
61.9	940	1120	1170
73	—	1430	1050
$\pi$ Mode z [cm]	X-ray Endpoint Energy [keV]	Electron KE [keV] $S0 = 13.266$ cm	Electron KE [keV] $S0 = 13.5$ cm
13.4	577	1750	1860
22	—	93	—
28.8	900	1060	951
37.5	733	1110	1290
45.6	878	1690	2080
55.3	—	1140	1620
65.4	—	720	1450
78.6	1073	607	945
$\frac{4\pi}{6}$ Mode z [cm]	X-ray Endpoint Energy [keV]	Electron KE [keV] $S0 = 13.266$ cm	Electron KE [keV] $S0 = 13.5$ cm
21.5	745	3580	3580
28.5	670	—	1120
37.1	750	—	—
45.0	771	—	362
55.0	—	—	968
64.0	—	493	1180
70.1	669	1410	1930

## 6.3 Cavity #1

For cavity #1, the x-ray flux was greater for the  $\pi$  mode than the  $\frac{5\pi}{6}$  mode, indicating a higher  $E_{em}$ .  $E_{em}$  is higher for the  $\pi$  mode than the  $\frac{5\pi}{6}$  mode in cells #2, #3, #4, and #5 (Figure 5.4). A reasonable match to the data, satisfying both the  $\pi$  and the  $\frac{5\pi}{6}$  modes, could not be found in those cells. A field emitter displaying reasonable agreement with both modes, after binning both the data and the simulated power spectrum, was found in cell #1.

### 6.3.1 $\pi$ Mode

The nearest match of the simulated power spectrum to the data power spectrum, was for a field emitter located in cell #1,  $S_0 = -13.47$  cm, and  $E_{p\pi} = 23.1 \frac{\text{MV}}{\text{m}}$ . This choice for  $E_{p\pi}$  is low, but provided the best match with the data ( $23.8 \frac{\text{MV}}{\text{m}} \leq E_{p\pi} \leq 26.4 \frac{\text{MV}}{\text{m}}$ ). Energy binning was also employed for electrons with a minimum of  $K_f = 500$  keV. The simulated power spectrum was normalized to the peak at 42 cm. The power spectrum, binned for electrons with a minimum  $K_f = 500$  keV, is shown in Figure 6.7 (a), panel (b) shows all of the electron trajectories, and panel (c) the electron final kinetic energies. Table 6.5 shows a comparison of the x-ray endpoint energy with the electron kinetic energy.

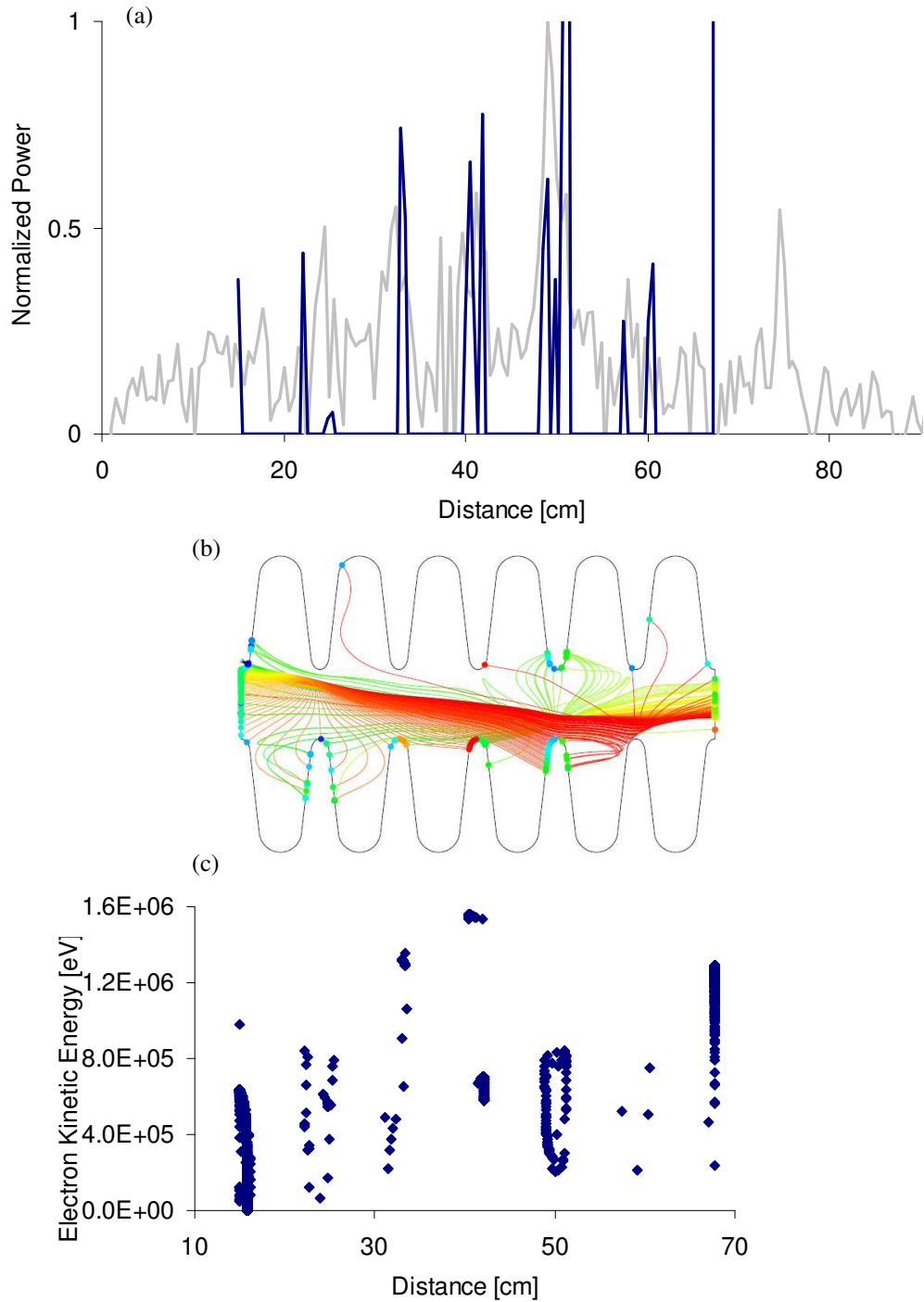


Figure 6.7: Cavity #1,  $\pi$  mode, power spectrum. Panel (a): The black line represents the simulated power spectrum for a field emitter located in cell #1,  $S_0 = -13.47$  cm,  $E_{p\pi} = 23.1 \frac{\text{MV}}{\text{m}}$ ,  $\beta_{FN} = 120$ , and  $A_e = 5.5 \times 10^{-10} \text{ cm}^2$ . The gray line represents the power spectrum for acquired data. Panel (b): 1000 field emitted electron trajectories. Panel (c): Final kinetic energy of 1000 electrons.

Table 6.5: Cavity #1,  $\pi$  mode, emitter in cell #1,  $S_0 = -13.47$  cm,  $E_{p\pi} = 23.1 \frac{\text{MV}}{\text{m}}$ ,  $\beta_{FN} = 120$ , and  $A_e = 5.5 \times 10^{-10}$  cm<sup>2</sup>.

z [cm]	KE [keV] Data	KE [keV] Simulation
14.4	913	976
23.5	846	838
31.5	926	1350
39.9	768	1450
47.8	1065	818
51	—	842
56.1	845	522
61.9	776	749
72.3	878	1280

The same method to determine the emitter area for cavity #2 was used for cavity #1 (Figure 6.8). An emitter area of  $A_e = 5.5 \times 10^{-10}$  cm<sup>2</sup> was used for the simulations.

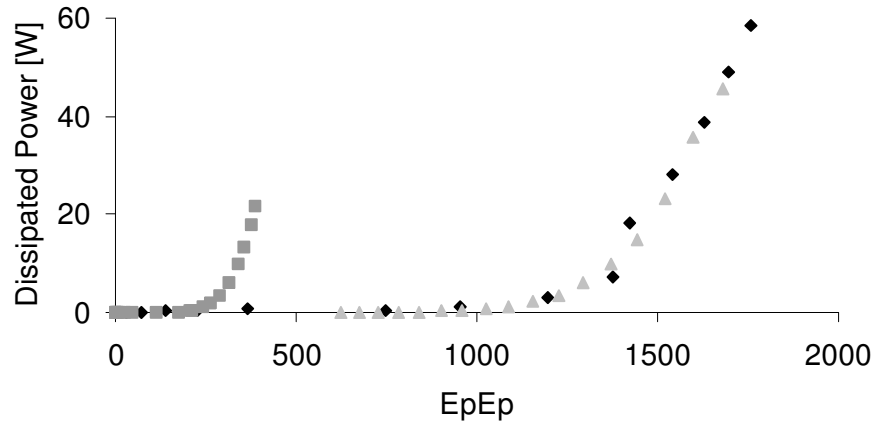


Figure 6.8: Cavity #2 Black diamonds - data acquired for the test just prior to this study. Medium-gray squares - data acquired for another cavity test. Light-gray triangles - simulated results for an emitter in cell #1,  $s_0 = -13.47$  cm,  $\beta_{FN} = 120$ ,  $E_{p\pi} = 23.1 \frac{\text{MV}}{\text{m}}$ , and  $A_e = 5.5 \times 10^{-10}$  cm.

### 6.3.2 $\frac{5\pi}{6}$ Mode

The input parameters, used for the  $\pi$  mode simulated power spectrum, were used as input for the  $\frac{5\pi}{6}$  mode.  $E_{p\frac{5\pi}{6}}$  was adjusted until the intensity of the power spectrum peak at 60 cm was in range of that of the  $\pi$  mode ( $E_{p\frac{5\pi}{6}} = 23.5 \frac{\text{MV}}{\text{m}}$ ). This value for

$E_p \frac{5\pi}{6}$  was lower than the measured range of  $29.6 \frac{\text{MV}}{\text{m}} \leq E_p \frac{5\pi}{6} \leq 32.8 \frac{\text{MV}}{\text{m}}$ . Energy binning was also utilized; electrons with a minimum  $K_f = 500 \text{ keV}$  for the simulated power spectrum and a minimum of 500 keV x-rays for the data power spectrum. The simulated and data power spectra are shown in Figure 6.9 (a), panel (b) shows all of the electron trajectories, and panel (c) the electron final kinetic energies. Table 6.6 shows a comparison of the x-ray endpoint energy with the electron kinetic energy.

A better fit of the simulation to the data may be to scale  $E_p \frac{5\pi}{6}$  with the peak at 68 cm and include a second field emitter to fill in the remainder of the spectrum. Peaks are emerging at 26 and 40 cm. It may be possible to adjust the input parameters more closely to find a more suitable match to the data.

It is reasonable for some simulated power peaks to be higher than data power peaks. The angle that electrons impact effects the data power spectrum since bremsstrahlung x-rays are anisotropic for 1 MeV electrons (Subsection 2.1.3). Some data power peaks could be lower by 30%. Calculation of the data power spectrum includes the lower energy of Compton scattered x-rays and x-rays with higher energies due to summation events (Subsection 4.2.2). The method of power binning may best be applied to individual peaks since the endpoint energy of x-rays varies for each peak.

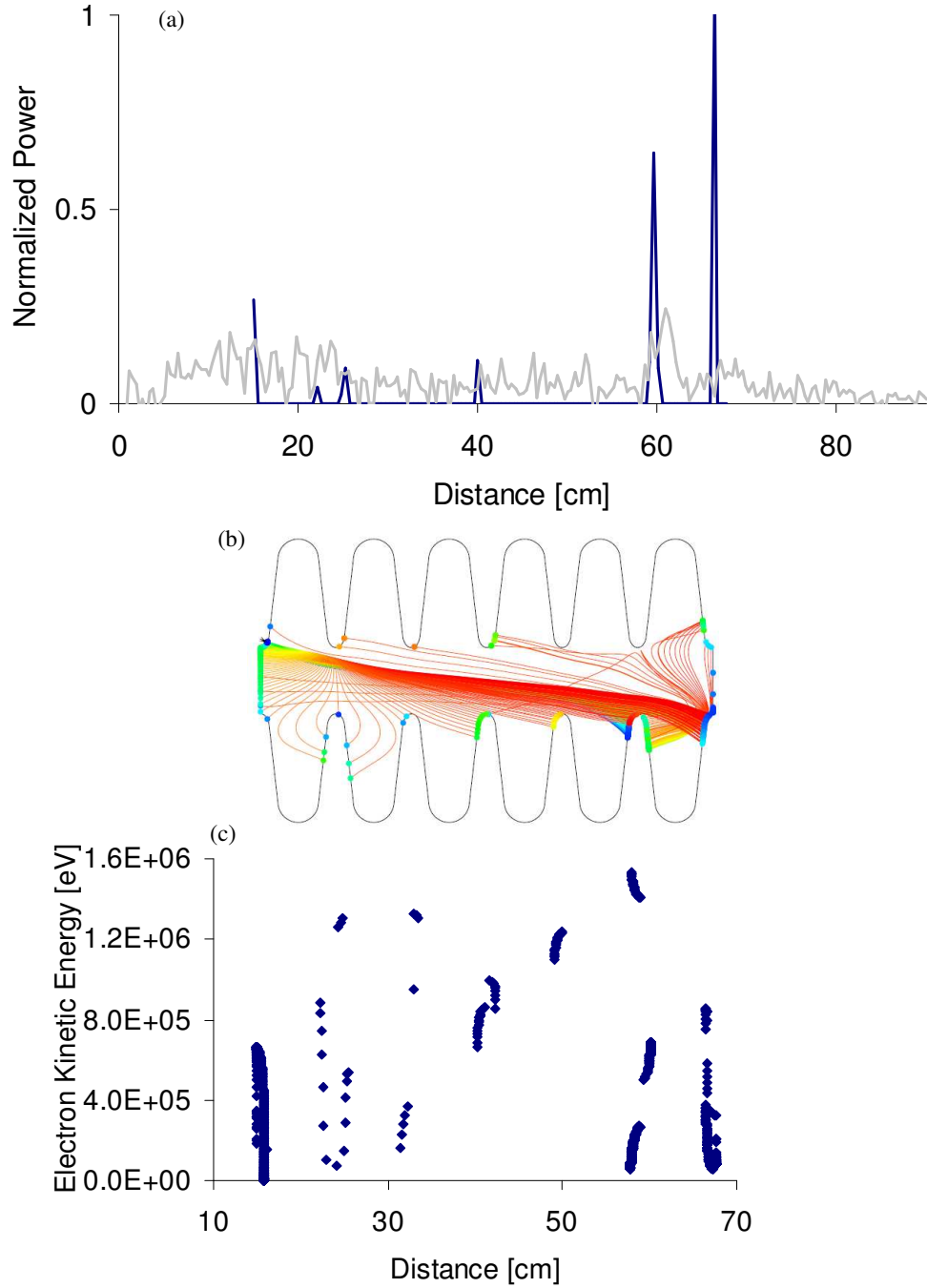


Figure 6.9: Cavity #1,  $\frac{5\pi}{6}$  mode, power spectrum. Panel (a): The black line represents the simulated power spectrum for a field emitter located in cell #1,  $S_0 = -13.47$  cm,  $E_p \frac{5\pi}{6} = 23.5 \frac{\text{MV}}{\text{m}}$ ,  $\beta_{FN} = 120$ , and  $A_e = 5.5 \times 10^{-10} \text{ cm}^2$ . The gray line represents the power spectrum for acquired data. Panel (b): 1000 field emitted electron trajectories. Panel (c): Final kinetic energy of 1000 electrons.

Table 6.6: Cavity #1,  $\frac{5\pi}{6}$  mode, emitter in cell #1,  $S_0 = -13.47$  cm,  $E_p \frac{5\pi}{6} = 23.5 \frac{\text{MV}}{\text{m}}$ ,  $\beta_{FN} = 120$ , and  $A_e = 5.5 \times 10^{-10} \text{ cm}^2$ .

z [cm]	KE [keV] Data	KE [keV] Simulation
15.1	556	658
22	733	887
26	—	1310
29.5	652	—
33.5	736	—
43.9	554	998
52.2	605	—
61.1	859	1540
68.8	937	850

# Chapter 7

## Discussion and Conclusion

### 7.1 Summary

This study examined a new method for locating defects in SRF cavities in operating accelerators and during the manufacturing of cavities. Two  $\beta = 0.47$  805 MHz six-cell cavities, encapsulated in a cryostat, were tested. An x-ray image was acquired for each mode tested for each cavity. A particle tracking code was used to determine a defect site. Operation of the cavities in other modes verified the location of the defect.

In an operating accelerator, contaminants could enter the cavity through vacuum system leaks or while cavities are vented for maintenance. Cavity defects may occur during the manufacturing process, and may result from improper clean room procedures, defective dies used to form the cavities, or impurities in the material.

Cavity defects enhance the surface electric field causing electrons to leave the surface or are field emitted. Field emitted electrons are accelerated by electric fields within the cavity and guided by the magnetic fields. The electrons strike the inner cavity walls or adjoining structures and generate bremsstrahlung x-rays, dissipate power, and create heat. The power dissipation degrades cavity performance by lowering the cavity  $Q$ .

The x-rays travel through the surrounding cryostat materials with Compton scat-

tering as the most probable interaction. There is a 25% probability that 1 MeV x-rays will have no interaction with the cryostat materials. A slit collimated NaI detector shielded with lead scans along the side of the cryostat, recording the number and energy of x-rays entering the detector in two second intervals. The flux of x-rays traveling through the slit and entering the detector is highest when the slit is opposite the x-ray source. There is a finite probability that x-rays may travel through the lead shielding and enter the detector. Data were acquired with the slit of the collimator open and closed so x-rays traveling through the lead shielding could be subtracted from those entering through the slit. To reduce the number of Compton scattered x-rays from the data, energy binning and subsequently power binning were employed.

The x-ray endpoint energy is deduced from the x-ray spectrum. The endpoint energy infers the highest final kinetic energy of the impacting electrons. This energy is used as a comparison with the particle tracking code.

Multiple cell cavities can be operated in different modes of excitation. The accelerating electric field within a cavity, operated in a mode other than the accelerating or  $\pi$  mode, is not symmetric within a cell or from cell to cell. The field emitted electrons impact at different sites and thus produce a different x-ray spectrum. In this study, it was demonstrated that electron trajectories and thus x-ray spectra are dependent upon the mode of operation.

The Multipacting/Field Emission Simulation was used as the particle tracking code. The code was modified to perform for other modes of operation. Input parameters for the code were estimated from previous cavity tests. The code generated an output that could be used to calculate power dissipated in the cavity walls. Since the simulation does not account for Compton scattered x-rays, the power was binned. The kinetic energy of the impacting electrons was also compared to the endpoint energy of the x-ray data.

A reasonable single emitter was found for cavity #1 operated in the  $\pi$  mode. This was verified by the simulated power spectrum for the  $\frac{5\pi}{6}$  mode. A single emitter for

cavity #2 was not confirmed. Another approach would be to start with the binned power spectrum when comparing the simulation with the data. The same binning could then be used as input for the other modes. There exists the possibility that the cavities have multiple emitters. Once either the defective cavity or specific defect site is identified, the cavity can be subjected to high power pulsed processing or helium processing to effectively eliminate or burn off the emitter.

For this study a range of  $\beta_{FN}$  values were inferred from previous tests of the  $\pi$  mode. The simulated power is proportional to current. The calculation of current is dependent up the measured quantities of  $E_p$  and  $\beta_{FN}$ .  $E_p$  values were determined from the acquired data, but not  $\beta_{FN}$ . A more accurate calculation of the simulated power would require the measurement of  $\beta_{FN}$  for each mode.

## 7.2 Previous Work

Area radiation monitoring equipment is a good indicator of x-ray exposure ( $\left[\frac{\text{R}}{\text{hr}}\right]$ ) but x-ray energy cannot be inferred from the measurement. X-ray energy is needed for comparison with the particle tracking code results. Area radiation monitoring equipment is also capable of distinguishing between areas of high and low x-ray exposure, but is incapable of pinpointing an x-ray source. X-ray source location must be accurate to some degree in order to determine the location of impacting electrons, also for comparison with the particle tracking code results.

The method of locating cavity defects developed in this study has an advantage over area radiation monitoring equipment because a NaI detector is used for measurement of x-ray energy. Slit collimation of the detector provides the means of locating x-ray sources to within the slit spatial resolution. Knowing the x-ray source location, or electron impact location, a comparison is made with the results of the particle tracking code to determine the electron source, or defect.

Extensive studies have been performed to locate cavity defects using thermometry.

Resistors are arranged on the entire outer cavity surface. A change in resistance signifies a change in temperature, indicating a region of electron impacts. Energy of the impacting electrons is inferred from the temperature change. A particle tracking code is used to locate the defect. Defects are verified by disassembling the cavity and viewing the region with a scanning electron microscope. This method is cost and labor intensive but has been proven successful for locating cavity defects. This method is not practical for operating accelerators where the cavities are sealed in cryostats and not accessible.

The method of locating cavity defects developed in this study has an advantage over thermometry in that it can be used on operating accelerators. Cavity defects are verified by operating the cavity in different modes of excitation. This noninvasive method for verifying cavity defects is simpler and less costly than thermometry.

### **7.3 Future Work**

This work can be expanded upon with development of a gamma camera to take a snapshot of the x-ray image. Not only could data be acquired more quickly, but the gamma camera could be positioned to acquire x-ray spectra in more than one dimension. Other dimensions would provide azimuthal defect location. Tomographic techniques could be used for image reconstruction. The method of locating cavity defects presented here could also be used on a liner accelerator in operation.

# Appendix A

## Electromagnetic Fields

### A.1 Fields Within a Rectangular Waveguide

The derivation of fields within a rectangular waveguide begins with Maxwell's equations:

$$\begin{aligned} \text{(i)} \quad \vec{\nabla} \cdot \vec{E} &= \frac{\rho}{\epsilon_0} & \text{(ii)} \quad \vec{\nabla} \times \vec{E} &= -\frac{\partial \vec{B}}{\partial t} \\ \text{(iii)} \quad \vec{\nabla} \cdot \vec{B} &= 0 & \text{(iv)} \quad \vec{\nabla} \times \vec{B} &= \mu_0 \vec{J} + \frac{1}{c^2} \frac{\partial \vec{E}}{\partial t}. \end{aligned}$$

In a region free of charge, or free of current, Maxwell's equations become:

$$\begin{aligned} \text{(i)} \quad \vec{\nabla} \cdot \vec{E} &= 0 & \text{(ii)} \quad \vec{\nabla} \times \vec{E} &= -\frac{\partial \vec{B}}{\partial t} \\ \text{(iii)} \quad \vec{\nabla} \cdot \vec{B} &= 0 & \text{(iv)} \quad \vec{\nabla} \times \vec{B} &= \frac{1}{c^2} \frac{\partial \vec{E}}{\partial t}. \end{aligned}$$

The wave equation, used for solving the fields, is derived by taking the curl of (ii):

$$\vec{\nabla} \times (\vec{\nabla} \times \vec{E}) = \vec{\nabla}(\vec{\nabla} \cdot \vec{E}) - \vec{\nabla}^2 \vec{E} = \vec{\nabla} \times \left( -\frac{\partial \vec{B}}{\partial t} \right) = -\frac{\partial}{\partial t}(\vec{\nabla} \times \vec{B}) = -\frac{1}{c^2} \frac{\partial^2 \vec{E}}{\partial t^2}$$

so that,

$$\left( \nabla^2 - \frac{1}{c^2} \frac{\partial^2}{\partial t^2} \right) \vec{E} = 0. \quad (\text{A.1})$$

A similar derivation by taking the curl of (iv) would yield

$$\left( \nabla^2 - \frac{1}{c^2} \frac{\partial^2}{\partial t^2} \right) \vec{B} = 0. \quad (\text{A.2})$$

Equations A.1 and A.2 have a solution for the z or longitudinal direction in Cartesian coordinates:

$$E(x, y, z, t) = E(x, y) e^{\pm i k_z z - i \omega t} \quad (\text{A.3})$$

and

$$B(x, y, z, t) = B(x, y) e^{\pm i k_z z - i \omega t}, \quad (\text{A.4})$$

where  $k_z$  is the propagation constant or wave number in the z direction,  $k_z = \frac{2\pi}{\lambda}$ ,  $\omega$  the angular frequency,  $\omega = 2\pi\nu = kv$ ,  $\nu$  the frequency, and  $v$  the velocity. The sign of k depends on the wave direction. Substituting Equations A.3 and A.4 into Equations A.1 and A.2 respectively:

$$\nabla^2 E = -\frac{\omega^2}{c^2} E = -k_z^2 E \text{ and } \nabla^2 B = -\frac{\omega^2}{c^2} B = -k_z^2 B.$$

From Maxwell's equations and Equations A.3 and A.4 respectively [31]:

$$\vec{\nabla} \times \vec{E} = -\frac{\partial \vec{B}}{\partial t} = i\omega \vec{B}, \quad (\text{A.5})$$

$$\vec{\nabla} \times \vec{B} = \frac{1}{c^2} \frac{\partial \vec{E}}{\partial t} = -\frac{i\omega}{c^2} \vec{E}. \quad (\text{A.6})$$

The Laplacian operator,

$$\nabla^2 E = \frac{\partial^2 E}{\partial x^2} + \frac{\partial^2 E}{\partial y^2} + \frac{\partial^2 E}{\partial z^2},$$

can be separated into two parts

$$\nabla^2 E = \nabla_T^2 E + \frac{\partial^2 E}{\partial z^2},$$

where T implies the tranverse plane and  $\frac{\partial^2}{\partial z^2}$  the derivatives in the longitudinal direction:

$$\nabla_T^2 E = \nabla^2 E - \frac{\partial^2 E}{\partial z^2} = - \left( \frac{\omega^2}{c^2} - k_z^2 \right) E, \quad (\text{A.7})$$

$$\nabla_T^2 B = \nabla^2 B - \frac{\partial^2 B}{\partial z^2} = - \left( \frac{\omega^2}{c^2} - k_z^2 \right) B. \quad (\text{A.8})$$

Let  $\frac{\omega^2}{c^2} - k_z^2 = k_c^2$  where  $k_c$  is the cutoff frequency,  $k_c = \sqrt{k^2 - k_z^2}$ . For  $k > k_z$  propagation of the mode occurs, but for  $k < k_z$  the modes are called cutoff, or evanescent and decay exponentially along the waveguide [32].

Two differential equations, A.7 and A.8, must be satisfied in dielectric regions or regions free of charge, as in this case. First the components of the fields are found using Maxwell's equations, Equations A.5 and A.6, and Equations A.3 and A.4:

$$i\omega B_x = \frac{\partial E_z}{\partial y} - \frac{\partial E_y}{\partial z} = \frac{\partial E_z}{\partial y} \mp ik_z E_y, \quad (\text{A.9})$$

$$i\omega B_y = -\frac{\partial E_z}{\partial x} + \frac{\partial E_x}{\partial z} = -\frac{\partial E_z}{\partial x} \pm ik_z E_x, \quad (\text{A.10})$$

$$i\omega B_z = \frac{\partial E_y}{\partial x} - \frac{\partial E_x}{\partial y}, \quad (\text{A.11})$$

$$\frac{i\omega}{c^2} E_x = \frac{\partial B_z}{\partial y} - \frac{\partial B_y}{\partial z} = \frac{\partial B_z}{\partial y} \mp ik_z B_y, \quad (\text{A.12})$$

$$\frac{i\omega}{c^2} E_y = -\frac{\partial B_z}{\partial x} + \frac{\partial B_x}{\partial z} = -\frac{\partial B_z}{\partial x} \pm ik_z B_x, \quad (\text{A.13})$$

$$\frac{i\omega}{c^2}E_z = \frac{\partial B_y}{\partial x} - \frac{\partial B_x}{\partial y}. \quad (\text{A.14})$$

Combining Equations A.9 and A.13 ... the fields within a rectangular waveguide are given dependent upon  $E_z$  and  $B_z$ :

$$E_y = \frac{i}{k_c^2} \left( \pm k_z \frac{\partial E_z}{\partial y} - \omega \frac{\partial B_z}{\partial x} \right), \quad (\text{A.15})$$

$$B_x = \frac{i}{k_c^2} \left( \pm k_z \frac{\partial B_z}{\partial x} - \frac{\omega}{c^2} \frac{\partial E_z}{\partial y} \right), \quad (\text{A.16})$$

$$E_x = \frac{i}{k_c^2} \left( \pm k_z \frac{\partial E_z}{\partial x} + \omega \frac{\partial B_z}{\partial y} \right), \quad (\text{A.17})$$

$$B_y = \frac{i}{k_c^2} \left( \pm k_z \frac{\partial B_z}{\partial y} - \frac{\omega}{c^2} \frac{\partial E_z}{\partial x} \right). \quad (\text{A.18})$$

By taking Equations A.15 to A.18 and substituting them into Equations A.11 and A.14,  $E_z$  and  $B_z$  are obtained independent of one another [6]:

$$\left( \frac{\partial^2}{\partial x^2} + \frac{\partial^2}{\partial y^2} + \frac{\omega^2}{c^2} - k_z^2 \right) E_z = 0, \quad (\text{A.19})$$

$$\left( \frac{\partial^2}{\partial x^2} + \frac{\partial^2}{\partial y^2} \right) E_z = -k_c^2 E_z = \nabla_T^2 E_z, \quad (\text{A.20})$$

$$\left( \frac{\partial^2}{\partial x^2} + \frac{\partial^2}{\partial y^2} + \frac{\omega^2}{c^2} - k_z^2 \right) B_z = 0, \quad (\text{A.21})$$

$$\left( \frac{\partial^2}{\partial x^2} + \frac{\partial^2}{\partial y^2} \right) B_z = -k_c^2 B_z = \nabla_T^2 B_z. \quad (\text{A.22})$$

Of interest here is the derivation of the transverse magnetic mode (TM) mode

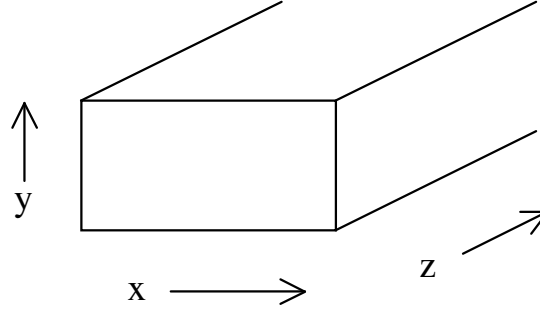


Figure A.1: Rectangular Waveguide where lengths  $x=a$  and  $y=b$ .

since it is the accelerating mode for particle propagation. A similar derivation could be carried out for the transverse electric mode (TE) where the magnetic field is in the direction of particle propagation. From Equation A.20,  $E_z$  is found by separation of variables: Let  $E_z = X(x)Y(y)e^{\pm ik_z z}$  then  $X''Y + XY'' = -k_c^2 XY$  after factoring out the  $e^{\pm ik_z z}$  term. Dividing through by  $XY$  leaves  $\frac{X''}{X} + \frac{Y''}{Y} = k_c^2$ . Since  $x$  and  $y$  can be changed independently of each other both  $\frac{X''}{X}$  and  $\frac{Y''}{Y}$  must be different constants.  $\frac{X''}{X} = -k_x^2$  and  $\frac{Y''}{Y} = -k_y^2$ . Solving  $X = A \cos(k_x x) + B \sin(k_x x)$  and  $Y = C \cos(k_y y) + D \sin(k_y y)$ , where  $A$ ,  $B$ ,  $C$ , and  $D$  are constants that will be determined. So  $E_z = XY e^{\pm ik_z z} = (A \cos(k_x x) + B \sin(k_x x))(C \cos(k_y y) + D \sin(k_y y))e^{\pm ik_z z}$  [6].

Boundary conditions dictate that  $E_z(x = 0, a) = 0$ ,  $E_z(y = 0, b) = 0$ , and  $E_z(x = \frac{a}{2}, y = \frac{b}{2}) = E_0$  (Figure A.1): So  $A$  and  $C$  must both equal zero, and so  $E_z = (B \sin(k_x x))(D \sin(k_y y))e^{\pm ik_z z}$ , which requires  $k_x a = m\pi$ ,  $k_y b = n\pi$  and  $BD = E_0$ . Altogether,

$$E_z = E_0 \sin \frac{m\pi x}{a} \sin \frac{n\pi y}{b} e^{\pm ik_z z}. \quad (\text{A.23})$$

For the TM mode, Equation A.23 is substituted into Equations A.15 to A.18 to solve for  $E_x$ ,  $E_y$ ,  $B_x$ , and  $B_y$  [6]:

$$E_x = \frac{i}{k_c^2} \left[ \pm k_z E_0 \frac{m\pi}{a} \cos \left( \frac{m\pi x}{a} \right) \sin \left( \frac{n\pi y}{b} \right) \right] e^{\pm ik_z z},$$

$$E_y = \frac{i}{k_c^2} \left[ \pm k_z E_0 \frac{n\pi}{b} \sin\left(\frac{m\pi x}{a}\right) \cos\left(\frac{n\pi y}{b}\right) \right] e^{\pm i k_z z},$$

$$B_x = \frac{i}{k_c^2} \left[ -\frac{\omega}{c^2} E_0 \frac{n\pi}{b} \sin\left(\frac{m\pi x}{a}\right) \cos\left(\frac{n\pi y}{b}\right) \right] e^{\pm i k_z z},$$

$$B_y = \frac{i}{k_c^2} \left[ -\frac{\omega}{c^2} E_0 \frac{m\pi}{a} \cos\left(\frac{m\pi x}{a}\right) \sin\left(\frac{n\pi y}{b}\right) \right] e^{\pm i k_z z}.$$

## A.2 Fields Within a Circular Waveguide

For waveguides of circular cross section, Equations A.15 to A.18 are transformed to cylindrical coordinates:

$$E_r = \frac{i}{k_c^2} \left( \pm k_z \frac{\partial E_z}{\partial r} + \frac{\omega}{r} \frac{\partial B_z}{\partial \phi} \right), \quad (\text{A.24})$$

$$B_r = \frac{i}{k_c^2} \left( \pm k_z \frac{\partial B_z}{\partial r} - \frac{\omega}{c^2 r} \frac{\partial E_z}{\partial \phi} \right), \quad (\text{A.25})$$

$$E_\phi = \frac{i}{k_c^2} \left( \pm \frac{k_z}{r} \frac{\partial E_z}{\partial \phi} - \omega \frac{\partial B_z}{\partial r} \right), \quad (\text{A.26})$$

$$B_\phi = \frac{i}{k_c^2} \left( \pm \frac{k_z}{r} \frac{\partial B_z}{\partial \phi} + \frac{\omega}{c^2} \frac{\partial E_z}{\partial r} \right). \quad (\text{A.27})$$

A similar set of equations could be derived for the TE mode [6].

Starting with the wave equation, Equations A.1 and A.2, the Laplace operator  $\nabla^2$ , in cylindrical coordinates, operating on  $E_z$  can also be separated into two parts, transverse and longitudinal:

$$\frac{1}{r} \frac{\partial}{\partial r} \left( r \frac{\partial E_z}{\partial r} \right) + \frac{1}{r^2} \frac{\partial^2 E_z}{\partial \phi^2} + \frac{\partial^2 E_z}{\partial z^2} - \frac{1}{c^2} \frac{\partial^2 E_z}{\partial t^2} = 0,$$

$$\frac{\partial^2 E_z}{\partial r^2} + \frac{1}{r} \frac{\partial E_z}{\partial r} + \frac{1}{r^2} \frac{\partial^2 E_z}{\partial \phi^2} + k_c^2 E_z = 0,$$

$$\nabla_T^2 E_z = \frac{\partial^2 E_z}{\partial r^2} + \frac{1}{r} \frac{\partial E_z}{\partial r} + \frac{1}{r^2} \frac{\partial^2 E_z}{\partial \phi^2} = -k_c^2 E_z.$$

This differential equation can also be solved by separation of variables. Let  $E_z = RF_\phi e^{\pm ik_z z}$ , where  $R(r)$  and  $F(\phi)$ :

$$R'' F_\phi + \frac{R'}{r} F_\phi + \frac{1}{r^2} R F_\phi'' = -k_c^2 R F_\phi \quad (\text{A.28})$$

where the  $e^{\pm ik_z z}$  term has been factored out. Dividing Equation A.28 by  $RF_\phi$  and multiplying by  $r^2$ :

$$-\frac{F_\phi''}{F_\phi} = r^2 \frac{R''}{R} + r \frac{R'}{R} + k_c^2 r^2. \quad (\text{A.29})$$

If both sides of Equation A.29 are equal they must be equal to a constant, say  $m^2$ :

$$-\frac{F_\phi''}{F_\phi} = m^2 \quad (\text{A.30})$$

$$\text{or } r^2 R'' + r R' + (k_c^2 r^2 - m^2) R = 0. \quad (\text{A.31})$$

Equations A.30 and A.31 have solutions of the form  $F_\phi = C \cos(m\phi) + D \sin(m\phi)$  and  $R = AJ_m(x) + BN_m(x)$ , where A, B, C, and D are constants,  $x = k_c r$ , and  $k_c = \frac{u_{mn}}{R}$  making  $x_{mn} = \frac{u_{mn} r}{R}$ . Since  $E_z = RF_\phi e^{\pm ik_z z}$ :

$$E_z = [AJ_m(x) + BN_m(x)][C \cos(m\phi) + D \sin(m\phi)]e^{\pm ik_z z}, \quad (\text{A.32})$$

where  $J_m$  is a Bessel function of the first kind [7]:

$$J_m(x) = \left(\frac{x}{2}\right)^m \sum_{j=0}^{\infty} \frac{(-1)^j}{j! \Gamma(j+m+1)} \left(\frac{x}{2}\right)^{2j},$$

and  $N_m$  a Bessel function of the second kind [7]:

$$N_m(x) = \frac{J_m(x) \cos(m\pi) - J_{-m}(x)}{\sin(m\pi)}.$$

$N_m(x)$  approaches  $\infty$  at integer values of  $m$  (at the origin) so  $B=0$  in Equation A.32.

The origin is chosen such that  $\phi = 0$  and only the  $\cos(m\phi)$  term varies there so  $D = 0$ .

Altogether,

$$E_z = AJ_m(x) \cos(m\phi) e^{\pm ik_z z} \quad (\text{A.33})$$

where the new constant for  $AC = A$  [6] [7]. Bessel functions have an infinite number of roots with zeros occurring at integer values of  $n$ :  $x_{m1}, x_{m2}, x_{m3} \dots$ . For integer values of  $m$ , the first few roots are

$$x_{01} = 2.405, x_{02} = 5.520, x_{03} = 8.654, \dots$$

$$x_{11} = 3.832, x_{12} = 7.016, x_{13} = 10.173, \dots$$

$$x_{21} = 5.136, x_{22} = 8.417, x_{23} = 11.620, \dots [8].$$

Since the electric field is perpendicular to a conducting surface and the magnetic field parallel, the boundary conditions for the circular waveguide are (Figure 2.2)  $E_z(r = R) = 0$ ,  $E_\phi(r = R) = 0$ , and  $B_r(r = R) = 0$ . These boundary conditions imply

$$x_{mn} = \frac{u_{mn} r}{R} = k_c r.$$

$$E_z = AJ_m\left(\frac{u_{mn} r}{R}\right) \cos(m\phi) e^{\pm ik_z z},$$

$$E_r = \frac{\pm ik_z R}{u_{mn}} AJ'_m\left(\frac{u_{mn} r}{R}\right) \cos(m\phi) e^{\pm ik_z z},$$

$$E_\phi = \frac{\mp ik_z m R^2}{u_{mn}^2 r} A J_m \left( \frac{u_{mn} r}{R} \right) \sin(m\phi) e^{\pm ik_z z},$$

$$B_r = \frac{i\omega m R^2}{u_{mn}^2 c^2 r} A J_m \left( \frac{u_{mn} r}{R} \right) \sin(m\phi) e^{\pm ik_z z},$$

$$B_\phi = \frac{i\omega R}{u_{mn} c^2} A J'_m \left( \frac{u_{mn} r}{R} \right) \cos(m\phi) e^{\pm ik_z z},$$

$$B_z = 0.$$

### A.3 Fields Within a Cavity

A cavity is formed when conductive ends are placed on the cylindrical waveguide at  $z = 0$  and at  $z = l$ . Now the cavity is filled with incident and reflected waves with additional boundary conditions  $E_r(z = 0, l) = 0$ ,  $E_\phi(z = 0, l) = 0$ , and  $B_z(z = 0, l) = 0$ . Since both incident and reflected waves are present:

$$\begin{aligned} E_z &= A J_m \left( \frac{u_{mn} r}{R} \right) \cos(m\phi) e^{\pm ik_z z} \\ &= A J_m \left( \frac{u_{mn} r}{R} \right) \cos(m\phi) (B^+ e^{+ik_z z} + B^- e^{-ik_z z}), \end{aligned}$$

where  $B^+$  and  $B^-$  are the wave amplitudes in the forward and backward direction. The condition  $E_z(r = 0, \phi = 0, z = 0, l) = E_0$  implies  $B^+ = B^-$  and  $2AB^+ = E_0$ :

$$E_z = E_0 J_m \left( \frac{u_{mn} r}{R} \right) \cos(m\phi) \cos(k_z z).$$

Again, since incident and reflected waves are present the radial electric field becomes:

$$E_r = \frac{\pm ik_z}{k_c} A J'_m \left( \frac{u_{mn} r}{R} \right) \cos(m\phi) (B^+ e^{+ik_z z} + B^- e^{-ik_z z}).$$

The boundary conditions require that  $E_r$  must vanish, so  $B^+ = -B^-$  so:

$$\begin{aligned} E_r &= \frac{\pm ik_z}{k_c} A J'_m \left( \frac{u_{mn} r}{R} \right) \cos(m\phi) \frac{2iB^+ (e^{+ik_z z} - e^{-ik_z z})}{2i} \\ &= \frac{\mp ik_z}{k_c} E_0 J'_m \left( \frac{u_{mn} r}{R} \right) \cos(m\phi) \sin(k_z z). \end{aligned}$$

$E_r(z = l) = 0$  implies  $k_z l = p\pi$  for some integer  $p$ :

$$E_r = \frac{\mp ik_z}{k_c} E_0 J'_m \left( \frac{u_{mn} r}{R} \right) \cos(m\phi) \sin\left(\frac{p\pi z}{l}\right).$$

Similar expressions can be obtained for  $E_\phi$ ,  $B_r$ , and  $B_\phi$ . Altogether the electric fields become:

$$E_z = E_0 J_m \left( \frac{u_{mn} r}{R} \right) \cos(m\phi) \cos\left(\frac{p\pi z}{l}\right),$$

$$E_r = \frac{\mp p\pi R}{lu_{mn}} E_0 J'_m \left( \frac{u_{mn} r}{R} \right) \cos(m\phi) \sin\left(\frac{p\pi z}{l}\right),$$

$$E_\phi = \frac{\pm mp\pi R^2}{rlu_{mn}^2} E_0 J_m \left( \frac{u_{mn} r}{R} \right) \sin(m\phi) \sin\left(\frac{p\pi z}{l}\right),$$

and magnetic fields:

$$B_z = 0,$$

$$B_r = \frac{i\omega_{mnp} m R^2}{u_{mn}^2 c^2 r} E_0 J_m \left( \frac{u_{mn} r}{R} \right) \sin(m\phi) \cos\left(\frac{p\pi z}{l}\right),$$

$$B_\phi = \frac{i\omega_{mnp} R}{u_{mn} c^2} E_0 J'_m \left( \frac{u_{mn} r}{R} \right) \cos(m\phi) \cos\left(\frac{p\pi z}{l}\right),$$

$$\text{where } k_c^2 = \frac{\omega^2}{c^2} - k_z^2 \Rightarrow \omega = c\sqrt{k_c^2 + k_z^2} = c\sqrt{\left(\frac{u_{mn}}{R}\right)^2 + \left(\frac{p\pi}{l}\right)^2} = \omega_{mnp},$$

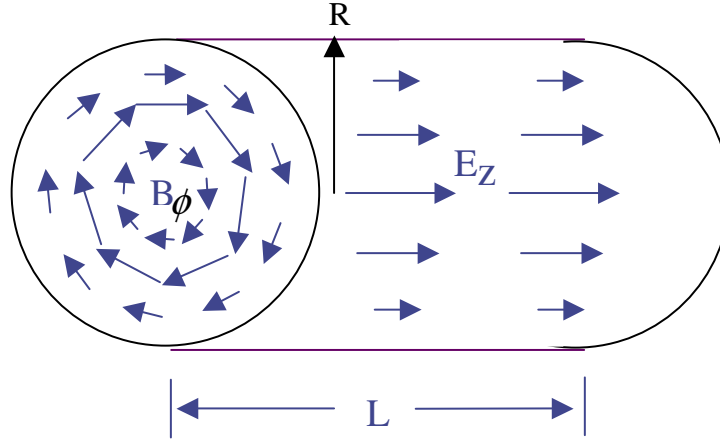


Figure A.2: Electric and magnetic fields in a cylindrical cavity. The maximum electric field occurs on axis to accelerate the beam and falls to zero at the cavity wall ( $R$ ). The magnetic field is zero on axis and has a maximum at  $0.77R$ .

$$\text{and } f_{mnp} = \frac{\omega_{mnp}}{2\pi} = \frac{c}{2\pi} \sqrt{\left(\frac{u_{mn}}{R}\right)^2 + \left(\frac{p\pi}{l}\right)^2}.$$

In the  $TM_{010}$  mode the zero order Bessel function provides an accelerating field in the longitudinal direction (direction of particle travel) and a magnetic field in the  $\phi$  direction.

# Appendix B

## Field Emission

### B.1 Transmission Coefficient $D(W)$

$$N(W) = \frac{2}{h^3} \int_{-\infty}^{+\infty} \int_{-\infty}^{+\infty} \frac{dp_y dp_z}{\exp\left(\frac{E-\zeta}{kT}\right) + 1} \quad (\text{B.1})$$

Equation B.1 is solved by using the following substitutions:

$$p_y = \rho \cos \theta \Rightarrow dp_y = -\rho \sin \theta d\theta + \cos \theta d\rho,$$

$$p_z = \rho \sin \theta \Rightarrow dp_z = \rho \cos \theta d\theta + \sin \theta d\rho.$$

The only term that survives in the product is  $\rho d\rho d\theta$ :

$$N(W) = \frac{2}{h^3} \int_0^\infty \int_0^{2\pi} \frac{\rho d\rho d\theta}{\exp\left(\frac{W-\zeta}{kT} + \frac{\rho^2}{2mkT}\right) + 1}. \quad (\text{B.2})$$

Substituting  $\left(u = \frac{W-\zeta}{kT} + \frac{\rho^2}{2mkT}\right)$  and  $du = \frac{\rho d\rho}{mkT}$  into Equation B.2 [10]:

$$\begin{aligned}
N(W) &= \frac{4\pi mkT}{h^3} \int_0^\infty \frac{du}{\exp(u) + 1} \\
&= \frac{4\pi mkT}{h^3} \left[ \left( \frac{W-\zeta}{kT} + \frac{\rho^2}{2mkT} \right) - \ln \left( \exp \left[ \frac{W-\zeta}{kT} - \frac{\rho^2}{2mkT} \right] + 1 \right) \right] \\
&= \frac{4\pi mkT}{h^3} \ln \left( 1 + \exp \left[ \frac{-W + \zeta}{kT} \right] \right). \tag{B.3}
\end{aligned}$$

The time independent Schrödinger equation [10]:

$$-\frac{\hbar^2}{2m} \frac{d^2}{dx^2} \psi = (W - V)\psi, \tag{B.4}$$

where  $\psi$  is a complex function that has both amplitude ( $A$ ) and phase ( $\phi$ ) [31],

$$\psi(x) = A(x)e^{i\phi(x)}, \tag{B.5}$$

$$\frac{d\psi}{dx} = A(x)ie^{i\phi(x)}\phi'(x) + A'(x)e^{i\phi(x)} = (A'(x) + iA(x)\phi'(x))e^{i\phi(x)},$$

$$\begin{aligned}
\frac{d^2\psi}{dx^2} &= A'(x)i\phi'(x)e^{i\phi(x)} + A''(x)e^{i\phi(x)} + iA(x)\phi'(x)i\phi'(x)e^{i\phi(x)} \\
&+ iA'(x)\phi'(x)e^{i\phi(x)} + iA(x)\phi''e^{i\phi(x)} \\
&= (A'' + 2A'i\phi' + Ai\phi'' - A(\phi')^2)e^{i\phi}. \tag{B.6}
\end{aligned}$$

Substituting Equation B.5 into into Equation B.4:

$$(A'' + 2A'i\phi' + Ai\phi'' - A(\phi')^2)e^{i\phi} = \frac{2m}{\hbar^2}(W - V)Ae^{i\phi}.$$

The real part [31]:

$$A'' - A(\phi')^2 = \frac{2m}{\hbar^2}(V - W)A,$$

$$A'' = \left( \frac{2m}{\hbar^2}(V - W) + (\phi')^2 \right) A,$$

is very difficult to solve, so the Wentzel-Kramers-Brillouin (WKB) approximation is used. Assume  $A''$  varies slowly or  $\frac{A''}{A}$  is much less than  $\frac{2m}{\hbar^2}(V - W)$  and  $(\phi')^2$ . Then:

$$\frac{2m}{\hbar^2}(V - W) = (\phi')^2 \Rightarrow \frac{d\phi}{dx} = \frac{\sqrt{2m(W - V)}}{\hbar},$$

$$\phi = \pm \frac{1}{\hbar} \int \sqrt{2m(W - V)} dx. \quad (\text{B.7})$$

The imaginary part [31]:

$$2A'i\phi' + Ai\phi'' = 0 \Rightarrow \frac{d}{dx}(A^2\phi'i) = 0,$$

$$A^2\phi' = \text{Constant} = C^2,$$

$$A = \frac{C}{\sqrt{2m(W - V)}}. \quad (\text{B.8})$$

Substituting Equations B.7 and B.8 into Equation B.5:

$$\psi(x) = \frac{C\hbar}{\sqrt{2m(W - V)}} \exp\left(\frac{\pm i}{\hbar} \int_{x_1}^{x_2} \sqrt{2m(W - V)} dx\right).$$

To the left of the barrier,  $x < x_1$ , there is a wave component traveling to the right

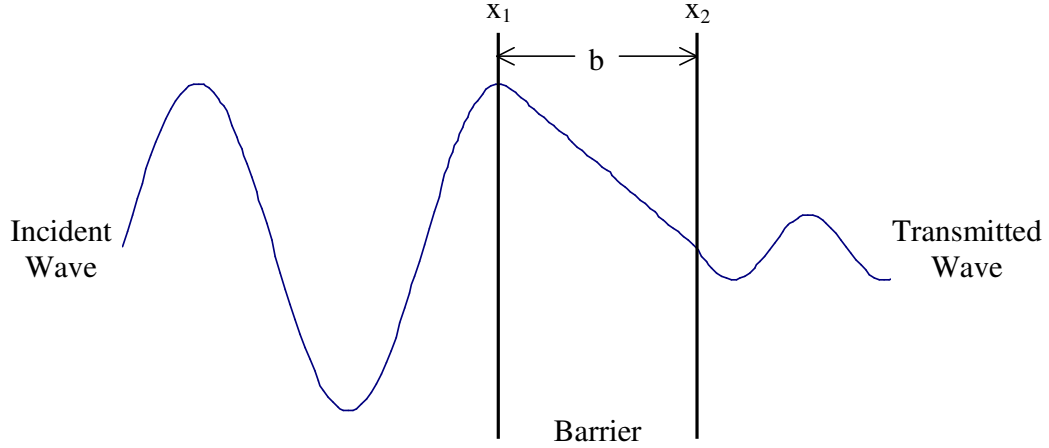


Figure B.1: An electron has a probability of tunneling through the potential barrier if the barrier is either too high or too wide.

and a reflected component traveling to the left:

$$\psi(x) = Ae^{ikx} + Be^{-ikx},$$

where  $k \equiv \frac{\sqrt{2mE}}{\hbar}$ . To the right of the barrier  $x > x_2$ :

$$\psi(x) = Fe^{ikx}.$$

Within the barrier  $x_1 < x < x_2$ :

$$\psi(x) = \frac{C\hbar}{\sqrt{2m(W-V)}} \exp \left[ \frac{+i}{\hbar} \int_{x_1}^{x_2} \sqrt{2m(W-V(x))} dx \right] + \frac{D\hbar}{\sqrt{2m(W-V)}} \exp \left[ \frac{-i}{\hbar} \int_{x_1}^{x_2} \sqrt{2m(W-V(x))} dx \right].$$

The tunneling probability (Figure B.1):

$$D(W) = T^2 = \frac{|F|^2}{|A|^2}.$$

If the barrier is very high or very wide the probability of tunneling is small, and the

(+) exponent term must go to zero [31] [10]:

$$\frac{|F|}{|A|} \sim \exp \left[ \frac{-i}{\hbar} \int_{x_1}^{x_2} \sqrt{2m(W - V)} dx \right],$$

$$D(W) = \exp \left[ \frac{-2}{\hbar} \int_{x_1}^{x_2} \sqrt{2m(W - V)} dx \right],$$

where  $x_1$  and  $x_2$  are the zeros of the randicand. The potential of an applied electric field is more complex:

$$\frac{8m}{\hbar^2} \left[ \frac{e^2}{4x} + eEx - W \right] = 0,$$

$$\begin{aligned} x &= \frac{|W| \pm \sqrt{|W|^2 - e^3 E}}{2eE} \\ &= \frac{|W|}{2eE} \left( 1 \pm \sqrt{1 - \frac{e^3 E}{W^2}} \right). \end{aligned}$$

Thus the transmission coefficient is written as:

$$-\ln D(W) = \int_{x_1}^{x_2} \sqrt{\frac{8m}{\hbar^2} \left( W - \frac{e^2}{4x} - eEx \right)} dx, \quad (\text{B.9})$$

Let  $y = \sqrt{\frac{e^3 E}{W^2}}$  and  $\xi = \frac{2eEx}{|W|} \Rightarrow d\xi = \frac{2eE}{|W|} dx$ . Thus  $\frac{y^2}{\xi} = \frac{e^2}{2|W|x} \Rightarrow \frac{e^2}{4x} = \frac{y^2|W|}{2\xi}$  and  $x = \frac{|W|}{2eE} \left( 1 \pm \sqrt{1 - y^2} \right) = \frac{|W|}{2eE} \xi$ . Substituting into Equation B.9:

$$\begin{aligned} -\ln D(W) &= \frac{|W|}{2eE} \int_{1-\sqrt{1-y^2}}^{1+\sqrt{1-y^2}} \sqrt{\frac{8m}{\hbar^2} \left( W - \frac{|W|\xi}{2} - \frac{y^2|W|}{2\xi} \right)} d\xi \\ &= \frac{2W^{3/2}\sqrt{m}}{2eE\hbar} \int_{1-\sqrt{1-y^2}}^{1+\sqrt{1-y^2}} \sqrt{2 - \xi - \frac{y^2}{\xi}} d\xi \\ &= \frac{\sqrt{W^3 m}}{eE\hbar} \int_{1-\sqrt{1-y^2}}^{1+\sqrt{1-y^2}} \sqrt{-\xi^2 + 2\xi - y^2} \frac{d\xi}{\sqrt{\xi}}. \end{aligned}$$

Let  $\eta = \sqrt{\zeta} \Rightarrow d\eta = \frac{d\zeta}{2\sqrt{\zeta}}$ :

$$-\ln D(W) = \frac{2\sqrt{W^3 m}}{eE\hbar} \int \frac{\sqrt{1+\sqrt{1-y^2}}}{\sqrt{1-\sqrt{1-y^2}}} \sqrt{-\eta^4 + 2\eta^2 - \left(1 + \sqrt{1-y^2}\right) \left(1 - \sqrt{1-y^2}\right)} d\eta.$$

Let  $a = \sqrt{1 + \sqrt{1-y^2}}$  and  $b = \sqrt{1 - \sqrt{1-y^2}}$ :

$$\begin{aligned} -\ln D(W) &= \frac{2\sqrt{W^3 m}}{eE\hbar} \int_b^a \sqrt{-\eta^4 + 2\eta^2 - a^2 b^2} d\eta \\ &= \frac{2\sqrt{W^3 m}}{eE\hbar} \int_b^a \sqrt{(a^2 - \eta^2)(\eta^2 - b^2)} d\eta. \end{aligned}$$

This is a standard form for an elliptical integral:

$$-\ln D(W) = \frac{4a\sqrt{m|W|^3}}{3eE\hbar} \left[ E(k) - b^2 K(k) \right],$$

where  $K(k) = \int_0^{\frac{\pi}{2}} \frac{d\psi}{\sqrt{1-k^2 \sin^2 \psi}}$ ,  $E(k) = \int_0^{\frac{\pi}{2}} \sqrt{1-k^2 \sin^2 \psi} d\psi$ , and  $k^2 = \frac{a^2-b^2}{a^2}$ .

Let  $v = \frac{1}{\sqrt{2}} a \sqrt{[E(k) - b^2 K(k)]}$  then

$$D(W) = \exp \left( -\frac{2\sqrt{2m|W|^3}}{3eE\hbar} v(y) \right). \quad (\text{B.10})$$

## B.2 Number of Electrons $P(W)$

The number of electrons within energy  $dW$  emerging from the surface per unit area [10]:

$$P(W)dW = N(W)D(W)dW, \quad (\text{B.11})$$

where  $N(W)$  is the number of supply electrons and  $D(W)$  the probability that they will leave the surface. Substituting Equations B.3 and B.10 into Equation B.11:

$$P(W)dW = \frac{4\pi mkT}{h^3} \ln \left[ 1 + \exp \left( \frac{-W + \zeta}{kT} \right) \right] \exp \left( \frac{-4\sqrt{2m|W|^3}}{3eE\hbar} v(y) \right),$$

Field emission electrons have energies  $W \sim \zeta$ , so the exponent of the tunneling probability is expanded in a power series at  $W = \zeta$ :

$$f(x) = f(a) + f'(a)(x - a) + \dots,$$

$$\begin{aligned} \frac{-4\sqrt{2m|W|^3}}{3eE\hbar} v(y) &\sim \frac{-4\sqrt{2m\phi^3}}{3eE\hbar} v(y) + \left( \frac{-4\sqrt{2m\phi^3}}{3eE\hbar} v'(y) \right) (W - \zeta) \\ &+ v(y) \left( \frac{2\sqrt{2m|\phi|}}{eE\hbar} \right) (W - \zeta) \end{aligned}$$

Substituting  $v' = \frac{dv}{d\zeta} = \frac{dv}{dy} \left( \frac{-y}{\zeta} \right)$ ,  $y = \frac{e^3 E}{\zeta} \Rightarrow dy = \frac{-\sqrt{e^3 E}}{\zeta^2} d\zeta$ , and  $d\zeta = \frac{-dy\zeta}{y}$  into the above equation:

$$\frac{-4\sqrt{2m|W|^3}}{3eE\hbar} v(y) \sim -c + \frac{W - \zeta}{d},$$

where

$$c = \frac{4\sqrt{2m\phi^3}}{3eE\hbar} v,$$

$$d = \frac{eE\hbar}{2\sqrt{2m\phi t}},$$

$$\text{and } t = v - \frac{2}{3} y \frac{dv}{dy},$$

$$\text{thus } P(W) = \frac{4\pi mkT}{h^3} \ln \left[ 1 + \exp \left( \frac{-W + \zeta}{kT} \right) \right] \exp \left( -c + \frac{W - \zeta}{d} \right).$$

In the low temperature limit [10]:

$$\begin{aligned}
 kT \ln \left( 1 + \exp \left( \frac{-W + \zeta}{kT} \right) \right) &= 0 && \text{when } W > \zeta \\
 &= \zeta - W && \text{when } W < \zeta
 \end{aligned}$$

$$\begin{aligned}
 \text{thus } P(W) &= 0 && \text{when } W > \zeta \\
 &= \frac{4\pi m}{h^3} \exp \left( -c + \frac{W - \zeta}{d} \right) (\zeta - W) && \text{when } W < \zeta.
 \end{aligned}$$

### B.3 Current Density $j$

The current density is found by integrating  $P(W)$  over all energies, i.e. from  $-W_a$  to  $\infty$ . Good and Müller [10] assumed  $-W_a$  is far below the Fermi energy  $\zeta$ , so the lower limit is  $-\infty$ :

$$\begin{aligned}
 j &= e \int_{-\infty}^{\zeta} P(W) dW \\
 &= e \int_{-\infty}^{\zeta} \frac{4\pi m}{h^3} \exp \left( -c + \frac{W - \zeta}{d} \right) (\zeta - W) dW.
 \end{aligned}$$

Let  $x = -c + \frac{W-\zeta}{c} \Rightarrow dx = \frac{dW}{d}$ :

$$\begin{aligned}
j &= \frac{4\pi me}{h^3} \int \exp(x) (-d(x+c)) dx \\
&= \frac{4\pi med^2}{h^3} \int [e^x(-dx) - e^x(dc)] dx \\
&= \frac{4\pi med^2}{h^3} (e^x(x+1) - e^x c) \\
&= \frac{4\pi med^2}{h^3} \left[ \exp\left(-c + \frac{W-\zeta}{d}\right) \left(-c + \frac{W-\zeta}{c}\right) + c \exp\left(-c + \frac{W-\zeta}{d}\right) \right]_{-\infty}^{\zeta} \\
&= \frac{4\pi med^2}{h^3} e^{-c} \\
&= \frac{e^3 E^2}{8\pi h \phi t^2} \exp\left(-\frac{4\sqrt{2m\phi^3} v}{3eE\hbar}\right) \\
&= \frac{1.54 \times 10^{-6} E^2}{\phi t^2} \exp\left(-6.83 \times 10^9 \frac{\phi^{\frac{3}{2}}}{E} v\right), \tag{B.12}
\end{aligned}$$

where  $h =$  Planck's constant,  $e^2 = \frac{197MeVfm(4\pi\epsilon_0)}{137}$ , and  $m = 9.109 \times 10^{-13}\text{Kg}$ .

The elliptic function is defined as [11]:

$$v(s) = 0.956 - 1.062s^2$$

$$s = 3.79 \times 10^{-5} \frac{E^{1/2}}{\phi}$$

Both Good and Müller [10] and Wang and Loew [11] set  $t = 1$  in Equation B.12 since  $1 \leq t \leq 1.11$ :

$$\begin{aligned}
j &= \frac{1.54 \times 10^{-6} E^2}{\phi} \exp\left[\frac{\phi^{3/2}}{E} \left(-6.529 \times 10^9 + 10.42 \frac{E}{\phi^2}\right)\right] \\
&= \frac{1.54 \times 10^{-6} \times 10^{4.52} \times \phi^{-\frac{1}{2}} E^2}{\phi} \left[ \exp\left(-6.529 \times 10^9 \frac{\phi^{3/2}}{E}\right) \right]. \tag{B.13}
\end{aligned}$$

## B.4 RF Current $\langle I \rangle$

Electron emission for RF fields is modified from the DC version by assuming that the microscopic electric field on a metal surface is of the form  $E = E_0 \sin \omega t$ . The average field emission current is calculated by a time averaging substitution into Equation B.13:

$$\begin{aligned} \langle I \rangle &= \frac{1}{T} \int_0^T I(t) dt \\ &= 1.54 \times 10^{-6} \times 10^{4.52} \exp(\phi^{-1/2}) A_e \beta_{FN}^2 E_0^2 \left( \frac{2}{T\phi} \right) \\ &\quad \int_0^{T/4} (\sin^2 \omega t) \exp \left( \frac{-6.529 \times 10^9 \phi^{3/2}}{\beta_{FN} E_0 \sin \omega t} \right) dt \end{aligned}$$

Let  $\mu = \frac{-6.529 \times 10^9 \phi^{3/2}}{\beta_{FN} E_0}$  and  $\sin(\omega t) = \frac{1}{x} \Rightarrow \omega \cos(\omega t) dt = -\frac{1}{x^2} dx \Rightarrow \cos(\omega t) = \sqrt{1 - \sin^2 \omega t} = \sqrt{1 - \left(\frac{1}{x^2}\right)}$  [11]:

$$\begin{aligned} \langle I \rangle &= C \frac{2}{T\omega} \int_{\infty}^1 \frac{1}{x^2} \exp(-\mu x) \left( \frac{-dx}{x^2 \sqrt{1 - \frac{1}{x^2}}} \right) \\ &= \frac{C}{\pi} \int_1^{\infty} \frac{\exp(-\mu x) dx}{x^3 \sqrt{x^2 - 1}} \\ &= \frac{0.53 e^{-\mu}}{\sqrt{\pi \mu}} \\ &= \frac{5.7 \times 10^{-12} \times 10^{4.52} A_e \beta_{FN}^{2.5} E_0^{2.5} \exp(\phi^{1.5})}{\phi^{1.75}} \exp \left( \frac{-6.529 \times 10^9 \phi^{1.5}}{\beta_{FN} E_0} \right), \end{aligned}$$

$$\ln \left( \frac{\langle I \rangle}{E^{2.5}} \right) = \ln \left( \frac{5.7 \times 10^{-12} A_e \beta_{FN}^{2.5}}{\phi^{1.75}} \right) + (10.41 \phi^{-0.5}) - \left( \frac{6.529 \times 10^9 \phi^{1.5}}{\beta_{FN} E_0} \right),$$

$$\begin{aligned}
\frac{d\left(\log_{10}\frac{\langle I \rangle}{E^{2.5}}\right)}{d\left(\frac{1}{E}\right)} &= \frac{-(\log_{10}e) 6.529 \times 10^9 \phi^{1.5}}{\beta_{FN}} \\
&= \frac{-2.84 \times 10^9 \phi^{1.5}}{\beta_{FN}}.
\end{aligned} \tag{B.14}$$

Similar to the DC case, but with a plot of  $\log_{10}\left(\frac{\langle I \rangle}{E^{2.5}}\right)$  versus  $\frac{1}{E}$ , one can obtain  $\beta_{FN}$  from the slope of the line and  $A_e$  from the intercept [11]. The Fowler-Nordheim parameters,  $\beta_{FN}$  and  $A_e$ , only express the dependence of the emitted current on the field. The physical significance of  $\beta_{FN}$  and  $A_e$  is still a matter of debate [4].

# Appendix C

## Photon Interactions

### C.1 Compton Effect

Energy of the scattered photon is found by combining equations 2.44 and 2.46:

$$\frac{h\nu'}{c} \sin \theta = \frac{\sqrt{T(T + 2m_0c^2)}}{c} \sin \varphi$$

$$\sin \varphi = \frac{h\nu' \sin \theta}{\sqrt{T(T + 2m_0c^2)}}.$$

Squaring each side and solving for  $\cos \varphi$ :

$$\cos \varphi = \sqrt{1 - \frac{(h\nu')^2 \sin^2 \theta}{T(T + 2m_0c^2)}}.$$

Substituting  $\cos \varphi$  and Equation 2.46 for p into Equation 2.43:

$$h\nu_0 - h\nu' \cos \theta = \sqrt{(h\nu_0)^2 - 2h\nu_0 h\nu' + 2m_0c^2(h\nu_0 - h\nu') + (h\nu')^2 \cos \theta},$$

squaring both sides and solving for  $h\nu'$ , the scattered photon energy is obtained [2]:

$$\begin{aligned} h\nu' &= \frac{h\nu_0 m_0 c^2}{h\nu_0 + m_0 c^2 - h\nu_0 \cos \theta} \\ &= \frac{m_0 c^2}{1 + \frac{m_0 c^2}{h\nu_0} - \cos \theta}. \end{aligned}$$

Let  $\alpha = \frac{h\nu_0}{m_0 c^2}$ :

$$h\nu' = \frac{m_0 c^2}{1 - \cos \theta + \frac{1}{\alpha}}, \quad (\text{C.1})$$

$$\frac{\nu'}{\nu_0} = \frac{1}{1 + \alpha(1 - \cos \theta)}. \quad (\text{C.2})$$

# Appendix D

## Definitions

Auger electron - A photon absorbed by an electron can excite the electron to a higher energy level. When an electron from an outer atomic shell fills the vacant inner shell, the excess energy may be either emitted as a characteristic X-ray or transferred to another outer electron which is ejected from the atom thus becoming the Auger electron. [2].

Bremsstrahlung radiation - As a charged particle travels through a medium it loses kinetic energy when it is deflected by other charged particles. The energy loss is emitted as electromagnetic radiation and ranges in energy from zero up to the kinetic energy of the charged particle [2].

Cerenkov radiation - Light emitted when the phase velocity of a charged particle exceeds  $c$  as it travels through an optically transparent material,  $\beta n > 1$ , where  $\beta$  is the ratio of the particle velocity in the material to  $c$  and  $n$  is the index of refraction of the material [19].

Compton scattering - The interaction between a photon and a free electron in which both the photon and electron are scattered [14].

Coulomb interactions - As a charged particle travels through a material it interacts with atomic electrons and the nucleus of atoms. Interactions with electrons include ionization and excitation [14].

Delbruck scattering - Referred to as elastic nuclear potential scattering when a photon is scattered by a nucleus and an electron pair is formed [2].

Delta ray - A free electron, freed by ionization, that has enough kinetic energy to create additional ions as it comes to rest [2].

Duane and Hunts Law - The maximum photon energy produced by a charged particle traveling through a material is equal to the energy of the incident particle [2].

Excitation - An atomic electron obtains sufficient energy to move to an unoccupied state of higher energy [14].

Exciton - Bound state of an electron with an electron hole [14].

Floquet theorem - For a given mode the electric field, separated by one period, differs by a constant factor ( $e^{\pm ik_z d}$ ) [33]:

$$\vec{E}(r, z + d, t) = \vec{E}(r, z, t)e^{\pm ik_z d}, \quad (\text{D.1})$$

where  $d$  is the period of the structure.

Geiger - Müller counter - Constructed similar to the ionization chamber but with a higher voltage applied to the electrodes. The number of electrons produced during ionizations does not depend on the nature of the initial radiation. The discharge pulses have equal amplitude that are displayed on a meter or audio device. No energy information is gathered from the incident radiation [19].

Group velocity - Velocity of electromagnetic energy [9].

Ionization - An atomic electron obtains sufficient energy to leave the atom [14].

Ionization chamber - Typically a metal chamber (cathode) surrounding a stretched wire, rod, or disk (anode) and filled with a gas (air, argon, krypton, neon,...). The electrodes are connected to a power supply. Radiation traveling through the gas creates ion pairs. As the ion pairs migrate to their respective electrodes additional ion pairs are created (avalanche). A current is measured and interpreted as dose.

Pair production - Pair production is an interaction between an incident photon with

an energy above 1.022 MeV and a nucleus within a material. The photon is completely absorbed and in its place a positron-electron pair appears. The positron is not a stable particle and travels only a short distance before combining with an electron or annihilating, creating two photons separated by  $180^\circ$  and each with energy of  $m_0$  (0.511 MeV). The electron travels a few millimeters at most before losing energy by ionization and excitation (Coulomb interactions) or by emission of bremsstrahlung radiation (Figure 2.19) [2] [19].

Phase velocity - Velocity that any frequency component of a wave propagates [9].

Phonon - A vibrational quantum of energy, a form of mechanical energy such as the way a sound wave propagates through a medium [34].

Photoelectric effect - Total absorption of an incident photon by an atomic electron. The photon disappears and the electron is ejected from the atom, creating an ion [14].

Proportional counter - Constructed similar to the ionization chamber. A low voltage is applied to the electrodes such that the number of electrons produced is due only to the initial ionizing event. The counter's output is thus proportional to the number of ions making it possible to distinguish between different types of radiation [19].

Q disease - Hydrogen, found in bulk Nb, precipitates to the RF surface and dissipates power, preventing an increase in cavity electric fields [4].

Rayleigh scattering - Scattering of photons by tightly bound atomic electrons. Scattering angles are small since the recoil imparted to the atom must not produce excitation or ionization [2].

Standing wave - A disturbance that is confined to a given space in a medium.

SUPERLANS - A computer code that calculates electromagnetic fields within axisymmetrical cavities, periodic structures, and cut-off frequencies in long homogeneous waveguides [28].

Traveling wave - A disturbance that travels through a medium, transporting energy.

Work Function - Energy required to take an electron from the Fermi level within a metal and remove it to infinity, assuming a particle at infinity has zero energy [19].

# Appendix E

## Floquet Theorem

### E.1 Derivation

The SUPERLANS code provides two real functions, the symmetric and antisymmetric standing waves, that can be combined using Floquet's theorem to construct another standing wave with a phase shift over a structure period.

A standing wave is the sum of two traveling waves so the symmetric and antisymmetric standing waves can be written as:

$$\vec{E}_{sym}(r, z, t) = \frac{1}{2}(\vec{E}(r, z, t) + \vec{E}(r, -z, t)) \quad (\text{E.1})$$

$$\vec{E}_{anti}(r, z, t) = \frac{1}{2}(\vec{E}(r, z, t) - \vec{E}(r, -z, t)), \quad (\text{E.2})$$

where  $\vec{E}(r, z, t)$  is a wave traveling in the  $+z$  direction and  $\vec{E}(r, -z, t)$  a wave traveling in the  $-z$  direction. Taking the sum and difference of the two equations yields:

$$\vec{E}(r, z, t) = \vec{E}_{sym}(r, z, t) + \vec{E}_{anti}(r, z, t) \text{ and} \quad (\text{E.3})$$

$$\vec{E}(r, -z, t) = \vec{E}_{sym}(r, z, t) - \vec{E}_{anti}(r, z, t) \quad (\text{E.4})$$

For example, let  $A \sin(\omega t - k_z z)$  be a wave traveling in the  $+z$  direction and  $A \sin(\omega t + k_z z)$  be a wave traveling in the  $-z$  direction. Then

$$E_{sym} = \frac{A}{2} (\sin(\omega t - k_z z) + \sin(\omega t + k_z z)) \quad (\text{E.5})$$

$$= \frac{A}{2} \left[ \frac{e^{i(\omega t - k_z z)} - e^{-i(\omega t - k_z z)} + e^{i(\omega t + k_z z)} - e^{-i(\omega t + k_z z)}}{2i} \right] \quad (\text{E.6})$$

$$= \frac{A}{4i} \left[ e^{-ik_z z} (e^{i\omega t} - e^{-i\omega t}) + e^{ik_z z} (e^{i\omega t} - e^{-i\omega t}) \right] \quad (\text{E.7})$$

$$= \frac{A}{4i} \left[ (e^{i\omega t} - e^{-i\omega t}) (e^{ik_z z} + e^{-ik_z z}) \right] \quad (\text{E.8})$$

$$= A \cos(k_z z) \sin(\omega t), \quad (\text{E.9})$$

a standing wave. Similarly:

$$E_{anti} = \frac{A}{2} (\sin(\omega t - k_z z) - \sin(\omega t + k_z z)) \quad (\text{E.10})$$

$$= A \cos(\omega t) \sin(-k_z z). \quad (\text{E.11})$$

The Floquet theorem states that for a given mode the electric field, separated by one period, differs by a constant factor ( $e^{\pm ik_z d}$ ) [33]:

$$\vec{E}(r, z + d, t) = \vec{E}(r, z, t) e^{\pm ik_z d}, \quad (\text{E.12})$$

where  $d$  is the period of the structure (Figure E.1).

The standing wave of the periodic structure is the sum of two such waves traveling in opposite directions:

$$\vec{E}_{+zdir}(r, z + d, t) = \vec{E}_{+zdir}(r, z, t) e^{ik_z d} \text{ and}$$

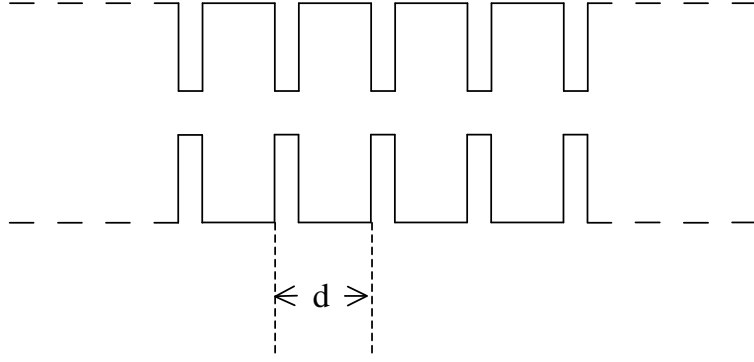


Figure E.1: Periodic structure with period  $d$ .

$$\vec{E}_{-zdir}(r, z + d, t) = \vec{E}_{-zdir}(r, z, t)e^{-ik_z d}.$$

$$\begin{aligned} \vec{E}(r, z + d, t) &= \vec{E}_{+zdir}(r, z + d, t) + \vec{E}_{-zdir}(r, z + d, t) \\ &= \vec{E}_{+zdir}(r, z, t)e^{ik_z d} + \vec{E}_{-zdir}(r, z, t)e^{-ik_z d}. \end{aligned} \quad (\text{E.13})$$

The amplitude of the two traveling waves differ by a phase:

$$\vec{E}_{-zdir}(r, z, t) = \vec{E}_{+zdir}(r, -z, t)e^{i\varphi},$$

$$\vec{E}(r, z + d, t) = \vec{E}(r, z, t)e^{ik_z d} + \vec{E}(r, -z, t)e^{-ik_z d}e^{i\varphi}. \quad (\text{E.14})$$

where the subscripts have been omitted.

Substituting Equations E.3 and E.4 into Equation E.14 yields:

$$\vec{E}(r, z + d, t) = (\vec{E}_{sym}(r, z, t) + \vec{E}_{anti}(r, z, t))e^{ik_z d} + (\vec{E}_{sym}(r, z, t) - \vec{E}_{anti}(r, z, t))e^{-ik_z d}e^{i\varphi}. \quad (\text{E.15})$$

Recombining terms in Equation E.15 yields:

$$\vec{E}(r, z + d, t) = 2e^{i\frac{\varphi}{2}} \left[ \vec{E}_{sym}(r, z, t) \cos(k_z d - \frac{\varphi}{2}) + i\vec{E}_{anti}(r, z, t) \sin(k_z d - \frac{\varphi}{2}) \right]. \quad (\text{E.16})$$

Continuing with the previous example where  $E_{sym} = A(\cos(k_z z) \sin(\omega t))$  and  $E_{anti} = A(\cos(\omega t) \sin(-k_z z))$ :

$$\begin{aligned} \vec{E}(r, z + d, t) &= A(\cos(k_z z) \sin(\omega t)) e^{ik_z d} + A(\cos(\omega t) \sin(-k_z z)) e^{ik_z z d} \\ &+ A(\cos(k_z z) \sin(\omega t)) e^{-ik_z d} e^{i\varphi} - A(\cos(\omega t) \sin(-k_z z)) e^{-ik_z z d} e^{i\varphi} \\ &= A(\cos(k_z z) \sin(\omega t)) \left( e^{ik_z d} e^{-\frac{i\varphi}{2}} + e^{-ik_z d} e^{\frac{i\varphi}{2}} \right) \\ &+ A(\cos(\omega t) \sin(-k_z z)) \left( e^{ik_z d} e^{-\frac{i\varphi}{2}} - e^{-ik_z d} e^{\frac{i\varphi}{2}} \right) \\ &= 2e^{i\frac{\varphi}{2}} \left[ \vec{E}_{sym}(r, z, t) \cos(k_z d - \frac{\varphi}{2}) + i\vec{E}_{anti}(r, z, t) \sin(k_z d - \frac{\varphi}{2}) \right], \end{aligned}$$

which was found above in Equation E.16.

Extending the Floquet theorem (Equation E.12) to multiple cells results in:

$$\begin{aligned} \vec{E}(r, z + 2d, t) &= \vec{E}(r, z, t) e^{\pm 2ik_z d} \\ &\cdot \\ &\cdot \\ &\cdot \\ \vec{E}(r, z + md, t) &= \vec{E}(r, z, t) e^{\pm mik_z d}. \end{aligned}$$

Equation E.16 becomes:

$$\vec{E}(r, z + md, t) = 2e^{i\frac{\varphi}{2}} \left[ \vec{E}_{sym}(r, z, t) \cos(mk_z d - \frac{\varphi}{2}) + i\vec{E}_{anti}(r, z, t) \sin(mk_z d - \frac{\varphi}{2}) \right], \quad (\text{E.17})$$

where  $\vec{E}(r, z + md, t)$  is the electric field along the  $z$  axis,  $m$  is the cell number,  $d$  is

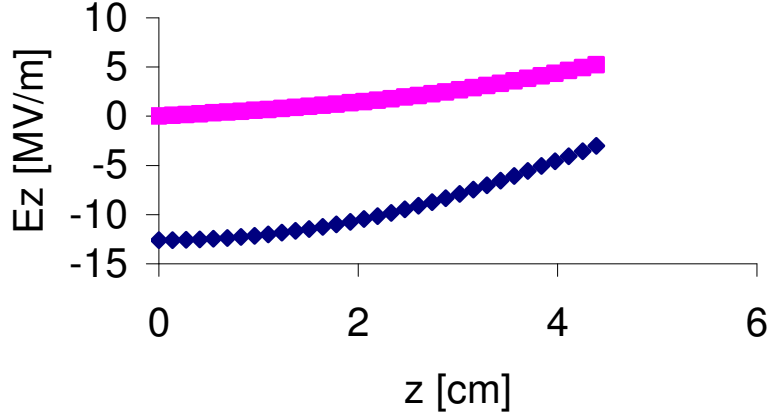


Figure E.2: Symmetric (diamonds) and antisymmetric (squares) wave output from SUPERLANS for the half cell geometry and the  $\frac{4\pi}{6}$  mode.

half a wavelength of the structure,  $\varphi$  is the phase advance per cell,  $k_z$  is the wave number in the  $z$  direction,  $k_z d = \varphi$ ,  $\vec{E}_{sym}(r, z, t)$  is the symmetric standing wave output from SUPERLANS, and  $\vec{E}_{anti}(r, z, t)$  is the antisymmetric standing wave output from SUPERLANS.

The symmetric and antisymmetric wave output from SUPERLANS, for the half cell geometry and the  $\frac{4\pi}{6}$  mode, is shown in Figure E.2. The symmetric and antisymmetric wave output from SUPERLANS, for the six-cell structure is shown in Figure E.3 panels (a), (b), and (c). The corresponding electric field on axis for the full six-cell structure is shown in Figure E.3 panels (d), (e), and (f).

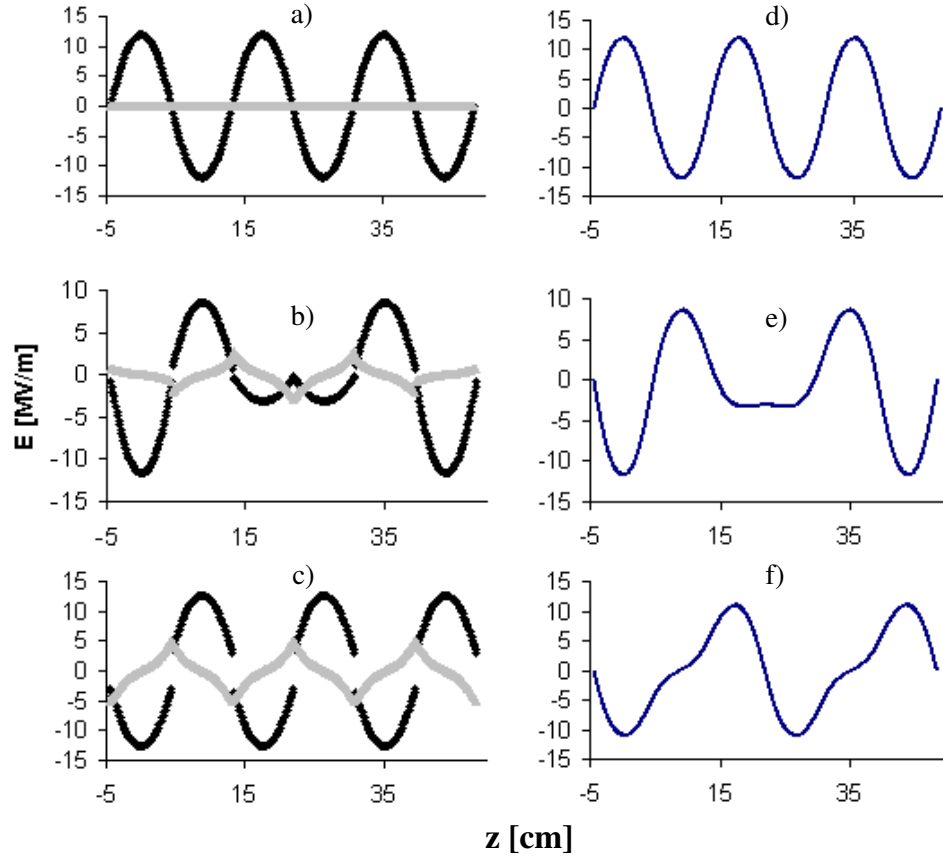


Figure E.3: Panels (a), (b), and (c): The dark symbols represent the symmetric standing wave output from SUPERLANS and the light symbols represent the antisymmetric standing wave output from SUPERLANS. Panels (d), (e), and (f): Electric fields on axis. Symmetric and antisymmetric standing waves were combined using the Floquet theorem. Modes observed in this study were  $\pi$ ,  $\frac{5\pi}{6}$ , and  $\frac{4\pi}{6}$ .

# Appendix F

## Data and Endpoint Energy

### F.1 Cavity #2 $\pi$ Mode

Two scans were made of each cavity, and each mode, to show that the results were reproducible. The x-ray energy spectra obtained from cavity # 2,  $\pi$  mode, are presented in Figure F.1. Panels a) and b) show the x-ray count with the background subtracted. Panels c) and d) show the data with energy binning applied. The high intensity peaks are numbered and questionable peaks labeled alphabetically. Table F.1 indicates the centroid and endpoint energy, obtained in ORIGIN, of the high intensity x-ray peaks identified in the corresponding figures.

Table F.1: Cavity #2,  $\pi$  mode, high intensity peak location and endpoint energy. Numbering corresponds to Figure F.1.

Cavity #	Mode	Scan #	Peak ID	Centroid [cm]	Endpoint Energy [keV]
2	$\pi$	1	A	$12.4 \pm 0.1$	$540 \pm 5$
"	"	1	1	$28.9 \pm 0.1$	$928 \pm 1$
"	"	1	2	$37.9 \pm 0.1$	$774 \pm 1$
"	"	1	3	$45.8 \pm 0.1$	$965 \pm 1$
"	"	1	4	$79.5 \pm 0.1$	$1066 \pm 1$
2	$\pi$	2	B	$13.4 \pm 0.1$	$577 \pm 2$
"	"	2	5	$28.8 \pm 0.1$	$900 \pm 2$
"	"	2	6	$37.5 \pm 0.1$	$733 \pm 2$
"	"	2	7	$45.6 \pm 0.1$	$878 \pm 1$
"	"	2	8	$78.6 \pm 0.1$	$1073 \pm 1$

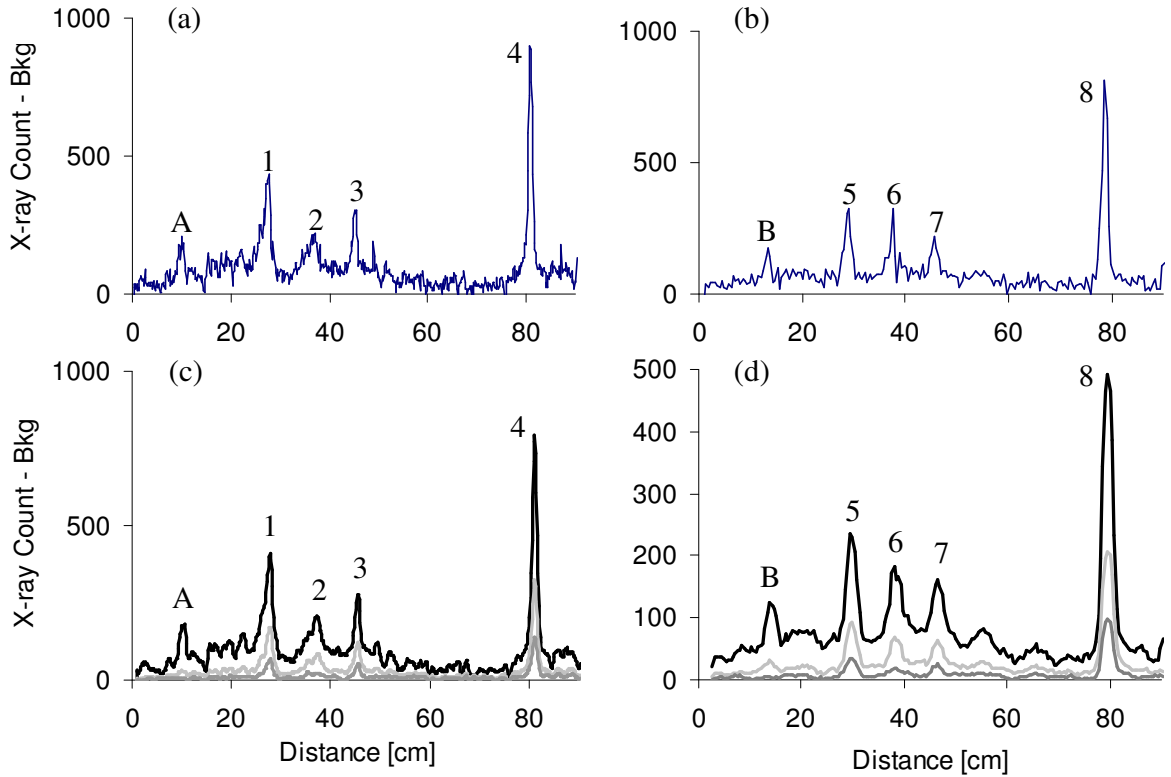


Figure F.1: Cavity #2  $\pi$  mode. Panels (a) and (b): Data accumulated for two scans of the cryostat with the background subtracted. Panels (c) and (d): Energy binning of data in panels (a) and (b). The black plot represents the number of x-rays at all energies, the light-gray plot represents the number of x-rays with energies of 400 keV and above, and the medium-gray plot represents the number of x-rays with energies of 600 keV and above. A moving average was applied to the data to smooth inconsistencies in adjacent two-second intervals.

## F.2 Cavity #2 $\frac{5\pi}{6}$ Mode

Two scans of cavity #2 were made in the  $\frac{5\pi}{6}$  mode. The x-ray energy spectra obtained from cavity # 2,  $\frac{5\pi}{6}$  mode, are presented in Figure F.2. Panels a) and b) show the x-ray count with the background subtracted. Panels c) and d) show the data with energy binning applied. The high intensity peaks are numbered and questionable peaks labeled alphabetically. Table F.2 indicates the centroid and endpoint energy, obtained in ORIGIN, of the high intensity x-ray peaks identified in the corresponding figures.

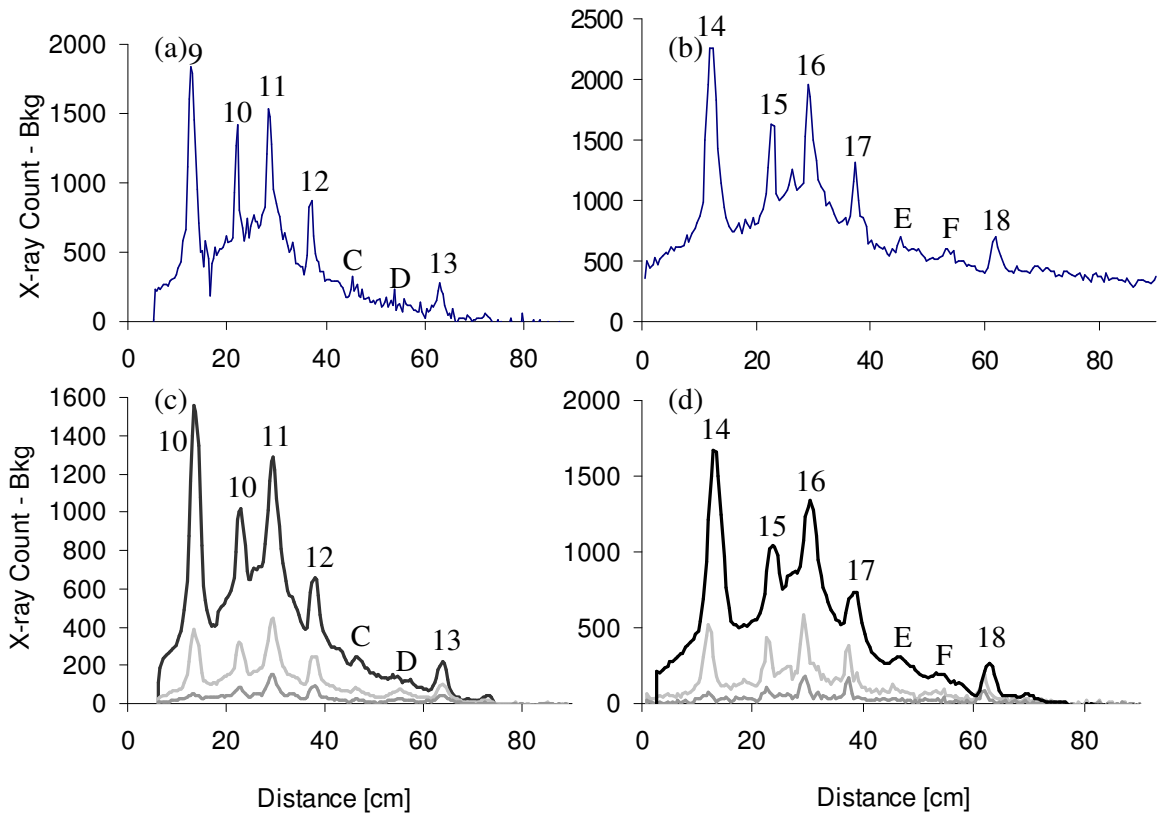


Figure F.2: Cavity #2  $\frac{5\pi}{6}$  mode. Panels (a) and (b): Data accumulated for two scans of the cryostat with the background subtracted. Panels (c) and (d): Energy binning of data in panels (a) and (b). The black plot represents the number of x-rays at all energies, the light-gray plot represents the number of x-rays with energies of 400 keV and above, and the medium-gray plot represents the number of x-rays with energies of 600 keV and above. A moving average was applied to the data to smooth inconsistencies in adjacent two-second intervals.

Table F.2: Cavity #2,  $\frac{5\pi}{6}$  mode, high intensity peak location and endpoint energy. Numbering corresponds to Figure F.2.

Cavity #	Mode	Scan #	Peak ID	Centroid [cm]	Endpoint Energy [keV]
2	$\frac{5\pi}{6}$	1	9	$12.9 \pm 0.1$	$756 \pm 1$
"	"	1	10	$22.0 \pm 0.1$	$857 \pm 1$
"	"	1	11	$28.6 \pm 0.1$	$979 \pm 1$
"	"	1	12	$37.0 \pm 0.1$	$957 \pm 1$
"	"	1	C	$45.6 \pm 0.1$	$723 \pm 3$
"	"	1	D	$53.7 \pm 0.1$	$728 \pm 2$
"	"	1	13	$63.0 \pm 0.1$	$902 \pm 2$
2	$\frac{5\pi}{6}$	2	14	$12.3 \pm 0.1$	$755 \pm 1$
"	"	2	15	$22.8 \pm 0.1$	$800 \pm 1$
"	"	2	16	$29.4 \pm 0.1$	$923 \pm 1$
"	"	2	17	$37.4 \pm 0.1$	$874 \pm 1$
"	"	2	E	$45.4 \pm 0.1$	$790 \pm 1$
"	"	2	F	$53.3 \pm 0.1$	$752 \pm 2$
"	"	2	18	$61.9 \pm 0.1$	$940 \pm 1$

### F.3 Cavity #2 $\frac{4\pi}{6}$ Mode

Two scans of cavity #2 were made in the  $\frac{4\pi}{6}$  mode. The x-ray energy spectra obtained from cavity # 2,  $\frac{4\pi}{6}$  mode, are presented in Figure F.3. Panels (a) and (b) show the x-ray count with the background subtracted. Panels c) and d) show the data with energy binning applied. The high intensity peaks are numbered and questionable peaks labeled alphabetically. Table F.3 indicates the centroid and endpoint energy, obtained in ORIGIN, of the high intensity x-ray peaks identified in the corresponding figures.

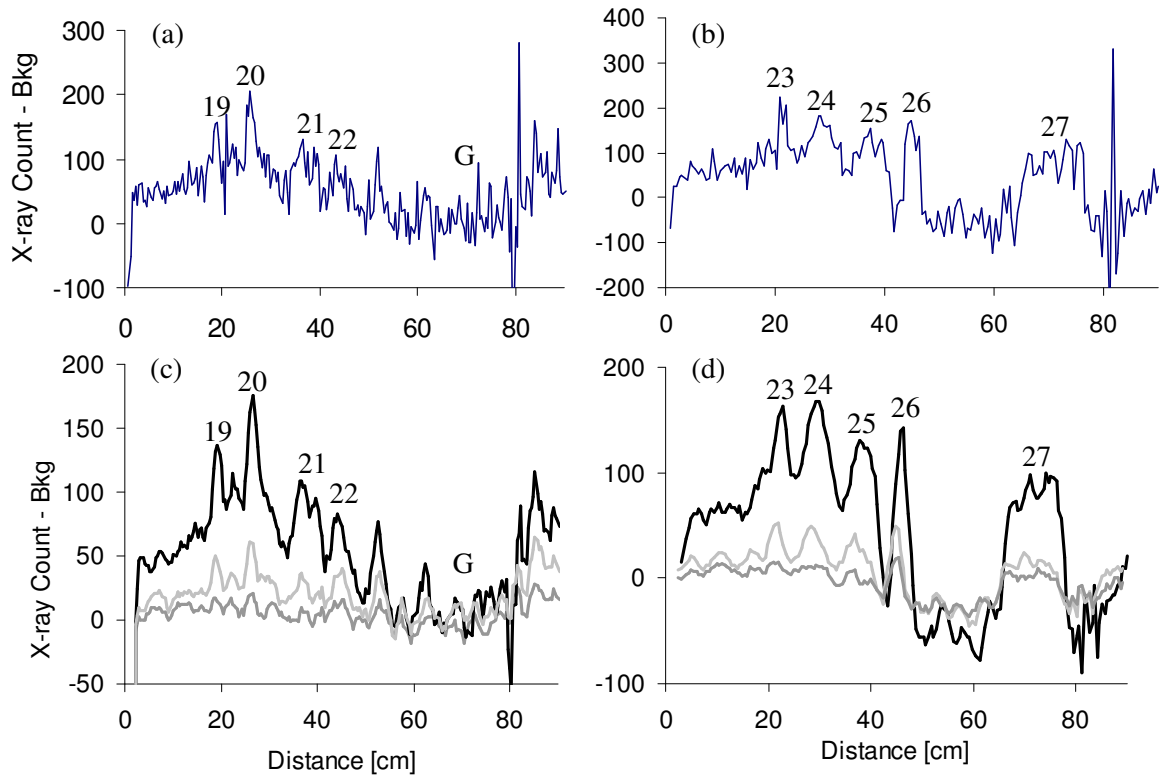


Figure F.3: Cavity #2  $\frac{4\pi}{6}$  mode. Panels (a) and (b) Data accumulated for two scans of the cryostat with the background subtracted. Panels (c) and (d): Energy binning of data in panels (a) and (b). The black plot represents the number of x-rays at all energies, the light-gray plot represents the number of x-rays with energies of 400 keV and above, and the medium-gray plot represents the number of x-rays with energies of 600 keV and above. A moving average was applied to the data to smooth inconsistencies in adjacent two-second intervals.

Table F.3: Cavity #2,  $\frac{4\pi}{6}$  mode, high intensity peak location and endpoint energy. Numbering corresponds to Figure F.3.

Cavity #	Mode	Scan #	Peak ID	Centroid [cm]	Endpoint Energy [keV]
2	$\frac{4\pi}{6}$	1	19	$18.6 \pm 0.1$	$678 \pm 2$
"	"	1	20	$26.3 \pm 0.1$	$724 \pm 2$
"	"	1	21	$36.2 \pm 0.2$	$814 \pm 5$
"	"	1	22	$43.3 \pm 0.1$	$813 \pm 2$
"	"	1	G	—————	—————
2	$\frac{4\pi}{6}$	2	23	$21.5 \pm 0.1$	$745 \pm 1$
"	"	2	24	$28.5 \pm 0.2$	$670 \pm 3$
"	"	2	25	$37.1 \pm 0.2$	$750 \pm 4$
"	"	2	26	$45.0 \pm 0.1$	$771 \pm 2$
"	"	2	27	$70.1 \pm 0.2$	$669 \pm 2$

## F.4 Cavity #1 $\pi$ Mode

The x-ray energy spectra obtained from cavity #1,  $\pi$  mode, are presented in Figure F.4. Panels (a) and (b) show the x-ray count with the background subtracted. Panels (c) and (d) show the data with energy binning applied. The high intensity peaks are numbered and questionable peaks labeled alphabetically. Table F.4 indicates the centroid and endpoint energy, obtained in ORIGIN, of the high intensity x-ray peaks identified in the corresponding figures.

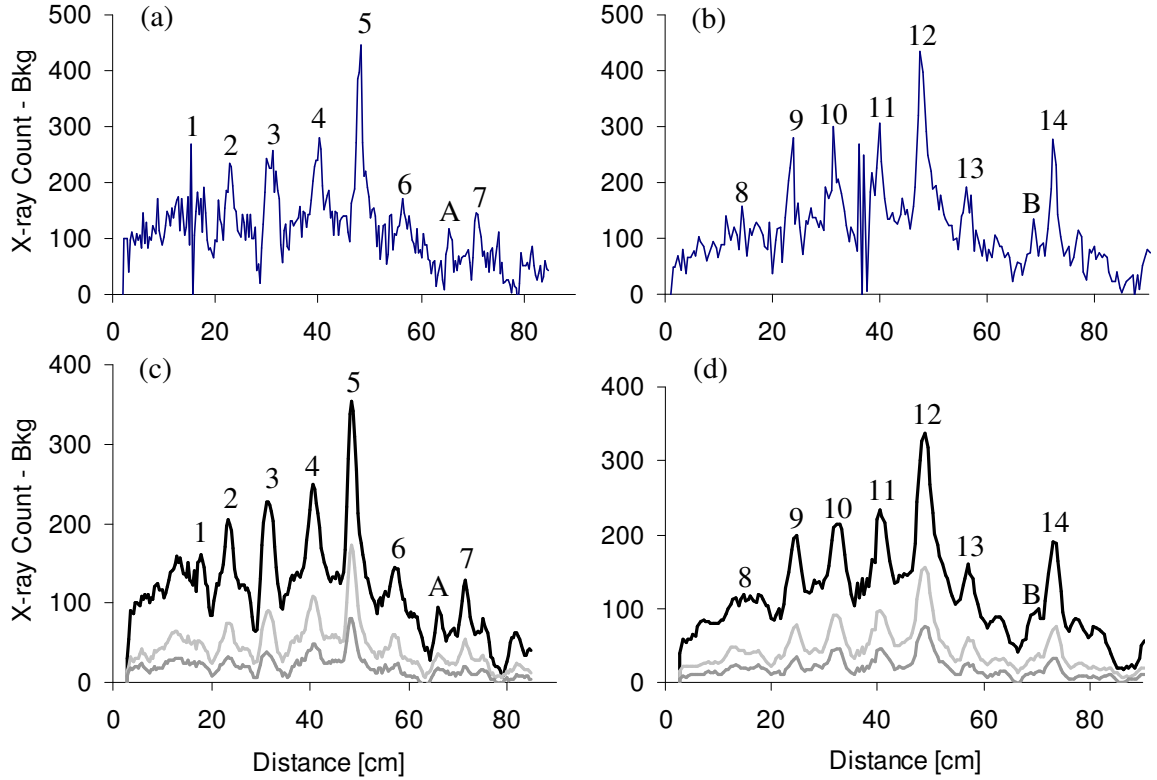


Figure F.4: Cavity #1  $\pi$  mode. Panels (a) and (b): Data accumulated for two scans of the cryostat with the background subtracted. Panels (c) and (d): Energy binning of data in panels (a) and (b). The black plot represents the number of x-rays at all energies, the light-gray plot represents the number of x-rays with energies of 400 keV and above, and the medium-gray plot represents the number of x-rays with energies of 600 keV and above. A moving average was applied to the data to smooth inconsistencies in adjacent two-second intervals.

## F.5 Cavity #1 $\frac{5\pi}{6}$ Mode

The x-ray energy spectra obtained from cavity #1,  $\frac{5\pi}{6}$  mode, are presented in Figure F.5. Panels (a) and (b) show the x-ray count with the background subtracted. Panels (c) and (d) show the data with energy binning applied. The high intensity peaks are numbered and questionable peaks labeled alphabetically. Table F.5 indicates the centroid and endpoint energy, obtained in ORIGIN, of the high intensity x-ray peaks identified in the corresponding figures.

Table F.4: Cavity #1,  $\pi$  mode, high intensity peak location and endpoint energy. Numbering corresponds to Figure F.4.

Cavity #	Mode	Scan #	Peak ID	Centroid [cm]	Endpoint Energy [keV]
1	$\pi$	1	1	$14.5 \pm 0.1$	$972 \pm 1$
"	"	1	2	$22.9 \pm 0.1$	$827 \pm 2$
"	"	1	3	$30.8 \pm 0.1$	$957 \pm 1$
"	"	1	4	$40.0 \pm 0.1$	$797 \pm 3$
"	"	1	5	$47.9 \pm 0.1$	$972 \pm 1$
"	"	1	6	$56.5 \pm 0.1$	$821 \pm 3$
"	"	1	A	$64.5 \pm 0.1$	$737 \pm 1$
"	"	1	7	$70.9 \pm 0.1$	$806 \pm 4$
1	$\pi$	2	8	$14.4 \pm 0.3$	$913 \pm 1$
"	"	2	9	$23.5 \pm 0.1$	$846 \pm 1$
"	"	2	10	$31.5 \pm 0.1$	$926 \pm 2$
"	"	2	11	$39.9 \pm 0.1$	$768 \pm 2$
"	"	2	12	$47.8 \pm 0.1$	$1065 \pm 1$
"	"	2	13	$56.1 \pm 0.1$	$845 \pm 2$
"	"	2	B	$61.9 \pm 0.1$	$776 \pm 1$
"	"	2	14	$72.3 \pm 0.1$	$878 \pm 1$

Table F.5: Cavity #1,  $\frac{5\pi}{6}$  mode, high intensity peak location and endpoint energy. Numbering corresponds to Figure F.5.

Cavity #	Mode	Scan #	Peak ID	Centroid [cm]	Endpoint Energy [keV]
1	$\frac{5\pi}{6}$	1	15	$15.1 \pm 0.1$	$556 \pm 10$
"	"	1	16	$22.0 \pm 0.2$	$733 \pm 2$
"	"	1	17	$29.5 \pm 0.1$	$652 \pm 3$
"	"	1	18	$33.5 \pm 0.1$	$736 \pm 2$
"	"	1	19	$43.9 \pm 0.1$	$554 \pm 6$
"	"	1	20	$52.2 \pm 0.1$	$605 \pm 2$
"	"	1	21	$61.1 \pm 0.1$	$859 \pm 1$
"	"	1	22	$68.8 \pm 0.1$	$937 \pm 2$
1	$\frac{5\pi}{6}$	2	23	$15.0 \pm 0.1$	$573 \pm 9$
"	"	2	24	$21.5 \pm 0.1$	$697 \pm 3$
"	"	2	25	$31.1 \pm 0.1$	$678 \pm 5$
"	"	2	26	$33.6 \pm 0.2$	$961 \pm 4$
"	"	2	27	$47.1 \pm 0.1$	$532 \pm 30$
"	"	2	28	$50.9 \pm 0.1$	$749 \pm 4$
"	"	2	29	$61.0 \pm 0.1$	$876 \pm 2$
"	"	2	30	$68.8 \pm 0.1$	$871 \pm 1$

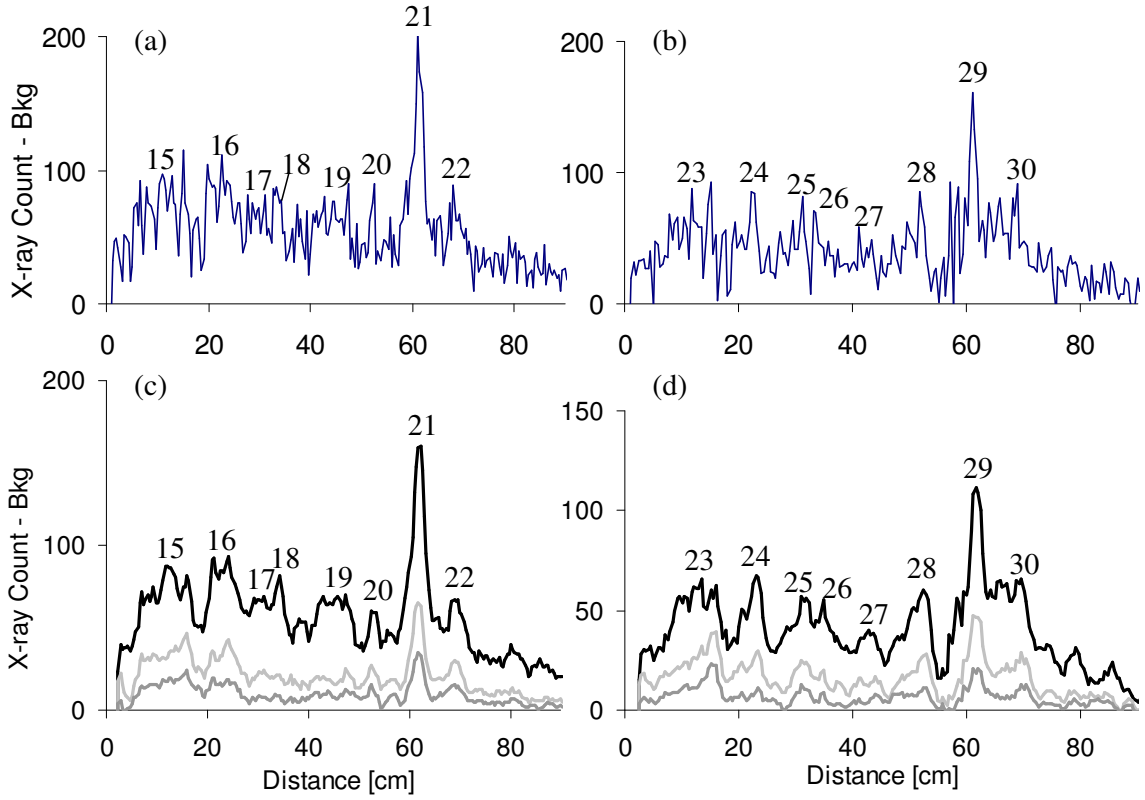


Figure F.5: Cavity #1  $\frac{5\pi}{6}$  mode. Panels (a) and (b): Data accumulated for two scans of the cryostat with the background subtracted. Panels (c) and (d): Energy binning of data in panels (a) and (b). The black plot represents the number of x-rays at all energies, the light-gray plot represents the number of x-rays with energies of 400 keV and above, and the medium-gray plot represents the number of x-rays with energies of 600 keV and above. A moving average was applied to the data to smooth inconsistencies in adjacent two-second intervals.

# Bibliography

- [1] S. E. Musser, J. Bierwagen, T. Grimm, and W. Hartung. X-ray imaging of superconducting rf cavities. In *Proceedings of the 2005 SRF Workshop*, 2005. 1, 2
- [2] R. D. Evans. *The Atomic Nucleus*. Robert E. Krieger Publishing Company, Malabar, Florida, 1982. 1, 2, 27, 28, 29, 30, 33, 34, 35, 36, 37, 38, 39, 40, 41, 42, 173, 174, 175, 176
- [3] Ph.D. J. Knobloch. *Advanced Thermometry Studies of Superconducting RF Cavities*. PhD thesis, Cornell University, 1997. 2, 7
- [4] H. Padamsee, J. Knobloch, and T. Hays. *RF Superconductivity for Accelerators*. John Wiley & Sons, Inc., New York, 1998. 3, 4, 5, 6, 7, 16, 17, 18, 19, 20, 21, 26, 59, 171, 176
- [5] V. Wu. *Design and Testing of a High Gradient Radio Frequency Cavity for the Muon Collider*. PhD thesis, University of Cincinnati, 2002. 7
- [6] S. Ramo, J. R. Whinnery, and T. Van Duzer. *Fields and Waves in Communication Electronics, 2nd Edition*. John Wiley & Sons, Inc., New York, 1984. 10, 153, 154, 155, 157
- [7] M. R. Spiegel and J. Liu. *Mathematical Handbook of Formulas and Tables, second edition*. McGraw-Hill, New York, 1999. 11, 157
- [8] M. Abramowitz and I. A. Stegun. *Handbook of Mathematical Functions, 10th Edition*. Dover Publications, Inc., New York, 1972. 11, 157
- [9] H. Wiedemann. *Particle Accelerator Physics I, 2nd Edition*. Springer, 2003. 12, 13, 175, 176
- [10] R. H. Good jr. and E. W. Müller. *Handbook der Physik*. Springer-Verlag, Berlin, Göttingen, Heidelberg, 1956. 19, 20, 22, 23, 24, 162, 165, 166, 168, 169
- [11] J. W. Wang and G. A. Loew. Field emission and rf breakdown in high-gradient room-temperature linac structures slac-pub-7684. Technical report, Stanford Linear Accelerator Center, 1997. 21, 24, 25, 26, 169, 170, 171
- [12] A. H. Compton and S. K. Allison. *X-rays in Theory and Experiment, 2nd Edition*. D. Van Nostrand Company, Inc., Princeton, New Jersey, 1960. 26

- [13] Garrett and Frey. [www.home.att.net/](http://www.home.att.net/) 27, 34
- [14] N. Tsouldfanidis. *Measurement and Detection of Radiation, 2nd Edition*. Taylor & Francis, Washington, DC, 1995. 27, 28, 29, 33, 36, 37, 38, 40, 41, 42, 46, 48, 49, 64, 174, 175, 176
- [15] H. Kuhlenkampff. *Annelan der Physik*, lxi:page 548, 1923. 30
- [16] H. A. Kramers. On the theory of x-ray absorption and of the continuous x-ray spectrum. *Philosophical Magazine*, 1923. 31
- [17] H. W. Koch and J. W. Motz. Bremsstrahlung cross-section formulas and related data. *Reviews of Modern Physics*, 31(4), 1959. 31
- [18] W. Heitler. *The Quantum Theory of Radiation, 3rd Edition*. Oxford at the Clarendon Press, 1970. 37
- [19] G. F. Knoll. *Radiation Detection and Measurement, 3rd Edition*. John Wiley & Sons, 1999. 39, 41, 46, 47, 48, 49, 65, 72, 174, 175, 176
- [20] H. R. Hulme, J. McDougall, R. A. Buckingham, and R. H. Fowler. *Proceedings of the Royal Society of London*, volume **149**, page 131. 1935. 40
- [21] NIST. <http://physics.nist.gov/physrefdata/xraymasscoef/cover.html>. 44, 45, 60
- [22] Efficiency calculations for selected scintillators. Saint-Gobain, 1995. 50
- [23] NIST. <http://www.boulder.nist.gov/div818/81803/2004//standardsforsuperconcharacter/index.html>. 58
- [24] C. C. Compton et. al. Prototyping of a multicell superconducting cavity for acceleration of medium-velocity beams. *Physical Review Special Topics - Accelerators and Beams*, **8**:042003, 2005. 59
- [25] T. L. Grimm et. al. Experimental study of an 805 MHz cryomodule for the rare isotope accelerator. In *XXII International Linear Accelerator Conference*, 2004. 59
- [26] D. R. Lide Ph.D. *CRC Handbook of Chemistry and Physics, 81st Edition*. CRC Press, 2000. 73, 108
- [27] D. G. Myashishev and V. P. Yakovlev. An interactive code superlans for evaluation of rf-cavities and acceleration structures. In *Proceedings of the 1991 Accelerator Conference*, page 3002. IEEE, 2004. 101
- [28] S. Belomestnykh. Superlans for pedestrians. SRF 941208-11, Cornell Laboratory of Nuclear Studies Internal Report, 1994. 101, 176
- [29] R. Ferraro. Guide to multipacting/field emission simulation software, sixth edition, 1996. 104, 107

- [30] R. Klatt, F. Krawczyk, W.-R. Novender, C. Palm, T. Weiland, B. Steffen, T. Barts, M. J. Browman, R. Cooper, C. T. Mottershead, G. Rodenz, and S. G. Wipf. Mafia—a three dimensional electromagnetic cad system for magnets, rf structures, and transient wake-field calculations. In *1986 Linear Accelerator Conference Proceedings*, page 276. SLAC-303, 1986. 105
- [31] D. J. Griffiths. *Introduction to Quantum Mechanics*. Prentice-Hall, Inc., New Jersey, 1995. 151, 162, 163, 165
- [32] J. D. Jackson. *Classical Electrodynamics, 3rd Edition*. John Wiley & Sons, Inc., New York, 1998. 152
- [33] T. Wangler. *RF Linear Accelerators*. John Wiley & Sons, 1999. 175, 178
- [34] S. S. M. Wong. *Introductory Nuclear Physics, 2nd Edition*. John Wiley & Sons, INC., 1998. 176